AXL TARGETING INDUCED EXPANSION OF TCF1^{+} CD8 T CELLS RESTORES PD-1 BLOCKADE SENSITIVITY OF STK11/LKB1 MUTANT NON-SMALL CELL LUNG CANCER

APPROVED BY SUPERVISORY COMMITTEE

John D. Minna, M.D.

Rolf A. Brekken, Ph.D.

Yang-Xin Fu, MD, Ph.D.

Ralph J. DeBerardinis, M.D., Ph.D.

Todd A. Aguilera, M.D., Ph.D.

Esra Akbay, Ph.D.

DEDICATION

To my mentors, and my family.

AXL TARGETING INDUCED EXPANSION OF TCF1^{+} CD8 T CELLS RESTORES PD-1 BLOCKADE SENSITIVITY OF STK11/LKB1 MUTANT NON-SMALL CELL LUNG CANCER

by

HUIYU LI

DISSERTATION

Presented to the Faculty of the Graduate School of Biomedical Sciences

The University of Texas Southwestern Medical Center at Dallas

In Partial Fulfillment of the Requirements

For the Degree of

DOCTOR OF PHILOSOPHY

The University of Texas Southwestern Medical Center at Dallas

Dallas, Texas

December, 2021

ACKNOWLEDGEMENT

Raising up a student through PhD study takes huge time and effort, and for my circumstances, it takes multiple labs and their people to make it come true. It is to these labs and people that I will be forever grateful, for their knowledge of science, reasoning, and curiosity.

I would like to express my utmost gratitude to Drs. John D. Minna, Rolf A. Brekken, and Yang-Xin Fu. While they are all supremely intelligent, dedicated, and collaborative scientists, their expertise in diverse fields and strengths flourished my study time here in various aspects. I can't imagine how I could make any of the progress without John's wisdom, tremendous support, and kind caring. John is fully supportive of any of your proposed studies, and he always being passionate and curious about it as well. He passes along the collaborative nature of his work to my project, which crosses multiple different fields and stimulated my passion. As a giant in lung cancer, he must be the most caring and kind giant I have ever met in my life. Not only in science, but his encouragements and supports had also prepared me better to move forward as a researcher in this field with professionalism and abilities to navigate through all things that I might encounter. Rolf always has an open door to students, and this project would not have initiated with his expertise and proposal. He really knows about the target AXL, which eventually became the target of treatment in my study. Rolf always stay up-to-date about the progress in the project, with his great enthusiasm and passion, he motivated me in exploring the science

forward. Last but not least, Yang-Xin's advanced knowledge and techniques in cancer immunology, had really opened up a whole new world to me, which attracts me with the beauty of the science. Yang-Xin always has sparkling ideas, which broaden the projects and leads to new discoveries. I cannot express enough my gratefulness to all of them, and their guidance will always enlighten my professional career.

I would also like to give my special thanks to the rest of my thesis committee: Drs. Esra Akbay, Todd Aguilera, and Ralph J. DeBerardinis. They provided invaluable suggestions and insightful comments, which incented my critical thinking abilities and widen my research values. Without the wonderful cell line models that Dr. Akbay had been provided, we would have been encountered much more difficulties in dissecting immune mechanisms.

My sincere thanks also go to everyone here at UT Southwestern Medical Center who helped contribute directly to my paper and provided a caring, supportive, and engaging working environment. Drs. Zhida Liu and Anli Zhang taught in detail immunology-related techniques and ways of exploring underlying mechanisms. These techniques were all complicated and fancy to me initially, and I cannot master them without their help. Dr. Longchao Liu strengthened my immunology knowledge from single cell level, with his expertise, our single cell RNA-seq data were able to be fully utilized. Dr. Chuanhui Han's insights in molecular biology combined with immunology, provided us with a fantastic platform for exploring immune mechanisms. Dr. Noah Sorrelle's wonderful multiplex immunohistochemistry

techniques with his enthusiastic support further enlightened my knowledge in immunohistochemistry. Hyunsil Park is always helpful and delightful to work with, and I could only survive from the tremendous amount of mouse work needed with her help. Dr. Luc Girard is the most helpful and knowledgeable “computer guy” I could always turn to for help, and he always could provide fantastic analyses with new knowledge I could learn. Kimberley Avila knows everything you need to know to do a wonderful western blot, and with her help, there was no tricky western blot to be unresolved. Drs. Kenneth Huffman Longshan Li, and Boning Gao are always trying to help with my projects with their insightful suggestions, and my life with their wisdoms, and their efforts raised up a kid to be a more professional scientist. I also want to expand my thanks to Drs. Michael Peyton, Amit Das, Paul Yenerall, Mahboubeh Papari-Zareei, Brenda Timmons, Jason Toombs, Huocong Huang, Changzheng Lu, and Xuezhi Cao for creating an awesome caring, supportive, fun, and engaging working environment. I want to thank all that had been worked with, but not named here, for their inputs and the fantastic working environment they provided. I’d also like to thank all the individuals in Ignacio Wistuba’s lab at UT MD Andersson Cancer Center and BerGenBio ASA, Norway that were a tremendous help in providing clinical data analyses – Luisa M. Solis, Carmen Behrens, Sharia Hernandez-Ruiz, Lu Wei, Austin Rayford, David Micklem, Hani Gabra, Gro Gausdal, and James B. Lorens.

My great appreciation also goes to Drs. Jill M. Siegfried and Mariya Farooqui, for their wonderful training and opportunities they provided to me. Their

encouragement and support stimulated me to continue my scientific career and made me believe that I could actually do a great job before anyone else told me so.

My gratitude also expands to Mikayla Stokes, Marianne Mercer, Zhaoning Wang, Qianbin Zhang, Yingjie Hu, Joshua Gagan, Dan Fan, and Rui Chen, for their encouragement and support during my graduate study at Dallas. Graduate school study encounters difficulties and challenges at times, but I can always ask for support and balance my life with them.

I specifically want to write in memoriam of Ze Zhang, a truly elegant collaborator and colleague of mine. I will always remember the moments that we debugged together from night to night, and your encouragement to me to proceed with coding-related analyses. I am really proud of the work you had done. As one of my dearest friends, I wish you rest in peace.

Last but not least, I would like to thank my parents and my other family members, for their support spiritually throughout my years of study and my life in general. They are always the ones you could turn to for help and support.

The journey of my PhD study is definitely unforgettable and I will always be appreciative of all the people I have met here. All of your knowledge, guidance, and support will accompany me for my future scientific journey, and for that, I will be forever grateful. I hope the valuable skills and knowledge I learned from all of you could be passed along to others and enlighten our understandings of nature and our life.

AXL TARGETING INDUCED EXPANSION OF TCF1^{+} CD8 T CELLS RESTORES PD-1 BLOCKADE SENSITIVITY OF STK11/LKB1 MUTANT NON-SMALL CELL LUNG CANCER

Huiyu Li, PhD

The University of Texas Southwestern Medical Center at Dallas, 2021

Supervising Professors: John D. Minna, MD, and Rolf A. Brekken, PhD

Mutations in *STK11/LKB1* in non-small cell lung cancer (NSCLC) are associated with poor patient responses to immune checkpoint blockade (ICB) for unknown reasons. We found that introduction of a *Stk11/Lkb1* (*L*) mutation into murine lung

adenocarcinomas driven by mutant *Kras* and *Trp53* (*KP*) resulted in an ICB refractory syngeneic *KPL* tumor. Mechanistically, this occurred because *KPL* mutant NSCLCs lacked TCF1-expressing CD8 T cells, a phenotype that was recapitulated in human *STK11/LKB1* mutant NSCLCs. We found that systemic inhibition of Axl results in increased type I interferon secretion from dendritic cells that expands tumor-associated $TCF1^+$ $PD\text{-}1^+$ CD8 T cells, restoring therapeutic response to PD-1 ICB for *KPL* tumors. This effect was observed in syngeneic immunocompetent mouse models and in humanized mice bearing *STK11/LKB1* mutant NSCLC human tumor xenografts. Anecdotal NSCLC patients with *STK11/LKB1* mutant tumors also demonstrated responses to the combination of AXL inhibitor bemcentinib and pembrolizumab. We conclude that AXL is a critical targetable driver of immune suppression in *STK11/LKB1* mutant NSCLC.

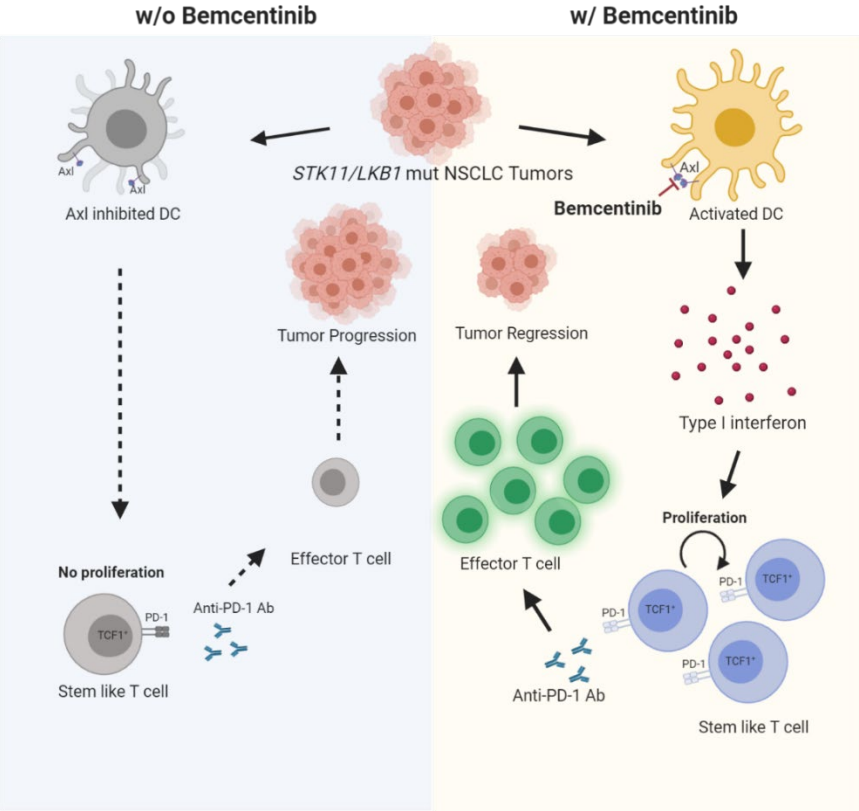
w/o Bemcentinib
w/ Bemcentinib
Axl
Axl
Axl inhibited DC
STK11/LKB1 mut NSCLC Tumors
Axl
Bemcentinib
Activated DC
Tumor Progression
Tumor Regression
Type I interferon
Effector T cell
Proliferation
No proliferation
Anti-PD-1 Ab
PD-1
TCF1+
Effector T cell
PD-1
TCF1+
PD-1
TCF1+
PD-1
TCF1+
Anti-PD-1 Ab
Stem like T cell
Stem like T cell

TABLE OF CONTENTS

PRIOR PUBLICATIONS

Zhang, A., Ren, Z., Tseng, K.F., Liu, X., **Li, H.**, Lu, C., Cai, Y., Minna, J.D. and Fu, Y.X., 2021. Dual targeting of CTLA-4 and CD47 on Treg cells promotes immunity against solid tumors. Science Translational Medicine, 13(605), p.eabg8693.

Mender, I., Zhang, A., Ren, Z., Han, C., Deng, Y., Siteni, S., **Li, H.**, Zhu, J., Vemula, A., Shay, J.W. and Fu, Y.X., 2020. Telomere stress potentiates STING-dependent anti-tumor immunity. Cancer Cell, 38(3), pp.400-411.

LIST OF FIGURES

LIST OF TABLES

LIST OF ABBREVIATIONS

NSCLC – Non-small cell lung cancer

SCLC – Small cell lung cancer

ICB – Immune checkpoint blockade

TME – Tumor microenvironment

LUAD – Lung Adenocarcinoma

AAH – Atypical adenomatous hyperplasia

CIS – Carcinoma in situ

TKIs – Tyrosine kinase inhibitors

CTLA-4 – Cytotoxic T-lymphocyte antigen-4

PD-1 – Programmed death protein 1

PD-L1 – Programmed death protein ligand 1

MSI – Microsatellite instability

GEMM – Genetically engineered mouse models

APCs- Antigen presenting cells

ADCP- Antibody-dependent cellular phagocytosis

DCs – Dendritic cells

MDSCs – Myeloid derived suppressor cells

ISGs – Interferon stimulated genes

CBMC – Cord Blood Mononuclear Cells

qPCR – Quantitative Polymerase Chain Reaction

OVA- Ovalbumin

BMDMs- Bone marrow derived macrophages

BMDCs- Bone marrow derived dendritic cells

ELISPOT – Enzyme-linked immunosorbent spot assay

ELISA – Enzyme-linked immunosorbent assay

GSEA – Gene set enrichment analysis

scRNAseq – Single-cell RNA sequencing

UMAP – Uniform Manifold Approximation and Projection

CHAPTER ONE
Introduction

1.1 Lung cancer - Introduction

As of 2020, lung cancer remains to have second highest number of cases diagnosed worldwide in both male and female patients, despite prostate cancer diagnosed in men and breast cancer diagnosed in women. Regardless of gender, lung cancer is the number one cause of cancer associated death with a five-year survival rate at ~18%. In 2021, the estimated patient numbers will be diagnosed with lung cancer will be reached to ~235,760, and the estimated lung cancer related death is ~131,880 in the United States (Siegel et al., 2021).

Occurrence of lung cancer is ~85% correlated with smoking history, with other risk factors including air pollution, indoor radon, occupational respiratory carcinogens, and asbestos (Brownson et al., 1992; Freedman et al., 2008; Kettunen et al., 2017; Lorenzo-González et al., 2019; Olsson et al., 2017; Pope Iii et al., 2002; Samet, 1991; Shankar et al., 2019). Other than environmental factors, nutrition patterns, chronic inflammation of the lung, chronic obstructive pulmonary disease, pulmonary fibrosis may also affect the lung cancer occurrence.

Based on the morphology, cell of origins, and clinical outcomes, lung cancer could be classified into two main classes, non-small cell lung cancer (NSCLC, ~80%-85%)

and small cell lung cancer (SCLC, ~15%-20%) (Larsen & Minna, 2011). Non-small cell lung cancer usually originated from bronchogenic or alveolar epithelium cells and could be further sub-classified into adenocarcinoma (~40%), squamous cell carcinoma (~30%), and large-cell neuroendocrine carcinoma (~15%). Adenocarcinoma cells tend to stain mucin positive and usually exhibit heterogenous histology. Low grade adenocarcinoma tumors resemble the normal glandular structure, whereas more de-differentiated tumors will lose this feature (Solis et al., 2012). Squamous cell carcinomas are characterized by keratinization and /or intercellular bridges as the most common features (Perez-Moreno et al., 2012). Large cell neuroendocrine carcinomas usually feature in a larger size of the anaplastic cells with an increased cytoplasmic-to-nuclear ratio. Small-cell carcinoma cells exhibit minimal amount of cytoplasm and its nuclei is usually highly similar as to adjacent cells, known as nuclear molding (Pass et al., 2012).

The formation of malignant lesions of lung cancer features the classic hallmarks of cancer, with uncontrolled growth of the tumor cells which could not be recognized and cleared by immune system. Tumor cells exhibit enabled replicative immortality, with their growth suppressors or programmed cell death regulation became dysfunction and become self-sustain for proliferation signals. With increased nutrition needs for outgrowth of tumor cells, angiogenesis usually occurs where tumor formed (Douglas Hanahan & Weinberg, 2011). In recent years, evading immune system supervision and reprogramming of the cellular metabolism have

also be considered as new hallmarks of cancer (D Hanahan & Weinberg, 2015; Pavlova & Thompson, 2016). Tumor cells gained these hallmarks through accumulative multistep genetic and epigenetic alterations within the cells. When mutation occurred, cells thereafter gained growth advantage will be favored, and who evade immune system clearance could be kept and formed a preneoplasia or premalignant lesions. Due to the error-prone highly proliferative features of those cells, eventually, an outgrowth and clonal expansion of these cells would further break the growth balance and immune supervision to form malignant lesions.

A subset of adenocarcinoma is believed developing from atypical adenomatous hyperplasia (AAH), due to the pathogenic mutations occurred in type II pneumocytes, a type of alveolar cells constitutes only ~3% of the alveolar surface of gas exchange airways, but able to regenerate. Squamous cell carcinoma is believed to progressed from bronchial squamous dysplasia and carcinoma in situ (CIS), which begins in the pathological progression from cells lining the larger bronchi in proximal airways. Neuroendocrine cell hyperplasia is believed to be a preneoplasia of neuroendocrine lung carcinomas, originated from neuroendocrine cells in the lung. Although small cell carcinoma cells also feature in neuroendocrine characteristics, its precursor lesion remain unclear (Wistuba & Gazdar, 2006).

Progression of malignant transformation usually occurs from a gain or loss of function mutation, deletion or amplification, and chromosomal alterations to gain

growth advantages. An increased activity of a proto-oncogenes through mutation, amplification or increased expression turns it into an oncogene. Continuously expression or activation of the gene could drive preneoplasia or tumor formation. These allow increased growth signal transduction through autocrine or paracrine loop, which could aid cellular proliferation. The dysfunction of tumor suppressor genes either through loss of heterozygosity, mutation, deletion, or promoter methylation, on the other hand, also play an important role in pathogenesis, as they otherwise could counteract the over-activation of oncogenes. Naturally, cells are resistant to malignant transformation, and successful transformation usually requires the co-operation of multiple oncogenes (Weinberg, 2013). In lung adenocarcinoma, the gain-of-function mutations of *EGFR*, *KRAS* and *MET*, the amplification of *MET*, *EGFR* and *MDM2* are most frequently seen in the patients. Squamous carcinoma patients usually exhibit amplified *EGFR*, *MET*, and *MYC* expression. For all NSCLC subtypes, *p53*, *PTEN*, *RB* or *CDKNA2A* loss have high incidence to occur. The gain of function genes in SCLC or neuroendocrine carcinomas have rarely been identified except *MYC* amplification and ASCL1 expression, defines the feature of neuroendocrine SCLC. *MYC* amplification in SCLC drives NEUROD1^{+} and YAP1^{+} subtypes development in SCLC. Non-neuroendocrine SCLC is believed to be developed from tuft cells, which features high *POU2F3* expression, and from EMT with intact *RB1* expression and high *YAP1* expression (Ireland et al., 2020; Rudin et al., 2019). However, the loss of *Rb* and *FHIT* are nearly universal in SCLC patients (Jamal-Hanjani et al., 2017; Pass et al., 2012). In recent years, heterogeneity of

tumors is being more recognized evaluated, including same type of tumor cells harbor different mutation patterns, or even a trans-differentiation from non-small cell tumor cells to small cell tumor cells (Ahmed et al., 2018). To date, several of kinase inhibitors had been developed to specifically inhibit oncogenic genes. Nevertheless, restoring tumor suppressor function pharmacologically remain impractical, due to the nature of loss-of-function genetic alterations in tumor suppressors. The detailed management and treatment of lung cancer patients will be discussed in the next section.

1.2 Current treatment regimen for lung cancer

Lung cancer management and treatment are determined following cancer TNM staging guidelines from NCCN. Where T indicates the primary tumor sizes, N indicates the number of lymph nodes were detected with tumor cells in surrounding regions, and M indicates whether the tumor had been metastasized. Primary tumor could be further staged based on size into T1 to T4, with sub-staging of a and b included in each stage. If the tumor cannot be found, patients will be classified as T0 stage. N0 indicates no observable cancer in lymph nodes, and N1 to N3 indicates different number and location of lymph nodes that could be detected with cancer. When patients were diagnosed as M0, no metastatic stie was identified. Otherwise, M1 will be assigned to patients if there was any metastatic site. For T and M

staging, the larger the numeric number refers to more advanced stages of disease. If the extent or size could not be measured, TX, NX, or MX will be assigned, respectively (Edge et al., 2010).

For NSCLC treatment, tumors at stage T1-T2, with none or limited lymph nodes with cancer (N0, N1) and no metastatic sites, surgical resections or CT-guided percutaneous ablation would be performed. To date, surgical resection remains to be optimal choice to patients have clean tumor margins with a 5-year survival rate of 63% and 35% for localized and regional NSCLC. Inoperable patients undergone CT-guided percutaneous ablation also shows promising survival times (Chan et al., 2021). Early detection is the key for optimal management of NSCLC.

However, metastasis usually occurs at early stage of NSCLC. Over half of the patients already had metastatic sites when diagnosed, leaves NSCLC inoperable (Badawy et al., 2018). Systematic treatments will then be the option for metastatic NSCLC patients, including chemotherapy, targeted gene inhibitor treatment, and immunotherapy. Chemotherapy employs toxic chemicals to target fast growing cells in NSCLC patients, utilizing the characteristic that tumor cells usually grow faster and applies to ~50% or NSCLC patients. Platinum-based chemotherapy binds a platinum compound to DNA to induce cell apoptosis (Siddik, 2002). Tubulin binding agents (paclitaxel and docetaxel), topoisomerase inhibitor (irinotecan, topotecan), DNA synthesis inhibitor (gemcitabine), or folate metabolism and purine and

pyrimidine synthesis inhibitor (pemetrexed) are usually given in combination with platinum-based chemotherapy. Due to the universal targeting of fast-growing cells in human body and less selective to tumor cells, chemotherapies are usually more toxic. Targeted therapy individualized patient treatment, to select corresponding tyrosine kinase inhibitors (TKIs) based on tumor genotyping. TKIs inhibit gain-of-function oncogene being constitutively activated in tumor cells, which aid growth advantages of ~25% NSCLC. To date, TKIs targeting *EGFR* (15-17%), *KRAS* G12C (4-8%), *ALK* (3-4%), *MET* exon 14 (2-3%), *ROS1* (1%), *BRAF/MEK* (1%), *NTRK* (<1%) mutation or amplification had been approved to treat NSCLC patients clinically. For *EGFR* and *ALK* mutations, multiple generations of inhibitors had been approved to treat NSCLC patients gained resistance to 1st generation TKIs (Araujo et al., 2021; Herbst et al., 2018). Although TKIs are more selective than chemotherapy, only ~25% of patients are qualified to the treatment, and resistance usually occurs within a year. Immune checkpoint blockade (ICBs) had revolutionized NSCLC treatment, with monoclonal antibodies targeting cytotoxic T-lymphocyte antigen-4 (CTLA-4) and programmed death protein 1 (PD-1) or programmed death-ligand 1 (PD-L1), to awake tumor associated immune cells to control NSCLC progression, which would be discussed in detailed in later section.

For NSCLC patients without druggable oncogenes to treat with TKIs (~75%), chemotherapy will be applied first before ICBs after resistance occurred, if patient PD-L1 expression and microsatellite instability (MSI) were low. Otherwise, ICBs will

be applied as a first line therapy, before chemotherapy. NSCLC patients with identified druggable tyrosine/kinase mutation are treated with TKIs as first line therapy, with chemotherapy or ICBs as second or third line of treatment when patient progressed from TKIs treatment. Criteria of treating these patients with either ICBs or chemotherapy also depends on PD-L1 expression and MSI status, same as above guidelines.

Small cell lung cancer treatment regimens are similar to NSCLC when the staging was early, and the tumor is operable with no metastasis. SCLC patients with restricted primary tumor site and limited lymph node spread, concurrent chemotherapy (carboplatin, and etoposide) plus radiation would be employed as first-line therapy. Although cure is possible, side effect is commonly seen. If not all tumor sites could be treated with radiotherapy, concurrent chemotherapy with ICBs are the stand of care. However, SCLC patients usually develop resistance to all chemotherapy treatment within 2 years, and the ICBs treatment response rate remain to be extremely low at ~3-5% (Pavan et al., 2019; Saltos et al., 2020). Therefore, more therapeutic strategies in treating SCLC are needed to improve the survival of SCLC patients.

1.3 Immunotherapy in lung cancer

Immunotherapy had revolutionized lung cancer treatment and become the standard of care in the field. Immunotherapy utilizes the host immune system to recognize, kill and clear “abnormal self” cancer cells. Currently, FDA approved immunotherapies targeting T cells in treating lung cancer primarily include anti-PD-1/PD-L1 therapy to prevent CD8 T cells exhaustion, and anti-cytotoxic T-lymphocyte-associated protein 4 (CTLA-4) therapy to prevent regulatory T cell suppression on CD8 T cells. PD-1 is primarily expressed on the surface of T and B cells as a receptor, when engaged with its ligand PD-L1, the activity of T cells will be suppressed. Although PD-1/PD-L1 axis are expressed to prevent over-activation of self-recognizing T cells and prevent autoimmunity in human body, lung tumor cells hijack the pathway. By upregulating PD-L1 expression in tumor cells, the activity of infiltrated T cells in tumors are inhibited thus failed to monitor and clear out tumor cells. Ipilimumab (anti-CTLA4) was the first FDA approved immune checkpoint inhibitor to treat metastatic melanoma in 2011 (Hodi et al., 2010; Leach et al., 1996). CTLA-4 is a protein receptor constitutively expressed in regulatory T cells and are upregulated in activated conventional T cells. When engaged with CD80/CD86 expressed in antigen presenting cells (APCs), it inhibits T cell activity. A more detailed discussion of anti-tumor responses generated from immune cells will be discussed in the next section.

To date, there are over 500 ongoing immunotherapy trails (Clinicaltrials.gov) involving three kinds of FDA approved ICB antibodies, including anti-PD-1

antibodies (nivolumab, pembrolizumab, and cemiplimab), anti-PD-L1 antibodies (atezolizumab and durvalumab), and anti-CTLA4 antibody (ipilimumab and tremelimumab) to treat NSCLC patients. In a phase 1 clinical trials reported in 2012 includes multiple type of advanced cancers, patients were treated with anti-PD-L1 therapy dosing based on body weight. For responding NSCLC patients, half of the patients responded for 1 year or longer and 10% of them managed to reach stable disease (Brahmer et al., 2012, 2013). Comparing to traditional chemotherapy, overall survival of patients received ICB were significantly longer than chemotherapy group (≥50% hazard ratio = 0.69) in KEYNOTE-042 with NSCLC patients have at least 1% of PD-L1 expression within tumors (Mok et al., 2019). For NSCLC patients with a PD-L1 expression larger than 50% in tumors, median overall survival was 30.0 months with pembrolizumab and 14.2 months with chemotherapy (hazard ratio = 0.63) in KEYNOTE-024 (Reck et al., 2019). Even for recurrent metastatic SCLC patients who usually experience relapse within 6 months, 61% of responding patients responses to pembrolizumab for more than 18 months in KEYNOTE-028/158 and 6-12 months to nivolumab or/and ipilimumab in CheckMate-032 and KEYNOTE-604 (Antonia et al., 2016; Chung et al., 2020; Rudin et al., 2020). In HANSHIN 0316 clinical trial, even patients ceased ICB treatments due to adverse events, the stable disease (SD) patients gained 4.9-months median progression free survival (PFS) benefit, and the median PFS was not reached for patients with a partial response (PS) (Tachihara et al., 2018). These trials indicated a long-lasting

protective effect in lung cancer patients treated with ICB therapy, which had never been achieved with any of the other systematic treatment applied clinically before.

However, major challenges remain for lung cancer immunotherapy. Although responding lung cancer patients gained significant prolonged survival time, objective response rates remain low at ~18-20% in NSCLC patients and ~10%-30% in SCLC patients (Antonia et al., 2016; Chung et al., 2020). Yet the biomarkers to identify potential benefiting patients are still limited.

As if for now, PD-L1 expression is the only biomarker approved clinically as ICB treatment responses (Ettinger et al., 2021). Investigations of the predictive value of microsatellite instability (MSI) status, tumor mutation burden (TMB), and tumor infiltrating T patterns are still ongoing. In KEYNOTE-001 clinical trials conducted by Merck, a significant correlation of better overall survival duration in response to pembrolizumab with PD-L1 expression was indicated in NSCLC patients (Garon et al., 2015). However, in KEYNOTE-028/158 trial, 2 patients achieved complete responses and 1 of them actually had PD-L1 negative tumor (Chung et al., 2020). In CheckMate 277 trial, both patients have >1% PD-L1 expression or <1% PD-L1 expression benefited from ICB treatment, and the hazard ratio for death did not correlate with PD-L1 expression (>1% with a hazard ratio of 0.79, <1% with a hazard ratio of 0.62) (Hellmann et al., 2019). In SCLC, PD-L1 expression is universal low

and poorly explored while some patients still able to gain significant clinical benefits (Carvajal-Hausdorf et al., 2019).

Microsatellite instability high (MSI-H)/mismatch repair deficient (dMMR) in tumors had been reported correlated to ICB responses, and approved as a biomarker for patient selection to treat with ICB in colon cancer (de la Chapelle, 2003; Marabelle et al., 2020). Patients exhibit MSI-H or dMMR have higher mutation numbers in their genome, a result from impaired DNA mismatch repair. With higher number of mutations generated, more neoantigens may generated for tumor cells to be recognized by immune system. However, the frequency of MSI-H found in NSCLC patients are as low as 0.8% and none had been indicated in SCLC patients (Chung et al., 2018; Warth et al., 2016).

Tumor mutation burden of NSCLC patients are characterized through whole-exosome sequencing to count the nonsynonymous mutation per megabase (Mb). Potential prognostic value of TMB was first reported in 2015, and NSCLC patients with higher TMB in two independent cohorts are associated with improved objective response, and 6-months longer PFS time (Rizvi et al., 2015). In CheckMate-026 clinical trial, patients with a high TMB (≥243 missense mutations) had 3.9-months prolonged PFS and 18.5% higher objective response rate, but no significant overall survival (OS) differences for patients undergone nivolumab or chemotherapy were found (Carbone et al., 2017). In CheckMate-277 and CheckMate-568 clinical trials,

which includes a large number of patients, there were 42% in CheckMate-277 and 34% in CheckMate-568 of tumors failed to obtain a TMB score (Hellmann et al., 2018; Ready et al., 2019). Failure of obtaining a TMB score mainly result from a poor quality and limited availability of tumor tissue, a longer storage time for obtained samples may also decrease mutations found in tissue (S. Chen et al., 2018). To date, there has not been a clear cutoff or standards for mutation burden evaluation in lung cancer patients. With an average of 2-3 weeks turnaround time to evaluate TMB, it exceeds the treatment decision windows recommended by the College of American Pathologists/International Association for the Study of Lung Cancer (Addeo et al., 2019). The TMB and correlation with ICB in SCLC has not been reported, however, a lower mutation burden is commonly seen in SCLC patients than NSCLC patients (Drapkin & Farago, 2019). Taken together, TMB serve as a biomarker to predict ICB treatment responses in lung cancer patients need further studies to become a reliable marker.

Recently, tumor immune microenvironment (TME), especially pre-infiltrating T cell status, has become an emerging biomarker for predicting immunotherapy responses and prognostic factor in lung cancer patients (Galon et al., 2014; Galon & Bruni, 2019; Hiraoka et al., 2006). Preclinically, T cell infiltration had been correlated with better anti-PD-1/PD-L1 response (Tang et al., 2016). In KEYNOTE-028 trial, there was a correlation of more T cell infiltration to better overall response rate (ORR) and longer PFS in small-cell lung cancer patients (Ott et al., 2019). However, limited

clinical analyses had been done in regard of immunotherapy responses with T cell infiltration status in NSCLC. The potential of utilizing TME as a biomarker for ICB treatment responses in lung cancer patients needs further evaluation.

Several oncogenes commonly seen in lung cancer, however, had been studied for their immunotherapy response pattern. In a phase II trial (NCT02879994) for treating EGFR mutant NSCLC patients, the study was terminated after 11 patients were treated with pembrolizumab as first-line treatment. None of the patients gained progression benefits, although over 73% of them had PD-L1 expression over 50% (Lisberg et al., 2018). In a meta-analysis of second line ICB treatment for lung cancer patients, Checkmate 057, Keynote-010, and POPLAR were included (Borghaei et al., 2015; Fehrenbacher et al., 2016; Herbst et al., 2016). In 1903 lung cancer patients, 1362 *EGFR* wildtype patients showed prolonged OS comparing to docetaxel group (hazard ratio = 0.66, favors PD-1/PD-L1 inhibitor). However, 186 *EGFR*-mutant NSCLC patients failed to gained OS benefit from ICB treatment (hazard ratio = 1.05) (Lee et al., 2017). These large number of patients studied validated the non-responsiveness of *EGFR* mutant lung cancer patients to ICB treatment.

Although *KRAS* mutated patients tend to have higher PD-L1 expression and tumor mutation burden, they failed to show significant prolonged PFS and OS in response to ICB treatment in multiple clinical trials worldwide (Gadgeel et al., 2019; Leena

Gandhi et al., 2018; Jeanson et al., 2019). Frost et al reported the potential positive prognosis of $KRAS^{G12C}$/TP53 co-mutated NSCLC patients treated with pembrolizumab as first line therapy. In their study conducted in Germany, this patient cohort achieved 100% response rate to pembrolizumab, with 33.3 months PFS and OS not estimable, comparing to $KRAS^{other}$/TP53 mutated NSCLC patients with an ORR = 27.3%, PFS = 3.9 months and OS = 9.7 months (Frost et al., 2021). In KEYNOTE-158 trial, however, significant improved prognosis of $KRAS^{G12C}$ patients was not observed, indicating a potential need of further stratification of patients based on their TP53 mutation status (Gadgeel et al., 2019; L. Gandhi et al., 2018).

As a tumor suppressor, TP53 mutation had been correlated with better ICB treatment responses in NSCLC patients. In a preliminary integrated analysis of public datasets, a prolonged PFS (hazard ratio = 0.32) was observed in TP53 mutated NSCLC patients (Biton et al., 2018). A retrospective study of 72 NSCLC patients treated with ICB in University of Paris showed a 10 months longer median OS in TP53 mutated NSCLC patients, indicating a promising prognosis for TP53 mutated NSCLC patients (Assoun et al., 2019). However, in the Stand Up to Cancer (SU2C) and CheckMate-057 clinical trials, NSCLC patients harboring additional TP53 mutation with KRAS did not show significant improved clinical benefits. For PFS, TP53 and KRAS (KP) co-mutated patients showed median responses for 3.0 months, comparing to KRAS (K) only patients with 2.7 months. Overall survival of

KP patients were 16.0 months, comparing to K patients with 16.1 months (Skoulidis et al., 2018a). Therefore, the value of TP53 mutation serve as a clinical biomarker for predicting ICB responses in NSCLC patients remain to be an open question.

STK11/LKB1 (*L*) is a tumor suppressor identified that usually co-mutated with *KRAS* with an incidence rate of ~11% in NSCLC patients (Skoulidis et al., 2015). In the SU2C and CheckMate-057 clinical trials, 924 NSCLC patients were treated with ICB treatment and evaluated with their therapeutic responses. When patients harboring *L* mutation, their PFS shortened to 2.7 months, comparing to *K*-only patients with 2.7 months of PFS. The OS were further shortened in *KL* patients with 6.4 months, comparing to *K* only patients with 16.1 months of OS (Skoulidis et al., 2018a). In two independent retrospective analysis of NSCLC patients received ICB treatment conducted by Bristol-Myers Squibb and AstraZeneca, they analyzed NSCLC patient data from Flatiron Health Clinico-Genomic Database (CGDB). GCDB integrated real-world clinical responses and genomic analyses of anonymized cancer patients, which had included over 4,000 lung cancer patients worldwide (Singal et al., 2017). In analysis conducted by Bristol-Myers Squibb, 2276 NSCLC patients were included for analysis, of which 574 were treated with ICB as first-line treatment. Although *L* patients showed worse clinical responses to ICB treatment, their PFS and OS time did not showed interaction between mutation status to ICB treatment responses (Papillon-Cavanagh et al., 2020). AstraZeneca reported that *STK11/LKB1* mutation in 2407 NSCLC patients lead to worse OS and PFS when treated with ICB as first-

line or second-line treatment, whereas this also applies to chemotherapy treatment responses (Shire et al., 2020). Similar findings were also reported in analyses with *KEAP1* mutation. Taken together, *STK11/LKB1* (*L*), and *KEAP1* mutation in lung cancer patients seems serve like a prognostic, but not predictive biomarkers to ICB treatment. Therefore, therapeutic targets for sensitizing these cohorts to ICB treatment remain to be explored.

Besides prognostic biomarkers exploration for predicting lung cancer patients to ICB treatment, combination strategies to sensitize NSCLC patients to ICB treatment are also being actively explored. Currently, concurrent treatment of anti-PD-1/PD-L1 with radiotherapy, tyrosine kinase inhibitors (TKIs), immunotherapy targeting stimulatory or inhibitory immune checkpoints, cytokine and chemokines, metabolic enzyme modulators had been explored both pre-clinically and clinically. As a widely applied adjuvant or neoadjuvant treatment, radiotherapy had been reported in multiple clinical trials for its ability to prolong the response duration of anti-PD-1/PD-L1 responses in NSCLC patients. Keynote-001 trial found significantly increased PFS (4.4 months vs. 2.1 months, hazard ratio = 0.56) and OS (11.6 months vs. 5.3 months, hazard ratio = 0.59) in NSCLC patients received any radiotherapy before pembrolizumab, comparing to patients without previous radiotherapy (Shaverdian et al., 2017). In PEMBRO-RT phase II trial (NCT02492568), significant improvements of PFS (1.9 months vs 6.6 months, hazard ratio = 0.71, favors combination therapy) and OS (7.6 months vs. 15.9 months, hazard ratio = 0.66, favors combination

therapy) were observed in 92 recurrent NSCLC metastatic patients, comparing the single arm treatment of pembrolizumab to combine with radiotherapy (Theelen et al., 2019). Clinical trials focusing on the effect of combining ICB with other immunotherapy targeting stimulatory or inhibitory immune checkpoints, cytokine and chemokines, metabolic enzyme modulators are also being actively investigated.

Most of TKIs, alike chemotherapy, tend to be immune suppressive and have limited benefits to combine with ICB therapy. As numerous trials have been focusing on the effect of combining TKIs targeting oncogenic drivers with ICB therapy, there are emerging evidence showing that TKIs targeting non-essential genes of tumor cells might able to synergize with ICB treatment. One possible explanation would be, that TKIs targeting essential genes could also introduce cytotoxicity to tumor infiltrated immune cells. Otherwise, dosing strategies for TKIs targeting essential genes need to be adjusted from traditional strategy, to limit toxicity to immune cells and trigger immune responses (Z. Liu et al., 2019; Mender et al., 2020).

Axl, a receptor tyrosine kinase, had been widely studied for their role in regulating tumor cell proliferation and colony formation, migration/invasion, epithelial to mesenchymal transition and angiogenesis (Abu-Thuraia et al., 2020; Aguilera et al., 2016; Antony & Huang, 2017; Goyette et al., 2018; D. Kim et al., 2019; Ludwig et al., 2018; Taniguchi et al., 2019). However, it serves as a non-essential gene in tumor cells with no direct cytotoxicity effect when inhibiting it (Matteson, 2010). However, it had been widely reported for their potential role in regulating immune

microenvironment of solid tumors (Aguilera et al., 2016; Lotsberg et al., 2020; Ludwig et al., 2018; Maier et al., 2020; Rothlin et al., 2007; Varnum et al., 1995). As an ongoing phase II clinical trial conducted by Bergen Bio and Merck & Co., Inc. (NCT03184571), more preliminary evidences are emerging clinically for its potentially to sensitize STK11/LKB1 mutant NSCLC patients to anti-PD-1/PD-L1 therapy (Arce-Lara et al., 2018). Therefore, it is worthwhile to dissect the underlying mechanism of responses as it currently remain unclear.

1.4 Major immune cell populations and anti-tumor immunity

Lymphocytes

CD8 T Cells

CD8 T cells are main executor for tumor cell specific killing and memory formation to recognize tumor cell specifically through neoantigens presented by malignant cells. Neoantigens are unique generated from tumor cells, either from somatic mutations resulting in amino acid changes, tumor-specific gene expression, and oncogenic virus production resulting in a high tumoral specific antigen production. Tissue-specific gene expression and gene overexpression generated neoantigens recognized by T cells have lower specificity to tumor cells (Butterfield et al., 2017). Neoantigens presented to naïve CD8 T cells circulating through spleen will activate successful TCR-neoantigen-MHC engaged CD8 T cells. Activated CD8 T cells will

rapidly proliferate and differentiate into cytotoxic T cells. Cytotoxic T cells could then engage with the neoantigen presenting tumor cells, and release perforin and granzyme B to lysis target cells. Some of the naïve T cells activated by antigen presenting cells (APCs) could also transit into memory T cells, which doesn't need the priming- neoantigens are presented by APCs to activate naïve T cells-to activate them again. The formation of memory T cells could last for long time or even more than 20 years for skin resident memory T cells. Therefore, the anti-tumor effect generated by CD8 T cells could be long-lasting.

At the same time, the activity of CD8 T cells is tightly regulated by other immune cells. Cytokines and chemokines secreted by innate immune cells and CD4 T cells, CD8 T cells could be activated or suppressed. By expressing CTLA4, CD8 T cell activity can be suppressed mainly by regulatory T cells (T_{reg}), and regulatory B cells (B_{reg}). APCs and other T cells could also express PD-L1 to engage with PD-1 expressed on CD8 T cells to induce anergy of CD8 T cells, mainly to prevent autoimmunity. However, tumor cells had adapted to suppress CD8 T cells by hijacking these pathway, largely limiting the ability of CD8 T cells to recognize the abnormality of malignant cells (Dangaj et al., 2019; Gajewski et al., 2013; Kortlever et al., 2017; Kurtulus et al., 2018).

Recently, stem-like T cell factor 1 (TCF1, encoded by *Tcf7*) expressing PD-1^{+} CD8 T cells had been identified as a key cell population that respond to PD-1/PD-L1

blockade in the TME (Z. Chen et al., 2019; Im et al., 2016; Miller et al., 2019; Siddiqui, Schaeuble, Chennupati, Fuertes Marraco, et al., 2019; Utzschneider et al., 2016). Existence of $TCF1^+$ $PD1^+$ CD8 T cells allows for the expansion of differentiated $TCF1^-$ $PD\text{-}1^+$ CD8 T cells in response to anti-PD-1/PD-L1 therapy, ultimately leading to tumor growth control. Therefore, tumor associated $TCF1^+$ $PD1^+$ CD8 T cells are key player for mediating anti-tumor T cell immunity upon anti-PD-1/PD-L1 treatment.

CD4 T Cells

Besides cross-priming of tumor associated CD8 T cells through antigen presented by APCs directly, Th1 CD4 T cells could be primed by APCs through MHC class II to facilitate the activation of CD8 T cells through releasing cytokines (S.-H. Kim et al., 2021; Song et al., 2007). The rest subtype of CD4 T cells, including Th2 CD4 T cells, Th17 CD4 T cells, and T_{reg} cells, tend to be associated with inflammation, angiogenesis, or immune suppressed tumor microenvironments (Bindea et al., 2013; Mantovani et al., 2008; Nosho et al., 2010). So far, limited evidence had been shown that CD4 T cells play an direct role in malignant cell lysis, and the prime of CD8 T cells are mainly through cross-presentation interaction between APCs and CD8 T cells directly.

Innate Lymphocytes - Natural Killer Cells

Traditionally, NK cells were considered as part of innate immune cells lack antigen specific reaction capability. In recent years, human CD1d-restricted invariant natural killer cells (iNKT) had been discovered that could recognize a range of bacterial-derived or endogenous lipids in a CD40-depedent manner (Cerundolo et al., 2009; Mori et al., 2016; Salio et al., 2014). By presenting lipid and other metabolite neoantigens, iKNT cells can activate cross-priming DCs potently in a short time of period. Activated cross-priming DCs could further prime tumor associated CD8 T cells, facilitating anti-tumor immune responses (Fujii et al., 2003, 2006; Hermans et al., 2003; Silk et al., 2004). However, due to the distinct distribution and biology of CD1d-restricted NKT cells in murine (diverse NKT cells, dNKT) and human (iNKT), limited studies had been done in elucidating their mechanisms for generating anti-tumor responses. However, by utilizing genome-wide CRISPR-Cas9 screening, MC.5.G5 T cells, a specific dNKT cell clone, could recognize MR1 positive melanoma cells specifically and potentially generate tumor specific immune responses. However, their *in vivo* specificity and reactivity still remain to be explored (Silk et al., 2004).

Antigen Presenting Cells (APCs)

Dendritic Cells

Dendritic cells are professional antigen presenting cells (APCs) specialized in priming T cells in TME and trigger anti-tumor immune responses. Conventional dendritic cells could be classified into cDC1 lineage ($CD8\alpha^+$, $CD103^+$) and cDC2 lineage ($CD11b^+$) (Schlitzer et al., 2015). Where cDC2 could prime conventional CD4 T cells effectively, cDC1 had been identified as major APCs in activating tumor associated CD8 T cells in TME. Cross-priming dendritic cells, a subset of cDC1 cells, had been proved to be the major force for priming tumor associated CD8 T cells and generating anti-tumor immune responses. By presenting neoantigens generated from tumor cells through major histocompatibility class I (MHC-I, or HLA-A/B/C), cross-priming DCs can prime and activate CD8 T cells directly without helper T cells involved. Plasmacytoid dendritic cells (pDCs) had been largely recognized as pro-tumorigenic which could induce $CD8^+$ T_{reg} cells and release immune suppressive cytokines and chemokines (Dress et al., 2019; Hartmann et al., 2003; Wei et al., 2005). In lung tumors, Langerhans cells could also be found, but their roles in regulating immune responses remain largely unexplored.

Macrophages

Macrophages, especially anti-tumor macrophages, could serve as antigen presenting cells in TME through major histocompatibility class II (MHC-II, or HLA-DR) to T and B cells (Junt et al., 2007; Tseng et al., 2013). Its activity was regulated by SIRPα, when engaging with CD47 expressed by other cells in TME, the priming

ability of macrophages will be inhibited. Macrophages could increase the priming of antigen specific CD8 T cells and decrease the priming of antigen specific CD4 T cells, when mediated by anti-CD47 antibody dependent cellular phagocytosis (ADCP) of tumor cells (Tseng et al., 2013). As CD47 is a broadly expressed surface protein on tumor cells, it had been reported as a potential immunotherapy target for solid tumors (Chao et al., 2010; Willingham et al., 2012; Zhang et al., 2021). Besides the potential antigen presentation role, macrophages had been intensively studied in cancer immunotherapy field for their roles in regulating anti-tumor immune responses. Generally, it had been classified into M1 (anti-tumor, anti-inflammatory) or M2 (pro-tumor, pro-inflammatory) macrophages. Tumor associated macrophages could be shifted into M2-like phenotype induced by interleukin-4 (IL-4) and IL-13 mainly produced by Th2 T cells (DeNardo et al., 2009; Pedroza-Gonzalez et al., 2011; Shiao et al., 2015). As M2 macrophages functioning in dampening the adaptive immune responses and triggering immune checkpoints, shifting macrophages status to M1 like had been largely explored for its anti-tumor effect. Considering the abundance of macrophages in lung tumors, macrophages in TME are therefore worthwhile for further study as a potential therapeutic strategy.

Neutrophils

Multiple studies had reported that neutrophils could internalize and present cognate antigens through major histocompatibility class II (MHC-II, or HLA-DR) to T cells or

transfer to dendritic cells through neutrophil extracellular traps (NETs) (Sangaletti et al., 2012; Vono et al., 2017). Similar to macrophages, neutrophils had been classified into N1 and N2 phenotypes based on their role in regulating anti-tumor immunity. Induced by IFN-β, N1 neutrophils could form NETs more efficiently with increased major histocompatibility class II expression, which are essential for neutrophil mediated cytotoxicity (Fridlender et al., 2009; Mishalian et al., 2013). By phagocytosis of tumor cells, N1 neutrophils release myeloperoxidase and H_2O_2 to lyse target cells (Gerrard et al., 1981). N2 neutrophils, on the other hand, had been proved to promote tumor progression, inflammation, and angiogenesis (Jablonska et al., 2010; Mishalian et al., 2013; Tazawa et al., 2003). Therefore, efforts in shifting neutrophil status to N1 would increase the anti-tumor immune responses either directly or through adaptive immune cells in TME.

Other Immune Cells

Myeloid Derived Suppressor Cells (MDSCs)

Known to be suppressive, limited evidence had been shown that MDSCs could be served as cancer immunotherapy target. Recruited by CCL2 and CCL5, chemokines usually highly expressed by lung tumor cells, MDSCs tend to be more suppressive in TME. Unlike in peripheral lymphoid organs, monocytic MDSCs are unable to differentiate into dendritic cells but rapidly transit into tumor associated

suppressive macrophages or remain as monocytes (Kumar et al., 2016). Polymorphonuclear MDSCs in TME, on the other hand, could differentiate into pro-inflammatory neutrophils (Di Carlo et al., 2001). With the high plasticity, targeting MDSCs alone for cancer immunotherapy might be insufficient.

1.5 Goal of this study

As outlined above, clinical therapeutic strategies to increase the response rate of immunotherapy in NSCLC patients are desperately needed. Especially for *STK11/LKB1* mutated NSCLC tumors (incidence rate ~11% in lung adenocarcinoma, LUAD), responses to ICB are usually abrogated (Cho et al., 2020; Koivunen et al., 2008; Shire et al., 2020; Skoulidis et al., 2018a, 2019). Mutations in *KRAS* and *STK11/LKB1* (*KL*) correlate with a more immunosuppressive tumor microenvironment (TME), which may account for the limited response to anti-PD-1/PD-L1 treatment (Kadara et al., 2017; Koyama et al., 2016a; Skoulidis et al., 2018a). Therefore, strategies that sensitize *KL* and *L* mutant NSCLC to ICB therapy would provide a significant clinical impact.

Furthermore, the status of TCF1$^+$ PD-1$^+$ CD8 T cells in *STK11/LKB1* mutated NSCLC tumors remain unexplored. In this study, we compared the immune landscape of mutant *KRAS*-driven NSCLC with and without *STK11/LKB1* mutations

and used mouse models of *KL* NSCLC to determine potential therapeutic targets to sensitize *STK11/LKB1* mutated NSCLC patients to anti-PD-1/PD-L1 therapy.

CHAPTER TWO:
Materials and Methods

2.1 Cell Lines

The KP and KPL cell lines were provided by Dr. Esra Akbay. The H2122 cell line was established by Drs. John Minna and Adi Gazdar at the NIH. A549 was obtained from ATCC. Lenti-X 293T cell line was obtained from Takara (Cat# 632180). TUBO cell line was obtained from Yang-Xin Fu lab. The RNAseq bioinformatic analysis of 143 NSCLC adenocarcinoma cell lines, of which referred to as Hxxxx (established at the NIH) or as HCCxxxx (established at UT Southwestern Medical Center) were established by Drs. John D. Minna and Adi Gazdar: A549, Calu-3, DFCI032, EKVX, H23, H358, H441, H522, H820, H920, H969, H1355, H1373, H1395, H1435, H1437,H1563, H1568, H1573, H1651, H1693, H1703, H1734, H1781, H1793, H1838, H1869, H1944, H1975, H1993, H2009, H2023, H2030, H2073, H2087, H2126, H2135, H2170, H2228, H2250, H2258, H2286, H2291, H2342, H2347, H2444, H2882, H2887, H3122, H3255, HCC15, HCC78, HCC122, HCC149, HCC193, HCC364, HCC515, HCC827, HCC1171, HCC1195, HCC1438, HCC1637, HCC1705, HCC1897, HCC1974, HCC2108, HCC2279, HCC2302, HCC2450, HCC2935, HCC3051, HCC4006, HCC4011, HCC4017, HCC4019, HCC4047, HCC4054, HCC4058, HCC4087, HCC4150, HCC4225, HCC4226, HOP-62, HOP-92, HCC1719, HCC2352, CAL-12T, H292, H596, H1650, H1666, H2405, HCC95, HCC1313, HCC1588, HCC1772, HCC1820, HCC1908, HCC1944, HCC2344, HCC2814, HCC3173, HCC3350, HCC3444, HCC3498, A427, Calu-1, Calu-6,

DFCI024, EBC-1, H125, H157, H322, H324, H460, H647, H650, H661, H838, H1299, H1623, H1648, H1792, H1819, H1915, H2085, H2086, H2110, H2122, H2172, HCC44, HCC366, HCC461, HCC1359, HCC2270, HCC2885, HCC4021, HCC4032, PC-9, SK-LU-1, HCC1501, HCC3195, HCC4190,and LOU-NH1.

2.2 Inhibitors/Peptides/Recombinant Protein Used

Bemcentinib (BGB324) was synthesized by Bergen Bio. FTY720 hydrochloride was purchased from Selleckchem (Cat# S5002). Recombinant murine GM-CSF (Cat# 315-03), murine IFN-γ (Cat# 210-10), murine IL-4 (Cat# 400-04), human GM-CSF (Cat# 300-03) and human TNFα (Cat# 300-01A) were purchased from Peprotech. Clophsome®-A-Clodronate Liposomes (Anionic) was purchased from FormuMax Scientific (Cat# F70101C-A). $OVA_{257-264}$ (SIINFEKL) was purchased from InvivoGen (Cat# vac-sin). Human Ppillomavirus (HPV) E7 protein (49-57) was purchased from GenScript (Cat# RP20249). Ovalbumin (10λ) was purchased from Sigma-Aldrich (Cat# RP20249). pCpGfree-OVA was purchased from InvivoGen (Cat# pcpgf-ova).

2.3 Antibodies

Therapeutic antibodies used include: InVivoMab anti-mouse PD-1 (RMP1-14, BioXCell, Cat# BE0146), InVivoMab rat IgG2a isotype control (2A3, BioXCell, Cat# BE0089), InVivoMab anti-human PD-1 (J110, BioXCell, Cat# BE0193), InVivoMab mouse IgG1 isotype control (MOPC-21, BioXCell, Cat# BE0083), InVivoMab anti-mouse IFNAR-1 (MAR1-5A3, BioXCell, Cat# BE0241), InVivoMAb anti-mouse

CD4(GK1.5, BioXCell, Cat# BE0003), InVivoMAb anti-mouse CD8α (53-6.7, BioXCell, Cat# BE0004), InVivoMab anti-mouse NK1.1 (PK136, BioXCell, Cat# BE0036) and anti-PD-1 (Pembrolizumab, Merck Co.).

Fluorophore conjugated antibodies used for flow cytometry at 6.25 μg/ml include: Anti Mouse Ki-67, PE (BioLegend, Cat# 652404), anti-mouse CD45, Pacific Blue (BioLegend, Cat# 103126), anti-mouse CD45, APC-Cyanine 7 (BioLegend, Cat# 103116), anti-mouse CD8a, Alexa Fluor700 (BioLegend, Cat# 100730), anti-mouse CD8b, PE-Cyanine 7 (BioLegend, Cat# 126616), anti-mouse CD62L, APC (BioLegend, Cat# 104412), anti-mouse CD62L, PE (eBioscience, Cat# 12-0621-83), anti-mouse CD44, Brilliant Violet 605 (BD Biosciences, Cat# 563058), anti-mouse CD44, Brilliant Violet 421 (BioLegend, Cat# 103039), anti-mouse CD279, APC/Cy7 (BioLegend, Cat# 135224), anti-mouse CD69, PerCP/Cy5.5 (BioLegend, Cat# 104522), anti-mouse CD3e, PE (BioLegend, Cat# 100308), anti-mouse CD4, APC/Cy7 (BioLegend, Cat# 100526), anti-mouse CD279, PerCP-Cy5.5 (BioLegend, Cat# 135208), anti-mouse Ki-67, BV605 (BioLegend, Cat# 652413), anti-mouse CD11b, FITC (BioLegend, Cat# 101206), anti-mouse CD11c, APC/Cy7 (BioLegend, Cat# 117324), anti-mouse F4/80, APC (BioLegend, Cat# 123116), anti-mouse Ly-6G, Brilliant Violet 605 (BioLegend, Cat# 127639), anti-mouse Ly6C, PE-Cyanine 7 (BioLegend, Cat# 128018), anti-mouse CD103, PE (BioLegend, Cat# 121406), anti-mouse CD366(TIM3), PE-Cyanine 7 (BioLegend, Cat# 134010), anti-mouse CD3e, Brilliant Violet 786 (BD Biosciences, Cat# 564379), anti-mouse active capase-3, Brilliant Violet 605 (BD Biosciences, Cat# 564094), anti-mouse/rat Foxp3, APC

(eBioscience, Cat# 17-5773-82), anti-mouse MHC II(I-A/I-E), Alexa Fluor 700 (eBioscience, Cat# 56-5321-82), OVA257-264 (SIINFEKL) peptide bound to H-2Kb monoclonal antibody (Flow cytometry, 25-D1.16), APC (eBioscience, Cat# 17-5743-82), anti-human/mouse TCF1/7, Alexa Fluor 488 (Cell Signaling Technologies, Cat# 6444), anti-human/mouse TCF1/7, Alexa Fluor 647 (Cell Signaling Technologies, Cat# 6709), anti-human/mouse phospho-Akt, Alexa Fluor 488 (Cell Signaling Technologies, Cat# 4071), anti-human/mouse phosphor-TBK1, Alexa Fluor 647 (Cell Signaling Technologies, Cat# 14590), anti-human CD45, APC-H7 (BD, Cat# 641408), anti-human CD3, PerCP-Cy5.5 (BioLegend, Cat# 300328), anti-human CD4, Alexa Fluor 700 (BioLegend, Cat# 317426), anti-human CD8a, FITC (BioLegend, Cat# 300906), anti-human CD25 (BioLegend, Cat# 302606), anti-human Foxp3, Alexa Fluor 647 (BD Biosciences, Cat# 560045), anti-human HLA-DR (BD Biosciences, Cat# 564231), anti-human CD279, PE-CF594 (BD Biosciences, Cat# 565024), anti-human CD16, Brilliant Violet 786 (BD Biosciences, Cat# 563689), anti-human CD56, PC7 (BD Biosciences, Cat# 557747), anti-human CD19, Brilliant Violet 421 (BD Biosciences, Cat# 562440), anti-human CD45, Pacific Blue (BioLegend, Cat# 304022), anti-human CD11c (BioLegend, Cat# 301614), anti-human CD141 (BD Biosciences, Cat# 559781), anti-human CD11b, Brilliant Violet 785 (BioLegend, Cat# 301346), anti-human CD16, Alexa Fluor 700 (BD Biosciences, Cat# 557920), anti-human CD33, PE-CF594 (BD Biosciences, Cat# 562492), anti-human CD14, PerCP-Cy5.5 (BD Biosciences, Cat# 562692), anti-human CD15 (BD Biosciences, Cat# 555401), anti-human CD68, PE- Cyanine 7

(BD Biosciences, Cat# 565595), anti-human CD206 (BD Biosciences, Cat# 321138). iTAg Tetramer/PE – H-2 Kb OVA (SIINFEKL) was purchased from MBL (Cat# TB-5001-1), and Tetramer/APC – H-2 K(b) chicken OVA 257-264 (SIINFEKL) was purchased from the NIH Tetramer Facility (IEDB ID# 58560, https://tetramer.yerkes.emory.edu/).

Anti-mouse Fcγiii/ii receptor (clone 2.4G2) (Cat# 553141) and anti-human Fc block (Cat# 564220) were purchased from BD Biosciences.

Biotin conjugated anti-mouse CD45 antibody was used for ELISPOT assay immune cell isolation at 6.25 µg/ml was purchased from BioLegend (Cat# 103104).

The following antibodies were used for IHC or/and western blot: CD8α (D4W2Z) XP® Rabbit mAb (Cell Signaling Technologies, Cat# 98941), LKB1 (D60C5) Rabbit mAb (Cell Signaling Technologies, Cat# 3047), AXL (C89E7) Rabbit mAb (Cell Signaling Technologies, Cat# 8661), Acetyl-CoA Carboxylase (C83B10) Rabbit mAb (Cell Signaling Technologies, Cat# 3676), phospho-Acetyl-CoA Carboxylase (Ser79) (D7D11) Rabbit mAb (Cell Signaling Technologies, Cat# 11818), mTOR (7C10) Rabbit mAb (Cell Signaling Technologies, Cat# 2983), phospho-mTOR (Ser2448) (D9C2) Rabbit mAb (Cell Signaling Technologies, Cat# 5536), AMPK alpha (D5A2) Rabbit mAb (Cell Signaling Technologies, Cat# 5831), phospho-AMPK alpha (Thr172) (D4D6D) Rabbit mAb (Cell Signaling Technologies, Cat# 50081), AKT (11E7) Rabbit mAb (Cell Signaling Technologies, Cat# 4685), phosphor-AKT (Ser473) (D9E) Rabbit mAb (Cell Signaling Technologies, Cat# 4060), GAPDH

(D16H11) Rabbit mAb (Cell Signaling Technologies, Cat# 5174), and Anti-rabbit IgG, HRP-linked Antibody (Cell Signaling Technologies, Cat# 7074).

2.4 Reagents/Commercial Assays

Sulfadiazine/ Trimethoprim (Aurora Pharmaceutical LLC) was purchased from UTSW-Veterinary Drug Services (Cat# 302). GE Healthcare Ficoll-PaqueTM Premium was purchased from Cytiva (Cat# 17544203). Clophsome®-A-Clodronate Liposomes (Anionic) was purchased from FormuMax Scientific (Cat# F70101C-A), Animal free Collagenase, type A was purchased from Sigma (Cat# SCR136), DNAse I was purchased from Roche (Cat# 11284932001), TMB Solution (1X) was purchased from eBioscience (Cat# 00-4201-56), Eosin Phloxine Alcoholic Working Solution was purchased from Poly Scientific (Cat# s176), Harris Modified Method Hematoxylin Stains Solution was purchased from Fisher Chemical (Cat# SH26500D), Surgipath® SelecTech® Hematoxylin 560 (for multiplex IHC staining) was purchased from Leica Biosystems (Cat# 3801571), CellTiter 96 Aqueous One Solution Cell Proliferation Assay (MTS) was purchased from Promega (Cat# G3582), OpalTM 520 Reagent Pack (Cat# FP1487001KT) and OpalTM 570 Reagent Pack (Cat# FP1488001KT) were purchased from PerkinElmer, ProLongTM Gold Antifade Mountant with DAPI was purchased from Invitrogen (Cat# P36931), Chromium I7 Multiplex Kit, 96 rxns was purchased from 10x Genomics (Cat# PN-120262), Mouse IFN-γ ELISPOT Sets (Cat# 551083) and Human IFN-γ ELISPOT Sets (Cat# 552138) were purchased from BD Bioscience. VeriKine-HS Mouse IFN

Beta ELISA Kit (Cat# 42410) and VeriKine Human IFN Beta ELISA Kit (Cat# 414101) were purchased from PBL Assay Science, Mouse Gas6 Quantikine ELISA Kit (Cat# MGA S60) and Proteome Profiler Mouse XL Cytokine Array (Cat# ARY028) were purchased from R&D Systems. True-NuclearTM Transcription Factor Buffer Set was purchased from BioLegend (Cat# 19853), Foxp3/Transcription Factor Staining Buffer Set was purchased from eBioscience (Cat# 00-5523-00). EasySep™ Mouse CD8+ T Cell Isolation Kit (Cat# 19853), EasySep™ Human CD34 Positive Selection Kit II (Cat# 18780), and EasySepTM Mouse Steptavidin RapidSpheres™ Isolation Kit (Cat# 19860) were purchased from STEMCELL Technologies. SuperSignal™ West Pico PLUS Chemiluminescent Substrate was purchased from ThermoFisher Scientific (Cat# 34577). ImmPRESS® HRP Horse Anti-Rabbit IgG Polymer Detection Kit was purchased from Vector Laboratories (Cat# MP-7401). e-Myco PCR Detection Kits was purchased from Bulldog Bio (Cat# 25233). CellTiter® 96 Aqueous One solution Cell Proliferation Assay kit (for MTS assay, Cat# G3582) and CellTox™ Green Cytotoxicity Assay kit (Cat# G8741) were purchased from Promega.

2.5 Cell Culture

All cancer cell lines were grown in 5% FBS (ThermoFisher Scientific, Cat# 26140079) supplemented RPMI 1640 (Millipore Sigma, R8758). TUBO was grown in 10% FBS supplemented Dulbecco's Modified Eagle Medium (DMEM) (ThermoFisher Scientific, Cat# 12430054). Cell lines were routinely tested using

mycoplasma contamination kit (E-myco, Cat# 25233, Bulldog Bio) and cultured under 5% CO_2 at 37 °C.

All primary immune cells isolated were grown in 10% heat deactivated (30 min, 56 °C) FBS (ThermoFisher Scientific, Cat# 26140079) and 1x 2-Mercaptoethanol supplemented RPMI 1640 (Millipore Sigma, R8758). Cells were cultured under 5% CO_2 at 37 °C.

2.6 Viability-based Drug Dose-response Curves

For cell cytotoxicity analysis, 1000-2000 cells for corresponding cell lines were plated into each well of a 96-well plate. After 24 hours, cells were treated with 4-fold serial dilutions of 8 different concentrations for 4 days. At the end time point of treatment, cell viabilities were determined using CellTiter 96 Aqueous One Solution Cell Proliferation Assay (MTS) (Promega, catalog# G3582) on a Molecular Devices SpectraMax 190 microplate reader under 450 nm wavelength. Dose response curve was analyzed through GraphPad Prism.

2.7 Hematoxylin and Eosin (H&E) Staining

Formalin fixed paraffin embedded slides (5 μm) were deparaffinized with xylene, ethanol, and deionized water. Slides were then stained with hematoxylin (Fisher Chemical, Cat# SH26500D) and washed/destained with acid ethanol. Eosin (Poly Scientific, Cat# s176) was then applied to slides and then washed with 95% ethanol. Stained slides were dehydrated with ethanol and xylene.

2.8 Immunohistochemistry (IHC)

2.8.1 General immunohistochemistry

Slides was deparaffinized in Xylene and rehydrated with decreased percentage of the ethanol solution. Slides was washed with 1x PBS buffer before antigen retrieval. Antigen retrieval was performed through placing slides into a bucket containing 1x antigen unmasking solution. For single round of staining or the second or later round of a multi-round staining, citrated based (Vector Laboratories, Cat# H-3300-250) was used. For the first round of multiple-round staining, tris-based antigen unmasking solution (Vector Laboratories, Cat# H-3301-250) was used. Slides were placed into pre-boiled antigen retrieval buffer and an Instagram Pressure Cooker for 8 min. Slides were cooled down to room temperature and washed 3 times with diH_2O and 1 time with PBS. Tissue sections were blocked with 2.5% or 10% goat serum (Vector Laboratories, S-1000-20) for 60 min followed by incubation with primary antibody diluted in blocking buffer overnight at 4℃. Slides were washed three times for 5 min in 1x PBS and incubated with HRP/AP conjugated secondary anti-rabbit/mouse/rat Antibody (ImmPRESS; Vector Laboratories, MP-7401) for 30 min on a shaker and washed 1 time with 1x PBS after incubation. Slides were then developed with corresponding chromogen kit(s) (Betazoid DAB, Cat# SKU DS900H; Warp Red, Cat# SKU WR806; and Ferangi Blue, Cat# SKU FB813H) purchased from Biocare Medical. DAB staining was always performed as the last staining signal. Slides were then counter stained with hematoxylin (Fisher Chemical, Cat#

SH26500D for single staining, Leica Biosystems, Cat# 3801571 for multiple staining) and sealed with VectaMount® AQ Aqueous Mounting Medium (Vector Laboratories, Cat# H-5501-60). Slides were dried overnight and scanned with Hamamatsu Nanozoomer under 40x resolution.

2.8.2 Multiplex immunohistochemistry

Multiplex immunohistochemistry (IHC) was performed as previously described (Sorrelle et al., 2018). Briefly, slides were warmed in a 60℃ oven for 10 min followed by deparaffinization and rehydration. Before antigen retrieval, slides were fixed in 10% neutral buffered formalin for 30 min followed by a PBS wash. Antigen retrieval was performed in antigen retrieval buffer (10 mM Tris-HCl, 1 mM EDTA with 10% glycerol [pH 9]) at 110℃ for 17 min (~4–5ψ). Slides were cooled down to room temperature and washed once with PBS. Tissue sections were blocked with 2.5% goat serum (Vector Laboratories, S-1012) for 30 min followed by incubation with primary antibody (CD8, 1:2000; Cell Signaling, 98941) overnight at 4℃. Slides were washed three times for 5 min in PBST (0.05% Tween 20 and 2 mM EDTA) and incubated with HRP conjugated secondary anti-rabbit Antibody (ImmPRESS; Vector Laboratories, MP-7401) for 30 min on a shaker. Slides were then washed three times for 5 min in PBST. For developing the fluorescence signal, TSA detection system (PerkinElmer) was used. We used Opal 520 to stain for CD8. Multiplex staining was performed by stripping the previous antibody in 10 mM citrate buffer (pH 6.2) plus 10% glycerol at 110℃ for 2 min before blocking and probing with the

next primary Ab: TCF1/7 (1:1000, Cell Signaling Technology, Cat# 2203). Following similar steps from the first round of staining, slides were developed with Opal570 to stain for TCF1/7. Slides were counter-stained with DAPI and then cover-slipped using ProLong Gold mount (Life Technologies, Cat# P36931). Slides were scanned at 20X using the Zeiss Axioscan.Z1 (Whole Brain Microscopy Facility, UT Southwestern). DAPI, AF488 (for Opal520) and AF555 (for Opal570) channels were used to acquire images.

2.9 Immunoblots

For protein detection, KP and KPL cells were cultured in vitro. Protein lysates were collected by washing cells with ice-cold PBS then incubated with a modified RIPA buffer (50 mM Tris, 150 mM NaCl, 0.1% SDS, 1% IGEPAL CA-630, 1% sodium deoxycholate, 2 mM MgCl2, pH 8) with 1 unit/µl benzonase (MilliporeSigma, Cat# E1014), protease inhibitors (MilliporeSigma, Cat# P8340) and phosphatase inhibitors (MilliporeSigma, Cat# 4906845001) on ice for 15 min. Lysed cells were scraped, and protein lysates were harvested. The concentration of total protein was quantified with Bradford Assay (Bio-Rad, Cat# 5000006) according to BSA standard (ThermoFisher Scientific, Cat# 23209). For each sample, 25 µg protein was mixed with loading dye and separated on a NuPAGE 4-20% TGX gel (Bio-Rad, Cat# 5671095) at 150V. Samples were transferred with the Trans-Blot Turbo RTA Mini Nitrocellulose transfer kit (Bio-Rad, Cat# 1704270) on a Trans-Blot Turbo Transfer System (Bio-Rad, Cat# 1704150) following manufacturer's recommended protocols.

The membrane was blocked with 5% milk (Bio-Rad, Cat# 1706404XTU) dissolved in 0.1% in PBST. Membranes were probed with primary antibodies: LKB1 (1:1000, Cell Signaling Technology, Cat# 3047) and GAPDH (1:2500, Cell Signaling Technology, Cat# 5174), blots were incubated at 4°C overnight. After washing with 0.1% PBST, the membranes were with secondary antibody (1:2000, Cell Signaling Technologies, Cat# 7074), washed and imaged with ECL substrate (Bio-Rad, Cat# 1705062), and visualized through a LiCor Odyssey Fc imaging system.

2.10 Plasmid Construction

For regular plasmid construction, Takara or NEB restriction enzyme digestion system were applied to linearize plasmid incubated at 37 °C in water bath for 30 min. Desired plasmid fragments were then cut out from ran gel and extracted using GeneJET Gel Extraction Kit (ThermoFisher, Cat# K0691) following manufacturer's protocol. Extracted fragments and linearized plasmid backbone were conjugated using DNA ligation kit (TaKaRa, Cat# 6021) and incubate at 16°C for 2 hours or overnight.

For CRISPR KO lines, the sgRNA sequences were designed based on the sequence provided by Feng Zhang's laboratory at The Broad Institute (Sanjana et al., 2014). For each target genes, at least two different set sgRNA were tested to achieve efficient gene knock-out. The plasmid backbone used for CRISPR knock out was PSpCas9 (BB)-2A-GFP (PX458), with GFP fused to the Cas9 protein. To clone the sgRNA sequence into the plasmid gRNA scaffold (BbsI digested), the

sgRNA sequence picked was synthesized as oligo as 5'-CACCGNNNNNNNNNNNNNNNNNN-3', and 3'-CNNNNNNNNNNNNNNNNNNNCAAA-5'. The sgRNA primers include:

ms sgAxl F1: caccgCGGAACCCGTGACCCTACTC,

ms sgAxl R1: aaacGAGTAGGGTCACGGGTTCCGc,

ms sgAxl F2: caccgAAGTGTCCCCGTGAGTCCTC,

ms sgAxl R2: aaacGAGGACTCACGGGGACACTTc,

ms sgAxl F3: caccg GAGGATGGGCAGGGTCCCGC,

ms sgAxl R3: aaac GCGGGACCCTGCCCATCCTCc,

ms sgCD53 F1: caccgGTTACGGAAGAGTACTCCAT,

ms sgCD53 R1: aaacATGGAGTACTCTTCCGTAACc,

ms sgCD53 F2: caccgGCCACAGCTCAACACTTTAG,

ms sgCD53 R2: aaacCTAAAGTGTTGAGCTGTGGCc,

ms sgTNFSF15 F1: caccgGAGCCTGCCCGCCTACTAAC,

ms sgTNFSF15 R1: aaacGTTAGTAGGCGGGCAGGCTCc,

ms sgTNFSF15 F2: caccgAGAACGTGGCCCCAAGGTAG,

ms sgTNFSF15 R2: aaacCTACCTTGGGGCCACGTTCTc,

ms sgKRAS F: caccgGTGGTTGGAGCTGATGGCGT,

ms sgKRAS R: aaacACGCCATCAGCTCCAACCACc,

hu sgKRAS F: caccgGTAGTTGGAGCTGATGGCGT,

hu sgKRAS R: aaacACGCCATCAGCTCCAACTACc.

Primers were denatured under 95°C for 4 min, then annealed by decreasing temperature at 0.1°C/s to 16 °C in a PCR machine for half an hour, then the product was ready to be conjugated to PX458 plasmid backbone using DNA ligation kit (TaKaRa, Cat# 6021) with 10:1 ratio of sgRNA and plasmid backbone.

For surface receptor knock-out validation, single cell clones were established using flow-cytometry sorting of GFP positive cells. After several passages, GFP and candidate gene negative single clones will be picked out based on flow cytometry. For intraceulluar knock-out cell lines, single clone of GFP negative cells were established after flow sorting for GFP positive cells and passage, and the knock-out was confirmed through western blot one by one.

2.11 Plasmid Production and Transfection

For transformation, 5 µl ligated reaction mix was added to 25 µl competent cells (TOP10). The mix was placed on ice for 4 min and then undergone heat shock at 42°C for 90 seconds, followed by incubation on ice for 10 min. The transformed cells were then recovered with 400 µl SOC medium (Millipore Sigma, Cat# 1797-10X5) at 37°C for 1 hour at 220 rpm speed. Transformed bacteria was then centrifuged down at 2500 rpm for 3 min to concentrate down to around 150 µl. Transformants were then plated onto agar dishes containing 100 µg/ml ampicillin. Agar plates were then incubated upside down at 37°C overnight. For each plate, 2-4 colonies were picked each into 3 ml LB + 100 µg/ml ampicillin and incubated at 37°C (220 rpm) for no more than 18 hours. Culturing could be scaled up by transferring

200 µl of bacteria containing medium to 300 ml LB medium + 100 µg/ml ampicillin and incubated at 37°C (220 rpm) for no more than 18 hours. Plasmids were then extracted with QIAprep Spin Miniprep Kit (Qiagen, Cat# 27104) or ZymoPURE II Plasmid Maxiprep Kit (Zymo Research, Cat# D4203).

To avoid immunogenicity problems associated with viral transduction of Cas9 *in vivo*, lipofectamine 2000 transfection reagent (ThermoFisher, Cat# 11668019) or PEI MAX® (Poly Sciences, Cat# 24765-1) mediated transfection of the Cas9 construct was used. During transfection, half volume of R10 (heated deactivated FBS) was mixed with FreeStyle™ 293 expression medium (Gibco™, Cat# 12338018). Plasmids containing medium was removed after 6-8 hours and GFP positive cells were sorted.

2.12 Lentivirus Generation and Transduction

For OVA over-expression in KP and KPL cell lines, the constructed pCDH- EF1α-OVA plasmid (10 µg) was packaged with psPAX2 (5 µg) and pMD2.G (5 µg) into 2 million Lenti-X 293T cells (Takara, Cat# 632180) using Lipofectamine 2000 transfection reagent (ThermoFisher, Cat# 11668019) following the manufacturer's protocol. During packaging process, half volume of R10 (heated deactivated FBS) was mixed with FreeStyle™ 293 expression medium (Gibco™, Cat# 12338018). Virus containing medium was removed after 6 hours and viral supernatant was collected after 48 hours and filtered through 0.45 µm filter. For virus infection, viral supernatant was mixed with polybrene (6 µg/ml, Santa Cruz, Cat# sc-134220) and

incubated with cells for 48 hours. Infected cells were then plated into 96-well plates to identify single clones. For OVA expression characterization, cells were stimulated with IFNγ (10 IU/ml) overnight then stained with OVA257-264 peptide bound to H-2Kb antibody (eBioscience, Cat# 17-5743-82). Two to three OVA expressing single clones with similar behavioral and growth pattern with parental KPL were pooled as KPL-OVA.

2.13 Quantitative Polymerase Chain Reaction (qPCR)

Cells were lysed directly in tissue culture container and RNA was isolated using the RNeasy Plus Mini Kit (Qiagen, Cat# 74134) following manufacturer's protocol. cDNA was synthesized from 1 µg of RNA using the iScript cDNA synthesis kit (Bio-Rad, Cat# 1708890) following manufacturer's protocol. qPCR was performed using iTaq Universal SYBER Green Supermix (Bio-Rad, Cat# 1725120). All qPCR primers sequences are listed in Appendix session. Relative mRNA expression was determined using the ΔC_t method.

2.14 Bone Marrow Derived Macrophages (BMDMs) Induction

To generate BMDMs, a single-cell suspension of bone marrow cells was collected from tibias and femurs of C57BL/6J wild-type or $Axl^{-/-}$ mice as previously described (Yang et al., 2014). Collected cells were cultured with 80% of complete RPMI 1640 medium (10% FBS, heat deactivated) and 20% L929 medium supplemented with 20 ng/ml recombinant mouse GM-CSF (rmGM-CSF) in a 10-cm dish at $2x10^6$ cell/dish

density. On day 3 and 6, equal volume of fresh media containing 20 ng/ml rmGM-CSF and 20% of L929 medium was supplemented. The BMDMs were harvested from adherent portion of tissue culture on day 7 by gentle scratching with cell scrapper.

2.15 Bone Marrow Derived Dendritic Cells (BMDCs) Induction

To generate BMDCs, a single-cell suspension of bone marrow cells was collected from tibias and femurs of C57BL/6J or $Axl^{-/-}$ mice as previously described (Yang et al., 2014). Collected cells were cultured with complete RPMI 1640 medium (10% FBS, heat deactivated) supplemented with 20 ng/ml recombinant mouse GM-CSF (rmGM-CSF) in a 10-cm dish at 2e6 cell/dish density. On day 3 and 6, equal amount of fresh media containing 20 ng/ml rmGM-CSF was supplemented. The BMDCs were harvested from tissue culture suspension on day 7.

2.16 Cross-priming of BMDCs and T Cells

For OVA specific $CD8^+$ T cells, the spleen and lymph nodes of OT1 transgenic mice were isolated with a negative $CD8^+$ T cell isolation kit (STEMCELL Technologies, Cat# 19853) following the manufacturer's instructions. For co-culture, 2×10^4 BMDCs were mixed with 2×10^5 $CD8^+$ T cells in the presence of 100 µg/mL OVA protein (Sigma-Aldrich, Cat# A2512) per well in a 96-well U-bottom plate to facilitate cell-cell interactions. *InVivo*Gen OVA (Cat# pcpgf-ova) was used when seeking weaker activation. BGB324 at 40 nM was added if there was a drug treatment. For in vitro

IFNα receptor blockade, 10 μg of anti-mouse IFNAR-1 antibody (BioXCell, Cat# BE0241) or corresponding IgG (BioXCell, Cat# BE0083) was added. For in vitro IFNα stimulation, 0.5 ng/ml of recombinant IFNα was added. After 48hr, all the cells were collected for analysis by flow cytometry and supernatant was collected for cytometric bead array (CBA) assay to evaluated cytokine/chemokine secretion.

2.17 CD3/CD28 T Cell Activation Assay

A 96-well flat bottom plate was coated with CD3 purified antibody (BioLegend, Cat# 100202) at a concentration up to 1 μg/ml (0.1 μg/ml or 0.02 μg/ml) in 100 μl of PBS overnight. When ready to use, flip the plate to get rid of liquid in 96-well plate, wash plate with PBS if needed. Plate $3x10^5$ splenocytes isolated from wild-type mice in 200 μl of RPMI1640+10% FBS medium with CD28 (equal amount to CD3, BioLegend, Cat# 102102) added. (Conc. Of splenocytes: $1.5x10^6$ cell/ml from splenocytes). Add drug with desired concentration to each duplicate or triplicate well. After 24/48-hour, harvest supernatant for CBA and cells for flow (CD45, CD3, CD8).

2.18 Cytometric Bead Array (CBA) Assay

Mouse Th1/Th2/Th17 cytokine kit (BD Biosciences, Cat# 560485) was used to examine the amount of T cell response related cytokine released from cross-priming assay and CD3/CD38 activation assay. For each sample, 2.5 μl of each of the 6 cytometric beads (15 μl total) was added to an Eppendorf tube. Vortex the mixed

beads and add 15 µl/well to a 96-well U-bottom plate. Then 40 µl of 2-fold diluted samples was added to each well on top of beads. Then 12 µl of PE detection reagent was added to each well on top of beads and samples. Then the plate was vortexed at lowest speed to mix the samples and avoid destructing the beads. Plate was then incubated for 2 hours at room temperature in the dark. When incubation was finished, 130 µl/well of CBA wash buffer was added to the plate and centrifuged down for 3 min at 1700 rpm. Discard supernatant by flicking plate gently to avoid bead loss. Beads were resuspended by placing plate on vortex set to highest setting or by tapping plate with 120 µl/well CBA wash buffer and transferred to 1.2 ml FACs tubes (Genesee Scientific, Cat# 14-361) in a 96-well rack. Then the data wa acquired on the FACSCalibur or CytoFLEX flow cytometer (Beckman Coulter, Inc) using the CBA acquisition template and the latest instrument settings file.

2.19 Animal Studies

Female C57BL/6J mice were purchased from the UT Southwestern breeding core or Taconic Biosciences. B6.129S7-Rag1^{tm1Mom}/J (*Rag1*$^{-/-}$), NOD.Cg-Prkdc^{scid} Il2rg^{tm1Wjl} Tg(CMV-IL3, CSF2, KITLG) 1Eav/MloySzJ (NSG-SGM3), B6.129P2(SJL)- *Myd88*$^{tm1.1Defr}$/J (Myd88$^{-/-}$), B6(Cg)- *Sting*1$^{tm1.2Camb}$/J (STING$^{-/-}$), B6(Cg)-Zbtb46$^{tm1(HBEGF)Mnz}$/J (zDC-DTR), B6.129S(C)-Batf3^{tm1Kmm}/J (*Batf3*$^{-/-}$), B6 (Cg)- *Ifnar1* $^{tm1.2Ees}$/J (*Ifnar1*$^{-/-}$), C57BL/6J-Tg(Cd8a*-cre)B8Asin/J (Cd8a-Cre ($E8_{III}$-Cre)), B6(Cg)-*Tcf7*^{tm1Hhx}/J (Tcf7^{GFP} flox), C129S4(B6)- Ifngtm3.Lky/J (IFNγ reporter) and C57BL/6J-Tg*(TcraTcrb)1100Mjb/J* (OT1 TCR transgenic) mice were purchased

from Jackson Laboratory. All mice were housed by the UTSW Animal Resource Center at 68-79°F, 30-70% humidity, in individually ventilated cages, with no more than 5 mice per cage on 12 hour on:off light:dark cycles. Mice were screened for and found free of MHV, Sendai virus, MPV, EDIM, MVM, PVM< TMEV-/GD-7, REO-3 virus, Mycoplasma pulmonis, pinworms, fur mites, LCMV, ECTRO, MAV, and K virus and had unrestricted access to RO chlorinated water and irradiated 2916 Teklab global diet (Envigo, Cat# 2916). Animal care and experiments were performed in complying with institutional and National Institutes of Health protocol and guidelines. This study has been approved by the Institutional Animal Care and Use Committee of the University of Texas Southwestern Medical Center (APN 2015-100921).

2.20 Xenograft Studies

For subcutaneous allografts, 1×10^6 cells in 100 µl phosphate buffered saline (PBS) were injected into right dorsal flanks of 6-8 wks old mice. For xenografts growing in humanized mice, 1.5×10^6 cells in 100 µl phosphate buffered saline (PBS) were injected into right dorsal flanks. Tumor bearing mice were randomly grouped into treatment groups when tumor volume was 100-150 mm^3. For each treatment group, 5 mice were assigned. 10 mg/kg PD-1 (BioXCell, Cat# BE0146) treatment was given intraperitoneally on day 0, day 4 and day 7 after treatment. Control animals were treated with 10 mg/kg rat IgG2a isotype control (BioX Cell, Cat# BE0089). BGB324 (50 mg/kg) was given through oral gavage twice daily. For tumor growth measurement, mice were treated for 3 weeks. For tumor microenvironment analysis,

mice were treated for 7 days, harvested tumors from control and treatment groups were within 20% in size for TME analysis. Tumor volumes were measured by length (a), width (b) and height (h) in every 3 days and calculated as tumor volume = abh.

2.21 CD34$^+$ Cells Isolation from Human Cord Blood

Human cord blood samples were obtained from UT Southwestern (UTSW) Parkland Hospital in compliance to the regulation and the use approval of human cord blood at UTSW medical center (IRB# STU 112010-047). Fresh 45ml of patient cord blood was filled in a heparin (Sigma, Cat# H3149-100KU) pre-filled 50ml canonical tube (1mg/ml, 5ml) and diluted with equal volume of 1x PBS prior to lymphocytes Ficoll isolation. Diluted cord blood was slowly layered onto the Ficoll-Paque solution (Cytiva, Cat# 17544203) previously added into the tube (15ml Ficoll + 35ml mixture). The ratio of Ficoll: samples should be ranging within 1:2-1:4. The tubes were centrifuged at 2000 rpm with break set up as accelerate 3 and down as 0 (natural stop) for 25-30 min at 22-24°C. Upper layer containing plasma and platelets were removed and the lymphocytes layer (white, cloudy band with a 25 ml pipet, do NOT disturb the bottom precipitations) was collected carefully. Equal volume of PBS was added, mixed well, and centrifuged at 500g for 10min. The cell pellet was resuspended with 10ml RPMI 1640 complete medium, centrifuge at 200g for 15 min to remove platelet cells. Isolated cells were then ready for counting and performing CD34$^+$ positive immunomagnetic isolation following the manufacturer's protocol (STEMCELL Technologies, Cat# 18780).

2.22 $CD34^+$ Cells Engrafted Humanized Mice Generation

Humanized mice were established as previously described (Mender et al., 2020). Briefly, 4-weeks-old NSG-SGM3 (Jackson Laboratories, Cat# 013062) female recipient mice were treated with 100 cGy (X-ray irradiation with X-RAD 320 irradiator) whole body irradiation within 24 hours prior to hematopoietic stem cells (HSCs) transplantation. For transplantation, $1x10^5$ isolated HSCs were intravenously injected into recipient mice ($1x10^4$ – $1x10^5$ cells per mice). Irradiated mice were orally administrated Sulfadiazine/Trimethoprim (Aurora Pharmaceutical LLC, Cat# 302) water for 14 days (Park et al., 2008; Wunderlich et al., 2010). Twelve weeks after engraftment, humanized mice reconstituted with over 45% human $CD45^+$ cells were used for tumor studies. Reconstitution rate of humanized mice were characterized through facial blood immune cell staining.

2.23 $CD8a^{Cre}TCF7^{fl/fl}$ knockout mice generation

C57BL/6J-Tg (Cd8a*-cre) B8Asin/J (Cd8a-Cre (E8III-Cre)) mice were breed with B6(Cg)-Tcf7tm1Hhx/J (Tcf7GFP flox) to generate heterozygous F1 pulps for both alleles. F2 pulps were genotyped for the CD8a Cre and TCF7 flox expression. Mouse DNA was extracted from clipped ear and boiled at 100°C in 200 µl of 50 mM NaOH. Then 20 µl of 1M Tris-HCl (pH = 8.0) was added for neutralization. After a brief vortex, sample was centrifuged at 13,000 rpm for 10 min to participate debris. Extracted DNA was then used for touch-down PCR genotyping for TCF7 flox

expression typing adjusted JAX website suggested program (1. 95°C, 3 min; 2. 95°C, 20s; 3. 65°C, 20s (-0.5°C per cycle); 4. 72°C, 30s; 5. repeat step 2-4 for 10 cycles; 6. 94°C, 20s; 7. 60°C, 20s; 8. 72°C, 30s; 9. Repeat step 6-8, 28x; 10. 72°C, 5min; 11. 16°C, hold for infinite time). For TCF7 flox expression, the common forward primer (5'-TCC TCG TGG GTC CCA TCT C-3'), wild type reverse primer (5'-TCC AGA CCT CCA CTT CGC G-3') and mutant reverse primer (5'-CAG ACC TTG GGA CCA CCT CA-3') were used with DreamTaq Green PCR Master Mix (ThermoFisher, Cat# K1081). Note that due to the differences of affinity for primers, the wild type and mutant PCR need to be performed individually to ensure accuracy. CD8a Cre was typed through qPCR with following primers: Transgene forward (5'-GCG GTC TGG CAG TAA AAA CTA TC-3') and transgene reverse (5'-GTG AAA CAG CAT TGC TGT CAC TT-3'), internal control forward (5'-CAC GTG GGC TCC AGC ATT-3') and internal control reverse (5'- CAC GTG GGC TCC AGC ATT-3'). For each typing, homogenous F1 mouse for CD8a Cre and TCF7 flox were used as positive and negative control. Homogenous F2 mice were breed for strain keeping. CD8a Cre heterogenous, TCF7 flox homogenous mouse was breed with TCF7 flox homogenous mouse, with littermates of conditional knock-out mice and wild-type mice would be produced.

2.24 Adoptive Transfer of T Lymphocytes

The spleen, mesenteric lymph nodes, pectoral, and axillary lymph nodes were isolated from the donor mice -wild-type (Jackson Laboratories, Cat# 000664) or

IFNAR knock-out mice (Jackson Laboratories, Cat# 028288)- were isolated and digested into single cell suspension. For splenocytes, 2 ml ACK lysis buffer per spleen was incubated for 1 min to lyse red blood cells. T cells were then isolated using EasySep™ Mouse T Cell Isolation Kit (STEMCELL Technologies, Cat# 19851) following manufacturer's instruction. Isolated T cells was then injected into recipient Rag1 knock out mice (Jackson Laboratories, Cat# 002216) through intravitreal injection. Isolated cells from each donor mice were transferred to 1-3 recipient mice. After 2-3 weeks, the reconstitution rates of T cells were characterized through blood collection and flow cytometry.

2.25 *In Vivo* Immune Cell Depletion

For FTY720 hydrochloride (Selleckchem, Cat# S5002) mediated T cell egression prevention, 20 μg/mouse of FTY720 was given at day 0 of treatment started, then 10 μg/mouse of FTY720 was given every other 2 days through intraperitoneal injection. Note FTY720 must be dissolved in 0.9% saline solution and do NOT vortex at any time.

For Clophosome liposome mediated macrophages depletion (FormuMax Scientific, Cat# F70101C-A), the amount of liposome recommended by corresponding COA was injected intraperitoneally into mice 1 day before therapy (BGB324 + anti-PD-1) treatment. After 5 days, a second liposome injection was performed.

For neutralizing antibody mediated CD4 (BioXCell, Cat# BE0003) and CD8 (BioXCell, Cat# BE0004) T cell depletion, 200 μg of antibody was injected

intraperitoneally into mice 1 day before therapy (BGB324 + anti-PD-1) treatment. After 3 days, a second 100 μg dose injection was performed. Then 100 μg dose injection was given every 7 days as long as needed for experiments.

2.26 *In Vivo* Interferon Alpha Receptor Blocking

For intratumoral IFNα receptor blocking, 50 μg IFNAR blocking (BioXCell, Cat# BE0241) antibody or control IgG (BioXCell, Cat# BE0083) were injected intratumorally 1 day before BGB324 + anti-PD-1 treatment started. IFNAR inhibition antibody was injected every other day.

2.27 *In Vivo* Recombinant Interferon Alpha Stimulation

For recombinant IFNα stimulation, 200 ng, 1 μg, or 5μg of IFNα or PBS was injected intraperitoneally 14 days after tumor inoculation.

2.28 Single Cell Preparation for Flow Sorting and Flow Cytometry

Tumor tissues were excised in gentleMACS C tubes (Miltenyi Biotec, Cat# 130-093-237) pre-filled with 7ml of 1x PBS with gentleMACS Octo Dissociator with Heaters (Miltenyi Biotec, Cat# 130-096-427) using pre-set mouse neo-heart program 2 times. Excised tumors were then transferred to 2ml of R5 medium in 6-well plate with 2mg/mL Collagenase A (Sigma, Cat# SCR136) and 1 mg/ml DNase I (Roche, Cat#11284932001) under 37 °C, 120 rpm shaking speed for 45 min. Digested

materials then were transferred to a 70 μm cell strainer to remove clumped cells. Digested cells were washed twice with FACs buffer and ready for downstream analysis.

2.29 Flow Cytometry

Total number of digested cells for each tumor sample was counted, and a single cell suspension of 1.5 million of cells was used to perform analysis. Samples were incubated with anti-FcγIII/II receptor (clone 2.4G2) for 15 min at 4 ℃ to block potential non-specific binding of conjugated antibodies. Indicated antibodies were incubated with digested tumor samples for 30 min at 4 ℃. Fixable viability Dye eFluor 506 (eBioscience, Cat# 65-0866-18) was used to exclude the dead cells. Ki67 and TCF1 were stained intracellularly using True-Nuclear transcription factor buffer set (BioLegend, Cat# 424401) following the manufacturer's instructions. Data were collected on CytoFLEX flow cytometer (Beckman Coulter, Inc) and analyzed by using FlowJo (Tree Star Inc., Ashland, OR) software.

2.30 Enzyme-linked Immunosorbent Spot Assay (ELISPOT)

KPL-OVA (1×10^6) cells were injected subcutaneously on the right flank of 6-8wks old C57BL/6J mice purchased from Taconic Biosciences. Seven days after treatment started, tumors were harvested and digested into single cells. For each well of a 96-well 0.45 μM filtration plate (Millipore Sigma, Cat# MAIPS4510) pre-coated with

capture antibody, tumor infiltrated lymphocytes (TILs) were isolated from 3×10^5 digested single cells by biotin labeling (BioLegend, Cat# 101304) followed by negative immunomagnetic selection (STEMCELL Technologies, Cat# 19860). Isolated TILs were cultured in RPMI 1640 medium or Iscove's Modified Dulbecco's Medium (IMDM) (ThermoFisher Scientific, Cat# 31980097) supplemented with 10% fetal bovine serum, 2 mmol/l L-glutamine, 100 U/ml penicillin, and 100 µg/ml streptomycin. For antigen specific $CD8^+$ T cell stimulation, 1 µg/ml of SIINFEKL peptide ($OVA_{257-264}$) or control RAHYNIVTF (E7) peptide were added. After 48 hr of incubation, IFN-γ production was determined with an IFN-γ ELISPOT assay kit according to the manufacturer's protocol (BD Biosciences, Cat# 551083). The visualized spots were enumerated with the CTL-ImmunoSpot® S6 Analyzer (Cellular Technology Limited) and normalized based on digested tumor cell counts.

2.31 Enzyme-linked Immunosorbent Assay (ELISA)

Co-culture of BMDCs with irradiated tumor cells to detect type I IFN was performed as previously described (Han et al., 2020). BMDCs (2×10^5) were co-cultured with 40g irradiated KPL cells (2×10^6), with or without BGB324 treatment (40 nM). After 24 hr, cell supernatant was collected for analysis. The concentration of IFNβ was measured by VeriKine-HS Mouse IFN Beta Serum ELISA kit (PBL Assay Science, Cat# 42410), or VerKine Human IFN Beta ELISA kit (PBL Assay Science, Cat# 414101) in accordance with the manufacturer's instructions. Finally, the plates were

visualized by adding 100 µL of TMB solution and read at 450 nm using the SPECTROstarNano (BMG LABTECH).

Gas6 ELISA from tumor lysates was measured using Mouse Gas6 Quantikine ELISA Kit (Cat# MGA S60) purchased from R&D Systems. The amount of sample loaded was normalized to total protein in each sample, and Gas6 amount was evaluated following manufacture's protocol.

2.32 Tissue homogenization and RNA extraction

Resected tissue or tumors were homogenized for protein level expression evaluation. Briefly, resected tissue or tumors were weighted (< 50 mg) and loaded onto homogenization tubes (MP Biomedicals, Cat# 5076400, 5065-005) pre-filled with 3-4 lysing matrix s beads (MP Biomedicals, Cat# 69250000). Then, 300 µl of 1x cell lysis buffer (Cell Signaling Technology, Cat# 9803) was added to each tube. Samples were then homogenized using FastPrep-24^{TM} 5G bead beating grinder and lysis system (MP Biomedicals, Cat# 6005500) following pre-set manufacture's program of mouse leg muscles for 2 times. Homogenized mixture samples were then centrifuged at 13,000 rpm at 4 °C for 10 min and supernatant was ready for downstream analysis.

To homogenize resected tissue or tumors for RNA extraction, 1 ml of Trizol was added to per 50-100 mg of tumor tissue and loaded onto homogenization tubes (MP Biomedicals, Cat# 5076400, 5065-005) pre-filled with 3-4 lysing matrix s beads (MP Biomedicals, Cat# 69250000). Samples were then homogenized using FastPrep-

24™ 5G bead beating grinder and lysis system (MP Biomedicals, Cat# 6005500) following pre-set manufacture's program of mouse leg muscles for 2 times. Homogenized mixture samples were then centrifuged at 13,000 rpm at 4 °C for 10 min and supernatant was transferred to 1.7 ml Eppendorf tubes. For phase separation stage, 400 ul of chloroform was added to supernatant and mixed vigorously by shaking. The mixture was incubated at room temperature for 5 min and then centrifuged at maximum speed (>12,000 x g) for 10 min. The upper aqueous phase liquid was then transferred carefully into a new Eppendorf tube without disturbing the interface. To precipitate RNA, 400 ul of acetone was added to each sample, mixed well, and incubated at room temperature for 10 min. Samples were then centrifuged at maximum speed for 10 min. Supernatant was then discarded, with 1ml of 70% EtOH to wash precipitated RNA. Washed samples were then centrifuged at maximum speed for 5 min. Supernatant was discarded and centrifuged again at max speed for another 1 min. Residual EtOH was taken out by sucking with 10 ul tip on 1 ml tip. The precipitated RNA pellets were air dried in a tissue culture hood until the pallet turned into transparent. To re-dissolve RNA, 100 µl of DEPC-treated water was added and samples may be incubated in the water bath at 55 to 60°C. DO NOT heat it at 37°C as enzymes would degrade RNA. Measure extracted RNA concentration using NanoDrop™ 2000 Spectrophotometers (ThermoFisher, Cat# ND-2000) at 260 nm/280 nm wavelength.

2.33 scRNA-seq and scTCR-seq

2.33.1 Library preparation and construction

KP (n=10) and KPL (n=10) allografts were harvested 14 days after subcutaneous implantation (average tumor size ~200 mm^3). For each sample, individual tumors harvested from different mice were pooled with live $CD45^+$ $CD3^-$: $CD45^+$ $CD3^+$ cells sorted and mixed back as 1:1 ratio. Single cell libraries and TCR libraries were generated with Chromium Single Cell V(D)J Reagent Kit (10x Genomics, PN-10000006, PN-10000009, PN-1000071) following per manufacturer's instruction. Pooled control group tumors from KPL tumors were also used to compare with KP tumors.

2.33.2 Data Pre-processing

Sequenced scRNA-seq samples were processed through Cellranger pipelines (v3.1.0). Cellranger count was used to align reads to mouse reference genome (mm10, 2020-A, from 10x Genomics) and generate single cell feature counts for single library. For scTCR-seq data, TCR reads were aligned to reference genome and TCR annotation was performed using the 10x cellranger vdj pipeline with provided reference (cellranger-vdj-GRCm38-alts-ensembl-4.0.0). Overall, 94% of T cells in scRNA-seq data were assigned a TCR and more than 70% had at least one full-length productive CDR3 for TRB. Cellranger aggr were applied next to aggregate each sample library for grouped analysis with same effective sequencing

depth. Seurat (3.2.1) package was used for multiple library data integration and downstream analysis including singlet filtration, dimensional reduction, data scaling, clustering and markers identification (Stuart et al., 2019).

2.33.3 Annotation and Visualization of Cell Clusters

To identify the cell clusters, we annotated the cell cluster identities based on (1) well-studied marker genes of different immune cell types were in the top rank of differential expressed genes and assign the identity to the most likely cell populations; (2) unbiased cell population identification package singleR (v1.3.8) (Aran et al., 2019). For visualization, we applied the uniform manifold approximation and projection (UMAP) to visualize cell clusters (Becht et al., 2019). For $CD8^+$ T cells sub-clustering, we split the CD3+ T cells according to the mutually exclusive expression of CD4 (CD4> 1 and CD8A< 1) and CD8A (CD4<1 and CD8A>1) genes based on their normalized expression. CD8+ T cells were then sub-clustered and annotated based on their highly enriched genes with well-known markers (Guo et al., 2018a).

2.33.4 Differential Expression Analysis

CD8a expressing T cells were subset and analyzed for differential expressed gene among KP and KPL samples using Seurat package (3.2.1). Then differential expressed genes were ranked based on log Fc value, with p value > 0.01 highlighted in grey, and p value < 0.01 highlighted in red. Then the graph was plotted using ggplot 2 package.

2.33.5 Gene Set Enrichment Analysis (GSEA)

The R packages fgesa and msigdbr were used to perform the gene set enrichment analysis. The pathway gene sets we used were extracted from online databases KEGG, BIOCARTA, REACTOME and curated Hallmark gene sets (PMID: 26771021). For a given cluster, GSEA was performed using each pathway gene set against ranked gene lists from comparison with other clusters. Pathways were considered enriched if the BH adjusted fdr < 0.1, and the normalized enrichment scores (NES) were calculated to represent the enrich level.

2.33.6 T Cell Enrichment and State Transition Characterization

To measure the enrichment of specific T cell clusters in each sample induced by different treatment, we calculated the ratio of observed to expected cell number for each T cell cluster. Chisq-squared test was applied to test whether the distribution of T cell clusters across different samples was significantly deviates from random expectations. The extent of deviation for each combination of T cell cluster and sample is quantified by the Ro/e value:

$$R_{o/e} = \frac{N_o}{N_e}$$

Where N_o is the observed number cell for a given sample and cluster combination, while the *Ne* is the expected number obtained from Chi-square test. Theoretically, $R_{o/e} > 1$ suggests that cells identified in the given cluster shows higher frequency than random expectations for the analyzed sample, and vice versa. The

normalization and scaling of the shared clonotypes between CD8 T cell clusters was performed and analyzed based on previous publication (Guo et al., 2018a). The shared clone scores were also scaled with a constant of 10,000.

2.33.7 Pseudo-timing Analysis

To determine the potential lineage differentiation between those T cell populations with high TCR sharing. Monocle (version 2.0) (PMID: 24658644) was used to investigate transcriptional and developmental trajectories concerning different $CD8^+$ T cell clusters. The data of raw counts together with cluster annotations were taken as input to monocle, and the default parameters were set to run data normalization and dimension reduction. Next, Monocle leaned the kinetics of gene expression by using the reversed graph embedding approach and places each cell along an inferred pseudotime trajectory. According to the assumption that the trajectory has a tree structure, functional “State” is identified based on the segment of the tree-like structure.

2.33.8 RNA Velocity Analysis

To predict the future status and direction of each cells transitioning, RNA velocity analysis was performed (La Manno et al., 2018). Un-spliced mRNAs were generated as a loom file for each individual sample output from Cell Ranger and RNA velocity was calculated based on velocyto (v0.17.17, Linux R package). Generated loom files were then merged and projected to UMAP coordinates of single cells.

CHAPTER THREE:
STK11/LKB1 Mutated NSCLC Lacks anti-PD-1 Treatment Responsive T Cells in the TME

3.1 KP and KPL GEMM Model Characterization

To dissect the immune landscape of ST*K11/LKB1* mutant NSCLC, two isogenic pair of syngeneic murine lung adenocarcinoma cell lines were used derived from a tumor arising in a mutant *Kras/Tp53* knockout genetically engineered mouse model (GEMM) (referred to as “KP” tumor cells). KP9-1 and KP9-3 expresses wild-type *Stk11/Lkb1* while KPL9-1-9 and KPL9-3-1 was CRISPR engineered to also be *Stk11/Lkb1* deficient, with expected reduced AMPK phosphorylation (**Figure 3.1A**) (Hollstein et al., 2019; J. Kim et al., 2017; Shackelford & Shaw, 2009). We also probed protein level expression of acetyl-CoA carboxylase, mTOR and AKT and their phosphorylation, as they either had been reported being regulated by LKB1-AMPK axis or under study for their regulation relationship with AKT pathway(J. Kim et al., 2017; Soltys et al., 2006; Zhong et al., 2008). Although limited differences were observed, a more sensitive way for protein detection and special cell lysis buffer may further differentiate their expression levels, as phospho-AMPK was failed to observe differences between KP and KPL, when detecting their expression with fluorescence instead of chromogen (**Figure 3.1B**). KP9-1 and KPL9-1-9 were derived from same mouse, and KP9-3 and KPL9-3-1 were derived from same

mouse. KP and KPL cells form syngeneic tumors injected subcutaneously exhibited classic lung adenocarcinoma histology in C57BL/6J mice (**Figure 3.1C**). In regard of their ability of tumorigenesis, proliferation, and histology features, these two pairs exhibited highly similar patterns.

3.1.1 Characterization of KP and KPL cell lines and allografts

Comparing to KP tumors (KP9-1 and KP9-3), KPL tumors (KPL9-1-9 and KPL9-3-1) exhibited more aggressive phenotype and were able to grow established tumor subcutaneously on C57BL/6J wild-type mice (**Figure 3.1D**). This growth differences were likely coming from better immune system supervision in KP tumors, as the tumor genesis ability for KP and KPL tumors were same when implanted onto NSG mice (**Figure 3.1E**). When grew in immunodeficient NSG mice subcutaneously, KP tumors grew slightly faster than KPL tumors (**Figures 3.1F**). While grew tumors onto immune intact C57BL/6J mice, KPL tumors grew faster than KP tumors (**Figures 3.1G**). Importantly, when these cells are injected into *Rag1*-knockout (KO) mice, the resulting tumors exhibit similar growth patterns (**Figure 3.1H**), suggesting tumor progression differences caused by loss of *Stk1/Lkb1* are mainly mediated by the host immune system and therefore the *Stk1/Lkb1* mutation plays an important role in regulating TME.

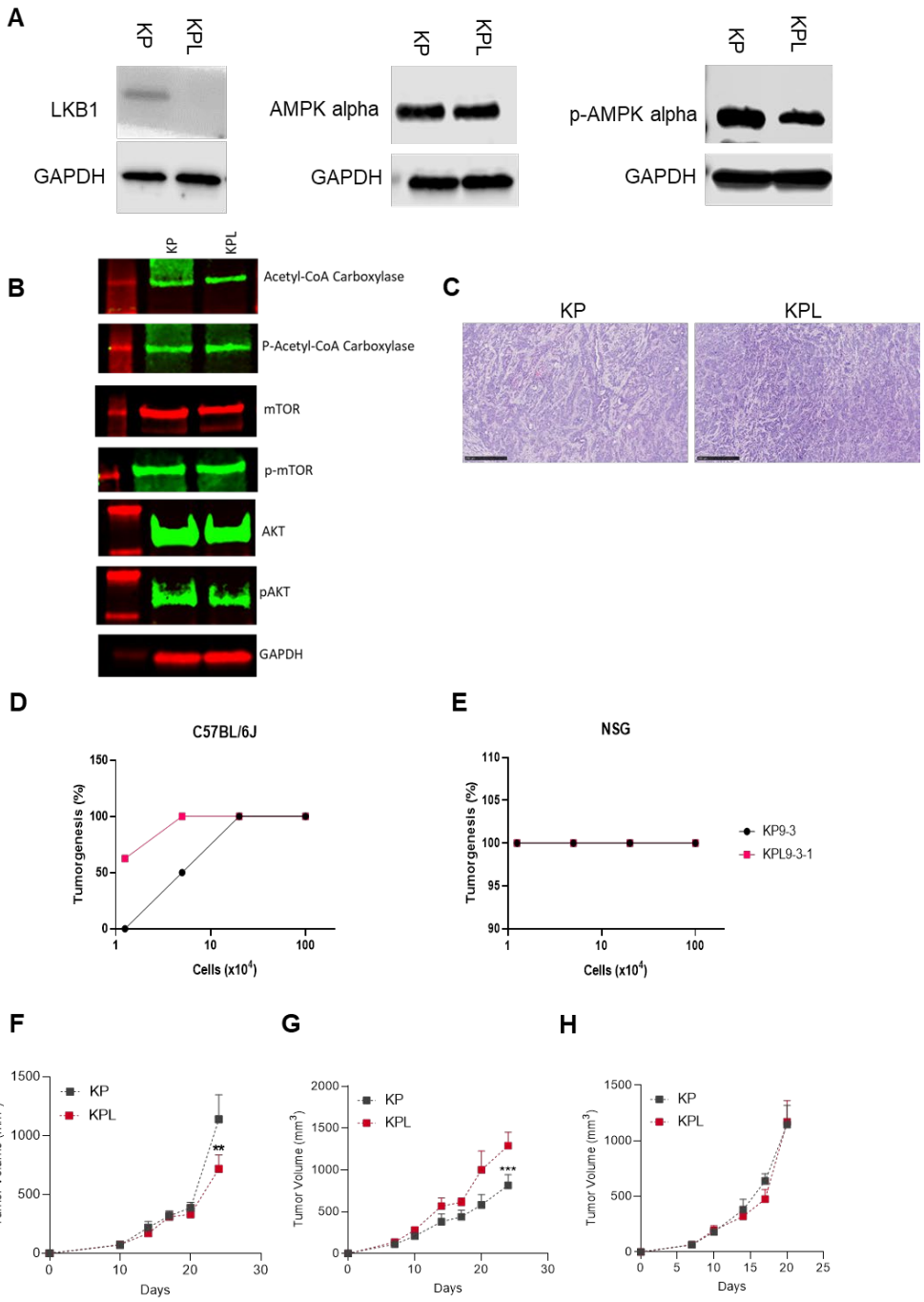

Figure 3.1 Characteristics of KP and KPL cell lines.

(A) LKB1, AMPK alpha, phospho-AMPK alpha, and GAPDH protein expression in KP and KPL cells detected by western blot. Cell lysates were harvested from *in vitro* culture.

(C) Representative H&E histology of KP and KPL subcutaneous tumors in C57BL/6J mice.

(D) C57BL/6J mice (n = 5) were injected subcutaneously with KP or KPL tumor cells (1E4, 5E4, 1E5, 1E6). Tumor growth was monitored every 3 days for 60 days, and tumors above 75 mm^3 were considered as grown tumor.

(E) NSG-SGM3 mice (n = 5) were injected with subcutaneously KP or KPL tumor cells (1E4, 5E4, 1E5, 1E6). Tumor growth was monitored every 3 days for 60 days, and tumors above 75 mm^3 were considered as grown tumor.

(F) NSG-SGM3 mice (n = 6) were injected subcutaneously with 1 x 10^6 KP or KPL tumor cells. Tumor growth was measured every 3 days.

(G) C57BL/6J mice (n = 5) were injected with subcutaneously 1 x 10^6 KP or KPL tumor cells. Tumor growth was measured every 3 days.

(H) *Rag*$1^{-/-}$ mice (n = 5) were injected subcutaneously with 1 x 10^6 KP or KPL tumor cells. Tumor growth was measured every 3 days.

3.1.2 Overview of KP and KPL tumor immune microenvironment (TME)

To systematically analyze the immune microenvironment changes mediated by *Stk11/Lkb1* mutation, we performed single cell RNA-seq for allografts engrafted subcutaneously after tumors were established and reached ~100 mm^3 size. Myeloid cells ($CD45^+/CD3^-$) and T cells ($CD45^+/CD3^+$) were isolated from KP and KPL syngeneic murine tumors (n = 10) were digested and mixed as a single sample for flow sorting. KP and KPL tumor samples were then sorted and mixed back at 1:1 ratio as described (Zhou et al., 2020). In this way, an increased resolution of T cells

could be observed and analyzed more detailed, as normal T cell abundance are way less than myeloid cells in TME.

Major group of immune cells detected from scRNAseq in KP and KPL tumors were visualized into UMAP projection (resolution = 0.3), including malignant cells, double negative T cells, CD8 T cells, CD4 T cells, regulatory T cells, inhibitory T cells, natural killer cells, dendritic cells, macrophages, and monocytes/MDSCs (**Figure 3.2A**). Malignant cells were also detected, which were likely attached to the sorted immune cells and remains as a common challenge for preparing scRNAseq library (Zhou et al., 2020). When visualized the UMAP based on samples, KP and KPL sample were merged well, indicating little to none technical induced variations (**Figure 3.2B**). With the most recognized identification markers visualized on UMAP, they accord with the clusters identified at resolution = 0.3 (**Figure 3.2C**), suggesting a right resolution was chosen to cluster cells detected. Cell clusters were further annotated and validated with previous reported functional markers (**Figure 3.2D**). Markers used to annotate CD8 T cells were also plotted (**Figure 3.2E**), which aided the further analysis of CD8 T cells based on scRNAseq data in **section 3.2**.

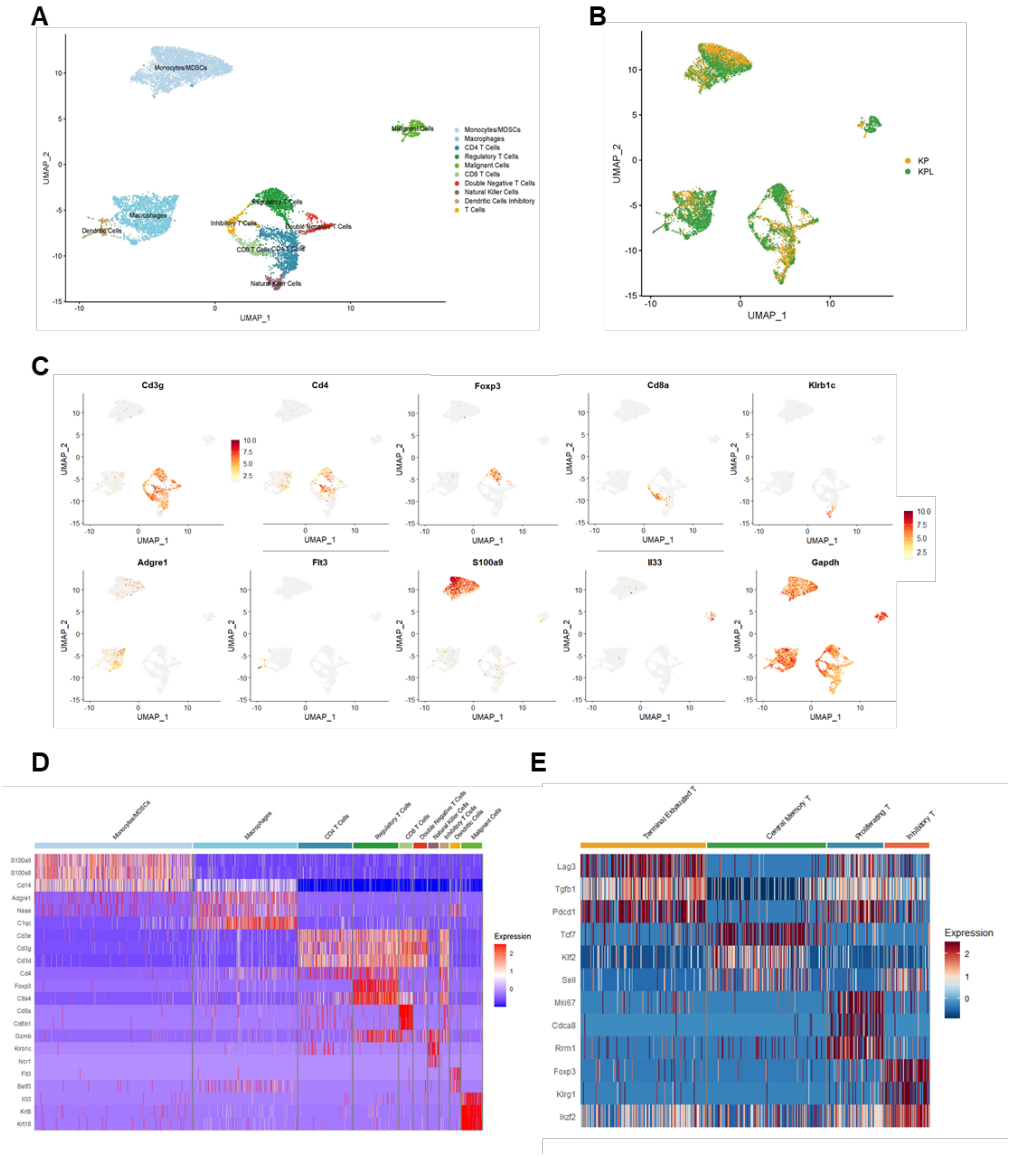

Figure 3.2 Overview of CD45^{+} immune cell populations in KP and KPL tumors.

(A) UMAP visualization for major clusters of cells detected by scRNAseq in KP and KPL tumor microenvironment. Each distinct cluster is denoted by different color.

(B) Distribution of cells from different clusters among KP and KPL tumors.

(C) UMAP projection of cell clusters with visualization of major marker genes expression supporting cell identity assignment.

(D) Heatmap visualization for markers for identifying clusters in (A).

(E) Heatmap visualization for CD8 T cell sub-clusters.

To analyze and quantify of immune cells changes mediated by *Stk11/Lkb1* mutation at protein level, we performed flow cytometry for allografts also harvested ~100 mm^3 size. From alive cells distinguished by live/dead dye negative staining, CD3 was used to classify T cells (**Figure 3.3A**), with further CD4 or CD8 positive to identify CD4 or CD8 T cells (**Figure 3.3B**). T_{reg} cells were further gated out from CD4 T cells based on positive FoxP3 staining (**Figure 3.3C**). B cells were identified when CD45 positive cells were also staining as CD19 positive (**Figure 3.3D**). Macrophages were classified as CD11b and F4/80 double positive (**Figure 3.3E**). Dendritic cells were defined as CD11c and MHC II double positive (**Figure 3.3F**), with cross-priming dendritic cells further identified as CD141 positive (**Figure 3.3G**). Neutrophils and MDSCs were stained for Gr-1 as a whole ((**Figure 3.3H**) or split into Ly-6C and Ly-6G for more accurate identification (not shown here) and the statistics were performed based on detailed staining. Also see APPRENDICES for markers used for flow cytometry analysis.

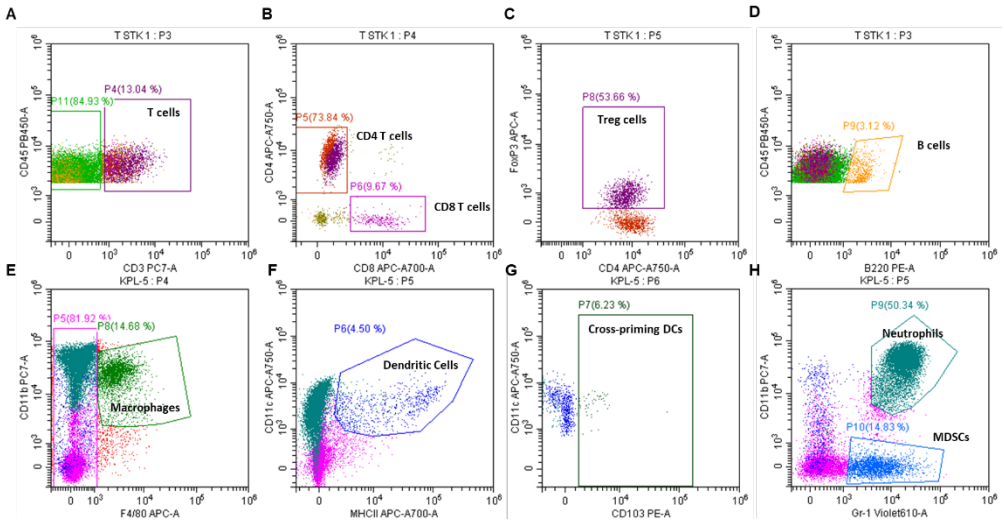

Figure 3.3 Flow cytometry gating strategy for characterizing TME of KP and KPL allografts. Gating strategy of T cells (A), CD4 and CD8 T cells (B), regulatory T cells (C), B cells (D), macrophages (E), dendritic cells (F), cross-priming dendritic cells (G), neutrophils and MDSCs (H).

Figure 3.4 showed the quantification of data obtained based on **Figure 3.3** strategy from each individual tumor samples engrafted onto different mouse.

Based on the flow cytometry data, *Stk11/Lkb1* mutation resulted in a significant reduction of infiltrated CD8 T cells in TME (**Figure 3.4A**). Less tumor associated CD8 T cells infiltrated or being activated were also inferred from less of exhausted CD8 T cells were observed (**Figure 3.4B**), and T cells need to be activated before transit into exhaustion state. B cells infiltration varies but little differences were observed when comparing KP and KPL tumors (**Figure 3.4C**). Although less CD4 T cells were infiltrated into KPL tumors (**Figure 3.4D**), regulatory T cell infiltrate percentage did not change significantly (**Figure 3.4E**). These data indicates that 1)

the ratio of T_{reg}/CD8 T cells increased in KPL TME, and 2) further less CD4 helper T cells functioning in helping prime CD8 T cells were infiltrated, since overall CD4 T cell infiltration decreased whereas T_{reg} cells were about the same. Taken together, the T cell status in KPL tumors are consistent with previous reports in *KL* mutated NSCLC patient tumors (Skoulidis et al., 2018b), and mouse KPL tumors exhibited a suppressive T cell infiltration pattern.

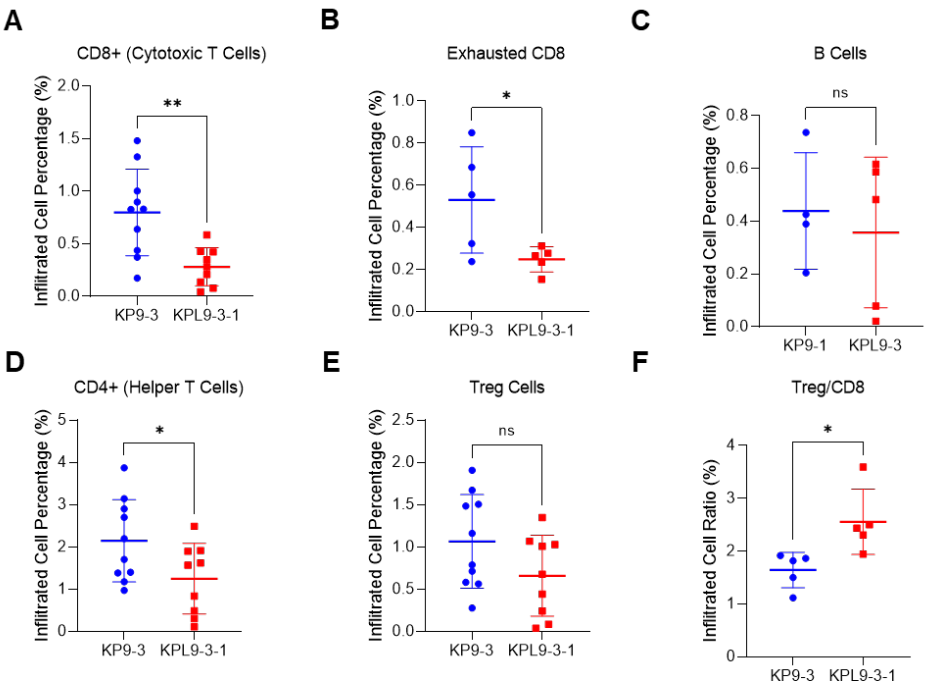

Figure 3.4 Characterization of KP and KPL allografts T cells TME. Flow cytometry analysis of tumor infiltrated CD8 T cells (A), exhausted CD8 T cells (B), B cells (C), CD4 T cells (D), regulatory T cells (E), T_{reg}/CD8 T cell ratios (F) in KP or KPL tumors in C57BL/6J mice (n = 5). Tumors were harvested at day 14 after tumor cell injection. Data points are pooled from 2 times of experiments if applicable.

When analyzing myeloid cell status changes in KPL tumors, a significant reduction of dendritic cells and cross-priming dendritic cells were observed (**Figure 3.5A-B**), which possibly also influenced tumor associated CD8 T cell infiltration, since less of the tumor associated antigen would be presented to recruit antigen specific T cells into TME. Although a reduction of infiltrated macrophages and neutrophiles were also observed (**Figure 3.5C-D**), due to their dual functions in regulating TME (Albrengues et al., 2018; Andzinski et al., 2016; Hao et al., 2012; X. Liu et al., 2015; Teijeira et al., 2020), it remains unclear of their effect on tumor progression control. Although MDSCs infiltration also decreased in KPL tumors (**Figure 3.5E-F**), it might not enough to counteract the effect of increased T_{reg}/CD8 T cells ratio in KPL TME, since MDSCs are usually less potent than T_{reg} and it may regulated by T_{reg} cells (Holmgaard et al., 2015).

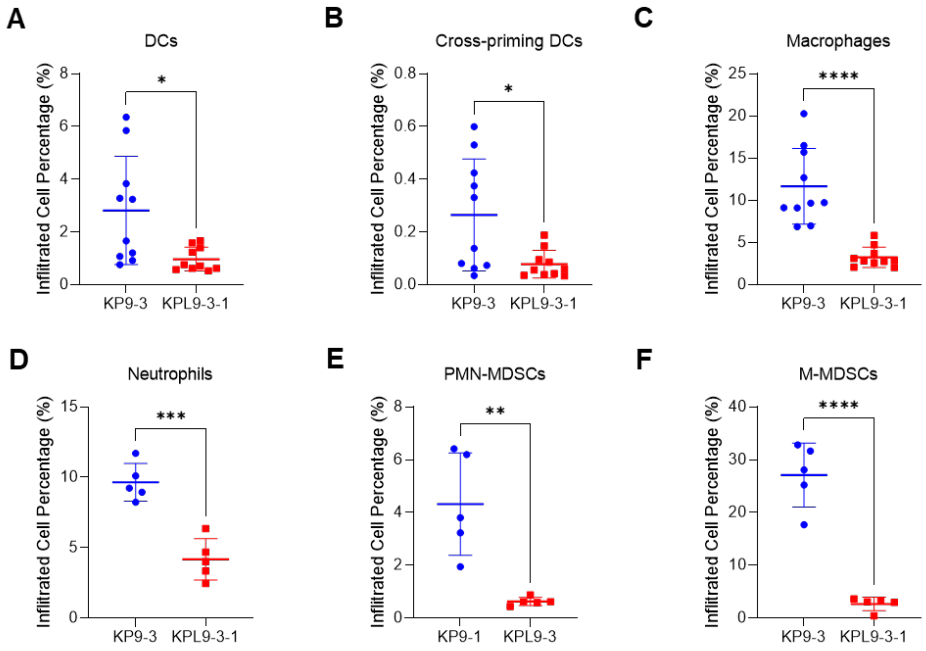

Figure 3.5 Characterization of KP and KPL allografts myeloid cells TME. Flow cytometry analysis of tumor infiltrated dendritic cells (A), cross-priming dendritic cells (B), macrophages (C), neutrophils (D), polymorphonuclear MDSCs (E) and monocytic MDSCs (F) in KP or KPL tumors in C57BL/6J mice (n = 5). Tumors were harvested at day 14 after tumor cell injection. Data points are pooled from 2 times of experiments if applicable.

Immunohistochemistry (IHC) was performed on 5 μM thickness allograft tumor sections to localize infiltrated CD4 and CD8 T cells in KP and KPL tumors. KP tumors features in well infiltrated CD8 T cells into tumor island even in the central tumor area, which allowing for the physical contact of CD8 T cells with tumor cells to potentially perform killing (**Figure 3.6A**). However, most of the infiltrated CD8 T cells in KPL tumors were stuck at the tumor edge within stromal portion, which further inhibited the ability for CD8 T cells to control tumor progression (**Figure 3.6B**).

Similar to CD8 T cell infiltration, CD4 T cells in KP tumors could disperse well and contact tumor cells directly in the central tumor area whereas were most excluded from tumor island (**Figure 3.6C-D**).

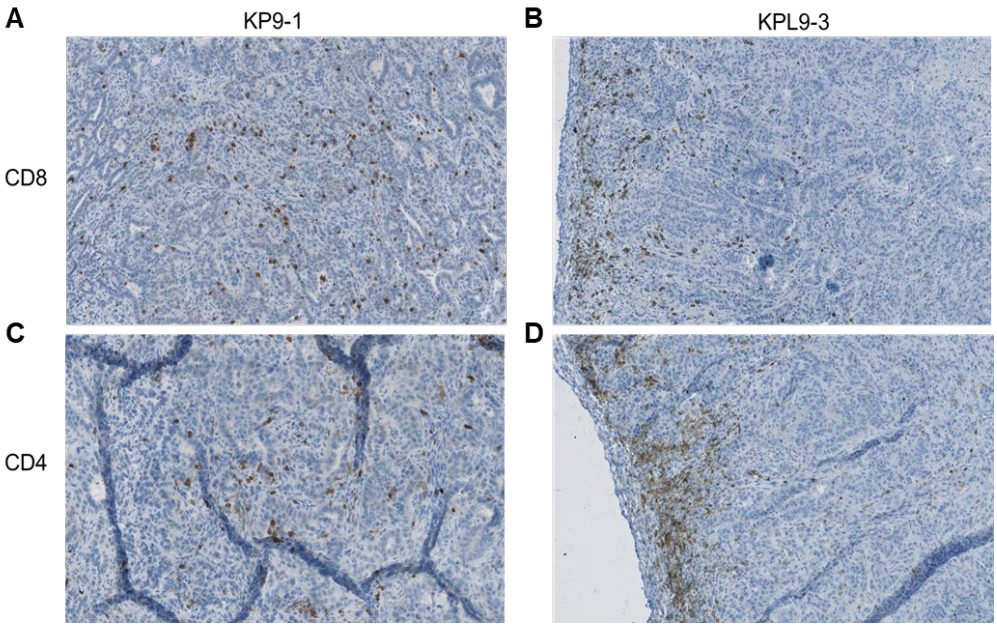

Figure 3.6 Localization of T cells in KP and KPL allografts.
(A-B) Immunohistochemistry staining of CD8α in KP (A) and KPL (B) allografts.
(C-D) Immunohistochemistry staining of CD4 in KP (A) and KPL (B) allografts.

In summary, Stk1/Lkb1 mutation on tumor cells plays an important role in creating a suppressive immune TME, including less anti-tumor immune cells infiltration and exclusion of immune cells.

3.2 Therapeutic Responses and CD8 T cell Status in KP and KPL TME

Consistent with previous reports in *KL* mutated NSCLC patient tumors (Skoulidis et al., 2018b), we found that mouse KPL tumors not only mimic the immune suppressive TME, they also exhibited poor responses to anti-PD-1 therapy (**Figure 3.7A**). Since CD8 T cells are the main responder to anti-PD-1 therapy, and main executor for tumor cell killing, the effect of *Stk11/Lkb1* mutation on CD8 T cells of NSCLC was assessed through sub-clustered CD8 T cells in scRNAseq (resolution = 0.2). CD8 T cells from KP and KPL tumors were aggregated and clustered into terminal exhausted T cells, central memory T cells, proliferating T cells and inhibitory T cells (**Figure 3.7B; Figure 3.2E**) (Guo et al., 2018b; Luoma et al., 2020). The percentage of CD8 T cells from KP and KPL tumors in each cluster demonstrates that loss of *Stk11/Lkb1* expression in tumor cells is associated with a more suppressive CD8 T cell composition in the TME (**Figure 3.7C**). Notably, KPL tumors, in contrast to KP tumors, showed a decreased abundance of *Tcf7* expressing T cells that exhibit stem like or central memory features, indicating a deficit of TCF1 expressing CD8 T cells in the KPL TME (**Figure 3.7D**). These scRNAseq observations were confirmed by comparing $TCF1^{+}PD\text{-}1^{+}$CD8 T cells in KP and KPL tumors through flow cytometry and immunohistochemistry (**Figures 3.7E-F**). Furthermore, $TCF1^{+}PD\text{-}1^{+}$CD8 T cells also tend to be non-proliferative in KPL TME (**Figures 3.7G-H**), suggesting a potential cause for low abundance of this group of cells mediated by *Stk11/Lkb1* loss.

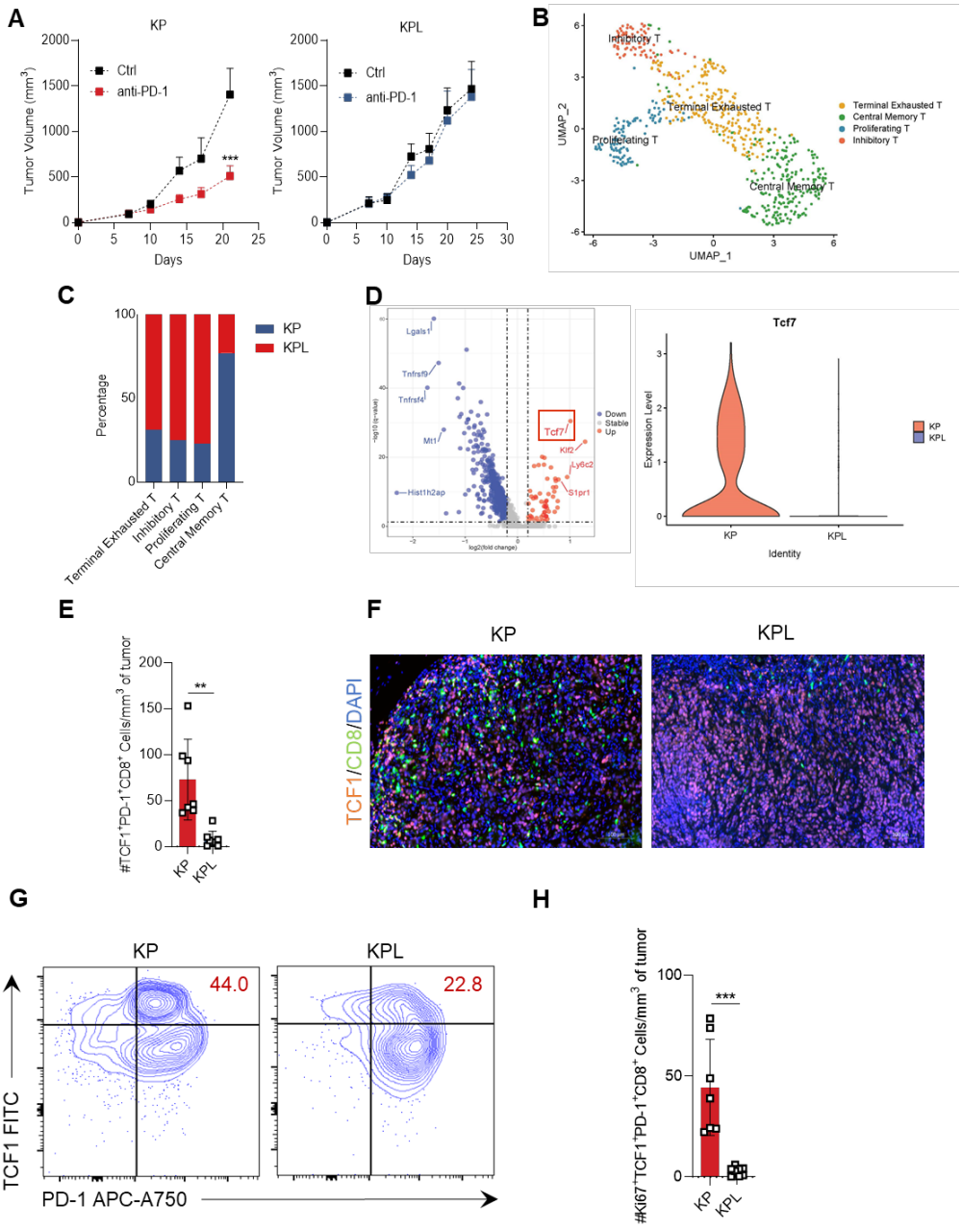

Figure 3.7 *Stk11/Lkb1* mutant NSCLC lacks anti-PD-1 responsive T cells.

(A) C57BL/6J mice (n = 5) were inoculated with 1 x 10^6 KP (left) or KPL (right) tumor cells and treated with anti-PD-1 (10 mg/kg, day 7, 10, 14). Tumor volume was measured every 3 days.

(B) UMAP of sub-clustering tumor infiltrating CD8 T cells in KP and KPL tumors. T cell clusters are denoted by color.

(C) UMAP of tumor infiltrated CD8 T cells in KP and KPL tumors (top). Abundance of CD8 T cells in each cluster from each sample are calculated (bottom).

(D) Volcano plot (left) for up- (red) and down- (blue) regulated genes in central memory T cell cluster with *Tcf7* highlighted. The expression level of *Tcf7* in CD8 T cells of KP and KPL are compared and visualized through a violin plot (right).

(E) Abundance of $TCF1^+PD\text{-}1^+$ cells among gated CD8 tumor infiltrating lymphocytes (TILs) (per mm^3 of tumor) on day 14 post tumor cell injection.

(F) Visualization and localization of $TCF1^+$ (orange) expressing $CD8^+$ (green) T cells in KP (left) and KPL (right) tumor microenvironment through immunohistochemistry.

(G) Representative infiltrated $TCF1^+PD\text{-}1^+$ cell percentages among gated CD8 tumor infiltrating lymphocytes (TILs).
(H) Abundance of proliferating $TCF1^+PD\text{-}1^+$ cells among gated $CD8^+$ (TILs) (per mm^3 of tumor).

We also evaluated central memory like CD8 T cell infiltration status in lung adenocarcinoma patients. First, immunohistochemical analysis of 62 of our NSCLC patient tumors showed *STK11/LKB1* mutant tumors exhibited reduced $CD8^+$, Granzyme B^+ (GzB^+) or $CD45RO^+$ cells compared to *STK11/LKB1* WT tumors (**Figure 3.8A**). As granzyme B marks activated CD8 T cells and CD45RO is a marker for naïve/central memory T cells, this cohort of patients likely also exhibited less of central memory CD8 T cells when having *STK11/LKB1* mutation.

Second, we examined the Cancer Genome Atlas (TCGA) database using TIMER deconvolution (B. Li et al., 2017). In this dataset, *TCF7* expression positively correlated with CD8 T cell infiltration (correlation = 0.31, p-value = 2.43e-12), and

CD8 T cell infiltration was reduced significantly in patients whose tumors harbor a mutation in *STK11/LKB1* (**Figure 3.8B**).

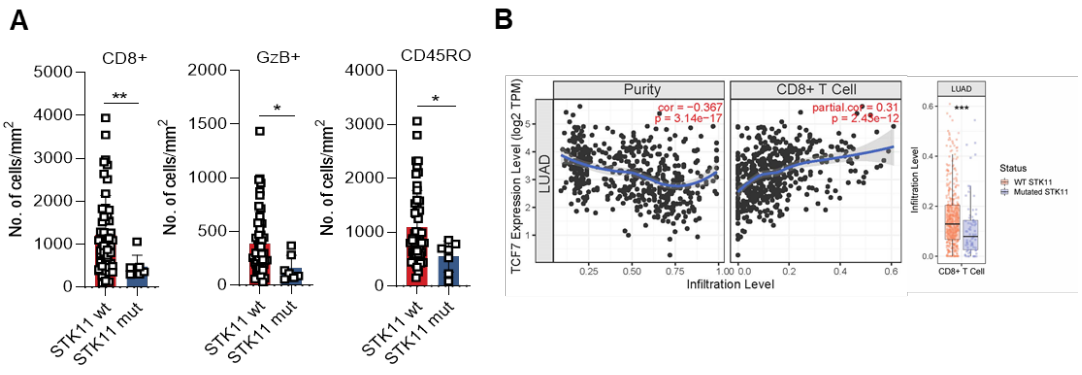

Figure 3.8. Characterization of central memory CD8 T cell status in NSCLC patients.
(A) Quantification of immunohistochemistry staining of CD8, Granzyme B (GzB) and CD45RO in *STK11/LKB1* wild type and mutant patients.

(B) Correlation of *TCF7* expression, tumor purity and CD8 T cell infiltration in TCGA lung adenocarcinoma patients (left). The expression of *TCF7* negatively correlates with tumor purity, suggesting the main source of *TCF7* expression detected is stromal and immune cells (correlation = -0.367, p-value = 3.14e-17). The correlation of CD8 T cell infiltration and *STK11/LKB1* mutation in lung adenocarcinoma patients modified from TIMER deconvolution (right).

As TCF1 expressing CD8 T cells exhibit central memory features, lack of these cells in, our own and the TCGA datasets, indicates the lack of tumor associated memory T cells in the TME of *STK11/LKB1* mutant NSCLC. Collectively, these results suggest that TCF1^{+} CD8 T cells in the TME correlate with CD8 T cell infiltration, which could impact response to anti-PD-1/PD-L1 treatment.

3.3 *Stk11/Lkb1* Mutation Mediated Immune Signaling Pathway Regulation

Up to date, several groups had reported the role of *Stk11/Lkb1* mutation in influencing TME (Ji et al., 2007; Koyama et al., 2016a; Skoulidis et al., 2018a), whereas little is known for how immune signaling pathway or features are being regulated by *Stk11/Lkb1* loss on tumor cells. It is worthwhile for exploring the underlying mechanism, which could provide potential therapeutic opportunities for *SKT11/LKB1* mutated NSCLC patients.

3.3.1 Signaling pathway regulated by Stk11/Lkb1 mutation

KP and KPL tumors were implanted onto either *Myd88*$^{-/-}$ mice (Jackson Laboratories, Cat# 017537) or *STING*$^{-/-}$ mice (Jackson Laboratories, Cat# 009088) to analyze whether Stk11/Lkb1 loss could impact innate sensing signaling, which further regulates TME. Comparing to KP tumors, KPL tumors paralyzed the Myd88-TLR signaling pathway (**Figure 3.9A-B**). Unlike KP tumors grew faster on *Myd88*$^{-/-}$ mice, no growth difference observed for KPL tumors grown on *wild-type* or *Myd88*$^{-/-}$ mice, indicating that Myd88-TLR signaling pathway was dysfunctional in KPL tumors already. On the contrary, both KP and KPL tumors were grew faster on *STING*$^{-/-}$

mice, suggesting the cGAS-STING pathway was not affected by Stk11/Lkb1 mutation in NSCLC tumors (**Figure 3.9C-D**).

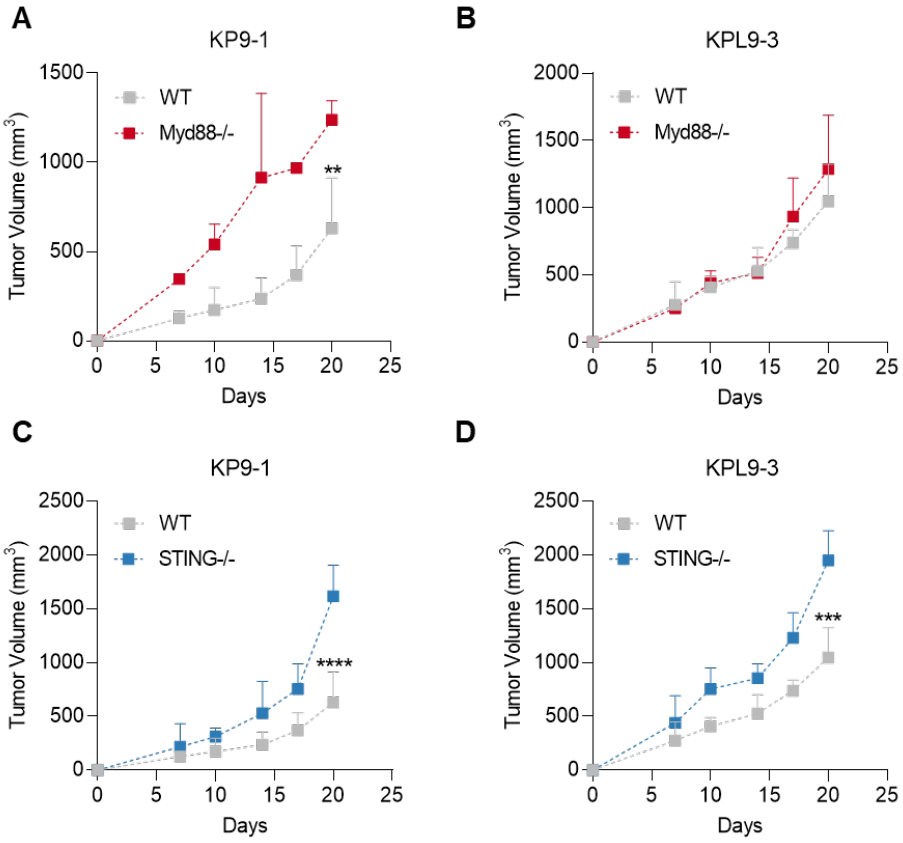

Figure 3.9 *Stk11/Lkb1* mutation mediated innate sensing pathway regulation changes.

(A-B) Wild-type (WT) or *Myd88*$^{-/-}$ mice (n = 5) were injected subcutaneously with 1 x 10^6 KP or KPL tumor cells. Tumor growth was measured every 3 days.

(C-D) Wild-type (WT) or *STING*$^{-/-}$ mice (n = 5) were injected subcutaneously with 1 x 10^6 KP or KPL tumor cells. Tumor growth was measured every 3 days.

Next, downstream modulations of innate sensing pathway resulted from Stk11/Lkb1 mutation were analyzed to further link to TCF1$^+$PD-1$^+$CD8 T cells infiltration changes

and anti-PD-1/PD-L1 therapeutic responses. Type I interferon produced from innate sensing pathway in myeloid cells is critical for promoting anti-tumor response (Diamond et al., 2011; Woo et al., 2014; Yang et al., 2014). When block Type I interferon signaling pathway in KP tumors by intra-tumoral injection of anti-mouse IFNAR-1 antibody (BioXCell, Cat# BE0241), the abundance of $TCF1^{+}PD\text{-}1^{+}CD8$ T cells in KP tumors turned to be similar to KPL tumors (**Figure 3.10A**). Gene-set enrichment analysis (GSEA) of CD8 T cells from scRNAseq also indicated that KPL tumors defected in interferon signaling pathway (**Figure 3.10B**). Taken together, defection of type I interferon production and signaling pathway are the main cause for $TCF1^{+}PD\text{-}1^{+}CD8$ T cells reduction in KPL tumors, which may be regulated by *Stk11/Lkb1* mutation and ultimately leading to anti-PD-1 treatment responses.

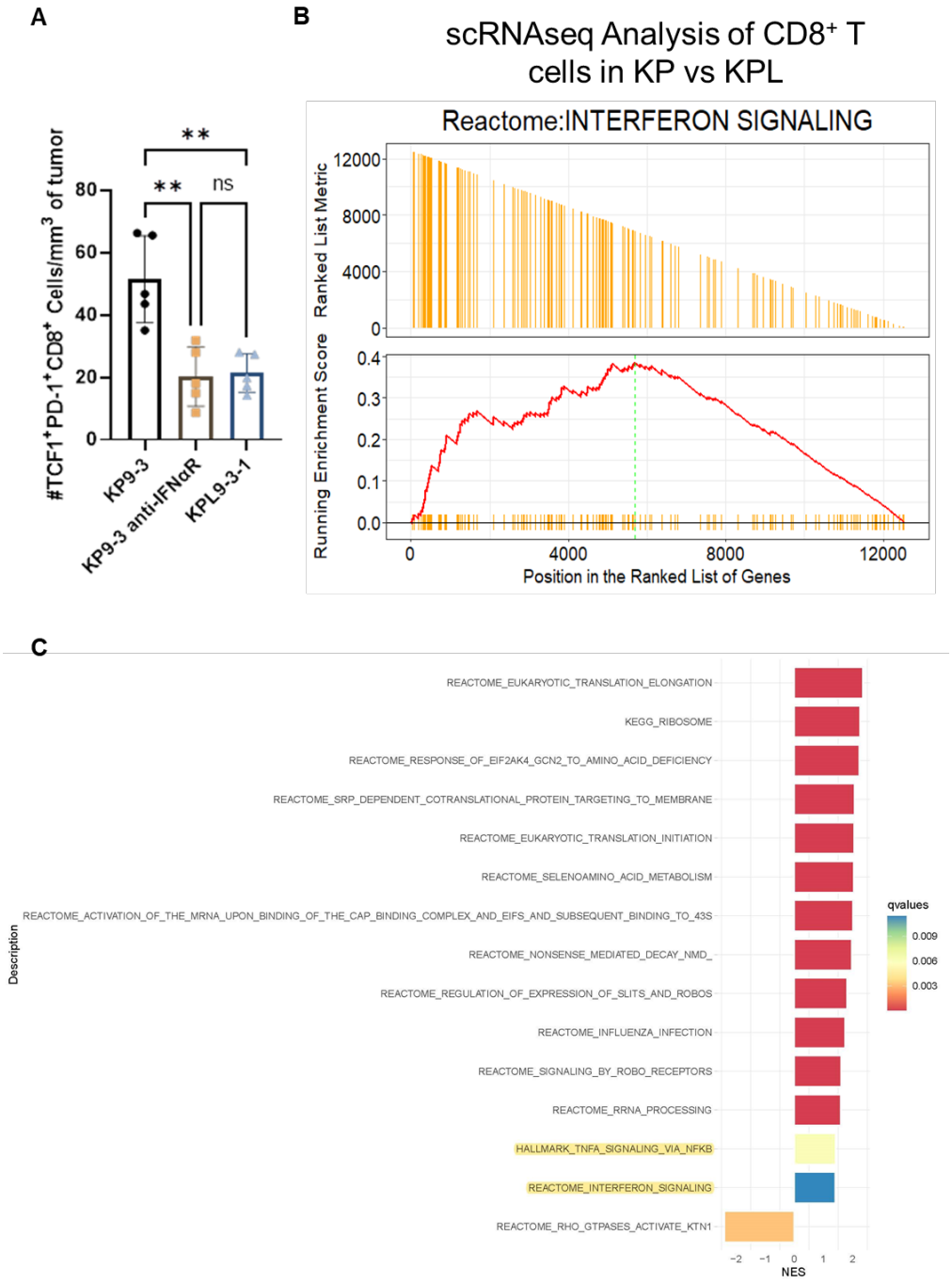

Figure 3.10 *Stk11/Lkb1* mutation defects interferon signaling in TME.

(A) Abundance of $TCF1^{+}PD\text{-}1^{+}$ cells among gated CD8 tumor infiltrating lymphocytes (TILs) (per mm^3 of tumor) on day 7 post treatment initiation.

(B) Gene set enrichment analysis (GSEA) plot of CD8 T cells in KP vs KPL allografts based on scRNAseq.

(C) Significant altered GESA pathway ranked by national evaluation series (NES) score of CD8 T cells in KP vs KPL allografts based on scRNAseq.

Full list of significant up- or down- regulated signaling pathway analyzed from gene-set enrichment analysis (GSEA) of CD8 T cells from scRNAseq were ranked based on national evaluation series (NES) score and listed below (**Figure 3.10C**; **Table 3-1**). CD8 T cells in KPL tumors were less active in ribosome assembling and translation, as well as NF-κB signaling pathway activation. These further suggested a less active CD8 T cells in KPL tumors mediated by Stk11/Lkb1 mutation.

Description	Set Size	Enrichment Score	NES	pvalue	p.adjust	qvalues
KEGG_RIBOSOME	83	0.642473	2.248944	1.00E-10	1.77E-08	1.73E-08
REACTOME_EUKARYOTIC_TRANSLATION_ELONGATION	88	0.6648	2.343172	1.00E-10	1.77E-08	1.73E-08
REACTOME_EUKARYOTIC_TRANSLATION_INITIATION	115	0.572053	2.051063	1.00E-10	1.77E-08	1.73E-08
REACTOME_NONSENSE_MEDIATED_DECAY_NMD_	111	0.550885	1.971566	1.00E-10	1.77E-08	1.73E-08
REACTOME_REGULATION_OF_EXPRESSION_OF_SLITS_AND_ROBOS	152	0.495651	1.808992	1.00E-10	1.77E-08	1.73E-08
REACTOME_RESPONSE_OF_EIF2AK4_GCN2_TO_AMINO_ACID_DEFICIENCY	97	0.626195	2.224125	1.00E-10	1.77E-08	1.73E-08

REACTOME_SELENOAMINO_ACID_METABOLISM	106	0.571379	2.039654	1.00E-10	1.77E-08	1.73E-08
REACTOME_SRP_DEPENDENT_COTRANSLATIONAL_PROTEIN_TARGETING_TO_MEMBRANE	108	0.578055	2.066135	1.00E-10	1.77E-08	1.73E-08
REACTOME_INFLUENZA_INFECTION	147	0.477981	1.738587	6.45E-10	1.01E-07	9.94E-08
REACTOME_ACTIVATION_OF_THE_MRNA_UPON_BINDING_OF_THE_CAP_BINDING_COMPLEX_AND_EIFS_AND_SUBSEQUENT_BINDING_TO_43S	58	0.593065	2.010917	2.03E-09	2.87E-07	2.82E-07
REACTOME_RRNA_PROCESSING	195	0.432301	1.595707	4.27E-09	5.49E-07	5.39E-07
REACTOME_SIGNALING_BY_ROBO_RECEPTORS	187	0.437007	1.610621	9.11E-09	1.07E-06	1.05E-06
REACTOME_RHO_GTPASES_ACTIVATE_KTN1	10	-0.72212	-2.39542	2.93E-05	0.003186	0.003126
HALLMARK_TNFA_SIGNALING_VIA_NFKB	180	0.385656	1.418136	6.15E-05	0.006209	0.006093
REACTOME_INTERFERON_SIGNALING	152	0.384954	1.404979	0.000124	0.011648	0.011429

Table 3-1 GSEA analysis of CD8 T cells in KPL vs KP TME. Gene set enrichment analysis (GSEA) statistics of pathways that significantly upregulated or downregulated on CD8 T cells in KP vs KPL allografts.

3.3.2 Genes and other immune features regulated by Stk11/Lkb1 mutation

To further dissect how *LKB1/STK11* mutation changes tumor cell features which further influences immune signaling and TME, a systematic analysis for features

differs in *LKB1/STK11* wild-type or mutated NSCLC human cell lines was done based on whole-exosome sequencing and RNA-seq information.

While *LKB1/STK11* mutated NSCLC cell lines did not increase the mutation burden of tumor cells (**Figure 3.11A**), it down-regulated MHC expression on tumor cells (**Figure 3.11B**). As MHC expression is critical for presenting antigens to APCs, down-regulation of MHC expression may lead to a decreased infiltration of immune cells into TME.

In addition, significant up- or down- regulated genes based on RNA-seq data was analyzed through DGEs analysis (**Figure 3.11C**). As two of the most differentially expressed genes, ALDH1A1 and SP-D had been reported for their roles in suppressing immune cells function (Bakdash et al., 2015; Haczku, 2008; Oliveira et al., 2018). When comparing the *ALDH1A1* and *SP-D* mRNA expression in human NSCLC cell lines, these two genes were significantly upregulated when NSCLC cell lines harbored *LKB1/STK11* mutation, suggesting their potential roles in creating a more immune suppressive TME (**Figure 3.11D-E**). However, their functions in regulating TME need to be further validated through CRISPR knock-out and rescue expression for the candidate genes.

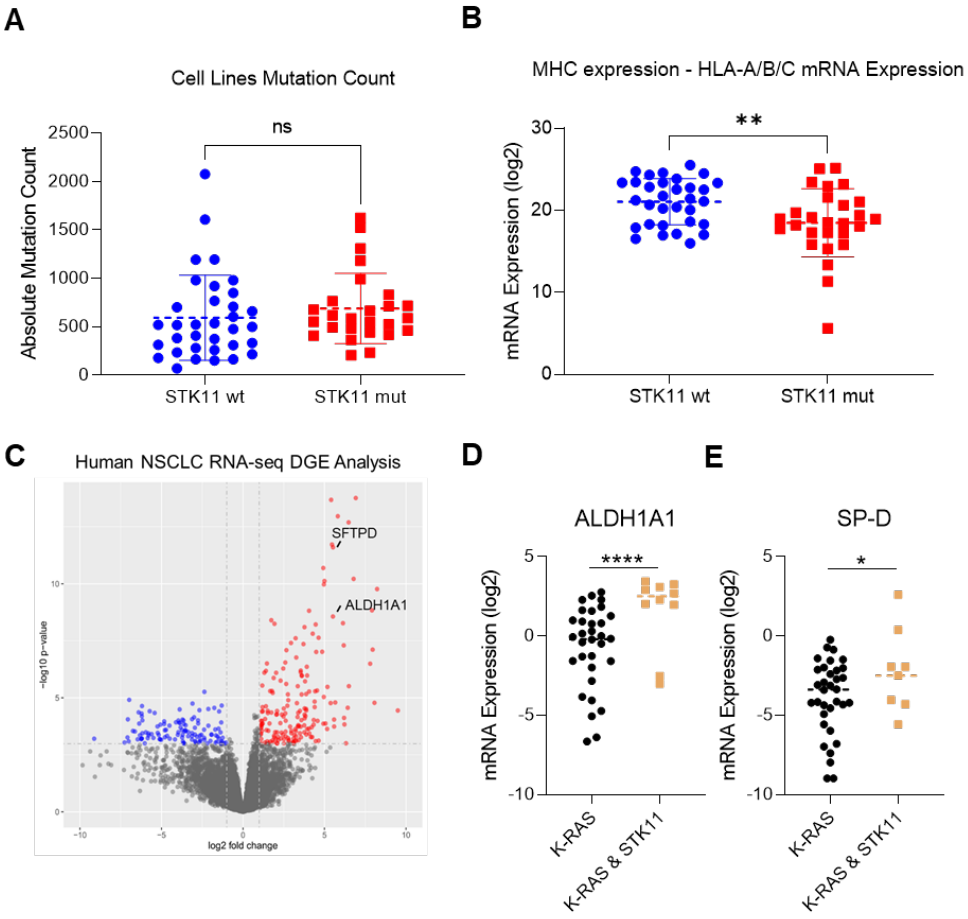

Figure 3.11 Effect of *STK11/LKB1* mutation on human NSCLC cell lines.

(A) Mutation count of human NSCLC cell lines w/o or with *STK11/LKB1* mutation based on whole-exosome sequencing.

(B) MHC expression based on RNA-seq of human NSCLC cell lines w/o or with *STK11/LKB1* mutation.

(C) Volcano plot of genes upregulated or downregulated mediated by *STK11/LKB1* mutation based on RNA-seq in human NSCLC cell lines.

(D-E) ALDH1A1(D) and SP-D (E) mRNA expression in human NSCLC cell lines w/o or with *STK11/LKB1* mutation based on RNA-seq.

In addition to *ALDH1A1* and *SP-D*, the full list of significantly up- and down-regulated genes in *LKB1/STK11* mutated human NSCLC cell lines were listed below (**Table 3-2**). Some of genes listed here also had been reported for their role in regulating TME, and their further validation need to be done through knock-out and rescue of gene expression. For further detailed mechanism study, a mouse KPL cell lines exhibit similar gene expression pattern need to be utilized for immune cell *in vivo* depletion study.

Genes	logFC	logCPM	LR	PValue	LogPValue	FDR
PTPRC	6.918	3.0367	58.808	1.74E-14	13.75976	1.64E-10
CD36,GNAT3	5.409	1.7431	58.448	2.09E-14	13.68033	1.64E-10
HVCN1	5.816	2.9616	55.196	1.09E-13	12.96227	5.7E-10
RP11-507M3.1,FAM228A	6.48	0.5126	53.974	2.03E-13	12.69223	7.97E-10
CLCA2	5.458	2.1447	49.586	1.9E-12	11.72156	5.96E-09
SFTPD	5.52	1.7813	49.025	2.53E-12	11.59737	6.61E-09
SUSD2	4.926	5.1567	44.938	2.03E-11	10.69163	4.56E-08
GPR97	6.786	1.5038	42.787	6.1E-11	10.21451	1.2E-07
BAAT	4.999	1.3007	42.368	7.56E-11	10.12143	1.32E-07
FER1L6	4.965	1.73	41.698	1.06E-10	9.972664	1.67E-07
DPPA2	8.229	0.8753	40.777	1.71E-10	9.767989	2.43E-07
PAX7	7.911	-0.878	36.59	1.46E-09	8.836331	1.83E-06
SCN3A	4.055	1.2027	36.508	1.52E-09	8.818139	1.83E-06
ALDH1A1	5.517	7.9369	35.37	2.73E-09	8.5644	3.06E-06
NHSL1	1.739	4.6712	34.641	3.96E-09	8.40186	4.15E-06
CRISP3	6.134	2.4092	34.061	5.34E-09	8.272391	5.24E-06
CREM	1.931	4.9677	33.942	5.68E-09	8.245821	5.24E-06
CLDN16	4.458	1.7525	33.805	6.09E-09	8.215265	5.31E-06
MPZ	3.772	0.7978	33.279	7.98E-09	8.097879	6.59E-06
ASB4	4.277	1.308	31.998	1.54E-08	7.811588	1.21E-05

MGAT4C	4.638	0.2702	31.202	2.33E-08	7.633476	1.74E-05
SLC26A4	3.228	2.0822	31.101	2.45E-08	7.611012	1.75E-05
SLC9A3	2.947	2.7292	30.191	3.92E-08	7.407195	2.67E-05
DCDC1	3.71	0.9348	29.962	4.41E-08	7.355958	2.88E-05
ABCA8	6.181	3.5615	29.709	5.02E-08	7.299276	3.15E-05
COL11A1	7.953	5.8642	28.874	7.72E-08	7.112201	4.66E-05
LEPREL1	2.663	6.3151	28.768	8.16E-08	7.088324	4.74E-05
CDH17	4.858	3.4319	28.459	9.57E-08	7.019041	5.27E-05
C1QL4	4.49	1.5047	28.424	9.75E-08	7.011188	5.27E-05
RAPGEF4	3.268	1.888	27.337	1.71E-07	6.767281	8.94E-05
RGS2	2.595	4.8594	26.359	2.84E-07	6.547404	0.000143
PTP4A1	1.468	8.1858	26.172	3.12E-07	6.50545	0.000152
CGA	7.801	3.072	26.129	3.19E-07	6.495839	0.000152
KCNH3	3.915	2.6746	25.525	4.37E-07	6.359865	0.000201
NOSTRIN,SPC25	2.47	2.9126	25.191	5.19E-07	6.284624	0.000233
SLC2A9,DRD5	3.545	1.7473	24.791	6.39E-07	6.194645	0.000278
LANCL1	1.407	6.2245	24.725	6.61E-07	6.179623	0.00028
PCDH9	3.536	4.3499	24.474	7.53E-07	6.123169	0.000311
XPR1	1.311	7.0263	24.374	7.93E-07	6.100516	0.000315
TMEM144	2.032	4.3593	24.353	8.02E-07	6.095894	0.000315
WNT16	3.937	1.0382	23.827	1.05E-06	5.977154	0.000395
DLG2	3.6	1.693	23.822	1.06E-06	5.976148	0.000395
FAM198B	3.612	3.9354	23.77	1.09E-06	5.96424	0.000396
STARD4	1.882	5.5291	23.355	1.35E-06	5.870759	0.00048
RGS5	2.305	2.2293	22.827	1.77E-06	5.751501	0.000618
ITIH2	3.809	0.6347	22.699	1.89E-06	5.722445	0.000646
COL4A3	2.653	2.6244	22.199	2.46E-06	5.609482	0.00082
MFF	1.181	7.0413	21.884	2.9E-06	5.538218	0.000947
CDH19	6.496	1.5094	21.768	3.08E-06	5.511901	0.000971
DLGAP1	3.359	1.6386	21.756	3.1E-06	5.509265	0.000971
XYLT1	5.182	1.8673	21.619	3.33E-06	5.478159	0.001023
GPR133	4.544	4.3443	20.911	4.81E-06	5.317845	0.001451
CTSL	1.78	7.7344	20.831	5.02E-06	5.299651	0.00147
ZNF219,TMEM253	1.667	-0.5096	20.813	5.06E-06	5.295443	0.00147
COL15A1	4.423	3.5023	20.779	5.15E-06	5.287869	0.00147
FGF14	4.061	0.1088	20.723	5.31E-06	5.275216	0.001487

RASSF4,C10orf10	-2.369	2.2076	20.665	5.47E-06	5.261985	0.001506
ARL4D	1.826	4.5114	20.458	6.09E-06	5.215106	0.001648
EMILIN3	3.877	-2.3507	20.242	6.82E-06	5.165952	0.001815
ITIH4,RP5-966M1.6	2.758	1.0128	20.167	7.09E-06	5.149048	0.001828
RBFOX3	3.596	-1.4409	20.164	7.11E-06	5.148349	0.001828
SLITRK3	4.958	1.3371	19.674	9.18E-06	5.03704	0.002324
DDX43	-6.979	2.6014	19.121	1.23E-05	4.911233	0.003055
PPP1R3C	2.775	4.051	19.056	1.27E-05	4.896462	0.003111
CEACAM5, CEACAM4, CEACAM7, CEA	4.394	4.2571	18.777	1.47E-05	4.832832	0.003547
MAPK4	5.659	1.8093	18.61	1.6E-05	4.794784	0.003813
DLK1	8.066	2.1233	18.544	1.66E-05	4.779881	0.003887
PSG6,PSG8	5.377	-0.0877	18.493	1.71E-05	4.7681	0.003888
NELL2	3.305	3.6485	18.488	1.71E-05	4.767045	0.003888
SLC2A12	-3.098	3.9837	18.404	1.79E-05	4.748014	0.004004
NEK6	-1.306	5.6031	18.012	2.2E-05	4.65847	0.004851
MRC1	2.725	-0.5296	17.984	2.23E-05	4.652106	0.004855
LOXL4	-6.195	4.2254	17.922	2.3E-05	4.638102	0.004945
PGD	1.408	8.7692	17.877	2.36E-05	4.627701	0.004996
VIL1	4.398	2.1148	17.726	2.55E-05	4.593273	0.005304
PHF10	1.194	6.3091	17.712	2.57E-05	4.590178	0.005304
KANK4	6.425	2.7457	17.592	2.74E-05	4.562589	0.005562
CAV1	-1.759	7.4955	17.573	2.77E-05	4.558246	0.005562
SLC24A3	3.773	-0.6969	17.449	2.95E-05	4.53002	0.005816
MTMR7	2.502	0.092	17.44	2.97E-05	4.527888	0.005816
KCNH3,MCRS1	3.869	1.0039	17.37	3.08E-05	4.511955	0.005921
PDE5A	-2.127	4.3756	17.359	3.09E-05	4.50937	0.005921
CCL28	-3.886	2.6876	17.276	3.23E-05	4.490441	0.00611
PIK3IP1	-2.67	1.6995	17.126	3.5E-05	4.456081	0.006535
HR	3.887	3.6529	17.086	3.57E-05	4.447112	0.006576
T	9.499	4.7586	17.069	3.6E-05	4.443129	0.006576
CREG1	1.518	5.5858	16.994	3.75E-05	4.42602	0.006691
PAPPA2	3.492	3.4994	16.984	3.77E-05	4.42371	0.006691
ID2	2.091	3.117	16.971	3.8E-05	4.420715	0.006691

DDX43,MB21D1	-5.722	1.9693	16.932	3.87E-05	4.411748	0.006721
ALDH3A2	1.218	7.9168	16.92	3.9E-05	4.409132	0.006721
UBTD1	-1.464	3.3587	16.893	3.95E-05	4.402964	0.006743
GCH1	1.16	3.5802	16.86	4.02E-05	4.395256	0.00679
OOEP	-6.403	-0.4861	16.718	4.34E-05	4.362836	0.007238
SLC39A8	1.744	6.6393	16.684	4.42E-05	4.354968	0.007293
NDNF	3.383	4.3339	16.62	4.57E-05	4.340449	0.007417
SIGLEC15	-5.419	-1.2651	16.598	4.62E-05	4.335381	0.007417
CPOX,GPR15	1.525	5.8619	16.593	4.63E-05	4.334135	0.007417
SLC5A11	2.597	-0.3238	16.531	4.79E-05	4.320032	0.007585
EPHX3	-6.221	2.8598	16.5	4.86E-05	4.313013	0.007631
AMDHD1	2.083	2.5955	16.353	5.26E-05	4.279298	0.008165
EDN1	2.044	3.8367	16.297	5.41E-05	4.266435	0.008255
PARM1	2.38	2.7519	16.293	5.43E-05	4.26541	0.008255
COL2A1	3.776	0.6938	16.277	5.47E-05	4.261848	0.008255
RAB10	0.695	7.307	16.161	5.82E-05	4.235286	0.008692
EPGN	3.833	2.862	16.003	6.32E-05	4.199103	0.009349
FPR1	-6.207	-0.2841	15.988	6.38E-05	4.195442	0.009349
PDE8A	0.912	6.656	15.94	6.54E-05	4.184556	0.009498
SLC7A7	2.485	3.194	15.914	6.63E-05	4.178671	0.009539
LRRC63	3.347	0.1268	15.826	6.94E-05	4.158337	0.009905
TNPO1	0.761	8.9243	15.791	7.07E-05	4.150309	0.009907
ATAD2B	0.823	5.0335	15.782	7.11E-05	4.148206	0.009907
PLIN4	-2.999	0.4161	15.775	7.14E-05	4.146589	0.009907
SCARA5	6.201	3.0061	15.66	7.58E-05	4.120236	0.010434
ZFYVE16	0.706	6.9373	15.63	7.7E-05	4.113477	0.010506
KIF26A	3.785	3.2975	15.575	7.93E-05	4.100685	0.010726
ITGA1,PELO	1.356	7.1009	15.449	8.48E-05	4.071856	0.011365
AC104532.2,VMAC,CAPS	-3.126	0.2194	15.422	8.6E-05	4.065536	0.011433
SLC6A20	-7.061	0.761	15.382	8.78E-05	4.056349	0.01158
ANXA13	5.587	2.1111	15.334	9.01E-05	4.045303	0.011687
IFFO1	-3.709	0.12	15.333	9.01E-05	4.045116	0.011687
COL25A1	4.339	0.8287	15.257	9.38E-05	4.027645	0.012067
A2M	3.582	2.93	15.235	9.49E-05	4.022622	0.012108
LIMD2	-2.758	2.0885	15.194	9.7E-05	4.013182	0.012186

MUC20	-6.168	5.323	15.193	9.71E-05	4.012835	0.012186
CSF1R	-3.648	1.3081	15.164	9.86E-05	4.006295	0.01224
C19orf38	-3.961	-0.1561	15.154	9.91E-05	4.004018	0.01224
NOSTRIN	2.619	1.0668	15.114	0.000101	3.994782	0.012374
IGF1R	1.103	6.6678	15.102	0.000102	3.992001	0.012374
MSR1	4.572	0.3882	15.089	0.000103	3.989138	0.012374
TACC2	1.165	6.3855	15.071	0.000104	3.984927	0.012399
ROBO4	-4.83	-0.0464	14.994	0.000108	3.967127	0.01282
GALNT9	-4.113	0.4467	14.817	0.000118	3.926412	0.013974
ADORA2B	-1.333	4.9637	14.783	0.000121	3.918627	0.014121
EFEMP2	-3.909	2.0759	14.737	0.000124	3.907935	0.014366
SPNS3	-3.872	0.1519	14.717	0.000125	3.903353	0.014411
COL4A4	2.291	3.6493	14.654	0.000129	3.88881	0.014793
ANKS4B,CRYM	5.065	-0.7261	14.595	0.000133	3.875177	0.01493
TRPM8	-2.746	-0.5336	14.589	0.000134	3.873978	0.01493
VPS37A,MTMR7	1.627	0.2002	14.587	0.000134	3.87352	0.01493
SLC23A2	1.208	5.2157	14.582	0.000134	3.872323	0.01493
WDR86	-6.368	-0.5013	14.567	0.000135	3.868924	0.014941
KRT6B	4.932	0.5868	14.549	0.000137	3.864761	0.01498
AOAH	-4.835	0.4647	14.495	0.000141	3.852172	0.015219
ACACB	1.166	4.0291	14.487	0.000141	3.850339	0.015219
POU3F2	-3.627	1.3949	14.48	0.000142	3.848868	0.015219
MMRN1	6.225	4.0244	14.411	0.000147	3.832778	0.015686
PLEKHS1	-5.062	1.4069	14.365	0.000151	3.822244	0.01586
SERPINB4, SERPINB3	4.334	1.2301	14.364	0.000151	3.822101	0.01586
LIMK2	1.135	4.4061	14.346	0.000152	3.817839	0.01591
CSMD3	3.391	1.7185	14.276	0.000158	3.801656	0.016404
IL4I1	-3.515	-0.3448	14.253	0.00016	3.79645	0.016493
SESN1	1.11	3.6594	14.231	0.000162	3.791307	0.016525
PHYHIPL	3.76	0.0933	14.225	0.000162	3.789936	0.016525
CLDN9	-4.508	1.6451	14.181	0.000166	3.779696	0.01681
DDN	-2.126	0.6181	14.163	0.000168	3.775751	0.016855
MYO1A	3.423	-0.0004	14.079	0.000175	3.756202	0.017518
LAMA4	-5.244	5.4804	14.02	0.000181	3.742539	0.017849
CDH10	5.59	3.7152	14.009	0.000182	3.739996	0.017849
CRISPLD1	2.892	5.164	13.988	0.000184	3.735284	0.017849

FAM110C	3.35	2.3442	13.988	0.000184	3.735152	0.017849
LIN7A	3.539	0.5538	13.985	0.000184	3.734464	0.017849
SPAG1,RNF19A	1.138	5.0909	13.942	0.000189	3.724501	0.018151
DOC2B	4.212	-0.0973	13.857	0.000197	3.704882	0.018874
MUS81,EFEMP2	-3.83	0.3788	13.845	0.000199	3.702203	0.018876
CARD9	-2.951	0.6548	13.78	0.000206	3.687078	0.019427
CTPS1	1.078	7.478	13.656	0.000219	3.658575	0.020621
CUL4A	0.889	7.4696	13.621	0.000224	3.650282	0.020835
CTNND2	4.036	0.2969	13.611	0.000225	3.648083	0.020835
CCNG2	-1.497	5.7432	13.604	0.000226	3.646359	0.020835
USH1C	5.163	3.8947	13.555	0.000232	3.635046	0.02126
SSTR1	3.935	0.5708	13.523	0.000236	3.627618	0.021501
COL5A2	3.21	7.3718	13.506	0.000238	3.623818	0.021564
PDP1	-1.702	8.031	13.446	0.000245	3.609982	0.022134
EMP1	-2.387	6.4248	13.418	0.000249	3.603336	0.022347
VWF	-4.722	2.6086	13.379	0.000254	3.594386	0.022683
FEZ2	0.966	6.0814	13.366	0.000256	3.59146	0.022707
SYT12	-3.742	5.0966	13.339	0.00026	3.585012	0.022822
GLCE	1.439	6.0141	13.336	0.00026	3.584394	0.022822
RARRES2	-3.539	-0.0416	13.313	0.000264	3.579142	0.022954
GMFG	-4.794	1.7162	13.304	0.000265	3.577054	0.022954
MXD1,AC019206.1	1.56	3.2504	13.213	0.000278	3.555846	0.023883
SLC44A1	1.168	7.4775	13.209	0.000279	3.55505	0.023883
NR5A2	2.968	2.3655	13.19	0.000282	3.550489	0.023909
CAV3,OXTR	-3.513	1.881	13.174	0.000284	3.546857	0.023909
RALGAPA1	0.732	6.4127	13.173	0.000284	3.546608	0.023909
ADAMTS12	-6.75	4.8365	13.167	0.000285	3.545201	0.023909
FOXI3	3.239	-1.1605	13.119	0.000292	3.534096	0.024324
GRPR	-3.585	0.8555	13.114	0.000293	3.533093	0.024324
C12orf60,SMCO3,ART4,MGP	-6.631	1.7988	13.078	0.000299	3.524535	0.024678
DDIT4L	2.611	1.2362	13.036	0.000306	3.514922	0.025098
ARMCX2	-3.357	4.6911	12.975	0.000316	3.500799	0.025793
NPL	1.972	1.5821	12.937	0.000322	3.491862	0.025911
B3GNT7	-3.967	2.2421	12.932	0.000323	3.490677	0.025911

TRPC6	3.761	1.05	12.92	0.000325	3.487997	0.025911
COL6A3	-5.96	5.3724	12.919	0.000325	3.48781	0.025911
CYFIP2	2.09	4.4316	12.918	0.000325	3.487629	0.025911
INSIG1	-1.376	5.6713	12.909	0.000327	3.485451	0.025911
PELI2	2.358	2.6176	12.861	0.000335	3.474369	0.026447
C1QTNF5	-5.232	-1.1064	12.814	0.000344	3.463475	0.026983
ENTPD5	0.788	3.9529	12.785	0.000349	3.456688	0.027046
COA6	0.81	5.6574	12.772	0.000352	3.453755	0.027046
MTFR1,PDE7A	0.921	4.5029	12.769	0.000352	3.453035	0.027046
DCDC2	2.967	2.5252	12.766	0.000353	3.452221	0.027046
SSPN	-3.127	2.1934	12.764	0.000353	3.451744	0.027046
PROM1	-6.173	2.5212	12.736	0.000359	3.445315	0.027205
PTPRZ1	3.494	3.8759	12.735	0.000359	3.44498	0.027205
CDK15	-5.799	1.2451	12.714	0.000363	3.440145	0.027347
LANCL2	1.102	4.8098	12.705	0.000365	3.438038	0.027347
CRABP1	4.074	-1.2565	12.698	0.000366	3.43646	0.027347
PADI3	-5.602	2.8237	12.583	0.000389	3.409688	0.028948
PLEKHF1	-1.934	2.5419	12.519	0.000403	3.394865	0.029812
EDARADD	3.887	2.1296	12.51	0.000405	3.392749	0.029817
TMC8	-2.945	1.6775	12.497	0.000408	3.389847	0.029877
RNF19A	1.089	5.8592	12.484	0.00041	3.38682	0.029946
HEY2	2.448	0.1794	12.474	0.000413	3.384442	0.029971
MAML2	-1.935	4.8712	12.457	0.000416	3.380568	0.029971
ZNF19,CHST4	-3.702	1.5064	12.456	0.000417	3.38033	0.029971
LTBP2	-2.548	6.7148	12.443	0.000419	3.377301	0.029971
SEC14L5	-3.995	0.1758	12.44	0.00042	3.376465	0.029971
MMP9	-5.169	3.52	12.425	0.000424	3.372992	0.030075
MCF2	3.149	1.2034	12.388	0.000432	3.364383	0.030539
OR4C6	-6.326	-0.4598	12.366	0.000437	3.359246	0.030764
ZNF521	-5.788	1.0863	12.347	0.000442	3.354975	0.030847
AC004076.9,VN1R1	-1.661	-0.1008	12.344	0.000442	3.354203	0.030847
CAPS	-2.64	0.5249	12.325	0.000447	3.349741	0.031027
CRTC3	0.97	4.4016	12.303	0.000452	3.344615	0.031258
PAG1	1.913	3.686	12.281	0.000458	3.339474	0.031491
STAG3	-4.653	3.0865	12.262	0.000462	3.335019	0.031677
SEC11C	0.961	5.221	12.223	0.000472	3.326014	0.0322

TGM4	-3.126	-0.5068	12.214	0.000474	3.323998	0.03221
BCL2L14	-3.359	0.1817	12.184	0.000482	3.317029	0.032578
ATP13A4	3.256	0.5658	12.177	0.000484	3.315315	0.032578
KMO	2.62	1.0292	12.15	0.000491	3.309136	0.032904
FBXO30	0.733	5.8936	12.12	0.000499	3.302011	0.033273
FOSL1	-1.551	6.6303	12.114	0.000501	3.300593	0.033273
MXRA8	-2.819	2.8065	12.09	0.000507	3.295157	0.03355
OTUD7A	2.144	-1.246	12.065	0.000514	3.289299	0.033863
SERPINB3, SERPINB11	4.164	1.7596	12.029	0.000524	3.280935	0.034377
KCNE4	4.249	4.8282	12.015	0.000528	3.277532	0.034503
CNTD1	-4.791	1.5934	11.981	0.000537	3.269629	0.034786
NTS	3.558	1.7582	11.978	0.000538	3.268953	0.034786
C5	1.918	5.8143	11.976	0.000539	3.268589	0.034786
APCDD1L	-7.083	1.6147	11.95	0.000547	3.262391	0.035141
ATG9B	-3.728	-0.1964	11.937	0.00055	3.259468	0.035234
C11orf68	-1.248	4.8229	11.89	0.000564	3.248452	0.035983
CATSPER1	-2.383	2.6655	11.876	0.000569	3.24526	0.035983
TARSL2	0.878	4.5272	11.875	0.000569	3.245046	0.035983
RGS4	-5.495	3.1546	11.863	0.000572	3.242249	0.03607
AMBP	2.767	-0.7166	11.832	0.000582	3.235033	0.036528
TH	-5.843	-1.3938	11.824	0.000585	3.232961	0.036556
PLXNA4	-6.201	1.3737	11.748	0.000609	3.21523	0.037762
CX3CL1	-6.223	3.6028	11.739	0.000612	3.213181	0.037762
RAB3B	2.331	3.1799	11.738	0.000612	3.213016	0.037762
CAPG	-1.478	7.0245	11.734	0.000614	3.211997	0.037762
C4orf26	-4.496	-0.6633	11.72	0.000618	3.208745	0.037801
LRP2	3.1	1.8436	11.715	0.00062	3.207606	0.037801
FAM101A,RP11-214K3.25	-9.128	0.8952	11.71	0.000622	3.206472	0.037801
SOWAHC	1.114	6.8397	11.663	0.000637	3.195585	0.038558
PSEN2	0.744	4.1999	11.652	0.000641	3.193019	0.038558
UNC5B	2.521	2.9493	11.652	0.000641	3.192835	0.038558
CYFIP2,FNDC9	2.026	3.0242	11.639	0.000646	3.189803	0.03868
SKAP1	-5.115	2.2406	11.627	0.00065	3.187088	0.038775
ANO2	-6.245	0.8531	11.615	0.000654	3.184233	0.038883
DOCK2	-5.082	2.0935	11.595	0.000661	3.179656	0.03901

CXCR3	-6.462	-0.8756	11.595	0.000661	3.179539	0.03901
MFAP4	-4.171	1.9959	11.581	0.000666	3.176313	0.039153
ABR	-0.819	6.8343	11.574	0.000669	3.174691	0.039153
CD40	-3.132	3.6348	11.549	0.000678	3.168917	0.039427
SPATS2	0.894	6.6275	11.547	0.000679	3.168443	0.039427
AFAP1L2	-2.629	4.6039	11.52	0.000688	3.162149	0.039854
CST6	-5.016	4.4498	11.509	0.000693	3.159482	0.039881
PLAU,C10orf55	-2.364	8.7933	11.497	0.000697	3.156691	0.039881
ENTPD1	2.813	-1.485	11.492	0.000699	3.155636	0.039881
HDDC3,UNC45A	0.806	3.5906	11.492	0.000699	3.155494	0.039881
CHD5	2.16	1.7377	11.446	0.000717	3.144762	0.040681
KRT17	3.415	5.9391	11.441	0.000718	3.143721	0.040681
SCUBE2	1.824	-0.8595	11.413	0.000729	3.137154	0.041153
FSTL4	3.191	4.3911	11.35	0.000754	3.122427	0.042419
PLA2G7	4.641	1.0816	11.34	0.000759	3.120012	0.042504
DIO2	3.262	2.8715	11.317	0.000768	3.11461	0.042882
BDKRB2,RP11-404P21.8	2.793	2.3064	11.301	0.000775	3.110908	0.042961
MPP3	0.888	2.6562	11.298	0.000776	3.110075	0.042961
TMEM25	-1.997	3.268	11.294	0.000778	3.109198	0.042961
TMEM229B	-2.934	-0.372	11.26	0.000792	3.101298	0.043597
ESM1	4.458	1.8386	11.253	0.000795	3.099776	0.043597
OOEP,DDX43	-7.009	-0.4159	11.213	0.000812	3.090397	0.044199
SH3D21,EVA1B	-2.623	2.2512	11.211	0.000813	3.089853	0.044199
MAML3	1.487	3.3407	11.209	0.000814	3.089282	0.044199
KCNN4	-1.296	5.4414	11.197	0.000819	3.086501	0.044299
SPON2	-3.685	1.1809	11.192	0.000822	3.085308	0.044299
FAM46A	1.671	4.2912	11.157	0.000837	3.077114	0.044988
ETS1	-1.324	6.2821	11.125	0.000852	3.069743	0.045602
FAM3C	-1.596	7.633	11.112	0.000858	3.066677	0.045769
GABRD	3.077	0.5647	11.071	0.000877	3.05705	0.046636
NFATC2	-2.909	2.7924	11.059	0.000883	3.054185	0.046786
EIF2B5,DVL3,AP2M1,ABCF3,VWA5B2	1.855	-0.1563	11.047	0.000888	3.051385	0.04693

HAL	3.06	2.9028	11.03	0.000896	3.047567	0.047186
COL6A1	-2.695	7.5036	11.003	0.00091	3.041012	0.047538
CYSLTR1	-7.265	0.4115	10.998	0.000912	3.040041	0.047538
EPAS1	1.344	7.5057	10.993	0.000915	3.038677	0.047538
DOC2A	-1.679	1.462	10.986	0.000918	3.037245	0.047538
LGALS1	-1.039	7.9149	10.986	0.000918	3.037108	0.047538
GKAP1	0.92	3.3825	10.948	0.000937	3.028333	0.048323
PLEKHM1	-0.702	5.0937	10.943	0.000939	3.027144	0.048323
FFAR4,RBP4	3.098	-0.2673	10.897	0.000963	3.016232	0.049248
TRAFD1	-0.737	5.7685	10.896	0.000964	3.016069	0.049248
SMC1B	-3.627	3.08	10.886	0.000969	3.013796	0.049251
EYA1	-3.642	2.8274	10.877	0.000974	3.011516	0.049251
TNFAIP3	1.58	4.8597	10.877	0.000974	3.011487	0.049251
WBSCR17	6.318	0.2292	10.855	0.000985	3.006532	0.049251
OLFML2A	2.089	3.9425	10.844	0.000991	3.00389	0.049251
IL37	-6.022	2.3814	10.844	0.000991	3.003814	0.049251
MAGI1	-1.113	5.3571	10.838	0.000995	3.002377	0.049251
SHC4	2.086	0.8481	10.834	0.000996	3.001549	0.049251
PDK4	2.508	5.5934	10.831	0.000998	3.000786	0.049251
NUDT14	0.851	3.8467	10.831	0.000998	3.000729	0.049251
SEMA7A	-2.187	4.825	10.829	0.000999	3.000332	0.049251
DISP1	1.113	4.2347	10.825	0.001001	2.999386	0.049251
DDX1	0.611	8.481	10.803	0.001013	2.994262	0.04968
IDS	-1.346	7.8253	10.79	0.00102	2.991297	0.049865

Table 3-2 Upregulated and downregulated gene list of *STK11/LKB1* mutation mediated gene expression changes (FDR < 0.05). Full list of significantly upregulated or downregulated mRNA expression of genes from differential gene expression analysis (DGEs) in *STK11/LKB1* wild-type or mutated human NSCLC cell lines. Genes were filtered with false discovery rate (FDR) < 0.05.

To dissect whether mouse KPL models mimic the human NSCLC cell lines, the microarray data from orthotopic GEMM models published were analyzed (Ji et al., 2007). For mouse KPL primary tumors, they replicated the observations in human

NSCLC and showed increased expression of *ALDH1A1* and *SFTPD* (encodes SP-D) (**Figures 3.12A-B**). In additional, mRNA expression of selected candidate genes was evaluated from KP and KPL cell lines cultured *in vitro*, to compare whether *Stk11/Lkb1* mutation caused same effect in candidate gene expression (**Figures 3.12C-D**). While part of expression was consistent with human NSCLC cell lines, some of genes did not show significant differences. Furthermore, there are variations of the differences in KP and KPL isogenic cell line pairs, which further complicates in studying these gene functions in regulating TME. Since the TME of KP and KPL allografts still mimic the clinical observation and therapeutic responses (Skoulidis et al., 2018b), how important this genes for their role in regulating TME remain to be an open question.

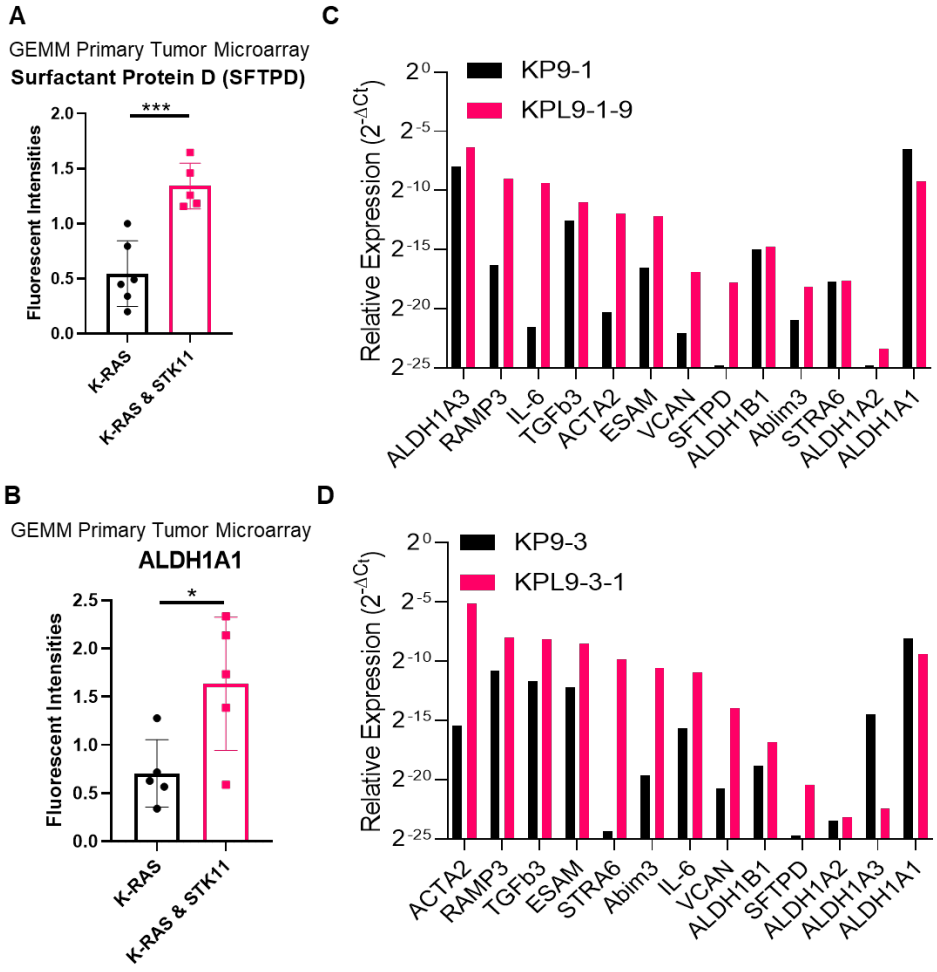

Figure 3.12 Mouse gene mRNA expression of selected candidate genes based on human NSCLC cell lines.

(A-B) SFTPD (A) and ALDH1A1 (B) mRNA expression from primary orthotopic tumor microarray of GEMM models in *K-Ras* mutated or *K-Ras* and *Stk11/Lkb1* double mutated tumors.

(C-D) mRNA expression of KP vs KPL cell lines *in vitro* based on qPCR.

Besides mutation counts, MHC expression and potential candidate genes changes mediated by *Stk11/Lkb1* mutation, cytokine/chemokine expression changes were

also analyzed. As cytokine and chemokine are main secreted signal for immune cell recruitment and crosstalk, changes in cytokine/chemokine expression on tumor cells may also changes TME.

Systematical evaluation of cytokine and chemokine expression pattern in human NSCLC cell lines were achieved through affinity propagation clustering based on cytokine and chemokine mRNA expression in RNA-seq data (**Figure 3.13A**). When clustered together, their expression pattern of cytokine and chemokine are closer. Central cell line is an exemplar of each cluster and cell lines harbors different oncogenic drivers were highlighted in different colors. Based on clustering, *STK11/LKB1* mutated NSCLC cell lines did not express similar pattern of cytokine/chemokine. The quantification of the pro-tumor and anti-tumor cytokine and chemokines need to further correlate to TME before any of conclusion could be made (**Figure 3.13B**). Besides, type I interferon is known for their high potency but low expression level in TME, and most of the times could not be captured due to the transient expression, the prediction value of the quantification needs to be further validated. The lower sensitivity of expressions in RNA-seq than specific qPCR primers detected cytokine/chemokine expression are also needed to consider when analyzing this data.

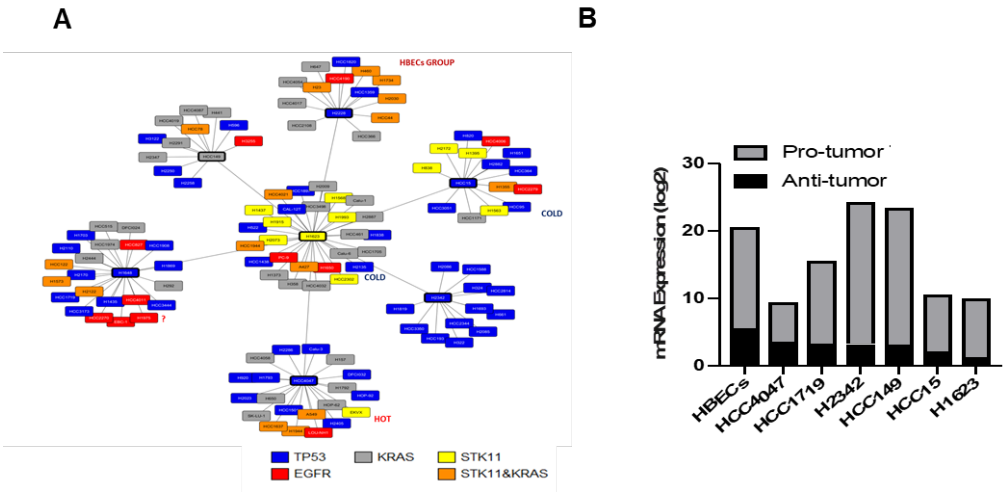

Figure 3.13 Cytokine/chemokine expression in human NSCLC.

(A) Affinity propagation clustering of human NSCLC cell lines based on cytokine/chemokine mRNA expression based on RNA-seq.

(B) Relative mRNA expression level quantification of pro-tumor and anti-tumor cytokine and chemokine. Each cell line name listed represents a group of clustered cell lines in (A) and the amount of mRNA were quantified based on the addition of individual cytokine/chemokine mRNA expression.

Cytokine and chemokine expression in mouse KP and KPL lines were also analyzed from *in vitro* culture through qPCR (**Figures 3.14A-B**). Similar to candidate gene expression, there were discrepancies in differences of cytokine/chemokine expression when it harbored *Stk11/Lkb1* mutation and limited conclusion could be draw from this experiment.

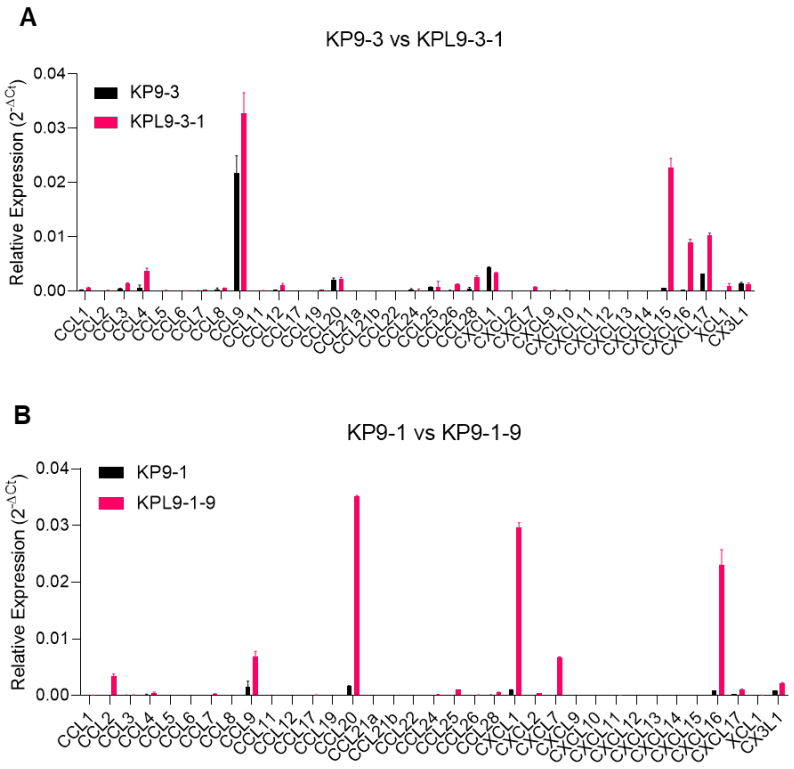

Figure 3.14 Characterization of cytokine and chemokine mRNA expression of KP and KPL cell lines. Cytokine/chemokine mRNA expression of KP vs KPL cell lines *in vitro* based on qPCR quantification. (A) indicates expression in KP9-3 vs KPL9-3-1, and (B) indicates expression of KP9-1 vs. KPL9-1-9.

Interestingly, a consistent response to interferon γ stimulation was observed from both isogenic mouse KP and KPL lines (**Figures 3.15A-B**). As interferon stimulating responses genes (ISGs), CXCL9-11 are chemokines released to recruit CD8 T cells. When stimulated KP and KPL lines with IFNγ (10 IU/ml) *in vitro*, KPL lines were not able to upregulate CXCL9-11 as much as KP lines. Therefore, *Stk11/Lkb1* mutation abrogated the ability for tumor cells to express ISGs, which may further influence their TME anti-PD-1/PD-L1 responses. Further evaluation of this signaling pathway

is needed to narrow down genes that could be knock-out or over-express to reverse ISGs responses upon stimulation.

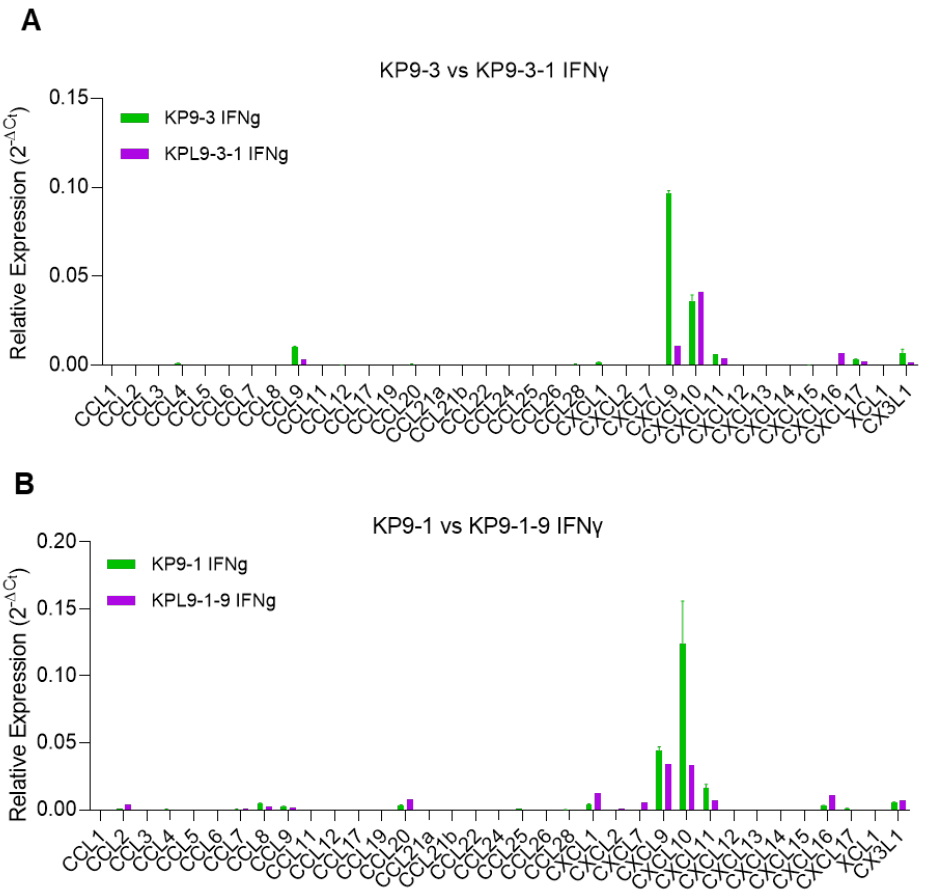

Figure 3.15 Characterization of cytokine and chemokine mRNA expression of KP and KPL cell lines. Cytokine/chemokine mRNA expression of KP vs KPL cell lines in response to IFNγ (10 IU/ml) stimulation *in vitro* based on qPCR quantification. (A) indicates expression in KP9-3 vs KPL9-3-1, and (B) indicates expression of KP9-1 vs. KPL9-1-9.

To evaluated cytokine and chemokine expression of KP and KPL lines at protein levels, mouse cytokine/chemokine XL profiling membranes (R&D Systems, Cat# ARY028) were used to detected cytokine and chemokine released into culturing medium (**Figures 3.16A-B**). Densitometric quantification for top differential released proteins were done using ImageJ to evaluate the differences in KP and KPL cell lines. Comparing to KP lines, KPL released less of CCL20, which could recruit Th17 cells and DCs (**Figure 3.16C**). Serpin E1 is a TGF-β ligands, GDF-15 and ICAM-1 could recruit T_{reg} cells in response to TGF-β (**Figures 3.16D-F**). Taken together, although TGF-β ligands did not upregulate upon *Stk11/Lkb1* mutation, their downstream molecule responsible for T_{reg} cells recruitment had already increased, which accord with a higher T_{reg}/CD8 T cell infiltration observation *in vivo*. Lipocaline-2/NGAL could suppress T cell recruitment and was increased in KPL cell line culturing medium (**Figures 3.16G**), which may explain for decreased T cell infiltration observed *in vivo*. However, how important the role is for specific cytokine/chemokines in contributing to TME changes in KPL tumors remains inconclusive. *In vivo* neutralizing of specific cytokine/chemokines individually need to be done to validate their importance in regulating TME.

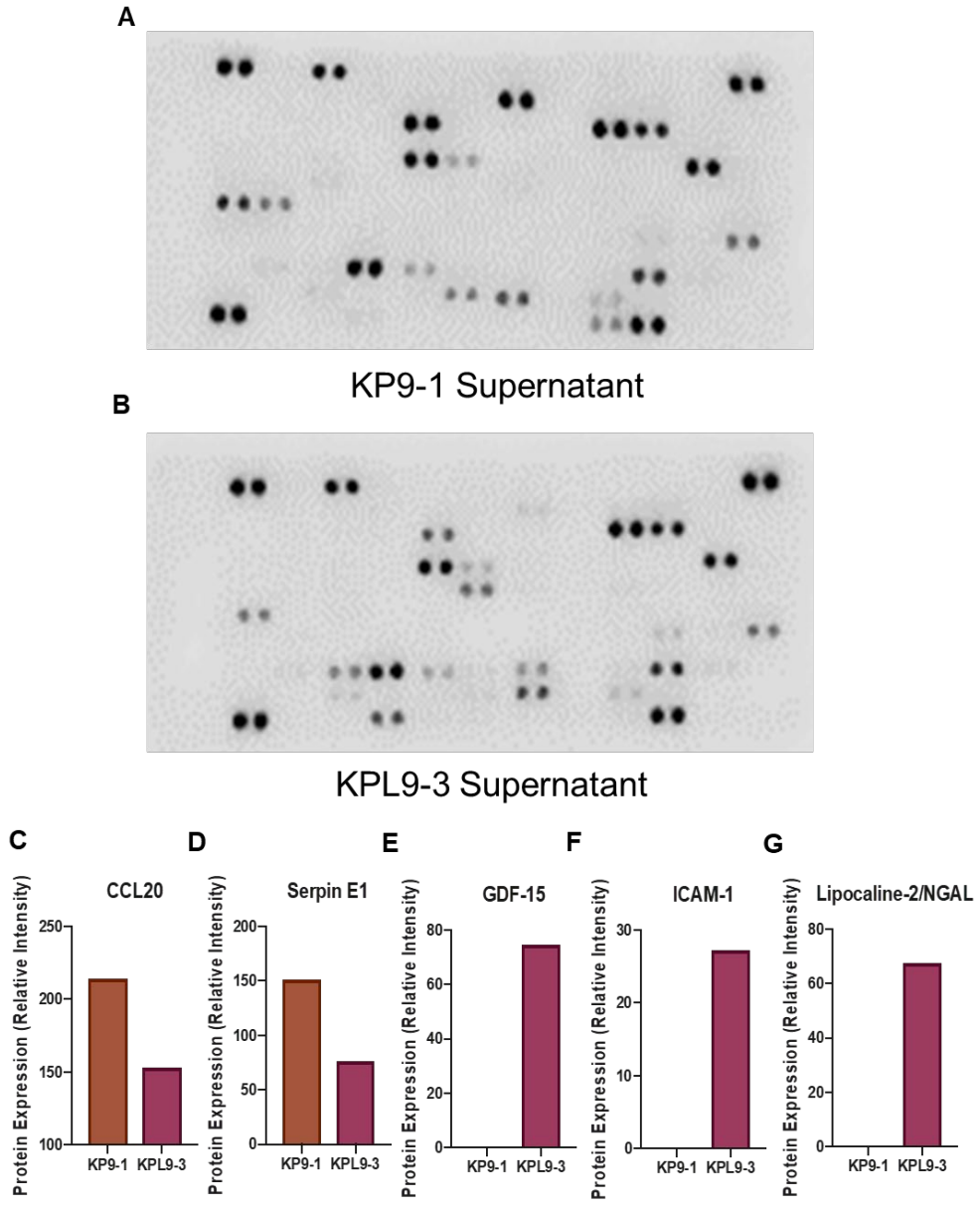

Figure 3.16 Characterization of cytokine and chemokine protein expression of KP and KPL cell lines.

(A-B) Mouse cytokine/chemokine XL profiling membrane for protein secreted in KP (A) and KPL (B) *in vitro* culture supernatant.

(C-G) Densitometric quantification analysis of CCL20 (C), serpin E1 (D), GDF-15 (E), ICAM-1 (F), and lipocaline-2/NGAL (G) secreted from KP (A) and KPL (B) *in vitro* culture supernatant based on (A-B).

CHAPTER FOUR:
Bemcentinib Mediated Axl Inhibition Sensitizes *Stk11/Lkb1* Mutant Tumors to anti-PD-1 Therapy

4.1 Bemcentinib Sensitizes *Stk11/Lkb1* Mutant Tumors to anti-PD-1 Therapy

Several studies have implicated that Axl expression by tumor or stromal cells participates in anti-tumor immune response and the tumor microenvironment (Aguilera et al., 2016; Lotsberg et al., 2020; Rothlin et al., 2007; Schmid et al., 2016; Tsukita et al., 2019; Zagórska et al., 2014). To investigate whether systemic inhibition of Axl might sensitize *KL* mutated tumors to anti-PD-1 treatment, we treated C57BL/6J mice bearing KPL tumors with the selective Axl kinase inhibitor bemcentinib (BGB324) alone, anti-PD-1 alone, or with a combination of anti-PD-1 + BGB324. Although neither treatment alone controlled tumor growth, the combination of BGB324 with anti-PD-1 showed sustained control of tumor progression (**Figure 4.1A**). Due to the technical challenging for staining Axl for *in vivo* tissues through both IHC and flow cytometry, gas6 abundance from tumor lysates were analyzed through ELISA to indirectly indicate potential Axl inhibition. As Axl was inhibited through BGB324, an increased gas6 secretion was observed from BGB324 and combination treatment group trying to activate Axl signaling pathway (**Figure 4.1B**). Importantly, BGB324 + anti-PD-1 treatment failed to control the growth of KPL tumors implanted in Rag1 KO mice, demonstrating the therapeutic effect of the combination is dependent on the adaptive immune system and through sensitizing

KPL tumors to anti-PD-1 (**Figure 4.1C**). To further identify the role of T cells in mediating therapeutic effects, we depleted CD4 T cells and CD8 T cells in vivo, respectively. When treating mice with CD4 T cells depleted, BGB324 + anti-PD-1 could control KPL tumors progression even better, indicating they are not mediators for therapeutic responses (**Figure 4.1D**). However, BGB324 + anti-PD-1 therapeutic effects do rely on CD8 T cells and depleting them abrogates the responses (**Figure 4.1E**). When further boosting the immune response through combining anti-PD-1 with anti-CTLA4, KPL tumors failed to show further benefits from the treatment, with BGB324 no longer synergize with immunotherapy (**Figure 4.1F**).

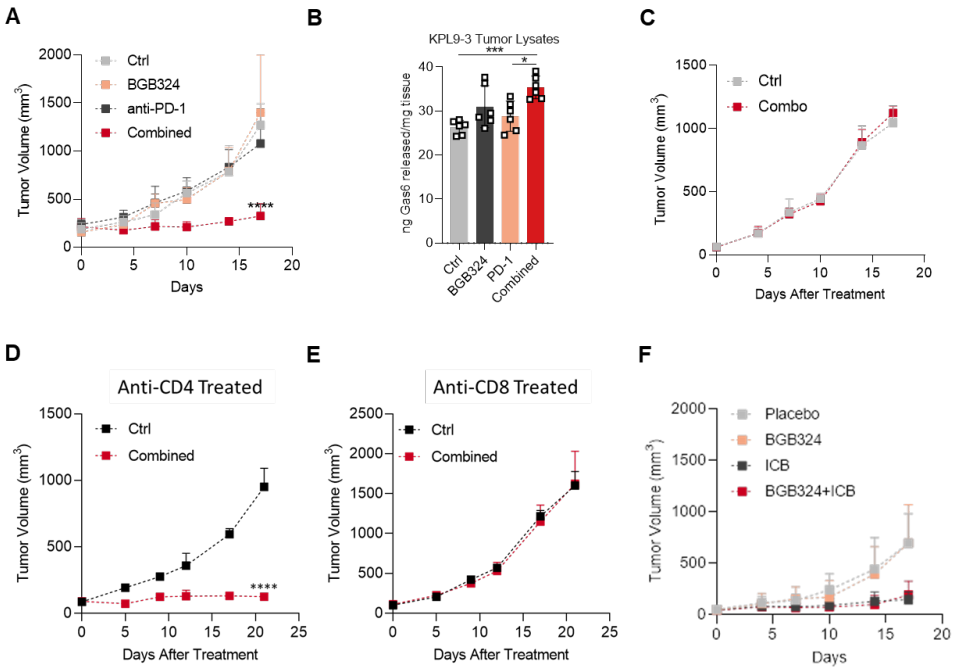

Figure 4.1 Bemcentinib (BGB324) sensitizes KPL tumors to anti-PD-1.

(A) C57BL/6J mice (n = 5) were inoculated with 1 x 10^6 KPL tumor cells and treated with BGB324 (50 mg/kg, twice daily), anti-PD-1 (10 mg/kg, day 7, 10, 14), or the combination starting on day 7 post tumor cell injection. Control animals were treated

with control IgG (10 mg/kg) and vehicle (50 mg/kg). Tumor volume was measured every 3 days.

(B) Same treatment schema as (A). Tumors were taken out 7 days post treatment initiation and homogenized into tumor lysates. Total amount of protein was normalized for each sample before loaded for ELISA.

(C) *Rag*1$^{-/-}$ mice (n = 4 for control group; n = 5 for treatment group) were injected with 1 x 10^6 KPL tumor cells. Mice were treated with BGB324 (50 mg/kg, twice daily) and anti-PD-1 (10 mg/kg, day 7, 10, 14) or corresponding IgG and vehicle starting on day 7 after tumor cell injection. Tumor growth was measured every 3 days.
(B) Same treatment schema as (A). Tumors were taken out 7 days post treatment initiation and homogenized into tumor lysates. Total amount of protein was normalized for each sample before loaded for ELISA.

(D) C57BL/6J mice (n = 5) were injected with 1 x 10^6 KPL tumor cells. Mice were treated with BGB324 (50 mg/kg, twice daily) and anti-PD-1 (10 mg/kg, day 7, 10, 14) or corresponding IgG and vehicle starting on day 7 after tumor cell injection. Mice were also treated with anti-CD4 antibody (10 mg/kg on day 6 prior treatment started, 5 mg/kg on day 9, then every 7 days) to deplete CD4 T cells *in vivo*. Tumor growth was measured every 3 days.

(E) C57BL/6J mice (n = 5) were injected with 1 x 10^6 KPL tumor cells. Mice were treated with BGB324 (50 mg/kg, twice daily) and anti-PD-1 (10 mg/kg, day 7, 10, 14) or corresponding IgG and vehicle starting on day 7 after tumor cell injection. Mice were also treated with anti-CD8 antibody (10 mg/kg on day 6 prior treatment started, 5 mg/kg on day 9, then every 7 days) to deplete CD4 T cells *in vivo*. Tumor growth was measured every 3 days.

(F) C57BL/6J mice (n = 5) were inoculated with 1 x 10^6 KPL tumor cells and treated with BGB324 (50 mg/kg, twice daily), anti-PD-1+ anti-CTLA4 (10 mg/kg, day 7, 10, 14), or the combination starting on day 7 post tumor cell injection. Control animals were treated with control IgG (10 mg/kg) and vehicle (50 mg/kg). Tumor volume was measured every 3 days.

4.1.1 Axl and *gas6* expression on *Stk11/Lkb1* mutated NSCLCs

Since BGB324 sensitizes KPL tumors to anti-PD-1 therapy through Axl inhibition, the Axl expression and Gas6 expression on tumor cell lines were then evaluated to analyze whether its effect was through tumor cell inhibition. In RNA-seq data of human NSCLC cell lines, KRAS mutation significantly upregulated *Axl* expression on tumor cells, whereas *STK11/LKB1* mutation suppressed the *Axl* expression (**Figure 4.2A**). In the RNA microarray data of mouse GEMM orthotopic tumors (Ji et al., 2007), there was a trend that *STK11/LKB1* mutation further upregulated *Axl* expression (**Figure 4.2B**). However, while KPL9-1-9 upregulated *Axl* comparing to KP9-1, KPL9-3-1 downregulated *Axl* expression with *Stk11/Lkb1* mutation (**Figure 4.2C**). Due to the discrepancy of *Axl* expression induced by *Stk11/Lkb1* mutation on KPL lines and to human NSCLC cell lines, it remains inconclusive that whether the *Axl* upregulation observed from microarray data was from tumor cells or stromal area.

When analyzing *Gas6* expression as the most potent ligand for Axl (Varnum et al., 1995), similar expression pattern of *Gas6* to *Axl* was found in human NSCLC cell lines (**Figure 4.2D**). While *Gas6* expression pattern from mouse GEMM microarray data showed similar trend to human *Gas6* expression (**Figure 4.2E**), the trend of increased *Gas6* expression in *K-ras* and *Stk11/Lkb1* double mutated GEMM tumors were not observed from cell lines established from GEMM tumors. When analyzing Gas6 protein level expression from both cell lysates and secreted into culturing medium *in vitro*, KPL lines exhibited lower Gas6 expression, comparing to KP lines (**Figures 4.2F-G**). Therefore, the ability for Axl inhibition to sensitize KPL tumors to

anti-PD-1 were likely not coming from the increased sensitivity of KPL lines from either increased Axl expression or Gas6 expression.

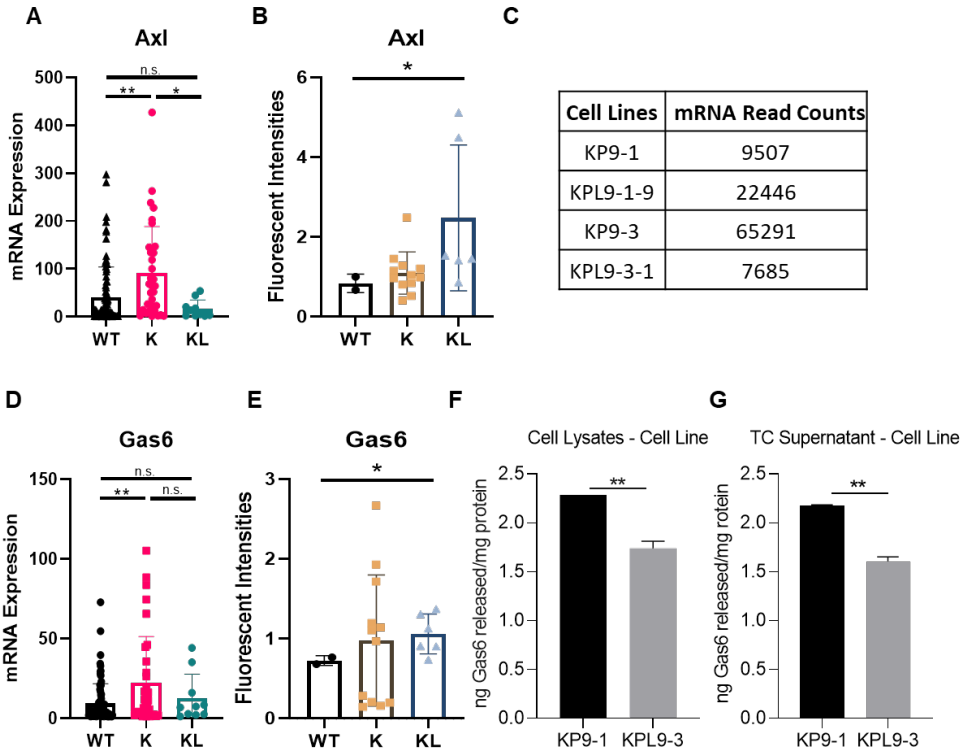

Figure 4.2 Axl and gas6 expression on mouse and human cell lines.

(A) *Axl* expression on human NSCLC cell lines based on RNA-seq. WT represents cell lines which have no *K-RAS* or *STK11/LKB1* mutation was detected based on whole-exosome sequencing, K represents *K-RAS* mutated NSCLC cell lines, and KL represents *K-RAS* and *STK11/LKB1* double mutated cell lines.

(B) *Axl* expression on mouse orthotopic GEMM models based on RNA microarray. WT represents cell lines which have no *K-RAS* or *STK11/LKB1* mutation was detected based on whole-exosome sequencing, K represents *K-RAS* mutated tumors, and KL represents *K-RAS* and *STK11/LKB1* double mutated tumors.

(C) *Axl* expression on KP and KPL lines based on RNA-seq. mRNA read counts were calculated from the sum of feature counts of *Axl* detected.

(D) *Gas6* expression on human NSCLC cell lines based on RNA-seq. WT represents cell lines which have no *K-RAS* or *STK11/LKB1* mutation was detected based on whole-exosome sequencing, K represents *K-RAS* mutated NSCLC cell lines, and KL represents *K-RAS* and *STK11/LKB1* double mutated cell lines.

(E) *Gas6* expression on mouse orthotopic GEMM models based on RNA microarray. WT represents cell lines which have no *K-RAS* or *STK11/LKB1* mutation was detected based on whole-exosome sequencing, K represents *K-RAS* mutated tumors, and KL represents *K-RAS* and *STK11/LKB1* double mutated tumors.

(F) Gas6 expression in lysed KP and KPL cells cultured *in vitro*. Samples loaded were normalized based on total amount of protein detected from medium.

(G) Gas6 released into medium from KP and KPL *in vitro* culture. Samples loaded were normalized based on total amount of protein detected from medium.

4.1.2 NSCLC cell lines drug responses to Bemcentinib inhibition

Next, the drug responses and half maximal inhibitory concentration (IC_{50}) of NSCLC cell lines were evaluated through *in vitro* culture treating with 4-fold serial diluted BGB324 treatment. Based on *Axl* expression detected from RNA-seq, 8 human NSCLC cell lines exhibiting highest *Axl* expression among 143 NSCLC cell lines (HCC4017, $\log_2$ relative expression = 7.068) to lowest *Axl* expression (H1993, $\log_2$ relative expression = 0.066) were selected for testing their drug responses to BGB324 treatment (**Figure 4.3A**). However, there was no clear separation for human NSCLC cell lines for their IC_{50} in response to Axl inhibition mediated by BGB324 treatment, regardless their *Axl* expression levels. Additionally, all of the IC_{50} detected from NSCLC cell lines were above 1μM, indicating a low specificity and potentially non-drug mediated inhibition effect. Especially, as the highest and lowest expression of Axl NSCLC cell lines, the drug responses of HCC4017 and H1993

behaved closest among selected cell lines (**Figure 4.3B**). Therefore, it is unlikely inhibition effect observed from BGB324 treatment responses were from Axl specific inhibition.

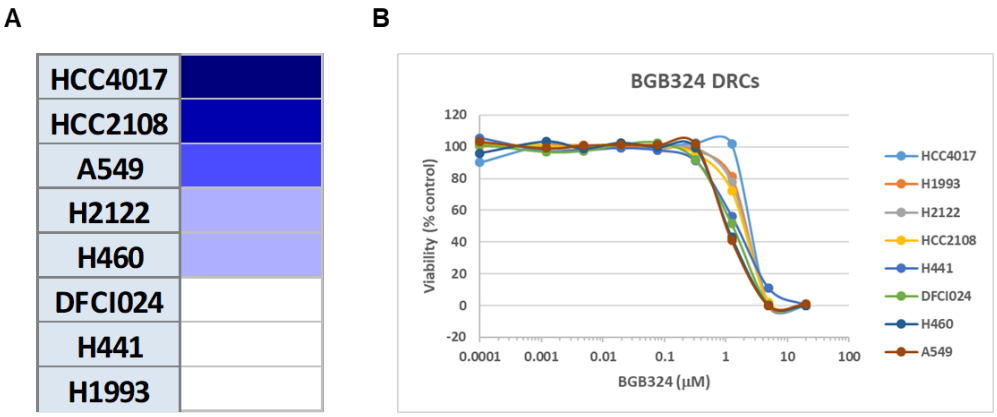

Figure 4.3 Bemcentinib (BGB324) responses in human NSCLC cell lines.

(A) *Axl* expression on selected human NSCLC cell lines based on RNA-seq ranked from highest expression (dark blue) to lowest (white) expression.

(B) Drug response curves of selected human NSCLC cell lines in (A) to BGB324 *in vitro*.

Similar drug response patterns of BGB324 inhibition in mouse cell lines were also observed. Besides KP and KPL lines, a mouse mammary carcinoma cell lines expressing *Her2/neu* transgene was selected for evaluating BGB324 drug responses as a negative control for Axl expression. When culturing cell lines in vitro, KP and KPL were stained positive for Axl expression while TUBO did not show Axl positive staining (**Figures 4.4A-C**). However, regardless of the Axl expression on tumor cell lines, their IC_{50} were very close (TUBO = 1.3 μM, KP = 2.2 μM, and KPL =

0.98 μM) and did not correlate with their Axl expression level (**Figures 4.4D-F**). These results indicating that BGB324 did not direct mediate tumor cell killing through Axl specific inhibition. Therefore, it is unlikely that the therapeutic effects of Axl inhibition sensitizing KPL tumors to anti-PD-1 therapy observed was through direct tumor cell killing.

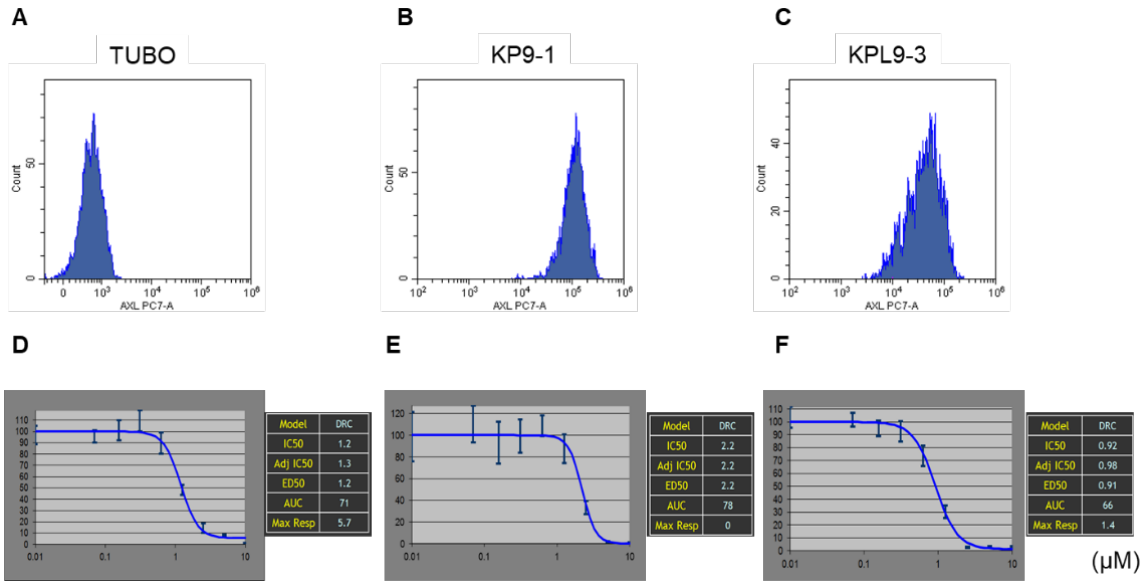

Figure 4.4 Bemcentinib (BGB324) responses in mouse cell lines.

(A) *Axl* expression on mouse cell lines cultured *in vitro* based on flow cytometry staining.

(B) Drug response curves of mouse cell lines in (A) to BGB324 *in vitro*.

Although Axl inhibition on tumor cell lines may not direct mediate killing, it is possible that the inhibition of Axl may induce immunogenic signal release to sensitizing KPL

tumors to anti-PD-1 therapy. To evaluate the potential immunogenic signal released from Axl inhibition of tumor cells, a dsDNA release assay was performed with CellTox Green™ Cytotoxicity Assay kit (Promega, Cat# G8741) in addition to MTS assay performed with CellTiter® 96 Aqueous One solution Cell Proliferation Assay kit (Promega, Cat# G3582). A non-permeable dsDNA fluorescent dye was utilized to measure the amount of dsDNA could be released and potentially presented as neoantigens to antigen presenting cells. If a double strand DNA release was induced from drug inhibition, an inverse proportional increase of dsDNA fluorescent signal to cell viability percentage was expected to be observed, like shown in H2073 treated with erlotinib (**Figure 4.5A**). However, KP and KPL lines did not show a proportional increased of dsDNA release in response to BGB324, regardless of cell viabilities observed (**Figures 4.5B-C**).

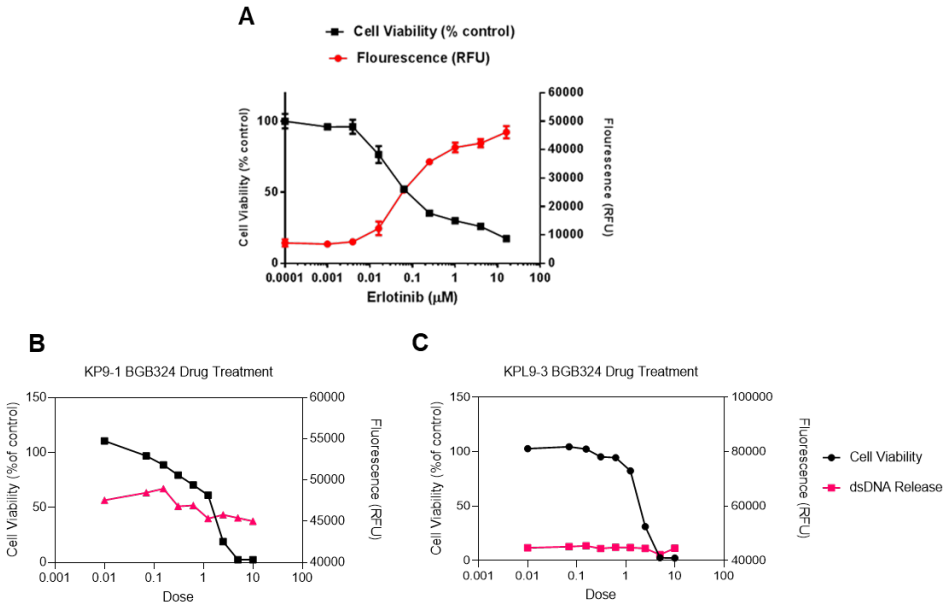

Figure 4.5 dsDNA release assay in response to BGB324 treatment.

(A) Cell viability (black) and fluorescent labeled dsDNA released (red) of H2073 cell line cultured *in vitro* in response to erlotinib treatment.

(A) Cell viability (black) and fluorescent labeled dsDNA released (red) of KP cell lines cultured *in vitro* in response to BGB324 treatment.

(B) Cell viability (black) and fluorescent labeled dsDNA released (red) of KPL cell lines cultured *in vitro* in response to BGB324 treatment.

4.2 Bemcentinib Induced Tumor Immune Microenvironment Changes in *Stk11/Lkb1* Mutant Tumors

To further validate BGB324 mediated Axl sensitizing KPL tumors to anti-PD-1 treatment to achieve progression control, the TME from each treatment group were characterized. KPL tumors were harvested from C57BL/6J mice and evaluated through flow cytometry. Upon BGB324 treatment, there was a trend of reduction of CD8 T cells, CD4 T cells and T_{reg} cells in KPL tumors TME. When combining with anti-PD-1 treatment, CD8 T cell infiltration percentage was restored and increased, while T_{reg} cells remained low for infiltration, comparing to control group (**Figures 4.6A-D**). Although none of them were tested statistically differently from each other, it is possible that 1) the therapeutic effect of combination treatment it's through regulating TME through BGB324 inhibition to sensitize KPL tumors to anti-PD-1

treatment, and 2) the effect was from increased CD8 T cell infiltration, or decreased T_{reg} cells infiltrated into KPL tumors.

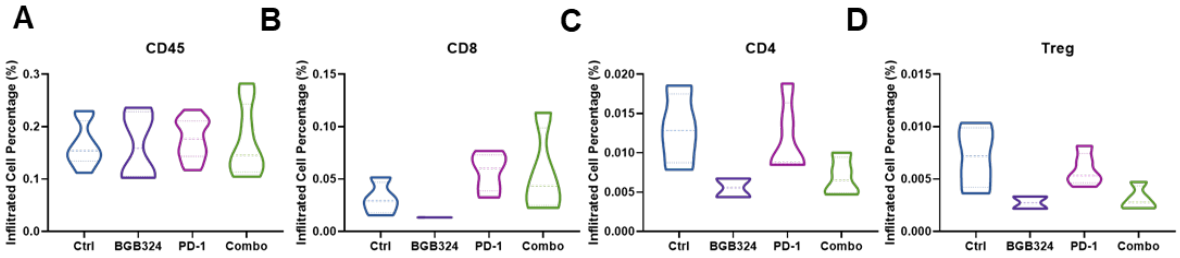

Figure 4.6 Infiltrated immune cell changes in response to treatment in KPL tumors.

(A) Infiltrated total immune cell ($CD45^+$) percentages among gated live cells changed in response to treatment in KPL tumors. C57BL/6J mice (n = 5) were inoculated with 1 x 10^6 KPL tumor cells and treated with BGB324 (50 mg/kg, twice daily), anti-PD-1 (10 mg/kg, day 7, 10, 14), or the combination starting on day 7 post tumor cell injection.

(B) Infiltrated cytotoxic T cell ($CD8^+$) percentages among gated total immune cells changed in response to treatment in KPL tumors. Mice were inoculated with KPL tumors and followed same experimental schema as (A).

(C) Infiltrated total helper T cells ($CD4^+$) percentages among gated total immune cells changed in response to treatment in KPL tumors. Mice were inoculated with KPL tumors and followed same experimental schema as (A).

(D) Infiltrated total regulatory T cells ($FoxP3^+$) percentages among gated infiltrated CD4 T cells changed in response to treatment in KPL tumors. Mice were inoculated with KPL tumors and followed same experimental schema as (A).

Further analysis of proliferation and apoptosis status of CD8 T cells and T_{reg} cells in TME upon treatment, Ki67 and cleaved caspase 3 were staining for CD8 T cells and T_{reg} cells isolated from TME. However, the proliferation of T_{reg} cells was not inhibited

from either of the single treatment group, but showed a trend of reduction in combination group, suggesting the inhibition of T_{reg} cells proliferation in TME was likely a result of other immune cell infiltration changes, instead of a cause for inducing therapeutic responses of KPL tumors (**Figure 4.7A**). At the meantime, the apoptosis of T_{reg} cells did not change much, but also showed a synergistic reduction in response to therapy, which further confirmed that the dynamics of T_{reg} cells in TME in different treatment groups were a result of other immune cell changes in TME (**Figure 4.7B**).

When analyzing CD8 T cell status, the proliferation of CD8 T cells tended to increase when treating with BGB324, and the combination treatment of BGB324 + anti-PD-1 also showed a milder proliferation but also higher than control group (**Figure 4.7C**). At the same time, the apoptosis of CD8 T cells did not differ from either single treatment or combination treatment group (**Figure 4.7D**). Therefore, the induction of CD8 T cells or a subgroup of CD8 T cells were likely to be the responder immune cells to BGB324 in TME.

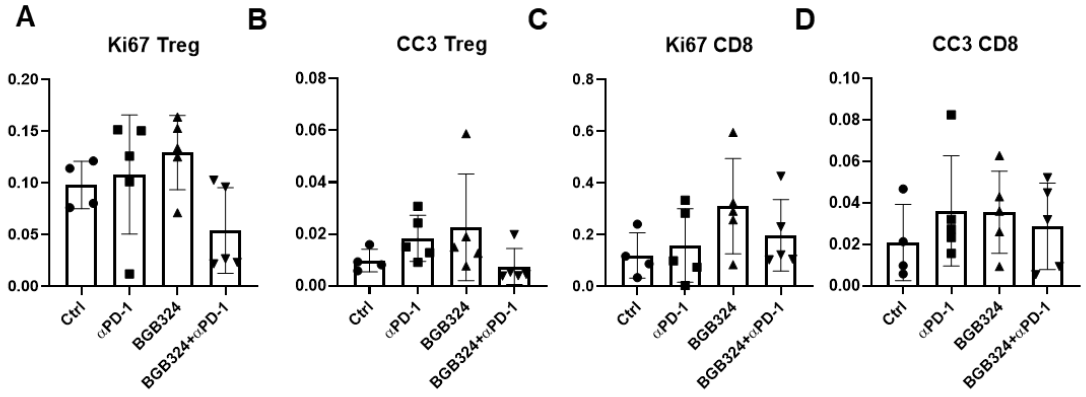

Figure 4.7 BGB324 induced T cells proliferation and apoptosis in TME.

(A) Infiltrated proliferating regulatory T cells changed in response to treatment in KPL tumors. C57BL/6J mice (n = 5) were inoculated with 1 x 10^6 KPL tumor cells and treated with BGB324 (50 mg/kg, twice daily), anti-PD-1 (10 mg/kg, day 7, 10, 14), or the combination starting on day 7 post tumor cell injection.

(B) Infiltrated regulatory T cells undergone apoptosis percentages changed in response to treatment in KPL tumors. Mice were inoculated with KPL tumors and followed same experimental schema as (A).

(C) Infiltrated proliferating CD8 T cells changed in response to treatment in KPL tumors. Mice were inoculated with KPL tumors and followed same experimental schema as (A).

(D) Infiltrated CD8 T cells undergone apoptosis percentages changed in response to treatment in KPL tumors. Mice were inoculated with KPL tumors and followed same experimental schema as (A).

As CD8 T cell changes in TME is likely from antigen presentation activation, the myeloid cell dynamics were also evaluated in different treatment group. Although anti-PD-1 treatment tend to induce DCs infiltration in TME, regarding that anti-PD-1 single treatment was not effective and BGB324 did not changes the infiltration comparing to DCs, this was unlikely to be responsible for therapeutic responses in

KPL tumors (**Figure 4.8A**). As the most critical or potent antigen presenting cells in TME, there was a change of cross-priming dendritic cells induced upon treatment. Cross-priming DCs were significantly reduced in BGB324 single treatment group and combination of BGB324 + anti-PD-1, it was likely that cross-priming DCs were being activated or induced upon the BGB324 treatment. As the induction of CD8 T cells could already be observed, activated or induced cross-priming DCs should had been killed by CD8 T cells recruited. Therefore, assuming taking out tumors at an earlier time point, an induction of cross-priming DCs may able to be observed from BGB324 treated tumors (**Figure 4.8B**). At the same time, infiltrated macrophages, neutrophils, monocytic MDSCs (M-MDSCs) or granulocytic MDSCs (PMN-MDSCs) in KPL tumors were not changed with BGB324 treatment, indicating a non-therapy relevant infiltration (**Figures 4.8C-F**). Therefore, the activation or induction of cross-priming DCs through BGB324 mediated Axl inhibition may contributed into sensitizing KPL tumors to anti-PD-1 treatment through priming CD8 T cells in TME.

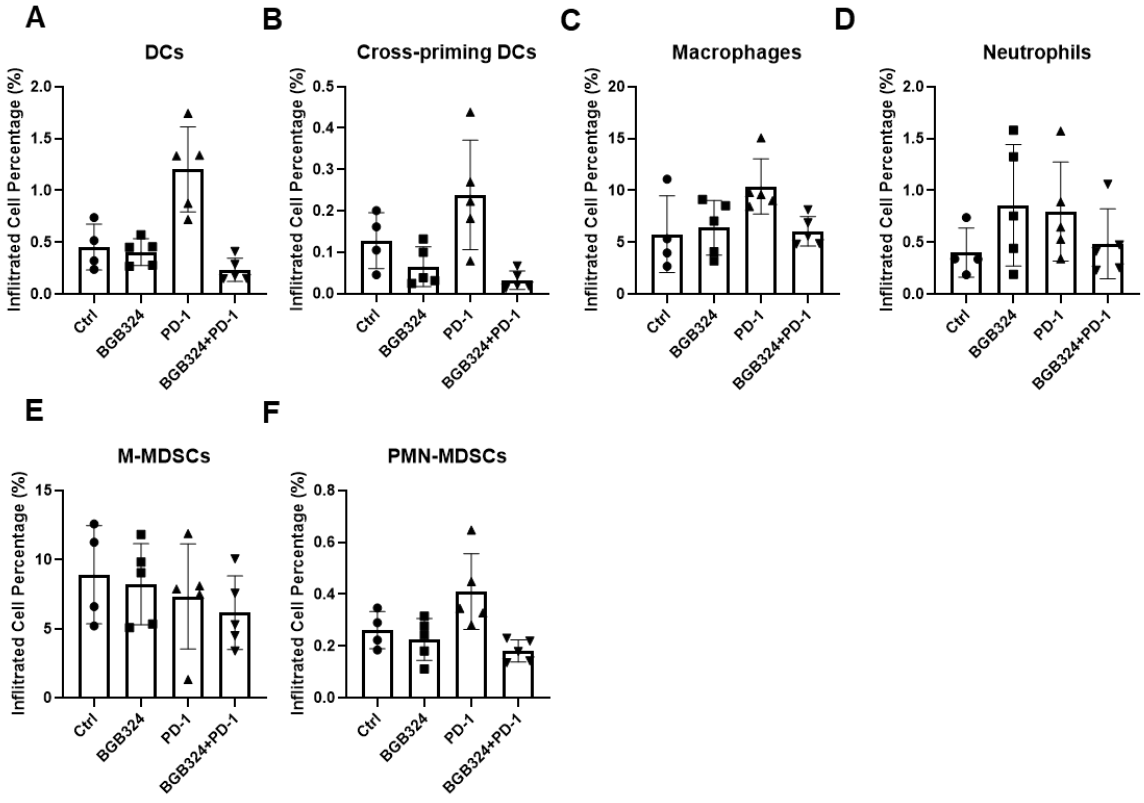

Figure 4.8 Infiltrated myeloid cell changes in response to treatment in KPL tumors.

(A) Infiltrated dendritic cell percentages changed in response to treatment in KPL tumors. C57BL/6J mice (n = 5) were inoculated with 1 x 10^6 KPL tumor cells and treated with BGB324 (50 mg/kg, twice daily), anti-PD-1 (10 mg/kg, day 7, 10, 14), or the combination starting on day 7 post tumor cell injection.

(B) Infiltrated cross-priming dendritic cells percentages among gated dendritic cells changed in response to treatment in KPL tumors. Mice were inoculated with KPL tumors and followed same experimental schema as (A).

(C) Infiltrated macrophages percentages changed in response to treatment in KPL tumors. Mice were inoculated with KPL tumors and followed same experimental schema as (A).

(D) Infiltrated neutrophils percentages changed in response to treatment in KPL tumors. Mice were inoculated with KPL tumors and followed same experimental schema as (A).

(E) Infiltrated monocytic MDSCs (M-MDSCs) percentages changed in response to treatment in KPL tumors. Mice were inoculated with KPL tumors and followed same experimental schema as (A).

(F) Infiltrated granulocytic MDSCs (PMN-MDSCs) percentages changed in response to treatment in KPL tumors. Mice were inoculated with KPL tumors and followed same experimental schema as (A).

The immune cells percentages in spleen from different treatment group were then analyzed to evaluate whether the BGB324 treatment and combination treatment induced immune cell changes were tumor specific. In spleen, CD8 T cells, CD4 T cells and T_{reg} cells were all showed similar percentage as total immune cells ($CD45^+$) detected in spleen (**Figures 4.9A-D**). Therefore, the BGB324 induced TME changes in sensitizing KPL tumors to anti-PD-1 treatment were tumor specific.

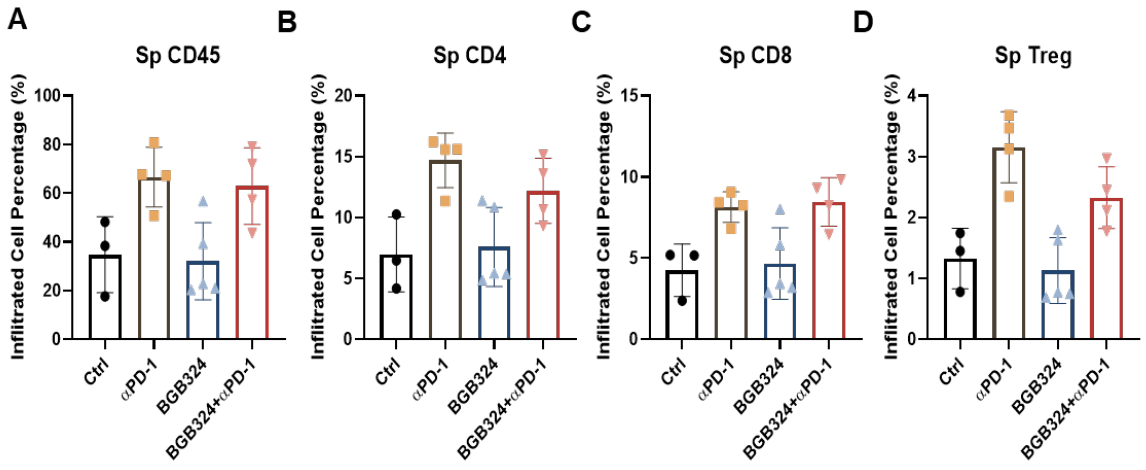

Figure 4.9 Immune cells in spleen changes in response to treatment in KPL tumors.

(A) Total immune cell ($CD45^+$) percentages among gated live cells in spleen changed in response to treatment in KPL tumors. C57BL/6J mice (n = 5) were

inoculated with 1 x 10^6 KPL tumor cells and treated with BGB324 (50 mg/kg, twice daily), anti-PD-1 (10 mg/kg, day 7, 10, 14), or the combination starting on day 7 post tumor cell injection.

(B) Cytotoxic T cell ($CD8^+$) percentages among gated total immune cells in spleen changed in response to treatment in KPL tumors. Mice were inoculated with KPL tumors and followed same experimental schema as (A).

(C) Total helper T cells ($CD4^+$) percentages among gated total immune cells changed in spleen in response to treatment in KPL tumors. Mice were inoculated with KPL tumors and followed same experimental schema as (A).

(D) Total regulatory T cells ($FoxP3^+$) percentages among gated infiltrated CD4 T cells in spleen changed in response to treatment in KPL tumors. Mice were inoculated with KPL tumors and followed same experimental schema as (A).

As a subgroup of CD8 T cells, the infiltration of stem-like central memory $TCF1^+PD\text{-}1^+CD8$ T cells was significantly increased with BGB324 treatment alone or in combination with anti-PD-1 (**Figures 4.10A-B**). These results indicated that the therapeutic effect was from the induction of $TCF1^+PD\text{-}1^+CD8^+$ T cells, and it needed anti-PD-1 to break the immune cell exclusion, which explained why none of the single treatment was able to control tumor growth. However, the underlying mechanism of how anti-PD-1 therapy could break the immune exclusion in KPL tumors need to be further explored.

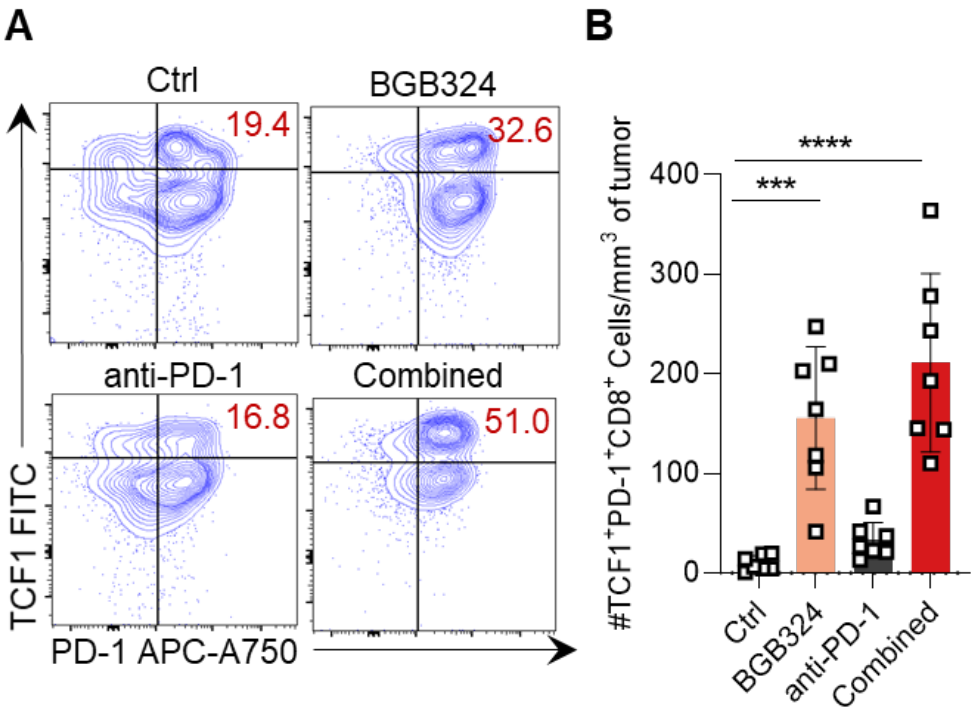

Figure 4.10 Bemcentinib induces TCF1⁺PD-1⁺ CD8 T cell expansion in TME.

(A) Representative infiltrated TCF1⁺PD-1⁺ cell percentages among gated CD8⁺ TILs at day 7 post therapy initiation.

(B) Abundance of TCF1⁺PD-1⁺ cells among gated CD8⁺ TILs (per mm^3 of tumor) on day 7 post therapy initiation (day 14 post tumor cell injection).

While BGB324 single treatment could control KP tumor growth effectively, it did not synergize with anti-PD-1 therapy (**Figure 4.11A**). When analyzing the abundance of TCF1⁺PD-1⁺CD8⁺ T cell in KP tumors, there was no induction upon BGB324 treatment alone or in combination with anti-PD-1 (**Figure 4.11B**). Therefore, the tumor progression control effect of BGB324 onto KP tumors were likely through distinct mechanism from KPL tumors which worth for further investigation.

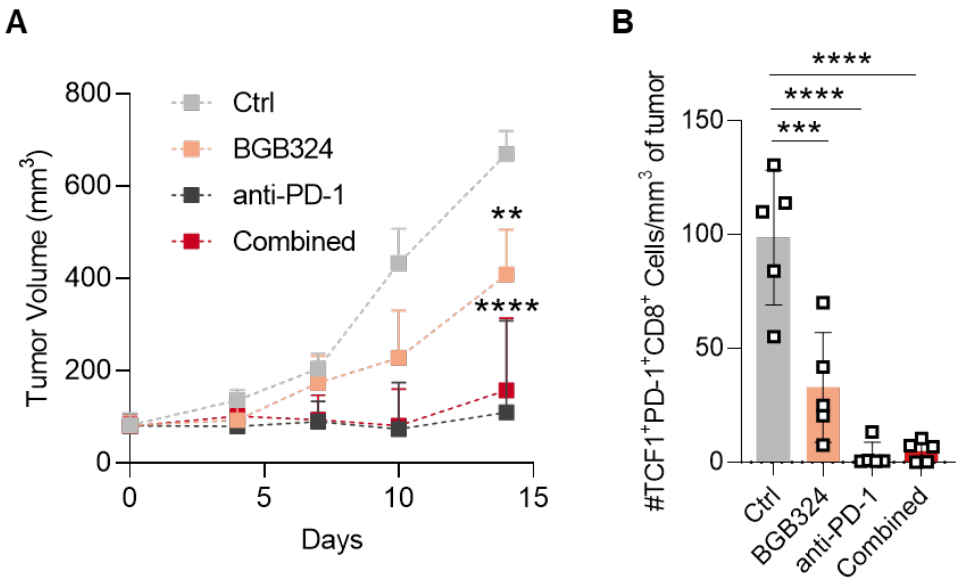

Figure 4.11 Bemcentinib synergize with anti-PD-1 in KP tumors.

(A) C57BL/6J mice (n = 5) were inoculated with 1 x 10^6 KP tumor cells and treated with BGB324 (50 mg/kg, twice daily), anti-PD-1 (10 mg/kg, day 7, 10, 14), or the combination starting on day 7 post tumor cell injection. Control animals were treated with control IgG (10 mg/kg) and vehicle (50 mg/kg). Tumor volume was measured every 3 days.

(B) Abundance of $TCF1^+PD\text{-}1^+$ cells among gated $CD8^+$ TILs (per mm^3 of tumor) on day 7 post therapy initiation (day 14 post tumor cell injection).

4.3 Bemcentinib Induced Antigen Specific CD8 T Cell Changes in *Stk11/Lkb1* Mutant Tumors

The use of KPL tumor allografts was then exploited to be engineered to express ova-albumin (KPL-OVA) to allow for tracking OVA antigen-specific T cells in their

TME. Upon expressing OVA in KPL tumors, they become more immunogenic as three doses of FTY720 (Selleckchem, Cat# S5002) were needed to establish KPL-OVA tumors onto C57BL/6J mice purchased from Jackson Laboratory. C57BL/6J mice purchased from Taconic Biosciences (Cat# B6NTac) could establish KPL-OVA tumors without FTY720 treatment and therefore were used for antigen specific T cell status analysis. When looking at their TME, KPL-OVA tumors also showed a significant increased CD8 T cell infiltration than KPL tumors (**Figure 4.12**). These OVA induced TME changes resulted in a more anti-PD-1 responsive KPL-OVA tumors, of which showed a non-treatment induced increased CD8 T cell infiltration in TME which naturally cannot be observed in KPL tumors.

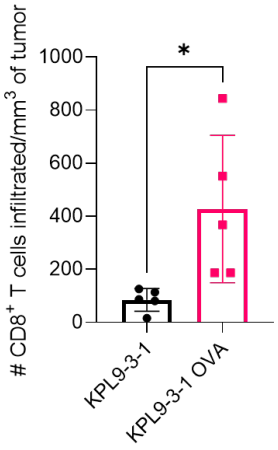

Figure 4.12 Ovalbumin expression in KPL tumors increases CD8 T cell infiltration into TME. C57BL/6J mice (n = 5) were inoculated with 1 x 10^6 KPL or KPL-OVA tumor cells and tumors were taken out on day 7 post tumor cell injection for analysis.

The number of OVA antigen specific CD8 T cells in the TME were quantified by staining dissociated OVA-expressing tumors with H-2Kb OVA MHC tetramer (SIINFEKL). Axl inhibition with BGB324 increased the number of OVA antigen specific CD8 T cells in the TME, and in combination with anti-PD-1 further facilitated T cell infiltration (**Figures 4.13A-B**). Although anti-PD-1 treatment also induced antigen specific CD8 T cell infiltration, it probably was because of increased CD8 T cell infiltration due to OVA expression. With further staining of TCF1 expression on isolated antigen specific CD8 T cells, BGB324 increased the number of OVA antigen specific TCF1$^+$ PD-1$^+$ CD8 T cells significantly, which cannot be achieved with anti-PD-1 therapy (**Figure 4.13C**). Although the combination group did not show an increase of OVA antigen specific TCF1$^+$ PD-1$^+$ CD8 T cells in TME, which may due to the tumor growth control of combination treatment group made them transit into effector CD8T cells, and therefore lost the TCF1 expression.

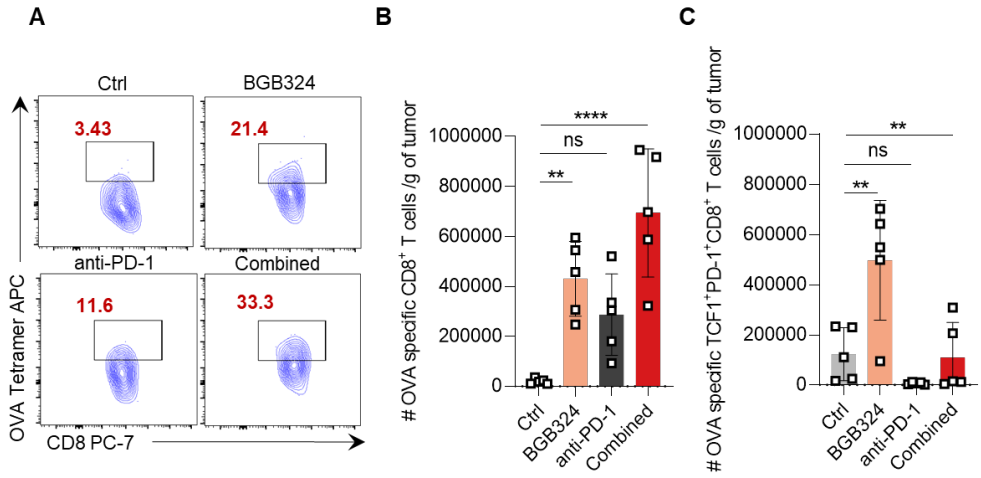

Figure 4.13 Tetramer staining for ovalbumin specific T cells in TME post treatment.

(A) Representative infiltrated OVA antigen specific cell percentages among $CD8^+$ T TILs in different treatment group of mice, analyzed at day 7 post therapy initiation.

(B) C57BL/6J mice (n = 5) were injected with 1 x 10^6 KPL-OVA tumor cells and treated with BGB324 (50 mg/kg, twice daily), anti-PD-1 (10 mg/kg, day 14, 17, 20), or the combination starting on day 14 post tumor cell injection. Control animals were treated with control IgG (10 mg/kg) and vehicle (50 mg/kg). Abundance of OVA antigen specific cells among $CD8^+$ T TILs (per gram of tumor) in each treatment group analyzed on day 7 post therapy initiation (day 14 post tumor cell injection)

(C) Same experimental schema as (B). Abundance of OVA antigen specific $TCF1^+PD\text{-}1^+$ cells among gated $CD8^+$ TILs (per mm^3 of tumor) in each treatment group on day 7 post therapy initiation (day 14 post tumor cell injection).

To confirm the hypothesis that the BGB324 induced $TCF1^+$ $PD\text{-}1^+$ CD8 T cells were activated by anti-PD-1 therapy and therefore lost their stem/central memory like T cell markers, ELISPOT was then performed to evaluate antigen specific T cell activation status in different treatment group. Splenocytes isolated from KPL-OVA tumors were stimulated with Ovalbumin peptide *in vitro*, and the IFNγ secretion spots from each individual tumor were visualized and quantified (**Figure 4.14A**). ELISPOT of KPL-OVA tumors confirmed that BGB324 treatment alone did not activate CD8 T cells directly. A combination of BGB324 with anti-PD-1 was required to transit T cells into effector cells with infiltration into tumor islands (**Figure 4.14B**). These further confirmed that antigen specific $TCF1^+$ $PD\text{-}1^+$ CD8 T cells were not capable of mediate tumor killing directly, and the anti-PD-1 therapy was needed to transit $TCF1^+$ $PD\text{-}1^+$ CD8 T cells into antigen specific effector T cells in KPL tumors.

When analyzing the draining lymph nodes antigen specific T cells, a similar pattern of antigen specific T cell induction was observed (**Figure 4.14C**). However, although there was an increased percentage of antigen specific T cells in spleen of combination treatment group mice, BGB324 treatment alone was not able to induce the abundance of antigen specific T cells in spleen (**Figure 4.14D**). This could be explained as more of the antigen specific T cells were recruited into KPL-OVA tumors, whereas combining with anti-PD-1 could further activate them therefore proliferating in the spleen. As primary lymphoid organ, the capacity of antigen specific CD8 T cells to expand should not be limited by the availability of them. The highest abundance of antigen specific T cells in spleen of combination group than other treatment group was therefore observed.

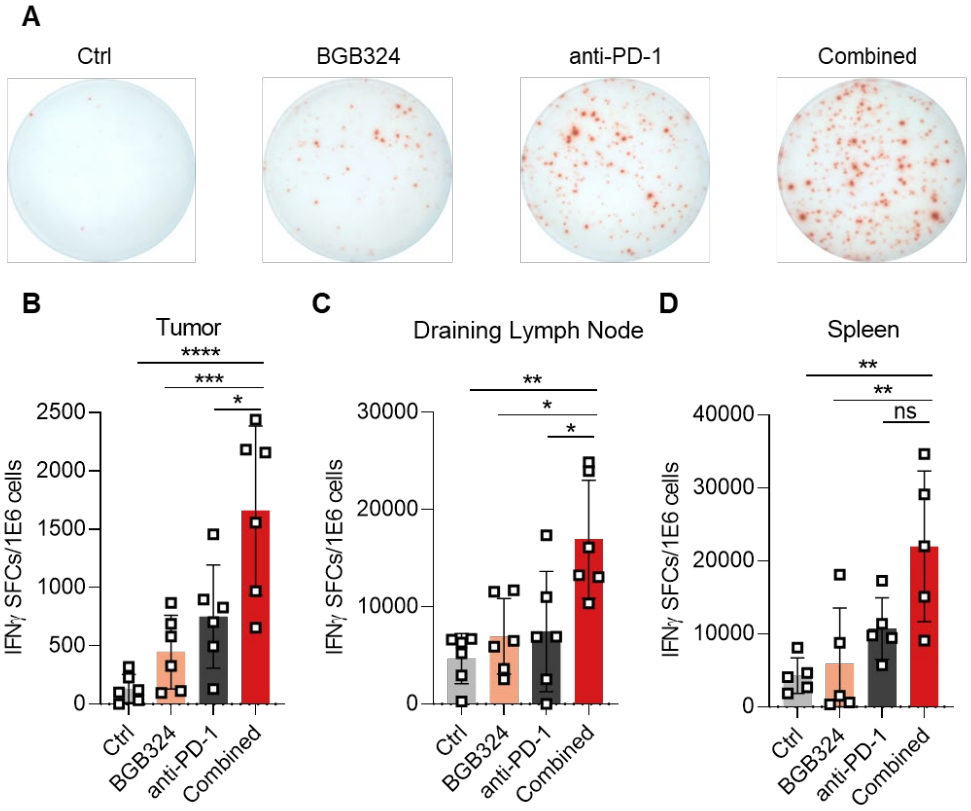

Figure 4.14 IFNγ ELISPOT for antigen specific T cells activation status post treatment.

(A) Representative ELISPOT assay for IFN-γ producing cells from different treatment groups. Splenocytes were isolated and re-stimulated with E7 peptide as negative control, or OVA peptide for 48h.

(B) C57BL/6J mice (n = 5) were injected with 1 x 10^6 KPL-OVA tumor cells and treated with BGB324 (50 mg/kg, twice daily), anti-PD-1 (10 mg/kg, day 14, 17, 20), or the combination starting on day 14 post tumor cell injection. Control animals were treated with control IgG (10 mg/kg) and vehicle (50 mg/kg). Statistical results for IFN-γ producing cells in tumors (per 1E6 cells isolated) from each treatment group. Splenocytes were isolated and re-stimulated with E7 peptide (negative control) or OVA peptide for 48h.

(C) Same experimental schema as (B). Statistical results for IFN-γ producing cells in draining lymph nodes (per 1E6 cells isolated) from each treatment group. Splenocytes were isolated and re-stimulated with E7 peptide (negative control) or OVA peptide for 48h.

(D) Same experimental schema as (B). Statistical results for IFN-γ producing cells in spleen (per 1E6 cells isolated) from each treatment group. Splenocytes were isolated and re-stimulated with E7 peptide (negative control) or OVA peptide for 48h.

As KPL tumors should have multiple antigens with multiple epitopes could potentially be recognized by CD8 T cells, and only T cells that specific to ovalbumin peptide 257-264 amnio acids was evaluated from above ELISPOT analysis, ELISPOT was then performed with splenocytes isolated from KPL tumors. Irradiated KPL tumor cells under 40 Gy were cultured overnight post-irradiation, to allowing for tumor cells to start release antigen into the medium when co-culturing with isolated splenocytes infiltrated into KPL tumors. Tumor associated T cells which were able to recognize KPL tumors neoepitopes were expected to be activated and secreting IFNγ to form colonies in ELISPOT wells (**Figure 4.15A**). Neither BGB324 nor anti-PD-1 single treatment could significantly increase the activated antigen specific T cells, while the combination treatment group showed a significantly increased number of antigen specific T cells in TME (**Figure 4.15B**). These data further confirmed that the antigen specific T cells induced by BGB324 need anti-PD-1 to transit into effector T cells to control tumor progression in KPL tumors.

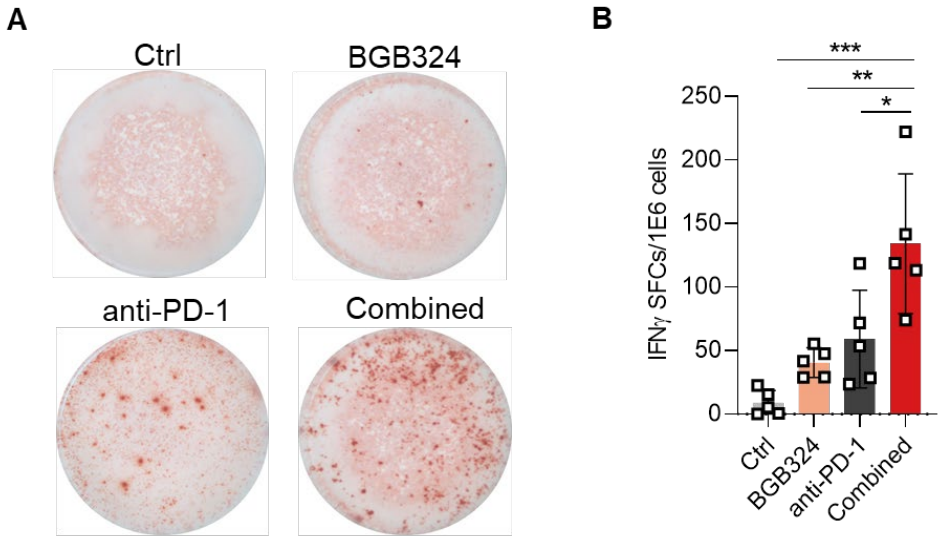

Figure 4.15 IFNγ ELISPOT for tumor associated T cells activation status post treatment.

(A) Representative ELISPOT assay for IFN-γ producing cells from different treatment groups. Splenocytes were isolated and re-stimulated 40g irradiated KPL tumor cells or B16 tumor cells (negative control) for 48h.

(B) C57BL/6J mice (n = 5) were injected with 1 x 10^6 KPL tumor cells and treated with BGB324 (50 mg/kg, twice daily), anti-PD-1 (10 mg/kg, day 14, 17, 20), or the combination starting on day 14 post tumor cell injection. Control animals were treated with control IgG (10 mg/kg) and vehicle (50 mg/kg). Statistical results for IFN-γ producing cells (per 1E6 cells isolated) from each treatment group. Splenocytes were isolated and re-stimulated with 40g irradiated KPL tumor cells or B16 tumor cells (negative control) for 48h.

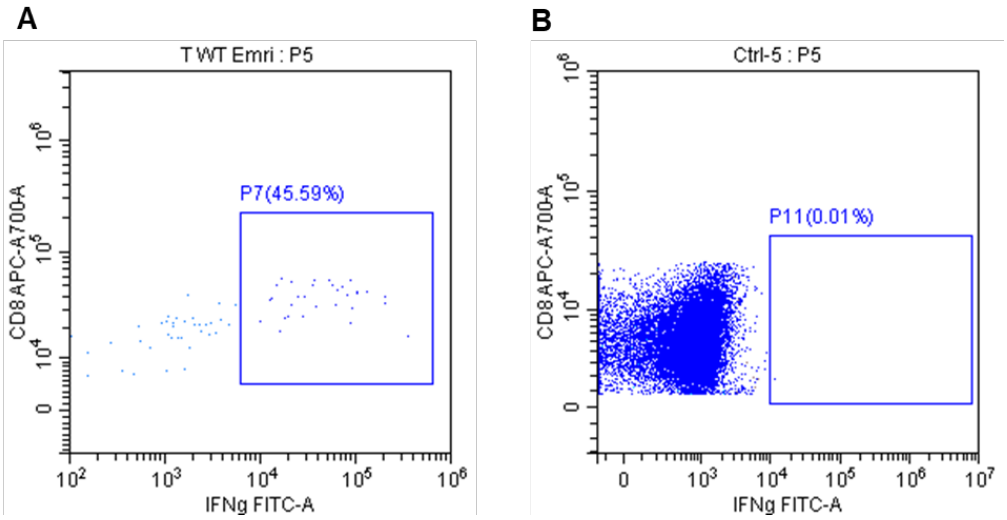

Figure 4.16 Evaluation of IFNγ secreting CD8 T cells infiltrated into tumors.

(A) Representative IFN-γ producing cells which were positive for YFP signal from MC38 treatment naïve tumors.

(B) Representative IFN-γ producing cells which were positive for YFP signal from KPL treatment naïve tumors.

To assess IFNγ secretion from CD8 T cells induced by treatment directly *in vivo*, Iterferon gamma reporter mice with endogenous expression of YFP controlled by IFNγ promoter (Jackson Laboratories, Cat# 017580) were utilized to implant tumors. When gating out CD8 T cells, a group of YFP positive CD8 T cells were found clustered well and abundant in MC38 tumors (**Figure 4.16A**). However, due to the nature of KPL tumors, very limited YFP positive CD8 T cells were found in KPL tumors. Which resulted in analyzing T cell activation *in vivo* remain unsolved (**Figure 4.16B**).

In summary, these data suggest that pharmacologic inhibition of Axl increases antigen specific TCF1^{+}PD-1^{+}CD8 T cells in KPL tumors and the expansion of

TCF1^{+}PD-1^{+}CD8 T cells could be the key population to sensitize KPL tumors to anti-PD-1 therapy.

4.4 Single-cell RNA Sequencing Analysis of Bemcentinib Induced Immune Landscape Changes in *Stk11/Lkb1* Mutant Tumors

To dissect the dynamic changes in the KPL TME after treatment, scRNAseq with paired single cell TCR sequencing was performed for four pooled samples of the tumor and its TME from each treatment group. Allografts engrafted subcutaneously after tumors were established and treated for 7 days accord with previous flow characterized TME. Myeloid cells (CD45^{+}/CD3^{-}) and T cells (CD45^{+}/CD3^{+}) were isolated from KPL syngeneic murine tumors (n = 10) from different treatment group were digested and mixed as a single sample for flow sorting. KPL tumor samples were then sorted and mixed back at 1:1 ratio as described (Zhou et al., 2020). Major group of immune cells detected from scRNAseq in tumors were visualized into UMAP projection (resolution = 0.2), including malignant cells, double negative T cells, CD8 T cells, CD4 T cells, regulatory T cells, inhibitory T cells, natural killer cells, dendritic cells, macrophages, and monocytes/MDSCs (**Figure 4.17A**). When visualized the UMAP based on samples, KPL samples from different samples were merged well after batch correction based on anchors (Stuart et al., 2019), indicating technical induced batches variation (**Figure 4.17B**). With the most recognized

identification markers visualized on UMAP, they accord with the clusters identified at resolution = 0.2 (**Figure 4.17C**), suggesting a right resolution was chosen to cluster cells detected. Cell clusters were further annotated and validated with previous reported representative functional markers (**Figure 4.17D**).

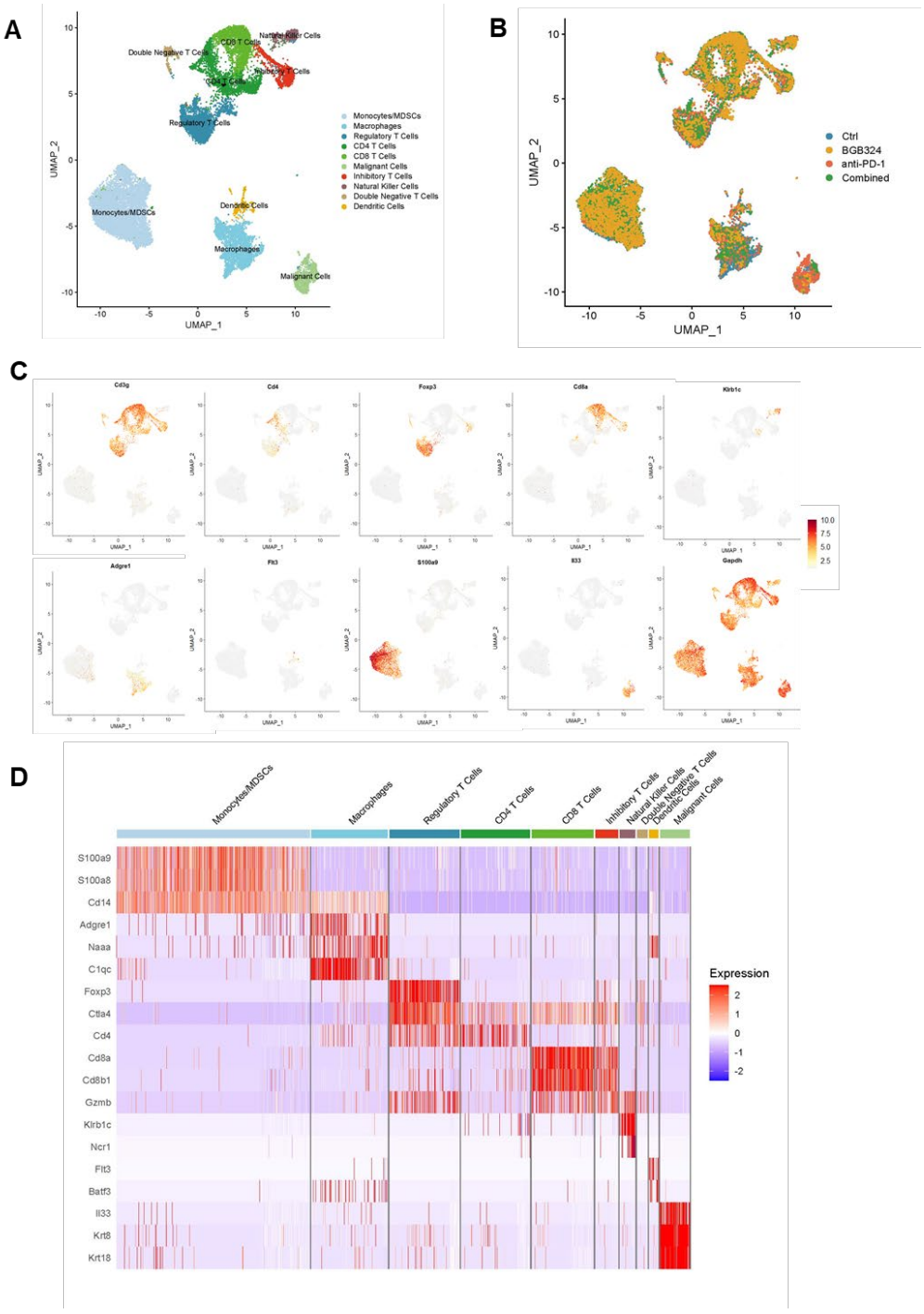

Figure 4.17 Overview of CD45^{+} immune cell populations in KPL tumors post treatment.

(A) UMAP visualization for major clusters of cells detected by scRNAseq in KPL tumors after therapy with vehicle (Ctrl), BGB324, anti-PD-1 (PD-1), or BGB324 + anti-PD-1 (combo). Each color annotates a distinct corresponding major cell population.

(B) Distribution of cells from different clusters among KPL tumors in control, BGB324, anti-PD-1 or combination treatment group.

(C) UMAP projection of cell clusters with visualization of major marker genes expression supporting cell identity assignment in (A).

(D) Heatmap visualization for markers define clusters identities in (A).

Sub-clustering of CD8 T cells (resolution = 0.6) from KPL tumors undergone different treatment revealed eight defined sub-populations (resolution = 0.4) in UMAP (**Figure 4.18A**). The identification of sub-populations was based on mRNA expression criteria from previous reports (Guo et al., 2018b; Yost et al., 2019). Markers selected for sub-population identification were plotted in heatmap (**Figure 4.18B**). Based on the number of cells detected from each sub-cluster in UMAP from different treatment groups, treatment induced preferred enrichment of cells in each cluster within the same treatment group were calculated and compared based on the number of cells observed divided by expected number of cells in each cluster, respectively. Note that due to the way of calculating the distribution preferences in each-clustered, the enrichment represents enriched within same treatment group, and the relative distributions among different treatment group were not comparable (**Figure 4.18C**). Among all different sub-group of CD8 T cells from scRNAseq, treatment of tumors with BGB324 alone significantly enriched CD8 T cells expressing unique TCRs clustered as clonal expanded CD8 T cells, with the stem like T cells and exhaustive

effector T cells also enriched (**Figure 4.18D**). Although the bystander T cells were also induced from BGB324 treatment, this group of cells did not express functioning markers nor increased cytokine/chemokine expression, suggesting that it was unlikely to contributing to sensitizing KPL tumors to anti-PD-1 treatment (**Figure 4.18C**). Therefore, clonal expanded CD8 T cells, stem like T cells and exhaustive effector T cells were likely to be the group of CD8 T cells responsible for sensitizing KPL tumors in response to anti-PD-1 treatment. When analyzing the effect of combination therapy on these sub-clusters of CD8 T cells, an enrichment of clonally expanded and exhaustive effector CD8 T cells was also observed, which further proved the potential role of these CD8 T cells in contributing to the therapeutic effect observed from KPL tumors (**Figure 4.18D**). To visualize CD8 T cells clustered and enriched from different treatment group, CD8 T cells captured from each individual treatment group were highlighted. Similar to observations from flow cytometry data, BGB324 could enrich clonal expanded T cells. However, little of BGB324 induced CD8 T cells infiltrated into TME was able to proliferate, which further confirmed that BGB324 induced CD8 T cells cannot be activated and proliferating. However, there was no synergistic effect could be clearly observed from combination group, as the number of CD8 T cells captured from anti-PD-1 treatment group was also significantly higher than the other group (**Figure 4.18E**). It could be explained as anti-PD-1 could enrich inhibitory T cells, bystander T cells and major groups of T cells in TME. However, anti-PD-1 treatment was unable to enrich clonal expanded and exhaustive effector T cells, which are the CD8 T cell populations that

responsible for achieving tumor growth control. Therefore, anti-PD-1 treatment seems like could break CD8 T cell exhaustion and proliferate all the CD8 T cells in TME unbiased, which may result in that the original balance of T cells suppression in TME could not be broke, as the relative abundance of different sub-clustered CD8 T cells were not changed.

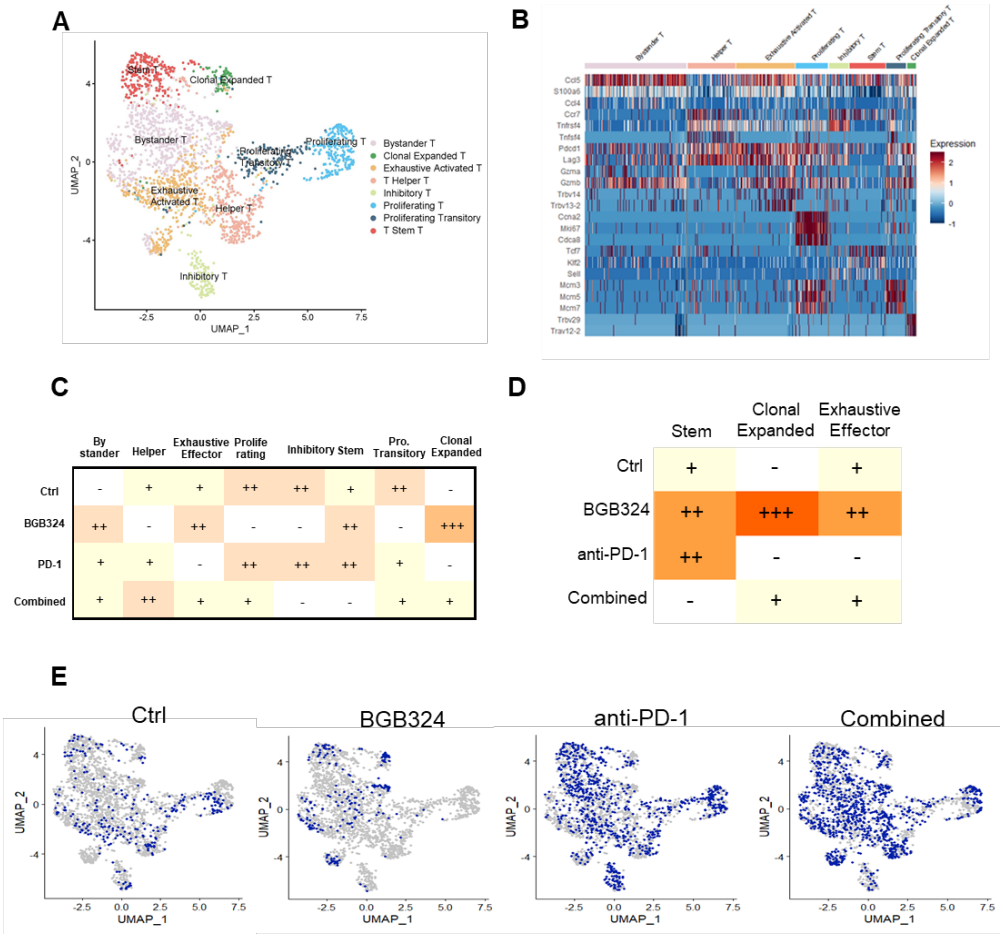

Figure 4.18 Treatment related CD8 T cells scRNAseq analysis in KPL tumors.

(A) UMAP projection for major clusters of sub-clustered $CD8^+$ T cells detected by scRNAseq in KPL tumors from treatment groups. Each color annotates distinct corresponding major cell population.

(B) Heatmap for classic markers expressed in each cell cluster in (A).

(C) Full treatment enriched distribution between each CD8 T cells clusters (see Methods). The ratio of observed cell numbers to random expectation estimated by $R_{o/e}$ index through chi-square test. +++ ($R_{o/e}\geq3$, $P<0.05$) represents highly enriched, ++ ($1.2\leq R_{o/e}<3$, $P<0.05$) represents enriched, + ($0.8\leq R_{o/e}<1.2$, $P<0.05$) represents weakly enriched, - ($0<R_{o/e}<0.8$, $P<0.05$) represents not significant or reduced.
(D) Treatment enriched distribution of stem, clonal expanded and exhaustive effector $CD8^+$ T cells. The criteria are same as (C).

(E) Visualization of T cells detected from individual treatment group in CD8 T cells UMAP cluster. Cells from individual treatment group detected were highlighted in blue.

To further confirm above hypothesis based on scRNAseq, the complementarity-determining region 3 (CDR3) of T cell repertoires were sequenced through scTCRseq and the β chain (CDR3β) information was added onto scRNAseq data. TCR lineage tracing was utilized to calculate shared TCR clone types between different clusters was performed as described by Guo et al (Guo et al., 2018b). Higher scores showed in heatmap indicate more shared TCR clonotypes between the two clusters. As stem like CD8 T cells group features high *Tcf7* expression and highest score with clonal expanded CD8 T cells among all the sub-clusters of CD8 T cells detected, it indicated that the origin of clonal expanded CD8 T cells were from stem like CD8 T cells (**Figure 4.19A**). When analyzing the score of shared TCR clonotypes within the therapeutic responsive CD8 T cell groups, it further the presence of stem like T cells correlated the most with clonally expanded T cells,

which develop into proliferating and exhaustive effector T cells capable of performing direct tumor cell killing (**Figure 4.19B**). The clone size of clonal expanded CD8 T cells was then calculated based on the sum clonal expanded T cells in each cluster (identical TRB sequences >= 2 in each cluster). Based on clonal expansion analysis of TCR sequences, BGB324 could specifically induce the expansion of stem like CD8 T cells while the others could not. Furthermore, BGB324 could induce more of clonal expanded cells other than exhaustive effector T cells, which were largely induced by combination treatment (**Figure 4.19C**). Therefore, TCF1^{+} PD-1^{+} CD8 T cells were likely to be the source of the effector CD8 T cells which were tumor associated and able to control KPL tumor growth with combination of BGB324 with anti-PD-1 treatment. And so far our scRNAseq + scTCRseq analysis accord well with our findings based on flow cytometry and ELISPOT analysis.

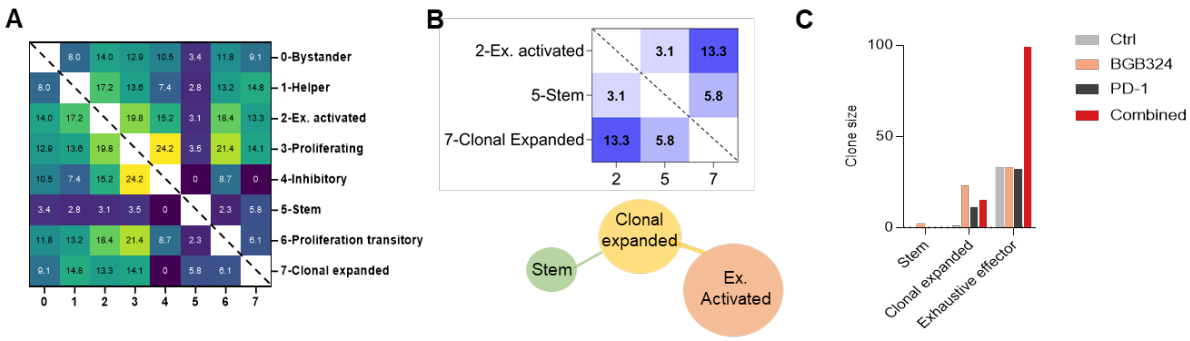

Figure 4.19 Treatment related CD8 T cells scTCRseq analysis in KPL tumors.
(A) Shared TCR clonotypes between each CD8 T cells clusters, see Methods.

(B) Shared clonotypes of TCR between clusters in CD8 T cells detected by scTCRseq (top). Visualization of heatmap into a network plot is shown (bottom). See Methods.

(C) Phenotype of single cell clusters with same TCR clone or TCR specificity group. The top five most abundant clones with TCR clone expanded (≥ e cells) that share a common cluster identity are shown.

Pseudo-time analysis was also performed (see Methods) to plot the dynamic changes of these treatment responsive CD8 T cells. CD8 T cells on the trajectory were colored based on the clusters they belonged to, with stem & naïve like CD8 T cells highlighted in red, clonal expanded CD8 T cells highlighted in blue, and exhaustive effector CD8 T cells highlighted in yellow (**Figure 4.20A**). Those cells were then evaluated for their expression of *Tcf7*, *Ifng* and *Pdcd1* as the main functioning markers to predict the timing and development of CD8 T cells. With the average expression of cells in each cluster visualized as a black line, the *Tcf7* expression was decreased, whereas the *Ifng* and *Pdcd1* expression was increased, as stem like CD8 T cell progressed into clonal expanded or exhaustive effector T cells (**Figure 4.20B**). These data further confirmed that the exhaustive effector CD8 T cells were the main cells responsible for controlling KPL tumors growth, and they originated from stem & naïve T cells and clonal expanded T cells. Visualization of the transition based on pseudo time also confirmed that stem & naïve T cells was the starting point of CD8 T cell development and transition in KPL tumors (**Figure 4.20C**). Cells detected from individual treatment groups were also plotted on the trajectory with control group highlighted in blue, BGB324 group highlighted in yellow, anti-PD-1 highlighted in red and combination

treatment group highlighted in green (**Figure 4.20D**). To better distinguish cells from different treatment group, they were also plotted individually onto the trajectory. The relative distribution abundances were accord with the enrichment analysis, and an enrichment of clonal expanded cells features high was induced by BGB324 (**Figure 4.20E**). However, the cells detected from BGB324 group plotted on trajectory were discrete, the pseudo time analysis was therefore remained less convincing probably due to the low T cell numbers detected from scRNAseq. Individual cells from each cluster in scRNAseq was then plotted on to trajectory separately, with stem like T cells highlighted in green, clonal expanded T cells highlighted in blue and exhaustive effector T cells highlighted in red. Clonal expanded T cells groups also featured high *Tcf7* expression, as some of cells were detected with stem like CD8 T cells markers (**Figure 4.20F**). Taken together, pseudo time analysis mostly accords with our findings from flow cytometry and ELISPOT analysis. However, the origins and the terminal end of the trajectory were defined manually, and *Tcf7* served as a main marker for defining the origins of CD8 T cells development. Because BGB324 induced $TCF1^{+}$ $PD\text{-}1^{+}$ CD8 T cells also features in *Tcf7* expression, which could interfere the trajectory prediction accuracy.

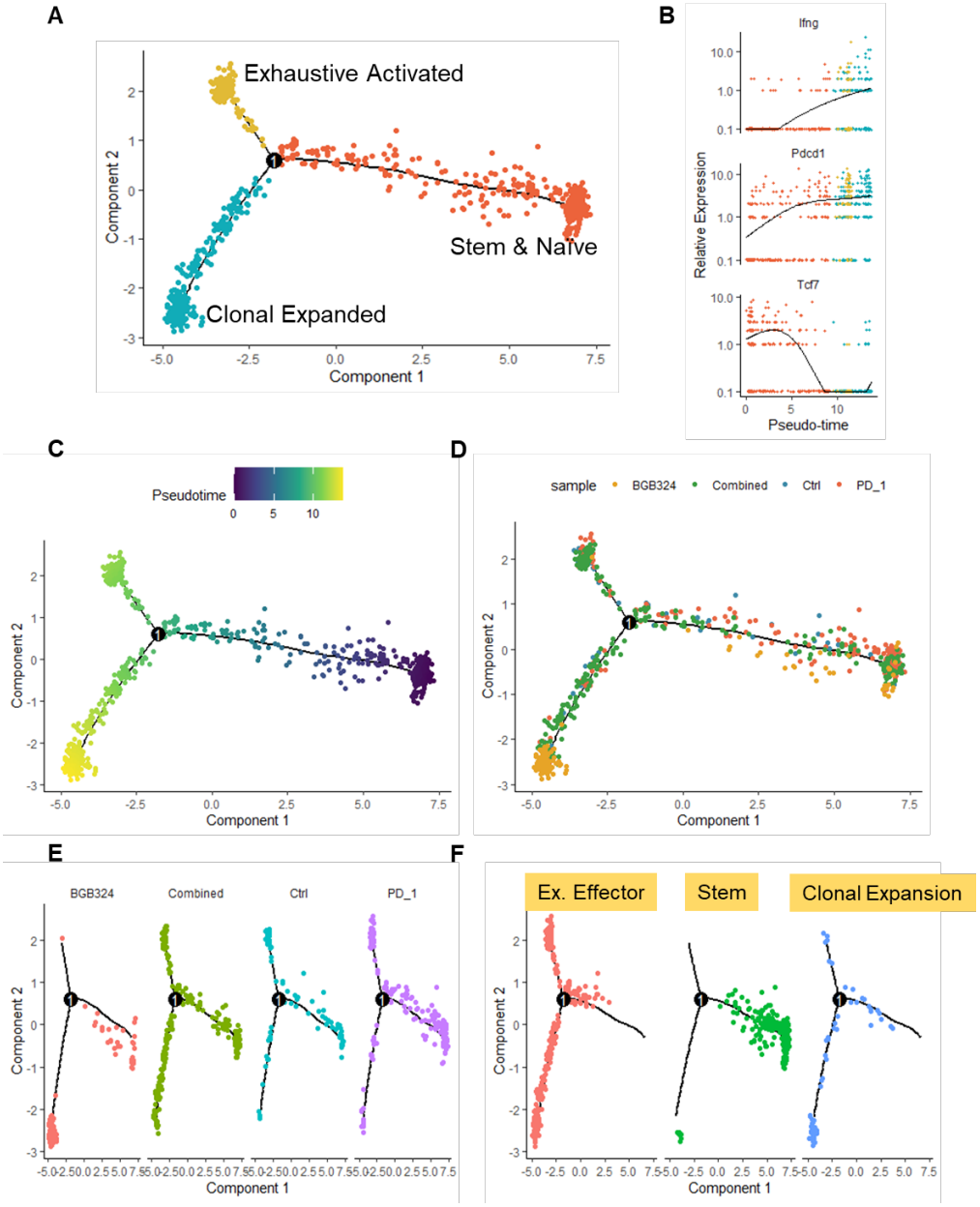

Figure 4.20 Pseudo time analysis of treatment related CD8 T cells in KPL tumors.

(A) Pseudo-timing plot of stem & naïve, clonal expanded, and exhaustive effector CD8$^+$ T cells. Cells are colored based on their status.

(B) Key markers (*Ifng*, *Pdcd*1, *Tcf7*) for identifying pseudo-timing trajectory directions. Cells were colored accord with their status and were same as (A). Average expression levels were drawing as a black line.

(C) Pseudo-timing plot visualized according to pseudotime as the scale bar showed. Where purple highlighted the starting point of the trajectory, and yellow indicated terminal or later status on time point.

(D) Pseudo-timing plot visualized according to different treatment.

(E) Visualization of cells on pseudo-timing trajectory from each individual treatment group.

(F) Visualization of cells on pseudo-timing trajectory from each individual T cell clusters with different status.

To resolve the artificial effect introduced by defining development direction in pseudo time analysis, RNA velocity analysis was performed (see Methods) to predict the future transition status of CD8 T cells in the TME. RNA velocity analysis predicts the future direction and position of cells development, based on the ratio of unspliced immature mRNA expression to mature mRNA expression in individual cells. With a longer arrow on the cells, the higher the probability that the cell would move to the pointing position at the next time point. Based on the UMAP clustering of CD8 T cells detected from KPL tumors in different treatment group (**Figure 4.21A**), RNA velocity was plotted onto it. To distinguish the therapeutic effect induced by different treatment, CD8 T cells detected from different group were visualized with RNA velocity information plotted, respectively. Based on the RNA velocity information, the control tumor group are immune suppressive as the majority of CD8 T cells were moving towards inhibitory or stem status, and limited activated CD8 T cells were present (**Figure 4.21B**). Similar to what we had observed from ELISPOT, BGB324 could reverse the inhibitory trend observed in control treatment groups and enhanced the stemness of clonally expanded cells, BGB324 mediated Axl inhibition

was incapable of being activated to achieve tumor progression control (**Figure 4.21C**). With the addition of anti-PD-1, now the combination treatment could induce the clonally expanded T cells into an activated state and therefore achieve tumor growth control (**Figure 4.21D**).

The relative velocity estimations based on *Tcf7* unspliced immature mRNA and mature RNA expression were then analyzed. The mRNA expression reads of spliced form of *Tcf7* (Tcf7 s), unspliced form of *Tcf7* (Tcf7 u) was fitted with liner regression to estimate the velocity (Tcf7 fit). The residual expression of *Tcf7* (Tcf7 resid) was also visualized based on the differences between observed and expected *Tcf7* expression in each treatment group. As expected, the highest *Tcf7* relative velocity was induced by BGB324 among different treatment group, and the *Tcf7* residual expression was observed to be higher in BGB324 group and also maintained in combination treatment group (**Figures 4.21E-G**). Therefore, RNA velocity analysis resolved the artificial effect induced by pseudo time analysis and provided a better support into our conclusion drew from flow cytometry and ELISPOT analysis.

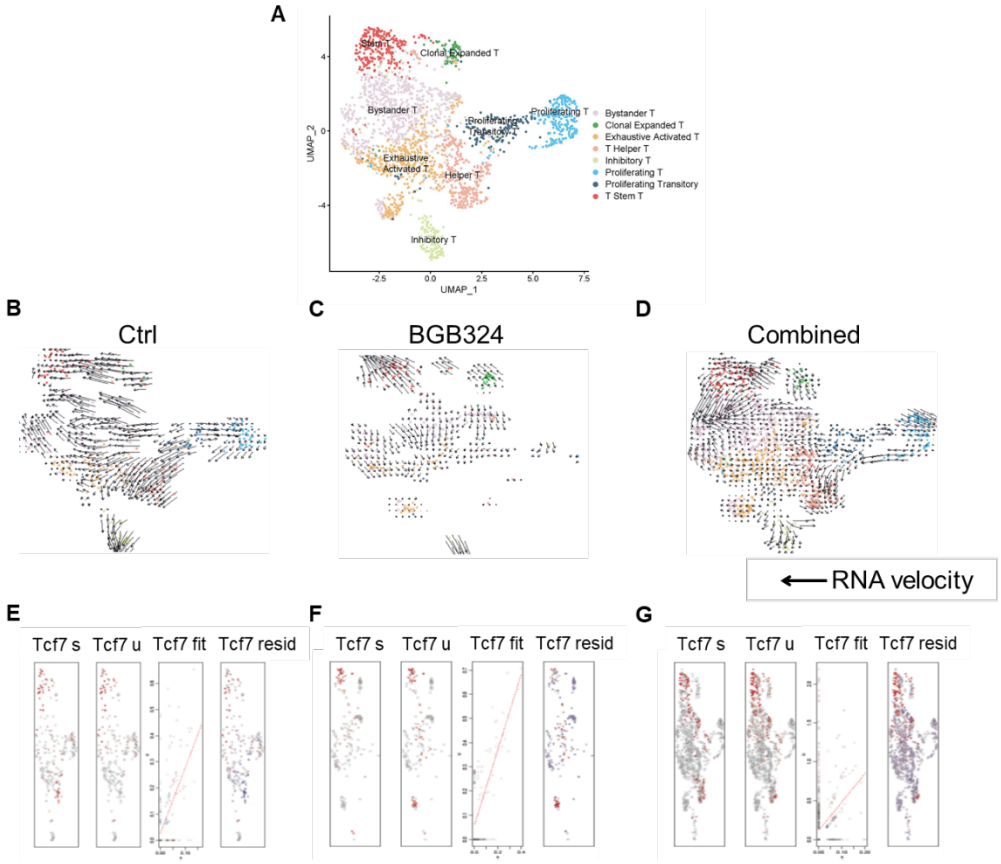

Figure 4.21 RNA velocity analysis of treatment related CD8 T cells in KPL tumors.

(A) UMAP projection for major clusters of sub-clustered CD8⁺ T cells detected by scRNAseq in KPL tumors from treatment groups. Each color annotates distinct corresponding major cell population.

(B-D) RNA velocity analysis of gene expression in CD8 T cells from ctrl (B), BGB324 (C) or combination (D) treatment groups. Arrows indicate potential dynamic paths of differentiation.

(E-G) *Tcf7* relative velocity estimation from ctrl (E), BGB324 (F) or combination (G) treatment groups. Spliced (s), unspliced (u), actual fit (fit) and residuals (resid, the differences between observed and expected unspliced mRNA abundance to track velocity) were visualized from left to right.

To conclusively identify whether TCF1 expressing CD8 T cells are the key mediator for BGB324 + anti-PD-1 therapy to control KPL tumors progression, *Tcf7* flox mice (Jackson Laboratories, Cat# 030909) were crossed with *Cd8a* Cre mice (Jackson Laboratories, Cat# 032080) to generate conditional knockout mice with TCF1 expressing CD8 T cells depleted. Littermates including $Cd8a^{wt}Tcf7^{fl/fl}$ and $CD8a^{Cre}Tcf7^{fl/fl}$ mice were then generated and confirmed their TCF1 expressing CD8 T cells knockout through flow cytometry (**Figure 4.22A**). When treating the mice with BGB324 + anti-PD-1, wild type $Tcf7^{fl/fl}$ mice were able to control KPL tumors progression effectively, while $CD8a^{Cre}Tcf7^{fl/fl}$ mice were no longer able to respond to therapy (**Figure 4.22B**). However, Cd4 Cre mice should be considered to use in the future for similar experiments, as Cd8 Cre mice may also affect $CD8^+$ DCs function in *vivo*, and CD8 T cells are all developed from $CD4^+CD8^+$ double positive T cells. Therefore, Cd4 Cre mice should be sufficient to deplete CD8 T cells and preserved $CD8^+$ DCs function.

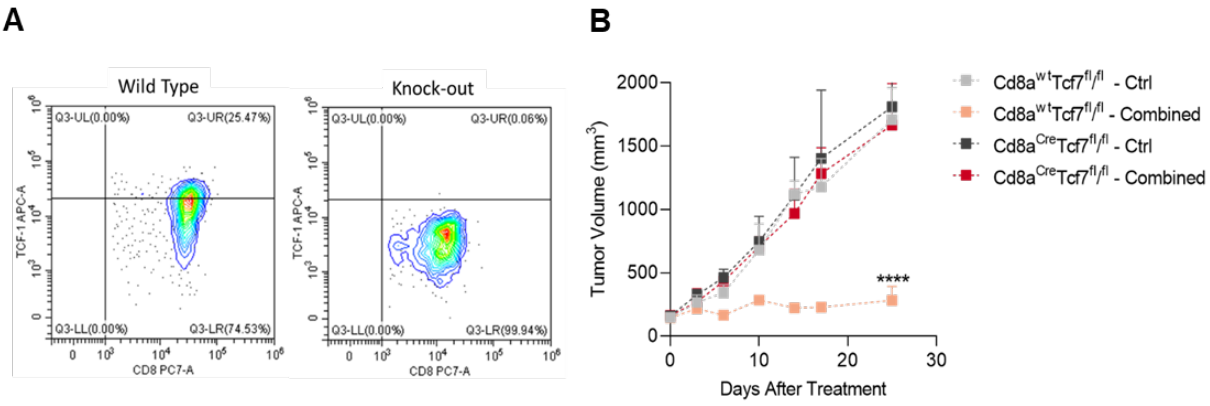

Figure 4.22 Therapeutic effects of treated KPL tumors in TCF1 CD8 T cells depleted mice.

(A) Abundance of $TCF1^{+}CD8^{+}$ T cells in spleen harvested from $Cd8a^{wt}Tcf7^{fl/fl}$ and $CD8a^{Cre}Tcf7^{fl/fl}$ mouse.

(B) Littermate mice of $Cd8a^{wt}Tcf7^{fl/fl}$ and $CD8a^{Cre}Tcf7^{fl/fl}$ (n = 6) were injected with 1 x 10^6 KPL tumor cells. Mice were treated with BGB324 (50 mg/kg, twice daily) and anti-PD-1 (10 mg/kg, day 7, 10, 14) or corresponding IgG and vehicle starting on day 7 after tumor cell injection. Tumor growth was measured every 3 days.

Although it had been confirmed that BGB324 could induce the proliferation of $TCF1^{+}$ $PD\text{-}1^{+}$ CD8 T cells in KPL tumors, it remains unclear that whether the proliferation or the recruitment of $TCF1^{+}$ $PD\text{-}1^{+}$ CD8 T cells into TME plays a more important role in sensitizing KPL tumors to anti-PD-1 treatment. In order to dissect this question, feature plot with expression of *Tcf7*, *Pdcd1* and *S1pr1* in CD8 T cells detected in scRNAseq was analyzed. When visualized based on T cell clusters, stem like T cells features high *Tcf7* and *S1pr1* expression, and the percentage of cells expressed these genes were relative the same. The same level expression of *Tcf7* and *S1pr1* were also observed in clonal expanded T cell groups, which indicated the potential co-expression of *Tcf7* and *S1pr1* on induced $TCF1^{+}$ $PD\text{-}1^{+}$ CD8 T cells (**Figure 4.23A**). This was further supported by visualizing *Tcf7*, *Pdcd1* and *S1pr1* based on different treatment group. BGB324 treated group showed a unique high expression of *Tcf7* and *S1pr1*, which was not observed from the other groups. The percentage of CD8 T cells detected with *Tcf7* and *S1pr1* expression remained similar in BGB324 treated group as well, which further supported the potential co-expression of *Tcf7* and *S1pr1* on induced $TCF1^{+}$ $PD\text{-}1^{+}$ CD8 T cells induced by BGB324 treatment

(**Figure 4.23B**). When blocking T cell egress from spleen when treatment started, BGB324 + anti-PD-1 treatment was no longer able to control KPL tumor progression, suggesting the TCF1$^+$ PD-1$^+$ CD8 T cells were newly recruited from spleen instead of the expansion of tumor pre-infiltrated TCF1$^+$ PD-1$^+$ CD8 T cells (**Figure 4.23C**).

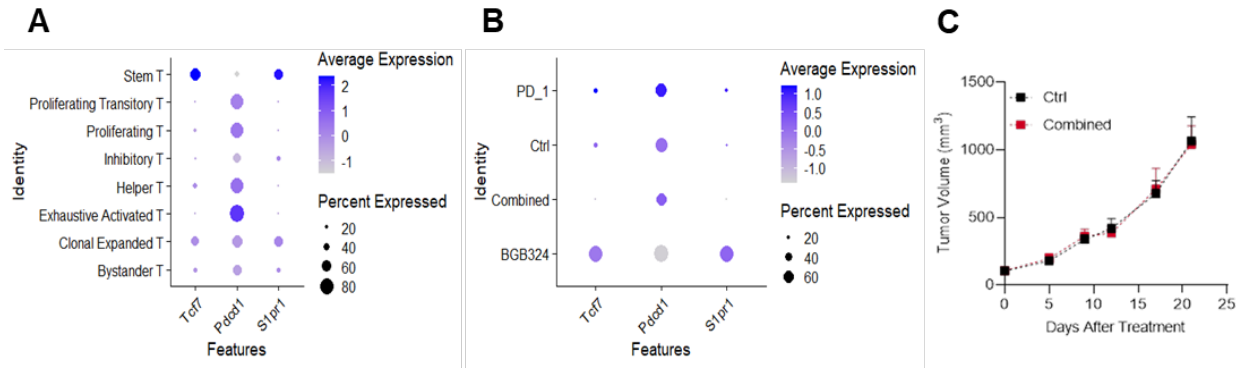

Figure 4.23 TCF1 CD8 T cells were recruited from spleen in treated KPL tumors.

(A) Average expression dot plot for *Pdcd*1, *Tcf7*, and *S1pr1* in different CD8 T cell sub-clusters detected from scRNAseq. Where the color indicated the level of expression, the size of dots represented the percentage of cells were detected for expression.

(B) Average expression dot plot for *Pdcd*1, *Tcf7*, and *S1pr1* in different treatment groups detected from scRNAseq. Where the color indicated the level of expression, the size of dots represented the percentage of cells were detected for expression.

(C) C57BL/6J mice (n = 5) were injected with 1 x 10^6 KPL tumor cells. Mice were treated with BGB324 (50 mg/kg, twice daily) and anti-PD-1 (10 mg/kg, day 7, 10, 14) or corresponding IgG and vehicle starting on day 7 after tumor cell injection. Mice were also treated with FTY720 hydrochloride every other day starting from day 6 (1 mg/kg on day 6, 0.5 mg/kg for following treatments) to prevent T cell egress from spleen *in vivo*. Tumor growth was measured every 3 days.

Taken together, the TCF1^{+} PD-1^{+} CD8 T cells expansion induced by BGB324 treatment are the key population of T cells which could achieve KPL tumor growth control upon anti-PD-1 treatment.

CHAPTER FIVE:
Inhibition of Axl in Dendritic Cells Is Required for Efficacy of anti-PD-1 in *Stk11/Lkb1* Mutant Tumors

5.1 Axl Inhibition in Host Cells Sensitizes *Stk11/Lkb1* Mutant Tumors to anti-PD-1 Therapy

Since Axl inhibition combined with anti-PD-1 controlled KPL tumor growth and this effect was dependent on immune activation, we used Axl-deficient mice to investigate whether loss of Axl in host cells is sufficient to sensitize KPL tumors to anti-PD-1 treatment. Treatment with anti-PD-1 alone was sufficient to control the growth of KPL tumors grown in *Axl* KO mice, indicating that the inhibition of Axl plays an important role in sensitizing KPL tumors to anti-PD-1 therapy (**Figure 5.1A**). Analysis of the immune landscape of these tumors demonstrated that the loss of Axl in host cells resulted in significant increased tumor infiltration by TCF1$^+$PD-1$^+$CD8 T cells compared to tumors implanted into *Axl* wild-type (WT) mice (**Figures 5.1B-C**). Therefore, Axl expression in host cells is critical for the suppression of the expansion of TCF1$^+$PD-1$^+$CD8 T cells in the *Stk11/Lkb1* mutant TME.

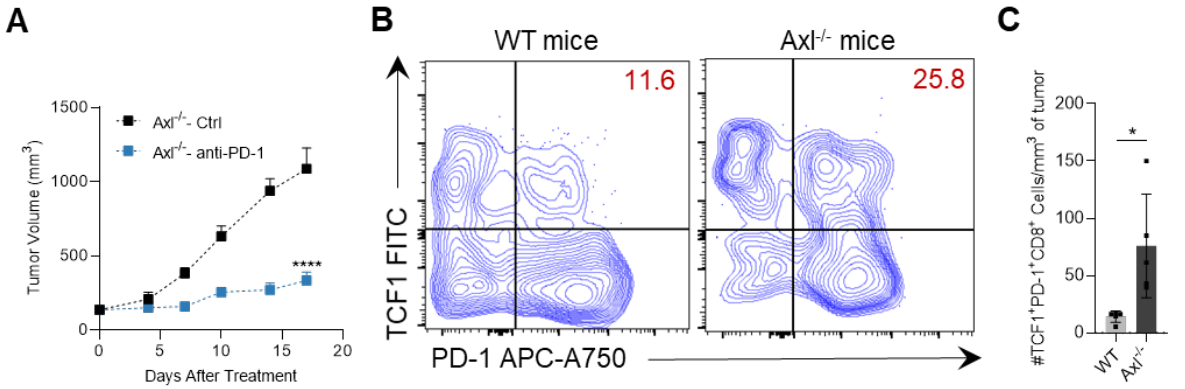

Figure 5.1 Axl depletion in hosts sensitizes KPL tumors to PD-1 blockade.

(A) *Axl*$^{-/-}$ mice (n = 5) were injected with 1 x 10^6 KPL tumor cells and treated with anti-PD-1 (10 mg/kg, day 7, 10, 14). Tumor volume was measured every 3 days.

(B) Representative infiltrated TCF1$^+$PD-1$^+$ cell percentage among gated CD8$^+$ TILs on day 7 post therapy initiation on *Axl*$^{-/-}$ mice.

(C) Abundance of TCF1$^+$PD-1$^+$ cells among gated CD8$^+$ TILs (per mm^3 of tumor) on day 7 post therapy initiation (day 14 post tumor inoculation).

5.2 Axl Inhibition in Dendritic Cells Is Required for Therapeutic Responses

To analyze *Axl* expression in KPL tumors TME, scRNAseq analysis was performed and analyzed for myeloid compartment, as Axl had been reported as an innate sensing checkpoint in TME (Rothlin et al., 2007; Schmid et al., 2016; Seitz et al., 2007). Integrated KPL tumor samples undergone different treatment group was used to subset myeloid cells (average expression of *Cd3e*, *Cd3g*, and *Cd3d* < 0.01) and sub-clustered (resolution = 0.1) as dendritic cells, macrophages, and monocytes/MDSCs (**Figure 5.2A**). The BGB324 treated tumor was sequenced

separately, as the first batch of BGB treated tumor samples were returned with over 20,000 cells whereas the average number of genes was around 500 (normally at least beyond 1,200). After the integration of scRNAseq data with the rest group based on expression of anchors, the data was merged well without observable batch effect when visualizing UMAP based on samples (**Figure 5.2B**). Representative markers used to define identities of myeloid cells in UMAP was visualized with their expression level (**Figure 5.2C**). In myeloid cells, *Axl* expression was detected in tumor-associated macrophages and dendritic cells (DCs) (**Figure 5.2 D**). When comparing myeloid cells in KP and KPL tumors, *Axl* expression was elevated when lacking *Stk11/Lkb1* expression (**Figures 5.2E**). Taken together, *Stk11/Lkb1* mutation in KPL tumors resulted in *Axl* upregulation in macrophages and dendritic cells in TME, which hindered the KPL tumors responses to anti-PD-1 treatment.

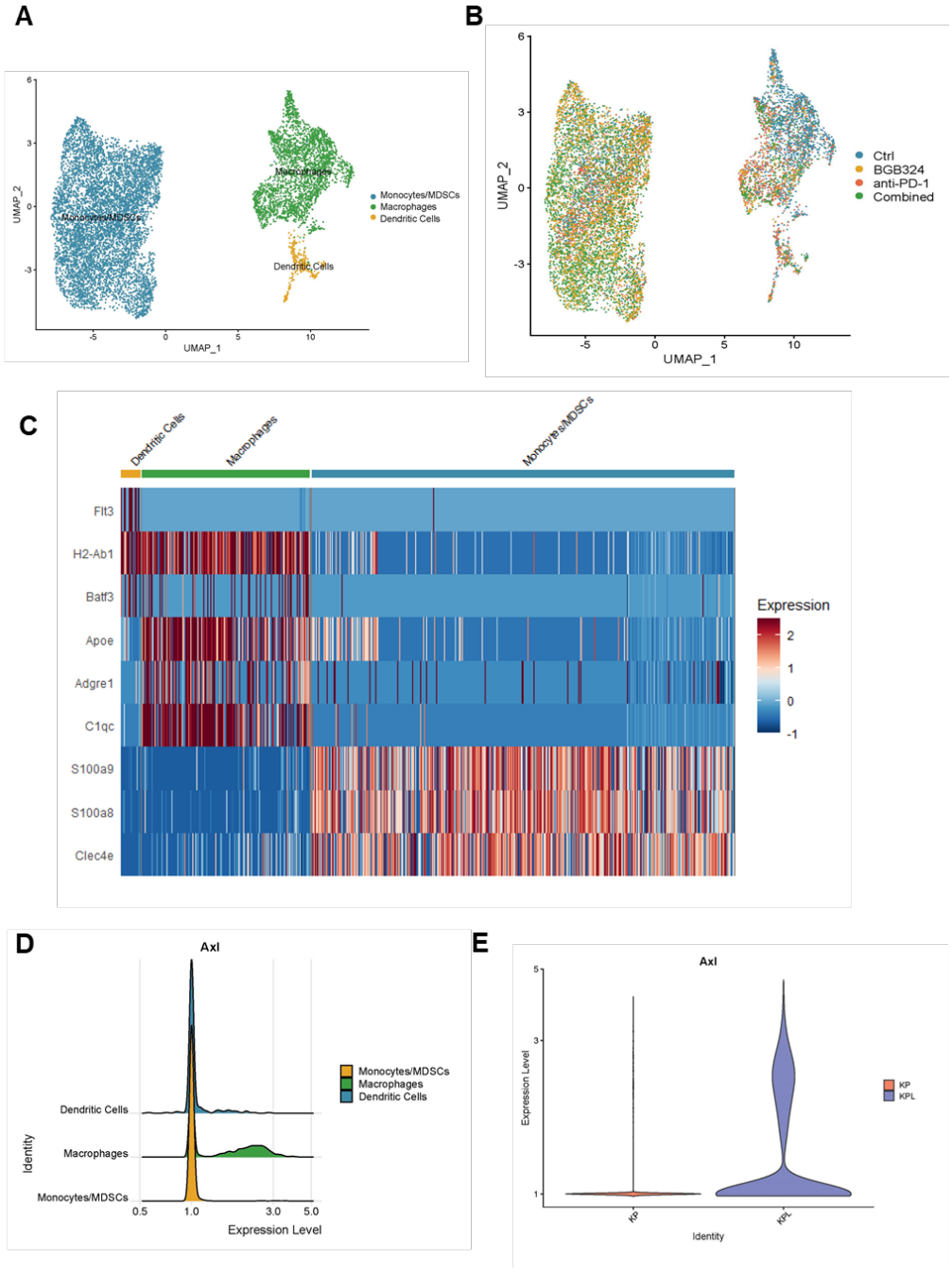

Figure 5.2 Axl expression in host immune cells.

(A) UMAP of sub-clustered tumor infiltrating myeloid cells in KPL tumors.

(B) Each individual treatment group visualized in UMAP clusters.

(C) Heatmap for representative markers used to define myeloid cells clusters in KPL tumor after therapy with vehicle (Ctrl), BGB324, anti-PD-1 (αPD-1) or the combination (Combined).

(D) Ridge plot of *Axl* expression on myeloid cells in KPL tumor myeloid cell clusters.

(E) Violin plot of *Axl* expression on myeloid cells in KP (blue) and KPL (red) tumors.

To determine which host cell component was critical for Axl inhibition and the therapeutic response to anti-PD-1, macrophages or DCs, were depleted *in vivo* respectively as described (Ren et al., 2017). Although *Axl* expression was higher in macrophages from scRNAseq analysis, depleting macrophages in KPL tumors did not impact the therapeutic effect of combined Axl and PD-1 inhibition, suggesting BGB324 mediated sensitization to anti-PD-1 is independent of macrophages (**Figure 5.3A**). By contrast, KPL tumors grown in *Batf3* KO mice, which lack functional $CD103^{+}$ DCs that are essential for cross-priming (Broz et al., 2014; Edelson et al., 2010) of tumor associated CD8 T cells in TME, did not respond to combined inhibition of Axl and anti-PD-1 (**Figure 5.3B**). These results indicate that inhibiting Axl on DCs is essential for the efficacy of combined Axl and PD-1 inhibition.

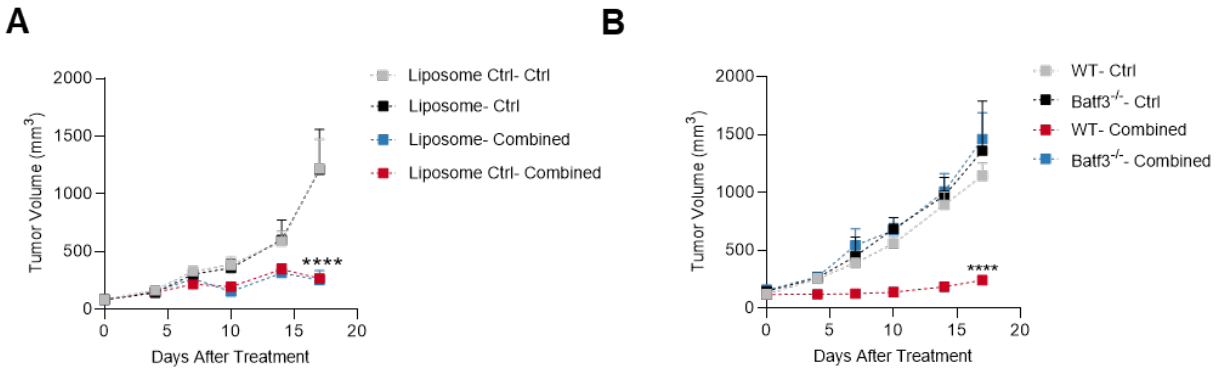

Figure 5.3 Inhibition of Axl in dendritic cells sensitizes KPL tumors to PD-1 blockade.

(A) C57BL/6J mice (n = 5) were injected with 1 x 10^6 KPL tumor cells and treated with macrophage depleting reagent (Liposome) or control liposomes (Ctrl) (see Methods). Mice were treated with BGB324 (50 mg/kg, twice daily) and anti-PD-1 (10 mg/kg, day 7, 10, 14) (Combined), or corresponding IgG and vehicle (Veh) starting on day 7 post tumor cell injection. Tumor volume was measured every 3 days.

(B) C57BL/6J mice (n = 5) and *Batf3*$^{-/-}$ mice (n = 4 for control group; n = 5 for treatment group) were injected with 1 x 10^6 KPL tumor cells. Treatment strategy same as (G).

Since the therapeutic effect of controlling KPL tumor progression with BGB324 + anti-PD-1 was through inhibiting Axl in infiltrated dendritic cells, dendritic cells detected from KPL treated tumor scRNAseq was taken out for further analysis. Subset dendritic cells were then sub-clustered into 4 clusters (resolution = 0.1), including plasmacytoid dendritic cells, cross-priming dendritic cells, Langerhans cells, and tolerogenic dendritic cells (**Figure 5.4A**). Same as total myeloid cell clustering, there was no obvious batch effect when clustering DCs (**Figure 5.4B**). The identities of each group of DCs were defined with their most up-regulated

functioning markers (Bros et al., 2011; Dixon et al., 2017; Dorner et al., 2009; Galibert et al., 2005; Linehan et al., 2015; Miyano et al., 2016; Roberts et al., 2016; Sancho et al., 2009) (**Figure 5.4C**).

To analyze treatment preferred enrichment of different group of DCs in KPL tumors, return of equity analysis were performed on clustered dendritic cells (see Methods). In KPL tumors, major group dendritic cells exhibited lung resident DCs markers and tolerogenic features, as *Ifitm3*, *Cfp*, and *Mgl2* were upregulated to prevent antigen presentation and homing of DCs. However, the relative abundance of both tolerogenic DCs and Langerhans cells did not change upon treatment. At the same time, plasmacytoid DCs were enriched in treatment naïve KPL tumors, with anti-PD-1 treatment decreased the relative abundance. The abundance of plasmacytoid DCs in BGB324 or combined treated KPL tumors were further depleted, indicating their changes were mediated by Axl inhibition by BGB324. An enrichment of cross-priming DCs upon BGB324 inhibition were also observed in BGB324 or combination treatment group, with increased expression of *Xcr1*, *Clec9a*, and *Cadm1* which had been reported for increasing antigen presentation in DCs (**Figure 5.4D**). These findings further indicated that the Axl inhibition in DCs could increase the activity of cross-priming DCs in TME, which is required for sensitizing KPL tumors to anti-PD-1 treatment. When visualizing Axl expression in different clusters of DCs, *Axl* expression was detected on both tolerogenic DCs and cross-priming DCs (**Figure 5.4E**). Therefore, either the inhibition of Axl in tolerogenic DCs mediated the transition and recruitment of cross-priming DCs into TME, or the Axl inhibition in

already infiltrated but inhibited cross-priming DCs was the key population in mediating therapeutic effects of KPL tumors. The latter seems more likely to be the explanation, as the abundance of cross-priming DCs in control group was not depleted as in anti-PD-1 treatment group. However, there is no effective way to prevent DCs exiting from spleen and draining lymph nodes, further validation of this hypothesis needs either more detailed staining with functioning markers of DCs, as well as more time point to dissect the dynamic changes in KPL tumors upon treatment.

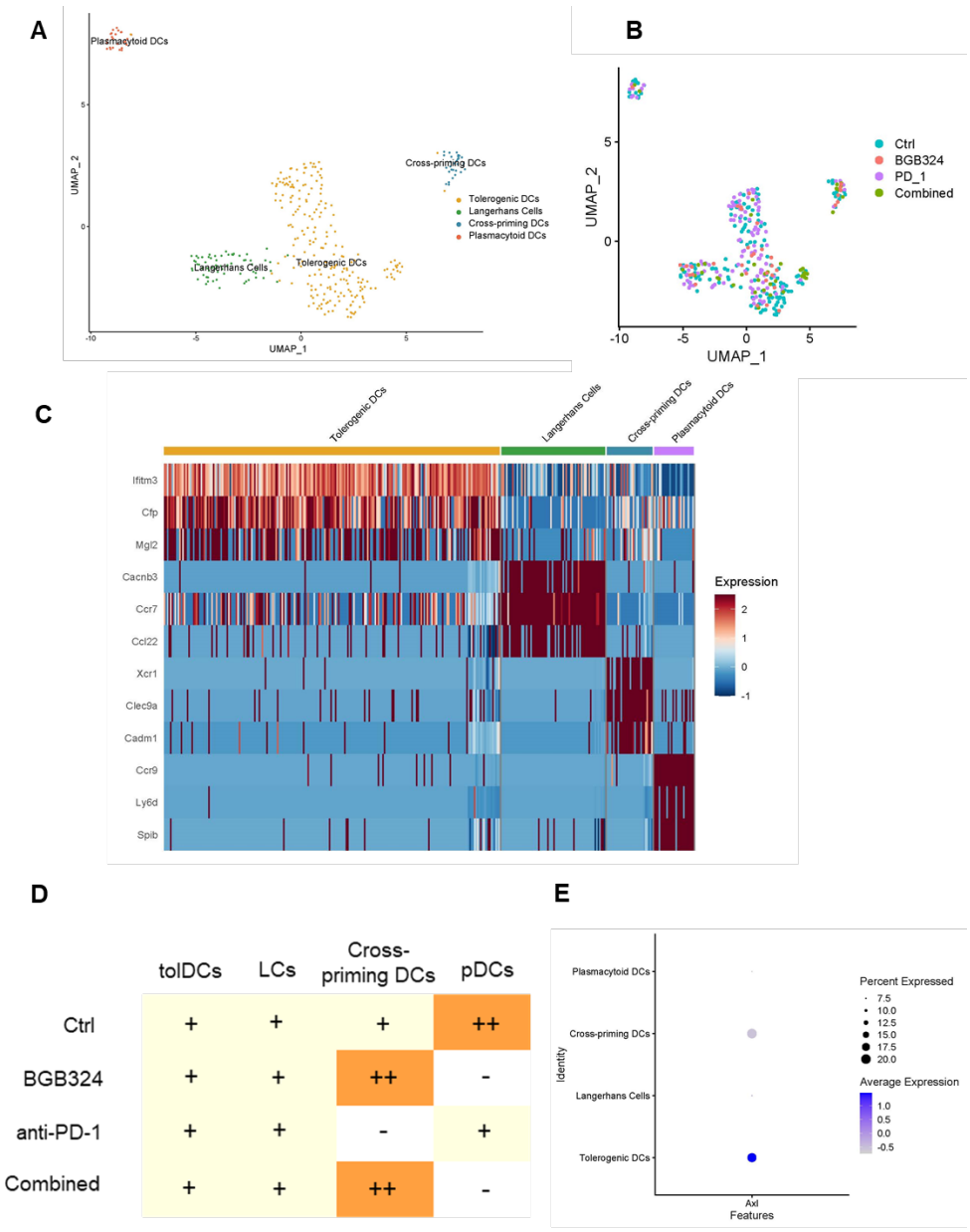

Figure 5.4 scRNAseq analysis of dendritic cells dynamics in treated KPL tumors.

(A) UMAP projection for major clusters of sub-clustered dendritic cells detected by scRNAseq in KPL tumors from treatment groups. Each color annotates distinct corresponding major cell population.

(B) Each individual treatment group visualized in UMAP clusters: control group as blue (Ctrl), BGB324 as red, anti-PD-1 as purple, BGB324 + anti-PD-1 as green (combined).

(C) Heatmap for classic markers expressed in each cell cluster in (A).

(D) Treatment enriched distribution of plasmacytoid DCs, cross-priming DCs, Langerhans cells, and tolerogenic DCs (see Methods). The ratio of observed cell numbers to random expectation estimated by $R_{o/e}$ index through chi-square test. +++ ($R_{o/e}\geq3$, $P<0.05$) represents highly enriched, ++ ($1.2\leq R_{o/e}<3$, $P<0.05$) represents enriched, + ($0.8\leq R_{o/e}<1.2$, $P<0.05$) represents weakly enriched, - ($0<R_{o/e}<0.8$, $P<0.05$) represents not significant or reduced.

(E) Dot plot for percentage of *Axl* expressing cells (dot sizes) and their average expression (dot color intensities) in different DCs sub-clusters.

To compare pathways altered in dendritic cells upon BGB324 treatment, gene set enrichment analysis was performed to compare BGB324, BGB324 + anti-PD-1 treated KPL tumors to control group and anti-PD-1 treated KPL tumors and ranked based on national evaluation series (NES) score.

Among significantly altered pathways,

GSE5679_CTRL_VS_RARA_AGONIST_AM580_TREATED_DC_UP,

GSE45365_WT_VS_IFNAR_KO_CD11B_DC_MCMV_INFECTION_DN,

GSE33292_WT_VS_TCF1_KO_DN3_THYMOCYTE_DN,

GSE45365_HEALTHY_VS_MCMV_INFECTION_CD11B_DC_IFNAR_KO_DN were enriched in BGB324 and combination treated KPL tumors, indicating the upregulation of type I interferon signaling and *Tcf7* related gene signatures in BGB324 and BGB324 + anti-PD-1 treated tumor myeloid cells. Highlighted pathways also hinted the upregulation of interferon induced CD8 T cells in TME, which accord

with other observations that BGB324 treatment could induced type I interferon signaling pathways. At the same time, the PD1 ligation of activated T cells were also upregulated, which provided further rational for combining BGB324 with anti-PD-1 treatment to potentiate therapeutic effects in KPL tumors (**Figure 5.5**).

Figure 5.5 GSEA analysis of dendritic cells in KPL treated tumors. Gene set enrichment analysis (GSEA) statistics of pathways that were significantly upregulated or downregulated on dendritic cells in BGB324 and BGB324 + anti-PD-1 group comparing to control and anti-PD-1 group. Pathways altered were ranked by national evaluation series (NES) score. Highlighted pathway were potentially induced by therapeutic effects.

However, pathways highlighted from GSEA analysis were not the most significant altered pathway, either ranked by adjusted p value or NES score. Several most significant altered pathways were T cell related, although this analysis was performed in DCs in TME. The proliferation and division of DCs were upregulated when inhibited Axl, which indicated a more activated status (**Table 5-1**). Ideally, all the conclusions drew from bioinformatic analysis needed to be confirmed experimentally. Under this case, a more detailed staining for DCs may help to validate the hypotheses.

Description	Set Size	Enrichment Score	NES	pvalue	p.adjust	qvalues
GSE15750_DAY6_VS_DAY10_EFF_CD8_TCELL_UP	90	0.528141	1.86144	3.25E-09	2.40E-05	2.36E-05
GO_CELL_CYCLE_PROCESS	192	0.444549	1.624301	8.85E-09	3.27E-05	3.22E-05
GO_CELL_DIVISION	113	0.484354	1.727321	2.56E-08	4.72E-05	4.65E-05
GO_CELL_CYCLE	246	0.419411	1.550821	2.40E-08	4.72E-05	4.65E-05
GSE14415_NATURAL_TREG_VS_TCONV_DN	84	0.517495	1.812014	4.72E-08	6.98E-05	6.87E-05
GSE15750_DAY6_VS_DAY10_TRAF6KO_EFF_CD8_TCELL_UP	97	0.49896	1.767228	9.91E-08	0.000105	0.000103

GO_MITOTIC_CELL_CYCLE	176	0.438806	1.597249	9.81E-08	0.000105	0.000103
HALLMARK_E2F_TARGETS	85	0.508859	1.783254	1.51E-07	0.000139	0.000137
REACTOME_CELL_CYCLE	100	0.490169	1.738833	1.72E-07	0.000141	0.000139
REACTOME_CELL_CYCLE_MITOTIC	90	0.498433	1.756733	2.14E-07	0.000158	0.000156
GSE30962_PRIMARY_VS_SECONDARY_ACUTE_LCMV_INF_CD8_TCELL_UP	84	0.50213	1.758215	3.28E-07	0.000221	0.000217
GSE13547_CTRL_VS_ANTI_IGM_STIM_BCELL_12H_UP	97	0.481918	1.706868	7.19E-07	0.000443	0.000436
GO_SPINDLE	55	0.526385	1.777118	5.63E-06	0.003046	0.003001
GO_MICROTUBULE_CYTOSKELETON	120	0.448186	1.604676	5.77E-06	0.003046	0.003001
GO_CHROMOSOME_SEGREGATION	55	0.523375	1.766958	7.16E-06	0.003524	0.003472
GSE35543_IN_VITRO_ITREG_VS_CONVERTED_EX_ITREG_UP	53	0.535623	1.80614	1.02E-05	0.003978	0.003919
GO_MITOTIC_NUCLEAR_DIVISION	65	0.500323	1.720736	1.04E-05	0.003978	0.003919
GSE13547_CTRL_VS_ANTI_IGM_STIM_BCELL_2H_UP	82	0.477318	1.667091	1.02E-05	0.003978	0.003919
GO_CHROMOSOME_ORGANIZATION	121	0.440777	1.578877	1.08E-05	0.003978	0.003919

GO_REGULATION_OF_CELL_CYCLE_PROCESS	109	0.441733	1.572011	8.68E-06	0.003978	0.003919
GSE29614_CTRL_VS_DAY7_TIV_FLU_VACCINE_PBMC_DN	47	0.535611	1.782886	1.58E-05	0.005556	0.005474
HALLMARK_MITOTIC_SPINDLE	46	0.536309	1.781709	1.69E-05	0.005674	0.00559
GO_MEIOTIC_CELL_CYCLE_PROCESS	24	0.620728	1.892557	1.82E-05	0.005803	0.005717
GO_ORGANELLE_FISSION	79	0.477318	1.663221	1.88E-05	0.005803	0.005717
HALLMARK_G2M_CHECKPOINT	71	0.487548	1.690404	2.44E-05	0.007221	0.007114
GSE25088_WT_VS_STAT6_KO_MACROPHAGE_IL4_STIM_DN	68	0.486797	1.681073	2.64E-05	0.007499	0.007388
GSE37532_WT_VS_PPARG_KO_VISCERAL_ADIPOSE_TISSUE_TREG_UP	49	0.528384	1.764931	2.75E-05	0.007534	0.007423
GO_NUCLEAR_CHROMOSOME_SEGREGATION	48	0.520604	1.73521	3.40E-05	0.008969	0.008836
GSE36476_CTRL_VS_TSST_ACT_72H_MEMORY_CD4_TCELL_YOUNG_DN	81	0.454815	1.586696	3.73E-05	0.009509	0.009368
GSE13547_2H_VS_12_H_ANTI_IGM_STIM_BCELL_UP	83	0.460828	1.61079	4.18E-05	0.010297	0.010145
GO_MITOTIC_SPINDLE	26	0.606029	1.86949	4.49E-05	0.010698	0.01054

GO_CHROMOSOMAL_REGION	52	0.513996	1.729516	4.74E-05	0.010743	0.010585
GSE14415_INDUCED_VS_NATURAL_TREG_DN	81	0.452273	1.57783	4.80E-05	0.010743	0.010585
GSE27241_WT_VS_RORGT_KO_TH17_POLARIZED_CD4_TCELL_UP	53	0.51814	1.747188	5.02E-05	0.010915	0.010754
GSE2405_S_AUREUS_VS_UNTREATED_NEUTROPHIL_DN	69	0.475222	1.644219	5.30E-05	0.011196	0.011031
GSE40274_CTRL_VS_FOXP3_TRANSDUCED_ACTIVATED_CD4_TCELL_UP	57	0.496788	1.683745	5.92E-05	0.012154	0.011975
GSE29614_CTRL_VS_TIV_FLU_VACCINE_PBMC_2007_DN	39	0.543155	1.763613	7.05E-05	0.014078	0.01387
GO_MITOTIC_CYTOKINESIS	20	0.638169	1.898227	9.51E-05	0.016005	0.015769
GO_ORGAN_GROWTH	28	0.590184	1.837756	8.45E-05	0.016005	0.015769
GSE39556_CD8A_DC_VS_NK_CELL_MOUSE_3H_POST_POLYIC_INJ_UP	60	0.479979	1.63756	8.97E-05	0.016005	0.015769
GSE12845_IGD_POS_BLOOD_VS_PRE_GC_TONSIL_BCELL_DN	65	0.473502	1.628491	9.08E-05	0.016005	0.015769
GSE36476_CTRL_VS_TSST_ACT_72H_MEMORY_CD4_TCELL_OLD_DN	74	0.46086	1.602722	9.53E-05	0.016005	0.015769

GSE21063_WT_VS_NFATC1_KO_8H_ANTI_IGM_STIM_BCELL_UP	72	0.461136	1.601674	8.63E-05	0.016005	0.015769
GSE24634_TEFF_VS_TCONV_DAY7_IN_CULTURE_UP	73	0.460885	1.600375	9.42E-05	0.016005	0.015769
GO_SISTER_CHROMATID_SEGREGATION	43	0.519631	1.712468	9.98E-05	0.016034	0.015797
GSE39110_DAY3_VS_DAY6_POST_IMMUNIZATION_CD8_TCELL_DN	88	0.441578	1.554373	9.98E-05	0.016034	0.015797
GO_ENDOCHONDRAL_BONE_MORPHOGENESIS	12	0.728591	1.972034	0.000118	0.018209	0.01794
GSE5679_CTRL_VS_RARA_AGONIST_AM580_TREATED_DC_UP	46	0.509334	1.692095	0.000119	0.018209	0.01794
GO_MESODERMAL_CELL_DIFFERENTIATION	10	-0.70216	-2.47782	0.000121	0.018209	0.01794
GO_CENTROSOME	54	0.491458	1.658829	0.000126	0.018229	0.01796
GO_MICROTUBULE_ORGANIZING_CENTER	66	0.466885	1.608926	0.000124	0.018229	0.01796
GSE45365_HEALTHY_VS_MCMV_INFECTION_CD11B_DC_IFNAR_KO_DN	45	0.504736	1.671039	0.000144	0.020069	0.019773
GSE24634_TREG_VS_TCONV_POST_DAY7_IL4_CONVERSION_UP	62	0.475894	1.627422	0.000142	0.020069	0.019773

GO_MEIOTIC_CELL_CYCLE	25	0.592441	1.819442	0.000149	0.020399	0.020098
KEGG_OOCYTE_MEIOSIS	12	0.719884	1.948466	0.000163	0.021603	0.021284
GO_CYTOSKELETON_DEPENDENT_CYTOKINESIS	22	0.607067	1.822697	0.000164	0.021603	0.021284
GSE25088_WT_VS_STAT6_KO_MACROPHAGE_DN	72	0.44821	1.556779	0.00021	0.027183	0.026782
GSE45365_WT_VS_IFNAR_KO_CD11B_DC_MCMV_INFECTION_DN	47	0.497317	1.65542	0.000219	0.027897	0.027486
GO_DNA_REPLICATION	46	0.499156	1.65828	0.000235	0.029387	0.028953
GSE11386_NAIVE_VS_MEMORY_BCELL_UP	49	0.497384	1.661385	0.000239	0.029488	0.029053
GO_CELL_CYCLE_PHASE_TRANSITION	94	0.429331	1.517868	0.000298	0.03615	0.035617
GO_MITOTIC_SISTER_CHROMATID_SEGREGATION	39	0.516875	1.678281	0.000321	0.038282	0.037717
REACTOME_M_PHASE	53	0.486623	1.640913	0.000339	0.03919	0.038612
GSE20366_EX_VIVO_VS_HOMEOSTATIC_CONVERSION_TREG_DN	60	0.461349	1.573997	0.000339	0.03919	0.038612
GSE14415_TCONV_VS_FOXP3_KO_INDUCED_TREG_DN	66	0.453061	1.56129	0.000349	0.039623	0.039038
GSE24634_TREG_VS_TCONV_PO	44	0.488957	1.613248	0.000385	0.041836	0.041218

ST_DAY10_IL4_CONVERSION_UP						
GSE14415_INDUCED_TREG_VS_TCONV_UP	62	0.462174	1.580504	0.000381	0.041836	0.041218
GSE33292_WT_VS_TCF1_KO_DN3_THYMOCYTE_DN	65	0.454679	1.563755	0.000385	0.041836	0.041218
GSE18893_TCONV_VS_TREG_24H_TNF_STIM_UP	44	0.488755	1.612582	0.000399	0.042083	0.041462
GO_REGULATION_OF_CELL_CYCLE	159	0.382338	1.384737	0.000394	0.042083	0.041462
GSE28726_NAIVE_CD4_TCELL_VS_NAIVE_VA24NEG_NKTCELL_UP	69	0.451791	1.56315	0.000417	0.043387	0.042747
GO_MICROTUBULE_CYTOSKELETON_ORGANIZATION	81	0.42554	1.484567	0.000463	0.04746	0.04676
GSE24026_PD1_LIGATION_VS_CTRL_IN_ACT_TCELL_LINE_DN	26	0.556951	1.718091	0.000493	0.048821	0.048101
GO_CONDENSED_CHROMOSOME	42	0.506635	1.66381	0.000499	0.048821	0.048101
GSE22886_UNSTIM_VS_IL15_STIM_NKCELL_DN	47	0.483835	1.610542	0.000509	0.048821	0.048101
REACTOME_CELL_CYCLE_CHECKPOINTS	45	0.485034	1.605811	0.000508	0.048821	0.048101
GSE21063_CTRL_VS_ANTI_IGM_S	54	0.469437	1.584499	0.000508	0.048821	0.048101

TIM_BCELL_16H_UP						

Table 5-1 GSEA analysis of dendritic cells in KPL treated tumors. Gene set enrichment analysis (GSEA) statistics of pathways that significantly upregulated or downregulated on dendritic cells in BGB324 and BGB324 + anti-PD-1 group comparing to control and anti-PD-1 group.

In summary, Axl inhibition in $CD103^{+}$ dendritic cells served as the key population in expanding $TCF1^{+}$ $PD\text{-}1^{+}$ $CD8^{+}$ T cells in KPL tumors and therefore sensitizing them to anti-PD-1 therapy. Although macrophages showed accumulated higher Axl expression, the depletion of macrophages delayed the therapeutic responses of KPL tumors, and eventually could be overcame in TME. Single cell RNA sequencing analysis further support the hypothesis. Inhibition of Axl in dendritic cell populations shifted the dendritic cell dynamics and distributions in TME, and the cross-priming DCs were enriched in BGB324 treated tumors. As cross-priming DCs had been known for its critical role in prime tumor associated CD8 T cells and the homing signal was not inhibited, this could be crucial for therapeutic responses. Ideally, conditional knock-out Axl in DCs mice could further validated the hypothesis.

CHAPTER SIX:
Bemcentinib Mediated Axl Inhibition Induced Type I Interferon Secretion Expands TCF1^{+}PD-1^{+}CD8^{+} T Cells

6.1 Direct Effect of Bemcentinib Mediated Axl Inhibition on CD8 T Cell Status

Before proceeding to study how bemcentinib regulate dendritic cell status to further induce TCF1^{+}PD-1^{+}CD8 T cells in KPL tumors, the direct effect of bemcentinib on CD8 T cells were analyzed. To further confirm the potential observed effects were from Axl inhibition instead of off-target effects from the compound, two Axl inhibitor from different companies, BGB324 and TP0903, were used for experiments. Under the dose we were able to observe TCF1^{+}PD-1^{+}CD8 T cells induction *in vitro* when co-cultured with BMDCs (will be discussed in detailed later in this chapter), BGB324 and TP0903 didn't affect the proliferation and apoptosis of CD8 T cells directly (**Figures 6.1A-B**). Therefore, BGB324 and TP0903 mediated Axl inhibition are likely not affecting T cell status directly under therapeutic dose.

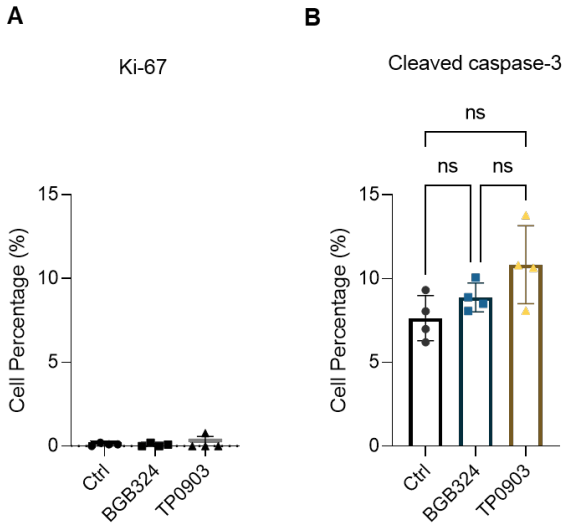

Figure 6.1 Axl inhibition does not affect T cell status directly.

(A) Proliferation of isolated OT1 CD8 T cells treated with BGB324 or TP0903 for 24h and subject to flow cytometry analysis.

(B) Apoptosis of isolated OT1 CD8 T cells treated with BGB324 or TP0903 for 24h and subject to flow cytometry analysis.

We then tried a series of different doses of BGB324 and TP0903 to test their potential on-target and off-target effects on CD8 T cells. For all the doses tested, there was no influences on CD8 T cell proliferations when treating with BGB324 (**Figure 6.2A**). Similar effect was observed when treating CD8 T cells with TP0903, suggesting Axl inhibition does not affect CD8 T cell proliferation directly (**Figure 6.2C**). When treating CD8 T cells with higher dose of BGB324, it may induce more of CD8 T cell apoptosis (**Figure 6.2B**). The induction of CD8 T cell apoptosis was more significant when treated with same dose of TP0903, suggesting a potential higher toxicity of TP0903 likely coming from off-target effect, as they were not strictly

dose-dependent (**Figure 6.2D**). It is still possible, though, the apoptosis may relate to Axl inhibition as well. However, as we don't have an effective way to detect Axl expression at protein level, it remains inconclusive for our observations.

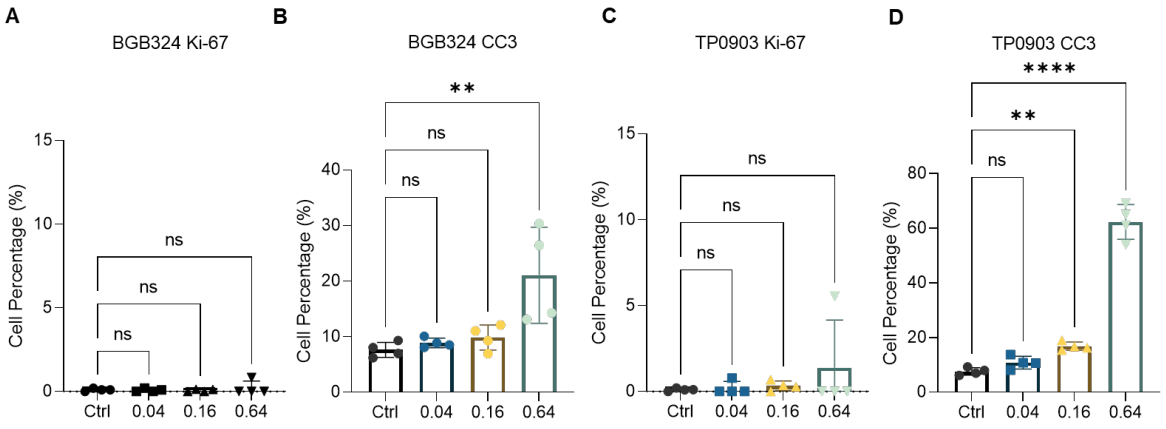

Figure 6.2 Dose responses to direct Axl inhibition in T cells.

(A) Proliferation of isolated OT1 CD8 T cells treated with various doses of BGB324 for 24h and subject to flow cytometry analysis.

(B) Apoptosis of isolated OT1 CD8 T cells treated with various doses of BGB324 for 24h and subject to flow cytometry analysis.

© Proliferation of isolated OT1 CD8 T cells treated with various doses of TP0903 for 24h and subject to flow cytometry analysis.

(D) Apoptosis of isolated OT1 CD8 T cells treated with various doses of TP0903 for 24h and subject to flow cytometry analysis.

At the therapeutic effect dose, BGB324 and TP0903 mediated Axl inhibition do not affect TCF1 expression in CD8 T cells directly (**Figure 6.3A**). However, similar to the toxicity effect observed directly by staining CD8 T cells with cleaved caspase-3, a

higher dose of BGB324 will eventually reduce TCF1 expressing CD8 T cell abundance significantly, possibly due to the apoptosis induced by the treatment (**Figure 6.2B**). Treating OT-1 CD8 T cells with TP0903 showed a larger impact of TCF1 expression in CD8 T cells, likely due to the off-target effect as well (**Figure 6.2C**).

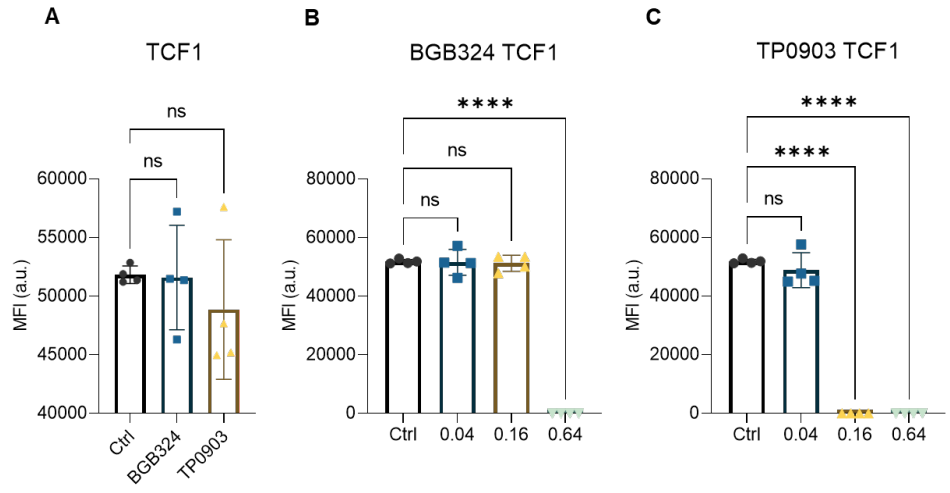

Figure 6.3 Direct effect of Axl inhibition in TCF1 expression in CD8 T cells.

(A) Mean fluorescent intensity (MFI) for TCF1 in $CD8^+$ OT-1 cells treated with vehicle (ctrl), BGB324 or TP0903.

(B) MFI for TCF1 in $CD8^+$ OT-1 cells treated with various doses of BGB324.

(C) MFI for TCF1 in $CD8^+$ OT-1 cells treated with various doses of TP0903.

Therefore, either the Axl inhibition, or BGB324 treatment, are unlikely to induce T cell proliferation or apoptosis status. However, the dose of BGB324 may need further optimization to avoid potential toxicity to CD8 T cells in KPL tumors.

We then explored whether BGB324 or Axl inhibition would affect CD8 T cells functionality by CBA assay. OT-1 CD8 T cells were isolated from spleen and directly activated by CD3/CD28 activation. Two different concentrations of CD3/CD28 were used to compare the effect on differential activated CD8 T cells. Although BGB324 treatment didn't affect CD8 T cell proliferation or apoptosis directly, differences in Th1/Th2/Th17 responses cytokines secreted were observed. When stimulated CD8 T cell with higher activation signal, a slight reduction of IL-10 was observed (**Figure 6.4A**). There was a global reduction of IL-17A, TNFα, and IFNγ secretion when stimulated with low dose of CD3/CD28. This effect was largely counteracted if stimulated with higher amount of CD3/CD28 (**Figures 6.4B-D**). On the contrary, the differences were further magnified for IL-6 and IL-4 secretion from CD8 T cells stimulated with high CD3/CD28 (**Figures 6.4E-F**). There was no significant difference in IL-2 secretion when treated with BGB324 (**Figure 6.4G**). However, these differences don't coordinate with *in vivo* therapeutic effects, and Axl expression hadn't been reported in CD8 T cells. Therefore, we didn't do following up experiments to identify the underlying mechanisms.

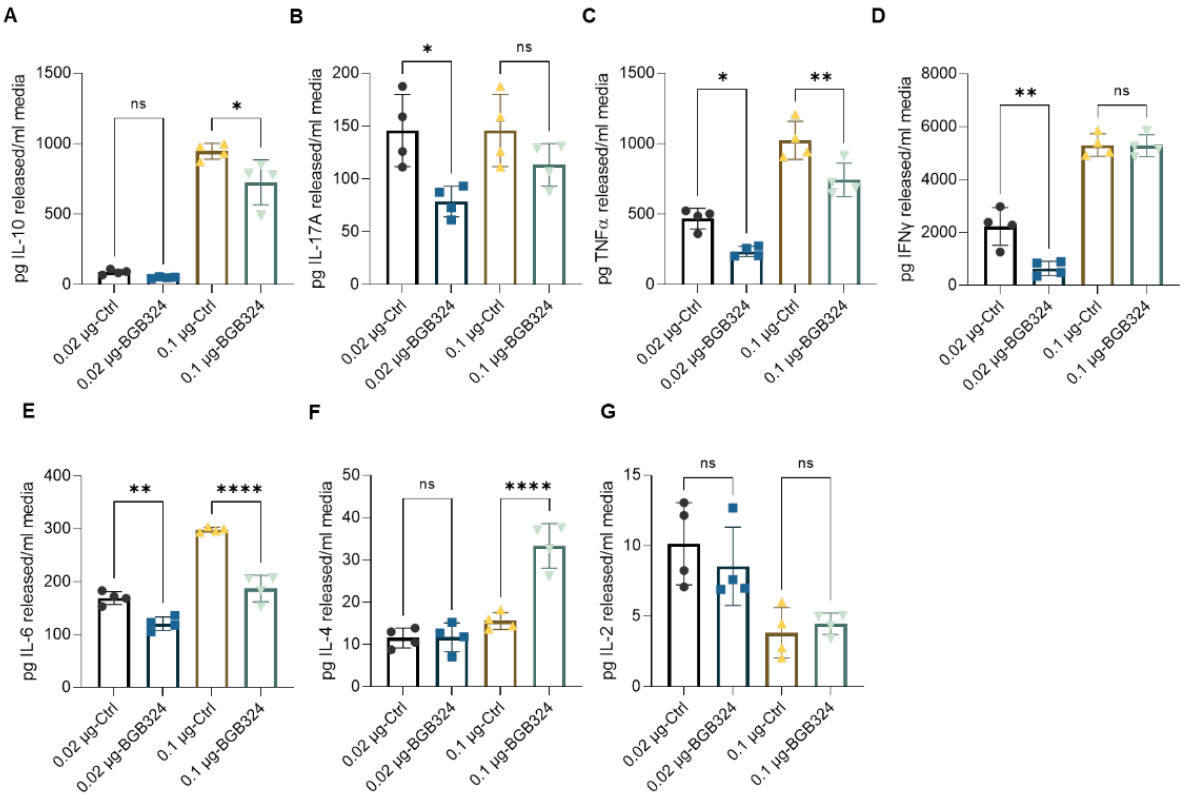

Figure 6.4 Cytokines secreted from activated T cells *in vitro*.

(A) IL-10 secreted from CD8 T cells isolated and activated with CD3/CD28 (0.02 μg or 1 μg), w/ or w/o BGB324 (40 nM) for 24h. Conditioned media was collected for CBA assay.

(B) IL-17A secreted from CD8 T cells isolated and activated with CD3/CD28 (0.02 μg or 1 μg), w/ or w/o BGB324 (40 nM) for 24h. Conditioned media was collected for CBA assay.

(C) TNFα secreted from CD8 T cells isolated and activated with CD3/CD28 (0.02 μg or 1 μg), w/ or w/o BGB324 (40 nM) for 24h. Conditioned media was collected for CBA assay.

(D) IFNγ secreted from CD8 T cells isolated and activated with CD3/CD28 (0.02 μg or 1 μg), w/ or w/o BGB324 (40 nM) for 24h. Conditioned media was collected for CBA assay.

(E) IL-6 secreted from CD8 T cells isolated and activated with CD3/CD28 (0.02 μg or 1 μg), w/ or w/o BGB324 (40 nM) for 24h. Conditioned media was collected for CBA assay.

(F) IL-4 secreted from CD8 T cells isolated and activated with CD3/CD28 (0.02 μg or 1 μg), w/ or w/o BGB324 (40 nM) for 24h. Conditioned media was collected for CBA assay.

(G) IL-2 secreted from CD8 T cells isolated and activated with CD3/CD28 (0.02 μg or 1 μg), w/ or w/o BGB324 (40 nM) for 24h. Conditioned media was collected for CBA assay.

Overall, BGB324 mediated on-target or off-target effect have limited effect to CD8 T cell status directly. The therapeutic effects observed from KPL tumors receiving BGB324 + anti-PD-1 were likely indirect and from dendritic cell mediated changes.

6.2 Axl Inhibition Induced Type I Interferon Secretion Expands TCF1 CD8 T Cells

As inhibition of Axl in DCs is sufficient to sensitize KPL tumors to anti-PD-1 treatment, we then investigated whether $TCF1^{+}PD\text{-}1^{+}$CD8 T cells are regulated by the Axl – IFNAR pathway (W. Li et al., 2020; Rothlin et al., 2007). Bone marrow derived dendritic cells (BMDCs) were co-cultured with dying KPL tumor cells and treated with BGB324 or DMSO (Han et al., 2020). BMDCs treated with BGB324 showed increased secretion of IFNβ (**Figure 6.5A**). Increased secretion of IFNβ was also observed through co-culturing *Axl*-deficient BMDCs with dying tumor cells, Thp-

1 derived human dendritic cells co-cultured with dying A549 tumor cells, as well as in KPL tumor lysates from tumors treated with BGB324 (**Figures 6.5B-D**). However, BGB324 treated BMDCs were unable to further increase their IFNβ secretion when co-cultured with dying KP cells, indicating a potential increased Axl activity in BMDCs co-cultured with KPL cells (**Figure 6.5E**). Due to the lack of working antibody for detecting Axl expression and activity in dendritic cells or tumor lysates, potential increased Axl activities in dendritic cells surrounding by KPL tumor cells cannot be further testified.

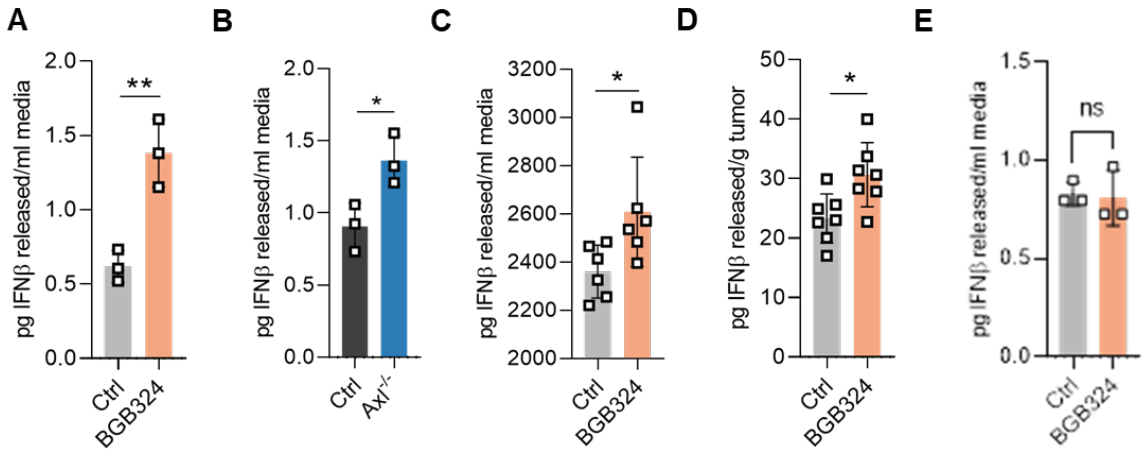

Figure 6.5 Axl inhibition induced IFNβ secretion from co-cultured DCs or tumor lysates.

(A) BMDCs were co-cultured with irradiated KPL cells (40 gy) and treated with BGB324 (40 nM) for 24h. Conditioned media was collected for IFNβ ELISA.

(B) Wild type and $Axl^{-/-}$ BMDCs were co-cultured with irradiated KPL tumor cells (40g) for 24h. Cell conditioned media was collected for IFNβ ELISA.

(C) Thp1 derived DCs were co-cultured with irradiated A549 tumor cells (40gy) for 24h. Cell conditioned media was collected for IFNβ ELISA.

(D) IFNβ ELISA in KPL tumor lysates. 1 x 10^6 of KPL cells were injected into C57BL/6J mice (n = 7). Mice were treated with vehicle (Ctrl) or BGB324 treatment (50 mg/kg, BID) starting on day 7 post tumor cell injection. Tumors were harvested for analysis on day 14 post tumor cell injection.

(E) BMDCs were co-cultured with irradiated KP cells (40 gy) and treated with BGB324 (40 nM) for 24h. Conditioned media was collected for IFNβ ELISA.

As the differences we observed from ELISA were modest, we extracted RNA from tumor lysates to analysis interferon related gene expression at mRNA level. However, significant increased secretion for either IFNα or IFNβ were failed to be observed in KPL tumors treated with BGB324 (**Figures 6.6A-B**). Type I interferon induced expression of MX2, QUSP or CXCL10 didn't show statistical differences as well, although there was a trend of reduction for MX2 expression or increased expression of CXCL10 (**Figures 6.6C-E**). Type I interferon changes fast in respond to stimulus within couple of hours or even minutes, and their abundance is quite low, despite their significant effect in regulating immune responses. All these may result in missing right time points for analysis with type I interferon expression and secretion. In our later experiments will be discussed later in this chapter, indicates that the key for inducing TCF1$^+$PD-1$^+$CD8 T cells abundance in TME is the slight induction, instead of huge increased, of type I interferon secretion.

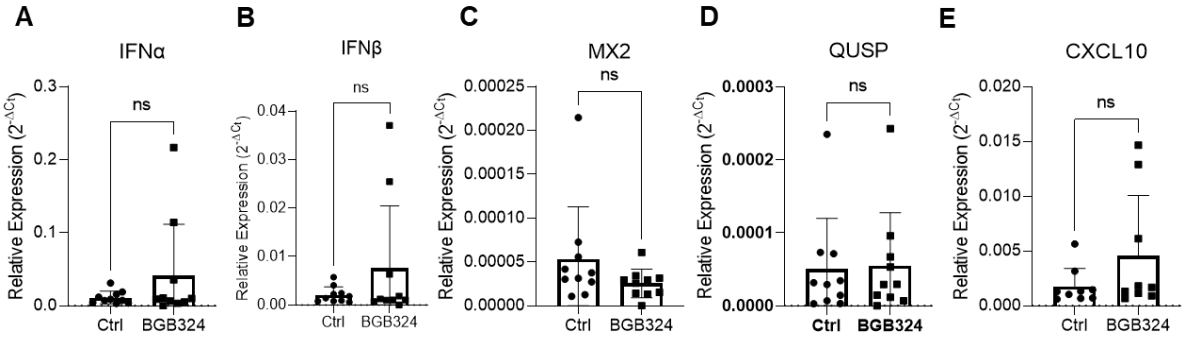

Figure 6.6 mRNA level expression of interferon and interferon induced genes in tumor lysates.

(A) IFNα mRNA expression in KPL tumors. C57BL/6J mice (n = 10) were injected with 1 x 10^6 KPL tumor cells. Mice were treated with BGB324 (50 mg/kg, twice daily) or vehicle (Ctrl) starting on day 7 post tumor cell injection for 7 days.

(B) IFNβ mRNA expression in KPL tumors. Experimental schema is same as (A).

(C) MX2 mRNA expression in KPL tumors. Experimental schema is same as (A).

(D) QUSP mRNA expression in KPL tumors. Experimental schema is same as (A).

(E) CXCL10 mRNA expression in KPL tumors. Experimental schema is same as (A).

To determine the contribution of type I interferon secretion to BGB324 sensitization of KPL tumors to anti-PD-1 treatment, we inhibited the IFNα receptor pharmacologically. Blocking IFNα receptor intratumorally diminished response to combined Axl and PD-1 inhibition (**Figure 6.7A**) and reduced the infiltration of total or proliferating TCF1$^+$PD-1$^+$CD8 T cells in the TME (**Figures 6.7B-D**). Therefore, increased type I interferon secretion in KPL tumors is essential for inducing TCF1$^+$PD-1$^+$CD8 T cells in TME.

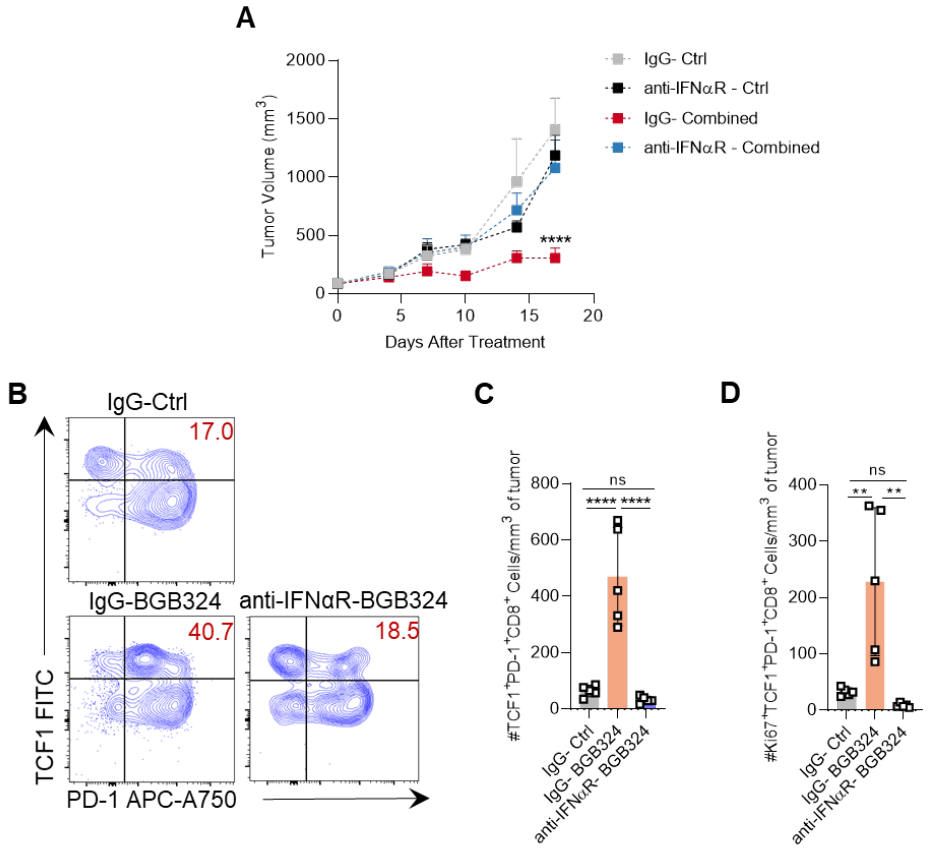

Figure 6.7 Bemcentinib induced type I interferon secretion is required for TCF1+PD-1+ CD8 T cell expansion *in vivo*.

(A) C57BL/6J mice (n = 5) were injected with 1 x 10^6 KPL tumor cells were treated with a control IgG (IgG) or interferon alpha receptor blocking antibody (anti-IFNαR, see Methods). Mice were treated with BGB324 (50 mg/kg, twice daily) and anti-PD-1 (10 mg/kg, day 7, 10, 14) (combined), or corresponding IgG and vehicle (Ctrl) starting on day 7 post tumor cell injection. Tumor volume was measured every 3 days.

(B) Representative $TCF1^+PD\text{-}1^+$ cell percentages among gated $CD8^+$ TILs at day 7 post therapy initiation.

(C) Abundance of $TCF1^+PD\text{-}1^+$ cells among gated $CD8^+$ TILs (per mm^3 of tumor) at day 7 post therapy initiation. Experimental schema is same as (A).

(D) Abundance of proliferating $TCF1^+PD\text{-}1^+$ cells among gated $CD8^+$ TILs (per mm^3 of tumor) at day 7 post therapy initiation. Experimental schema is same as (A).

To further study whether type I interferon receptor on T cells are the key mediator for therapeutic responses of BGB324 + anti-PD-1, we adoptively transferred CD8 T cells isolated from either *wild-type* or *Ifnαr1*$^{-/-}$ donor mice to *Rag1*$^{-/-}$ recipient mice. After 7 days post-reconstitution, recipient mice were able to recover their T cell abundances to normal percentage (15-25%) in peripheral blood at a similar abundance (**Figure 6.8A**). When T cells in mice lack IFNα receptor, they failed to control KPL tumor growth under combination therapy (**Figure 6.8B**). We also attempted to study the therapeutic effects in *Cd11c*^{Cre} *Ifnαr*1$^{fl/fl}$ mice, to determine whether increased type I interferon secretion will also regulate dendritic cells activity to affect combination therapy effects in KPL tumors. Unfortunately, *Cd11c*^{Cre} mice turned out to be leaky and resulted in a universal knockout of IFNα receptor in major immune populations, especially CD11c^{+} CD8^{+} T cells. In the future, zDC^{Cre} mice should be utilized as they are more specific to dendritic cell depletion. Overall, our current data suggests that type I interferon receptor on T cells are essential for mediating therapeutic effects, which further indicates that it may affect the TCF1^{+}PD-1^{+}CD8 T cells in TME.

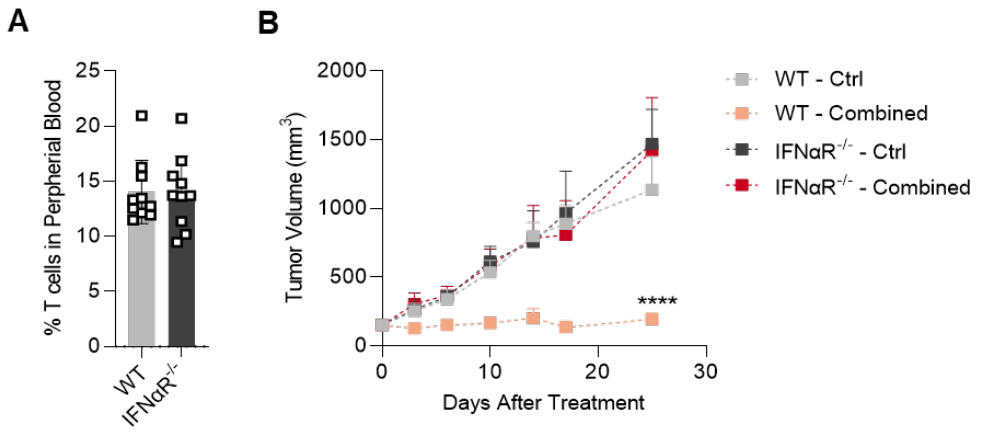

Figure 6.8 Type I interferon receptor on CD8 T cells is essential for therapeutic effects.

(A) *Wild-type* or *Ifnar1*$^{-/-}$ CD8 T cell percentage reconstituted in *Rag1*$^{-/-}$ mice 7 days post transfer.

(B) T cell transferred *Rag1*$^{-/-}$ mice (n = 5) were injected with 1 x 10^6 KPL tumor cells. Mice were treated with BGB324 (50 mg/kg, twice daily) and anti-PD-1 (10 mg/kg, day 7, 10, 14) (combined), or corresponding IgG and vehicle (Ctrl) starting on day 7 post tumor cell injection. Tumor volume was measured every 3 days.

We then utilized *in vitro* co-culture system with only dendritic cells and CD8 T cells involved to further test our hypothesis. As freshly isolated CD8 T cells from spleen have nearly 100% expression of TCF1 which will be decreasing gradually after isolation, the ability of maintaining TCF1 expression on these CD8 T cells were studied. Blocking the IFNα receptor counteracted BGB324 maintained TCF1 expression on CD8 T cells isolated from spleen in co-cultures of BMDCs with OT-1 CD8 T cells stimulated by OVA (see Methods). This suggests that increased TCF1 expression on CD8 T cells by BGB324 treatment is dependent on the Type I interferon-IFNαR axis (**Figures 6.9A-B**). These results were recapitulated using *Axl*

KO BMDCs, indicating the effect we observed with BGB324 treated BMDCs were from Axl inhibition (**Figures 6.9C-D**).

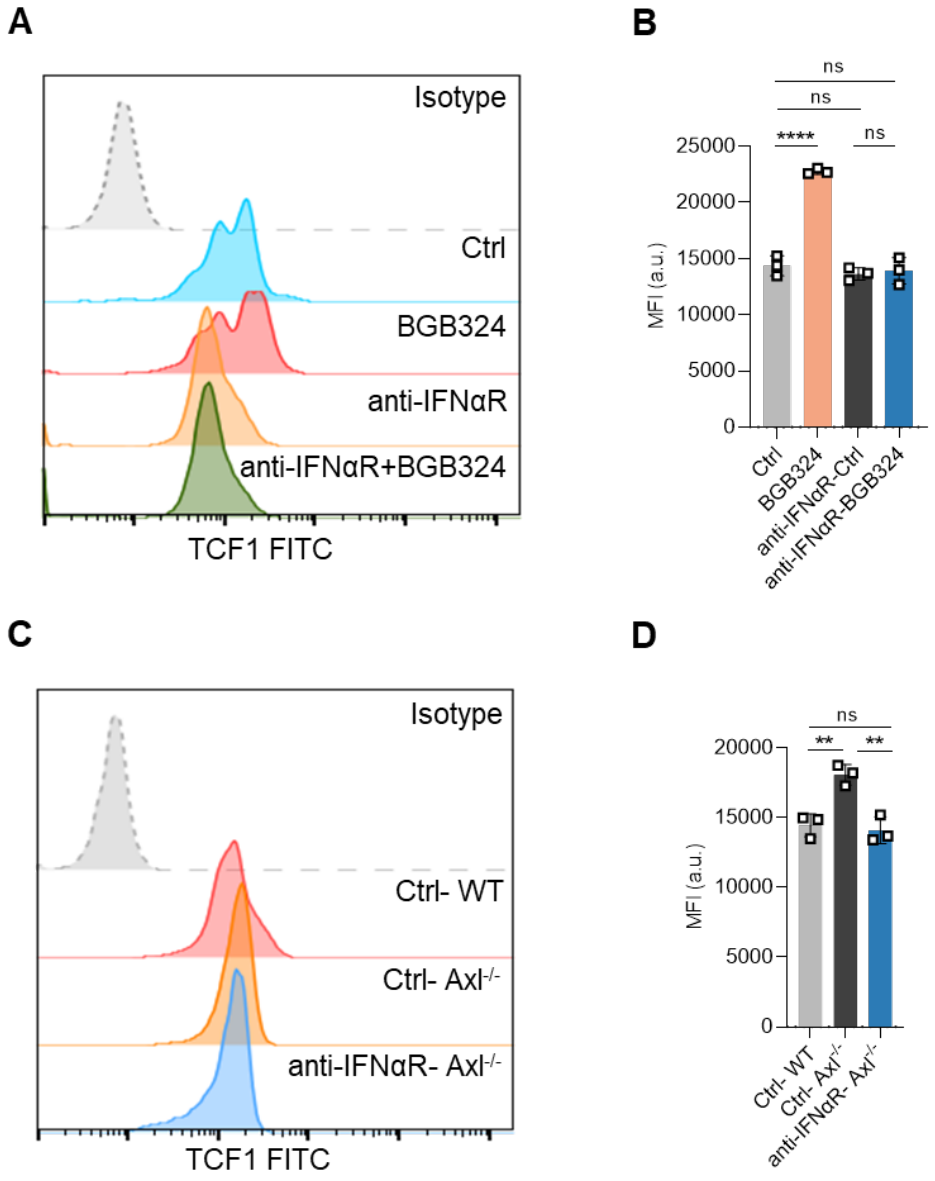

Figure 6.9 Axl inhibition induced type I interferon secretion maintains TCF1 expression of CD8 cell expansion *in vitro*.

(A) Representative MFIs of TCF1$^+$ cells among gated CD8$^+$ OT-1 cells.

(B) MFI for TCF1 in CD8$^+$ OT-1 cells. BMDCs were co-cultured with isolated CD8$^+$ T cells stimulated with ovalbumin (see Methods). Each dot represents one biological replicate.

(C) Representative MFI of TCF1$^+$ cells among gated CD8$^+$ OT-1 cells co-cultured with *wild-type* or *Axl*$^{-/-}$ BMDCs.

(D) MFI of TCF1 in CD8$^+$ OT-1 cells. Wild type BMDCs or *Axl*$^{-/-}$ BMDCs were co-cultured with isolated CD8$^+$ T cells stimulated with ovalbumin for 48h, respectively. IFNα receptor blocking strategy is same as (E).

BMDCs were then stimulated with recombinant IFNα and co-cultured with CD8 OT-1 T cells, where a higher maintain of TCF1 expression on CD8 T cell was observed *in vitro* (**Figures 6.10A-B**). This effect further confirmed that BGB324 mediated Axl inhibition could stimulate type I interferon secretion, which leads to increased abundance of TCF1$^+$ PD-1$^+$ CD8$^+$ T cells. The effect of type I interferon on inducing TCF1$^+$ PD-1$^+$ CD8$^+$ T cells was further tested by delivering recombinant IFNα intratumorally *in vivo*. Interestingly, as normal dose for our in house made IFNα to induce T cell activation and anti-tumor responses is 5 μg, it diminished the effect of inducing TCF1$^+$ PD-1$^+$ CD8$^+$ T cells in KPL tumors. When delivered IFNα intratumorally as low as 200 ng, a significant induction of TCF1$^+$ PD-1$^+$ CD8$^+$ T cells in KPL tumors could be seen (**Figures 6.10C-D**). When the dose increased to 1 μg, a discrepancy of effect occurred as some tumors had increased abundance of TCF1$^+$ PD-1$^+$ CD8$^+$ T cells, and the TCF1$^+$ PD-1$^+$ CD8$^+$ T cells in other tumors were gone (**Figure 6.10D**). These results actually confirmed our ELISA experiments, as the modest increased secretion of type I interferon is the key to induce TCF1$^+$ PD-1$^+$

$CD8^+$ T cells in KPL tumors. A stronger induction of type I interferon secretion may push the $TCF1^+$ $PD\text{-}1^+$ $CD8^+$ T cells pass the stem like T cell stage directly into effector T cells and lost their stemness (Siddiqui, Schaeuble, Chennupati, Marraco, et al., 2019), or they potentially induced the apoptosis of $TCF1^+$ $PD\text{-}1^+$ $CD8^+$ T cells. Either possibility needs to be further testified experimentally, which actually may have a huge impact, as the origins of $TCF1^+$ $PD\text{-}1^+$ $CD8^+$ T cells remain largely unknown.

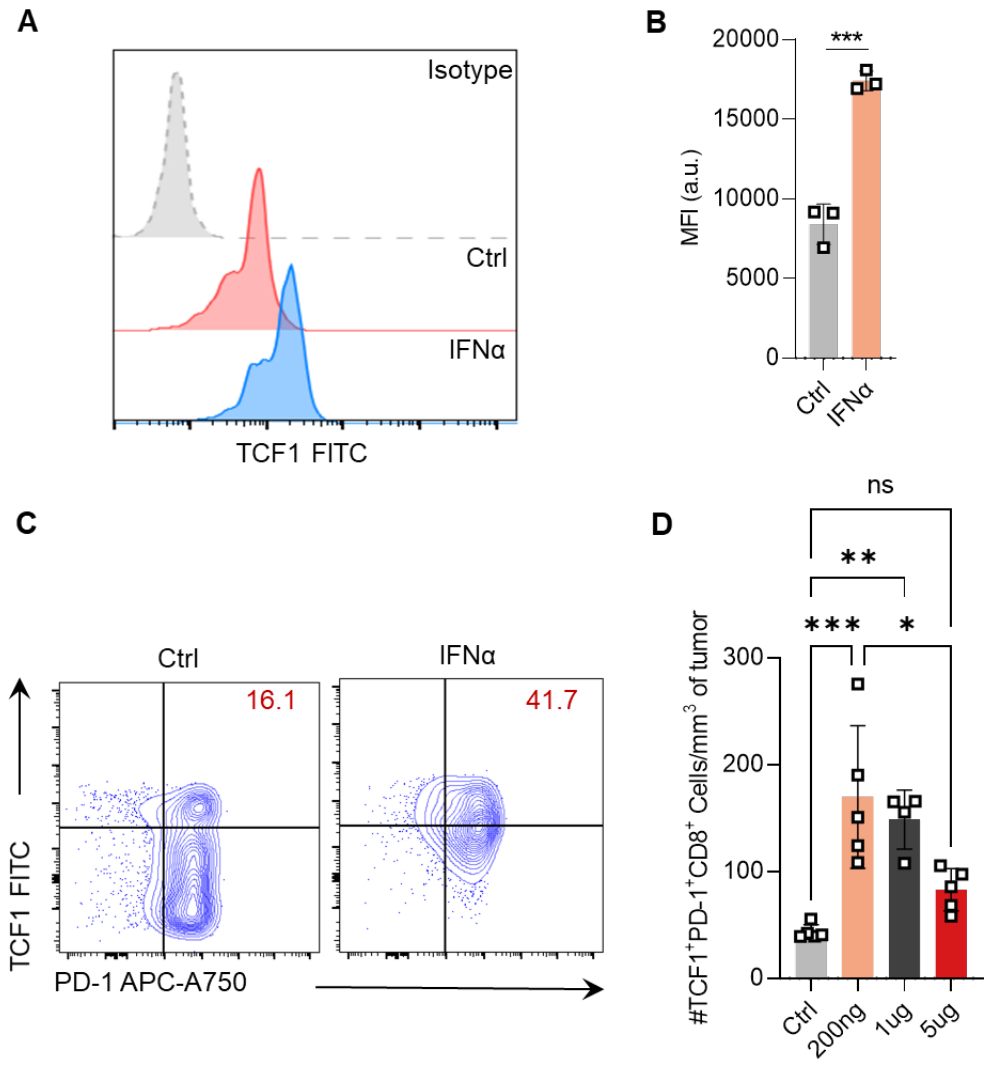

Figure 6.10 Modest increased type I interferon secretion stimulates TCF1 expressing CD8 T cells both *in vitro* and *in vivo*.

(A) Representative MFIs visualization for gated $CD8^+$ OT-1 cells co-cultured with BMDCs.

(B) MFI of $TCF1^+$ in $CD8^+$ OT-1 cells. BMDCs were co-cultured with isolated $CD8^+$ T cells stimulated with ovalbumin w/ or w/o IFNα (0.5 ng/ml) for 48h.

(C) Representative $TCF1^+PD\text{-}1^+$ cell percentages among gated $CD8^+$ TILs at 48h after intratumoral injection of IgG (Ctrl) or IFNα (200 ng).

(D) Abundance of $TCF1^+PD\text{-}1^+$ cells in gated $CD8^+$ TILs (per mm^3 of tumor) 48h post intratumoral injection of vehicle (Ctrl) or IFNα (200 ng, 1 μg or 5 μg).

Cytometric Bead Array (CBA) was also used to systematically evaluated Th1/Th2/Th17 immune responses key cytokines dynamics induced by treatment. A slight decrease of TNFα was observed when treating BMDCs co-cultured with OT-1 CD8 T cells with BGB324, and the difference was counteracted when blocking type I interferon receptor (**Figure 6.11A**). This may be caused by increased $TCF1^+$ CD8 T cell abundance, which wasn't being activated as effector T cells. When blocking type I interferon receptor, a further reduction of $TCF1^+$ CD8 T cell abundance and lack of T cell activation signal may further reduce the TNFα secretion. At the same time, BGB324 treatment or type I interferon receptor blocking did not significantly affect IFNγ, IL-10, IL-17A, or IL-4 secretion (**Figures 6.11B-D; Figure 6.11F**). A significant reduction of IL-6 were observed when treating BMDCs co-cultured with OT-1 CD8 T cells with BGB324, which had been reported to be effective to control KPL tumor progression (Koyama et al., 2016b). Furthermore, the reduction of IL-6 induced by BGB324 didn't diminish when blocking type I interferon receptor, indicating it's more likely to be a result from dendritic cell status changes but not directly related to therapeutic effects (**Figure 6.11E**). Although between there was no significant differences between control group or BGB324 treated group for IL-2 production, with or without type I interferon receptor blockage, a similar trend of overall decreased production of IL-2 to TNFα was observed (**Figure 6.11G**). These results may offer directions for more detailed T cell function and status study in the future.

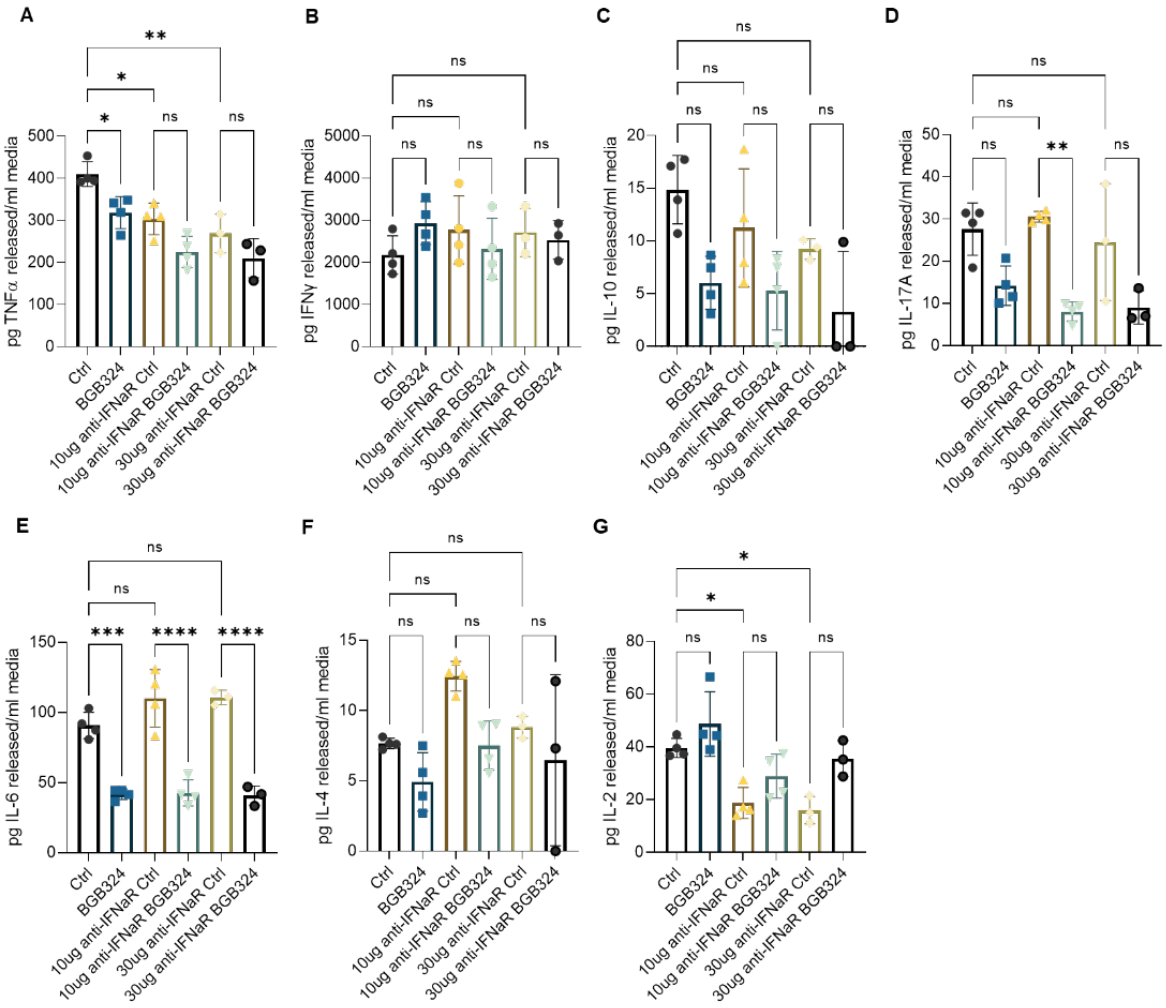

Figure 6.11 Cytokines secreted from T cells co-cultured with BMDCs *in vitro*.

(A) IL-10 secreted from CD8 T cells co-cultured with BMDCs, w/ or w/o BGB324 (40 nM) and/or anti-IFNαR treatment for 24h. Conditioned media was collected for CBA assay.

(B) IL-17A secreted from CD8 T cells co-cultured with BMDCs, w/ or w/o BGB324 (40 nM) and/or anti-IFNαR treatment for 24h. Conditioned media was collected for CBA assay.

(C) TNFα secreted from CD8 T cells co-cultured with BMDCs, w/ or w/o BGB324 (40 nM) and/or anti-IFNαR treatment for 24h. Conditioned media was collected for CBA assay.

(D) IFNγ secreted from CD8 T cells co-cultured with BMDCs, w/ or w/o BGB324 (40 nM) and/or anti-IFNαR treatment for 24h. Conditioned media was collected for CBA assay.

(E) IL-6 secreted from CD8 T cells co-cultured with BMDCs, w/ or w/o BGB324 (40 nM) and/or anti-IFNαR treatment for 24h. Conditioned media was collected for CBA assay.

(F) IL-4 secreted from CD8 T cells co-cultured with BMDCs, w/ or w/o BGB324 (40 nM) and/or anti-IFNαR treatment for 24h. Conditioned media was collected for CBA assay.

(G) IL-2 secreted from CD8 T cells co-cultured with BMDCs, w/ or w/o BGB324 (40 nM) and/or anti-IFNαR treatment for 24h. Conditioned media was collected for CBA assay.

Taken together, these results demonstrate that increased type I IFN secretion as a result of Axl inhibition is critical for inducing $TCF1^{+}PD\text{-}1^{+}$CD8 T cell expansion in KPL tumors and overcoming resistance to anti-PD-1 therapy.

6.3 Axl Inhibition Mediated Signaling Pathway Regulations in Immune Cells

In previous study published by Li et al., inhibiting Akt activity or activating TBK1 facilitates TCF1 expression in CD8 T cells (W. Li et al., 2020). Therefore, we explored phospho-Akt and phospho-TBK1 activity in OT-1 CD8 T cells co-cultured with BMDCs and stimulated with ovalbumin. By blocking type I interferon receptor in

co-culture system, expected decreased pTBK1 and increased pAKT1 were observed in CD8 T cells accompanied with decreased TCF1 expression (**Figures 6.12A, C**). However, significant changes in pAkt and pTBK1 were failed to be observed when co-culturing ovalbumin stimulated OT-1 CD8 T cells with $Axl^{-/-}$ BMDCs, despite a significant reduction of pTBK1 activity when blocking type I interferon receptor (**Figures 6.12B, D**). Due to the different response to ovalbumin stimulation from individual mouse, OT-1 CD8 T cells co-cultured with BMDCs treated with BGB324 undergone apoptosis due to strong activation signal and failed to analyze pAkt and pTBK1 activity. It is possible, though, that changing ovalbumin for stimulating $Axl^{-/-}$ BMDCs to higher dose might able to facilitate pAkt and pTBK1 differences. However, *in vivo* CD8 T cell signaling should be the gold standard for phenomenon as there was therapeutic effects were observed in KPL tumors undergone BGB324 + anti-PD-1 treatment.

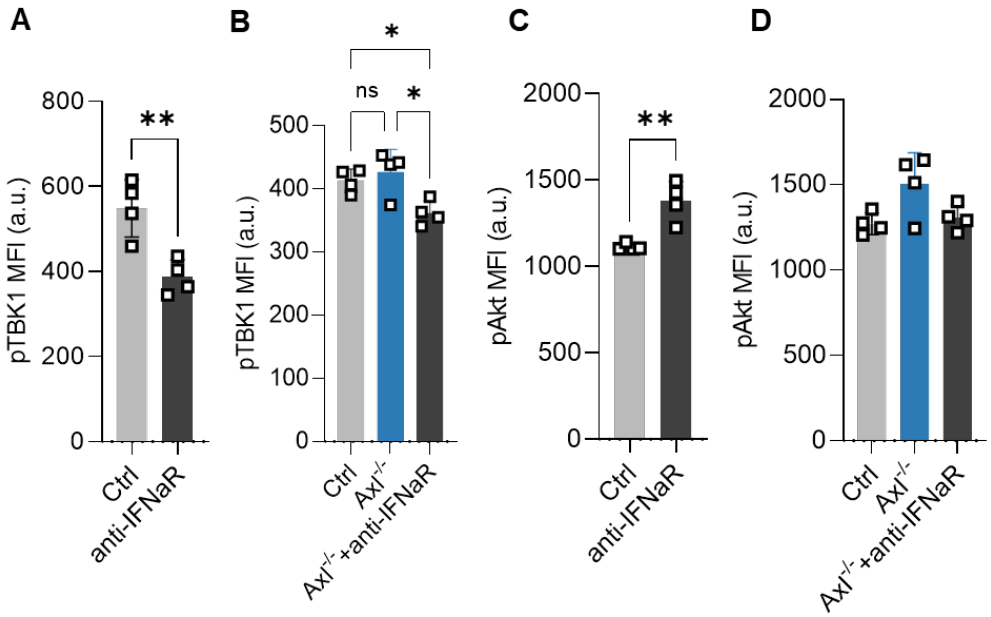

Figure 6.12 Activity of TBK1 and Akt in TCF1 CD8 T cells co-cultured with BMDCs.

(A) MFI of 188hosphor-TBK1in TCF1$^+$ PD-1$^+$ CD8$^+$ OT-1 cells. BMDCs were co-cultured with isolated CD8$^+$ T cells stimulated with ovalbumin for 48h.

(B) MFI of 188hosphor-TBK1in TCF1$^+$ PD-1$^+$ CD8$^+$ OT-1 cells. *Wild-type* or *Axl*$^{-/-}$ BMDCs were co-cultured with isolated CD8$^+$ T cells stimulated with ovalbumin for 48h.

© MFI of 188hosphor-Akt in TCF1$^+$ PD-1$^+$ CD8$^+$ OT-1 cells. BMDCs were co-cultured with isolated CD8$^+$ T cells stimulated with ovalbumin for 48h.

(D) MFI of 188hosphor-Akt in TCF1$^+$ PD-1$^+$ CD8$^+$ OT-1 cells. *Wild-type* or *Axl*$^{-/-}$ BMDCs were co-cultured with isolated CD8$^+$ T cells stimulated with ovalbumin for 48h.

We then explored which innate sensing pathway was involved in mediating therapeutic effects of BGB324 + anti-PD-1 in KPL tumors. While depleting TLR-Myd88 pathway didn't affect therapeutic responses of KPL tumors, paralyzing cGAS-STING pathway abrogated KPL tumor growth control (**Figures 6.13A-B**). Combining with previous findings, it's likely that dendritic cells defect in cGAS-STING pathway failed to induce TCF1$^+$PD-1$^+$CD8$^+$ T cells in KPL tumors, ultimately results in failed tumor growth control. To further confirm the hypothesis, combination treatment on KPL tumors need to be studied when implanting into zDC^{Cre}STING$^{fl/fl}$ mice.

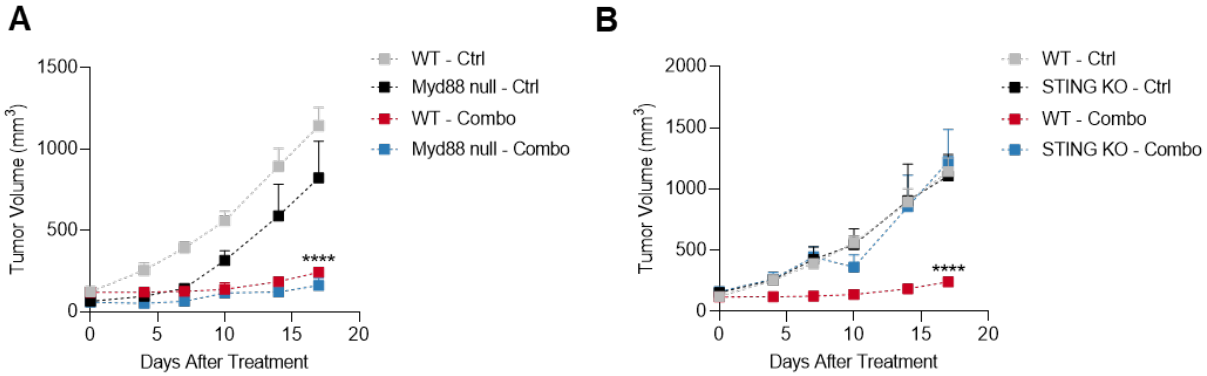

Figure 6.13 Bemcentinib activates immune response through cGAS-STING innate sensing pathway.

(A) *Wild type* or *Myd*88$^{-/-}$ mice (n = 5) were injected with 1 x 10^6 KPL tumor cells. Mice were treated with BGB324 (50 mg/kg, twice daily) and anti-PD-1 (10 mg/kg, day 7, 10, 14) or corresponding IgG and vehicle starting on day 7 after tumor cell injection. Tumor growth was measured every 3 days.

(B) *Wild type* or *STING*$^{-/-}$ mice (n = 5) were injected with 1 x 10^6 KPL tumor cells. Mice were treated with BGB324 (50 mg/kg, twice daily) and anti-PD-1 (10 mg/kg, day 7, 10, 14) or corresponding IgG and vehicle starting on day 7 after tumor cell injection. Tumor growth was measured every 3 days.

Therefore, Axl inhibition may aid in cGAS-STING pathway activation in dendritic cells infiltrated into KPL tumors, while detailed signaling changes in TCF1$^+$PD-1$^+$CD8$^+$ T cells need further exploration.

CHAPTER SEVEN:
Bemcentinib Sensitizes Human *STK11/LKB1* Mutant NSCLC to Pembrolizumab in a Humanized Mouse Model

To investigate whether the therapeutic effects of combined AXL and PD-1 inhibition apply to human *KL* mutant NSCLCs, we studied two human LUAD *KL* mutated cell lines, A549 and H2122, in a humanized NSG-SGM3 mouse model.

Although these cell lines all harbor *KRAS* and *STK11/LKB1* mutations (**Figure 7.1A**), A549 express AXL while H2122 has limited AXL expression (**Figure 7.1B**). However, the *in vitro* IC_{50} of BGB324 for growth inhibition of A549 and H2122 tumor cells were similar (**Figure 7.1C**). Besides, the IC_{50} of BGB324 for these two cell lines were 25-fold higher than the dose applied to induce dendritic cell mediated T cell responses, it's more likely that dendritic cells were affected before tumor cells got affected *in vivo*.

A

Cell Lines	KRAS	STK11	p53
A549	G12S	Q37*	wild-type
H2122	G12C	P281fs	C176F

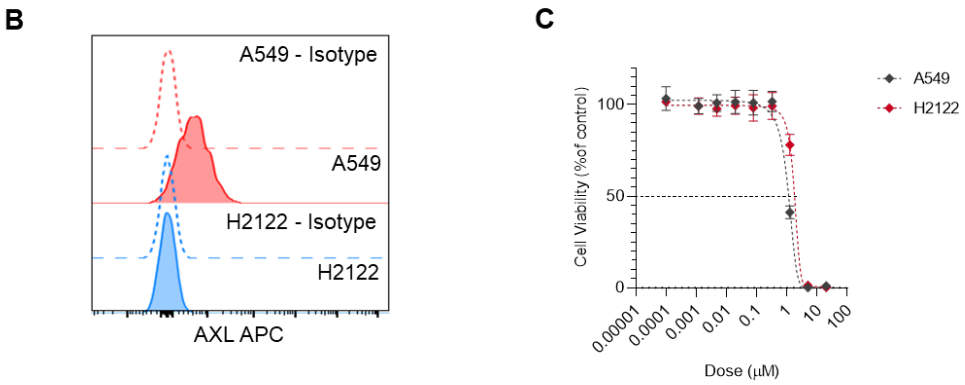

Figure 7.1 Characteristics of human NSCLC cell lines used for study.

(A) Key genetic mutations carried by A549 and H2122.

(B) Flow cytometric analysis of AXL expression in A549 and H2122 tumor cells *in vitro*. MFI is shown.

(C) Dose response curves of BGB324 on cell viability (IC_{50}) of A549 and H2122 cells.

Irradiated NSG-SGM3 mice (1 gy) were reconstituted with $CD34^+$ cells isolated from cord blood. After 12 weeks of transfer, we characterized the immune cell composition by staining immune cells isolated from peripheral blood. There was on average ~60% of total human immune cells detected, with ~40% among them were T cells (**Figures 7.2A-B**). Human dendritic cells and macrophages were also able to be detected in peripheral blood (**Figures 7.2C-D**). Therefore, our humanized NSG-

SGM3 mice had all key immune cell populations which may affected by our proposed BGB324 + anti-PD-1 treatment.

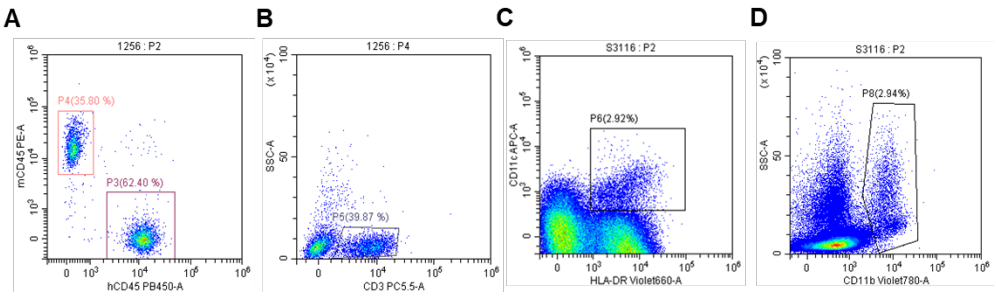

Figure 7.2 Major human immune cell abundances in humanized mice.

(A) Representative plot of human and mouse $CD45^+$ cell percentage after 12 weeks of reconstitution of humanized NSG-SGM3 mice.

(B) Representative plot of human $CD3^+$ cells percentage among gated human $CD45^+$ cells after 12 weeks of reconstitution in humanized NSG-SGM3 mice.

(C) Representative plot of human dendritic cells ($CD45^+CD11c^+HLA\text{-}DR^+$) percentage among gated human $CD45^+$ cells after 12 weeks of reconstitution in humanized NSG-SGM3 mice.

(D) Representative plot of human macrophages ($CD45^+CD11b^+$) percentage among gated human $CD45^+$ cells after 12 weeks of reconstitution in humanized NSG-SGM3 mice.

After human immune cells were reconstituted in humanized NSG-SGM3 mice, A549 or H2122 were injected subcutaneously onto the mice following described treatment schema (**Figure 7.3A**). When grown A549 or H2122 in humanized mice without any treatment, both xenograft models displayed human AXL expression as membrane expression or nuclear expression, indicating xenografts are suitable for BGB324 treatment to study their therapeutic effects (**Figure 7.3B**). Besides, dendritic cells and macrophages were able to infiltrate into A549 or H2122 xenografts implanted

onto humanized NSG-SGM3 mice (**Figures 7.3E-G**). Therefore, our proposed mechanism have targets available in these human NSCLC tumors.

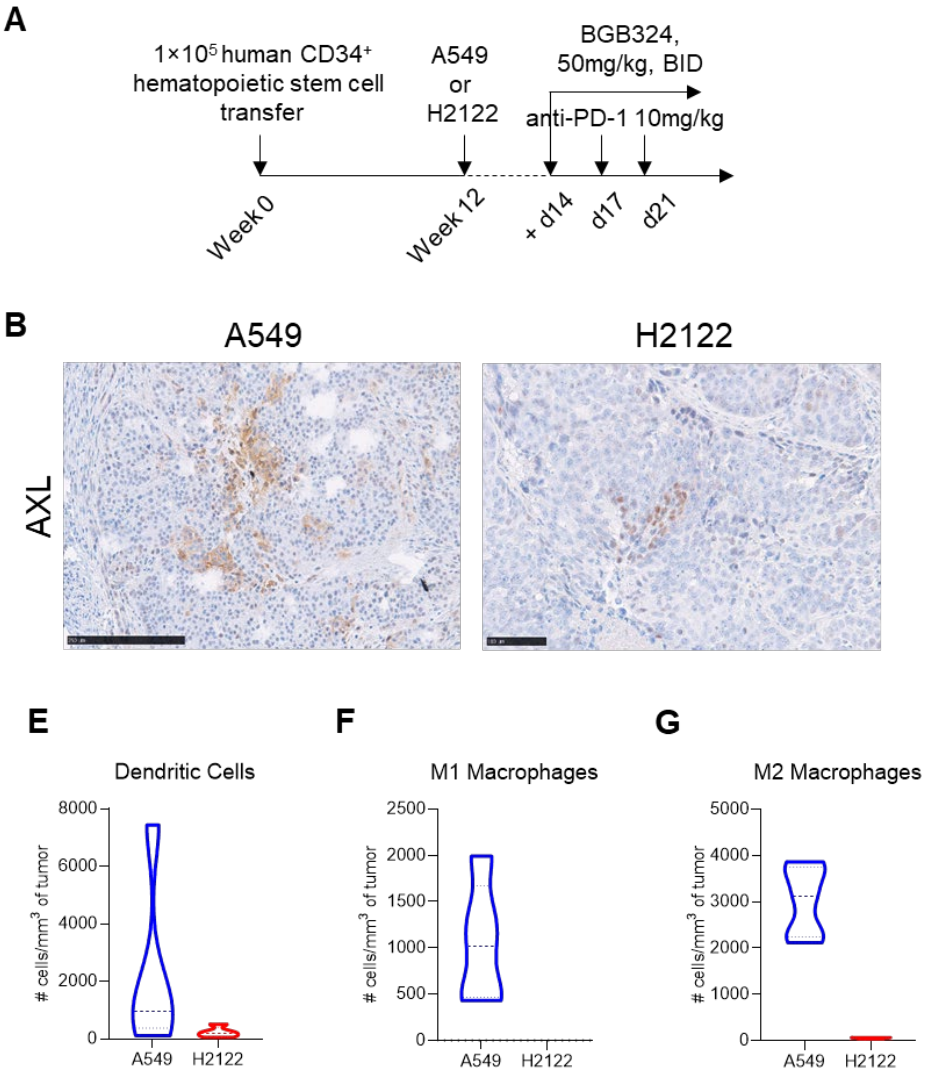

Figure 7.3 Experimental schema and characterization of tumor environment.

(A) Humanization and treatment strategy for tumor-bearing humanized mice.

(B) AXL immunohistochemistry in A549 and H2122 xenografts grown in humanized mice.

(E) Abundance of infiltrated dendritic cells (per mm^3 of tumor) on therapy initiation day.

(F) Abundance of infiltrated M1 macrophages (per mm^3 of tumor) on therapy initiation day.

(G) Abundance of infiltrated M2 macrophages (per mm^3 of tumor) on therapy initiation day.

Importantly, BGB324 sensitized A549 and H2122 tumors in humanized mice to pembrolizumab similar to the effect seen in mouse KPL syngeneic tumors in C57BL/6J mice (**Figures 7.4A-B**). Additionally, combination therapy resulted in a significant induction of human $TCF1^+PD\text{-}1^+CD8^+$ T cells in each *STK11/LKB1* mutant model (**Figure 7.4C-D**).

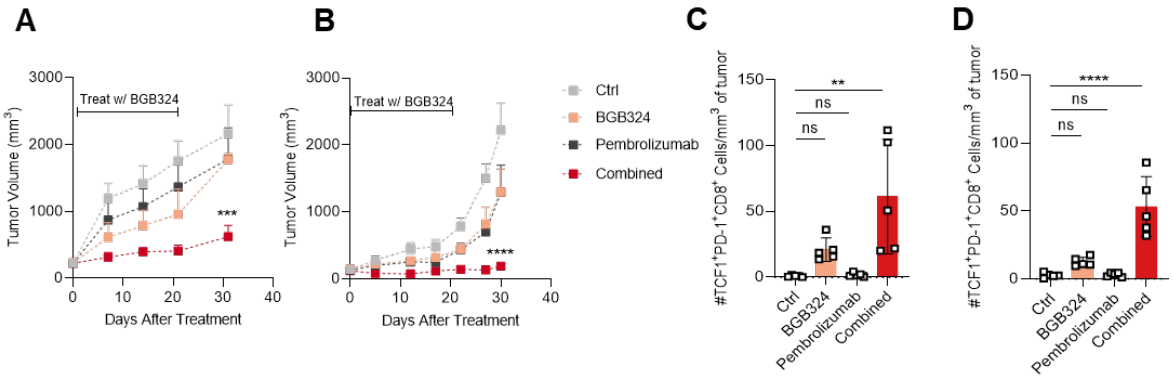

Figure 7.4 Therapeutic responses in A549 and H2122 xenografts.

(A) Humanized NSG-SGM3 mice were injected with 1.5 x 10^6 of A549 cells (n = 5, right flank) and treated with BGB324 (50 mg/kg, twice daily), pembrolizumab (10

mg/kg, day 7, 10, 14), or the combination. Control animals were treated with control IgG (10 mg/kg) and vehicle (Ctrl). Treatment was withdrawn after 20 days.

(B) Humanized NSG-SGM3 mice were injected with 1.5 x 10^6 of H2122 cells (n = 2 for control group and 3 for treatment group, bilateral). Treatment schema is the same as **Figure 7.3A**. Treatment was withdrawn after 20 days.

(C-D) Abundance of $TCF1^+PD\text{-}1^+$ cells among gated $CD8^+$ TILs (per mm^3 of tumor) on day 7 post therapy initiation in A549 (G) and H2122 (H) xenografts.

Therefore, BGB324 could sensitize patient derived *STK11/LKB1* mutant NSCLCs to anti-PD-1 treatment.

CHAPTER EIGHT:
Conclusions & Discussions

In this study, we systematically evaluated response to ICB therapy and the CD8 T cell status in preclinical murine and human models of *KL* mutant NSCLC. We found that mutation of *STK11/LKB1* in tumor cells results in reduced numbers of $TCF1^+PD\text{-}1^+CD8$ T cells in the TME, which prevents a productive response to anti-PD-1 therapy. We show that inhibition of Axl on DCs in *STK11/LKB1* mutant NSCLC tumors increases $TCF1^+PD\text{-}1^+CD8$ T cells in the TME and confers sensitivity to PD-1 blockade. Our data also indicate that Axl suppresses DC expression of type I IFNs, which are required for expansion of $TCF1^+$ CD8 T cells, thus providing mechanistic insight into the paucity of stem-like T cells in *STK11/LKB1* mutant tumors and a molecular rationale for the poor response of these tumors to PD-1 inhibition.

Despite the overall suppressive immune environment in KL mutated tumors, the lack of $TCF1^+$ expressing $CD8^+$ T cells may account for the main reason for KL tumors not responding to PD-1/PD-L1 therapy. As we compared TME of allografts derived from isogenic cell lines, *STK11/LKB1* mutation is likely to be the cause for decreased abundance of this group of T cells in TME. In TCGA lung adenocarcinoma patient samples,*Tcf7* expression on stromal cells positively correlates with $CD8^+$ T cell infiltration, indicating that it's less likely to observe $TCF1^+$ expressing $CD8^+$ T cells in KL mutated lung adenocarcinoma patient samples,

besides the overall fewer $CD8^+$ T cells infiltration in TME. It is worthwhile to further explore the underlying mechanisms for reduced infiltration of $TCF1^+$ expressing $CD8^+$ T cells in *STK11/LKB1* mutated tumors. From scRNAseq analysis, the infiltrated CD8 T cells in KP tumors showed significant enrichment of interferon signaling pathway related signature gene expression, comparing to KPL tumors. Therefore, the low expression and secretion of type I interferon from dendritic cells might partially explain the reason for KPL tumors with low $TCF1^+PD\text{-}1^+CD8$ T cells infiltration. As dendritic cells infiltrated into KPL tumors showed higher level expression of Axl, it is possible that KPL tumors had upregulated Axl expression in dendritic cells through signaling pathways regulated by *STK11/LKB1* in tumor cells. This crosstalk between KPL tumor cells and dendritic cells are crucial to understand, which may further aid for exploring more therapeutic strategies and identifying patients who may benefit from the combination therapy of bemcentinib with pembrolizumab.

As we shown in our scRNAseq analysis, that PD-1/PD-L1 treatment tend to expand all $CD8^+$ T cells populations unbiasedly in TME, and single treatment of it could not expand tumor associated $CD8^+$ T cells specifically. Similar treatment effects of PD-1/PD-L1 were also have been observed and reported in oral cavity carcinoma models (Friedman et al., 2020). On the other hand, existence of $TCF1^+$ $PD\text{-}1^+$ $CD8^+$ T cells are likely to contain tumor neoantigen specific $CD8^+$ T cells, whose expansion upon PD-1 treatment could control tumor growth effectively. On the

contrary, BGB324 mediated Axl inhibition could effectively induce TCF1$^+$ PD-1$^+$ CD8$^+$ T cells population expansion in *KL* mutated tumors. Accord with previous literature, TCF1$^+$ PD-1$^+$ CD8$^+$ T cells do not secret IFNγ or exhibit effector T cells characteristics directly (Siddiqui, Schaeuble, Chennupati, Fuertes Marraco, et al., 2019). However, based on our scRNAseq analysis with scTCRseq lineage tracing, BGB324 cannot only induce clonal expansion of a group of CD8$^+$ T cells effectively from stem cell like CD8$^+$ T cells, this group of T cells are likely to be tumor associated. Once being re-activated by PD-1 and transit into effector T cells (TCF1$^-$ PD-1$^+$ CD8$^+$ T cells), they are capable of controlling tumor growth effectively. Additionally, PD-1/PD-L1 treatment is needed to break the exclusion of TCF1$^+$ PD-1$^+$ CD8$^+$ T cells from the tumor island in KPL9-3-1 *KL* mutated tumors, with underlying mechanism worth for further investigation.

Our data suggested that Axl inhibition induced TCF1$^+$PD-1$^+$CD8 T cell expansion. This, to our knowledge, is the first time this population of T cells has been shown to expand after a systemic therapy. Prior studies suggest that that TCF1$^+$PD-1$^+$CD8 T cells do not secrete IFNγ or exhibit effector T cell characteristics directly (Siddiqui, Schaeuble, Chennupati, Fuertes Marraco, et al., 2019). Thus, while these cells are required for ICB therapy responses, they likely do so by differentiating into effector T cells. Our scRNAseq analysis with scTCRseq lineage tracing suggests that Axl inhibition induces clonal expansion of tumor specific CD8 T cells from stem cell-like

CD8 T cells. However, anti-PD-1 therapy was required for transition into effector T cells (TCF1$^-$ PD-1$^+$ CD8 T cells) who are capable of killing tumor cells.

Although Axl is expressed widely on tumor cells, vasculature and myeloid cells (Gay et al., 2017; Maier et al., 2020; Rothlin et al., 2007), inhibition of Axl on DCs appears to be the main executor in expanding TCF1$^+$PD-1$^+$CD8 T cells to achieve anti-PD-1-mediated control of *STK11/LKB1* mutant NSCLC growth control (Gay et al., 2017). As an innate sensing checkpoint on myeloid cells, inhibition of Axl on dendritic cells enhances type I interferon production in TME. Surprisingly, as low as 200 ng increase of type I interferon, it is sufficient to induce TCF1$^+$ PD-1$^+$ CD8$^+$ T cells expansion in tumors. Therefore, higher type I interferon secretion either could transit TCF1$^+$ PD-1$^+$ CD8$^+$ T cells directly into effector T cells capable of killing tumor cells directly and lost TCF1 expression, or higher dose may simply induce the apoptosis of TCF1$^+$ PD-1$^+$ CD8$^+$ T cells in TME, which is worthwhile for future exploration and study.

With similar therapeutic effects of BGB324 in sensitizing *KL* mutated tumors pre-clinically with patient derived cell line xenografts on humanized mice, as well as in our clinical trials, it is likely that *KL* mutated NSCLC patients could benefit from the combination treatment in the clinic. Since BGB324 could induce the expansion of TCF1$^+$ PD-1$^+$ CD8$^+$ T cells, it may benefit more PD-1 refractory patients from other

cancer types. Furthermore, our mechanism study indicates that type I interferon induction could expand tumor associated TCF1$^+$ PD-1$^+$ CD8$^+$ T cells, more therapeutic strategies could be developed to further increase the PD-1/PD-L1 treatment responses in cancer patients. While this study compared *STK11/LKB1* plus *KRAS/TP53* mutant LUADs to LUADs that had only *KRAS/TP53* mutations for the effects of Axl targeting on the TME, it is possible that the beneficial effect of Axl inhibition on immune checkpoint blockade will extend beyond *STK11/LKB1* mutant NSCLC. Ultimately, a significantly prolonged survival rate and time could be expected from cancer patients, with more patients could benefit from immunotherapies.

Although we confirmed that the increased abundance of TCF1$^+$ CD8 T cells is the key mediator of therapeutic response, our study has limitations. We were unable to study Axl expression at the protein level in tumor associated immune cells, due to the lack of an available Axl antibody to stain cells isolated from tumor tissues. With the newly ready to be used *Ax*$^{fl/fl}$ mice, a specific knock-out of Axl in dendritic cell by crossing with zDC Cre mice could further validate our findings that dendritic cell activity regulated by Axl expression is the key factor mediating resistance to anti-PD-1/PD-L1 therapy for KPL tumors.

Decreased abundance TCF1$^+$ PD-1$^+$ CD8$^+$ T cells in *KL* syngeneic tumors were also been confirmed from the biopsy of pre-treated NSCLC patients. With similar therapeutic effects of BGB324 in sensitizing *KL* mutated tumors pre-clinically with patient derived cell line xenografts on humanized mice, as well as in our clinical trials, it is likely that *KL* mutated NSCLC patients could benefit from the combination treatment in the clinic. Since BGB324 could induce the expansion of TCF1$^+$ PD-1$^+$ CD8$^+$ T cells, it may benefit more PD-1 refractory patients from other cancer types. Furthermore, our mechanism study indicates that type I interferon induction could expand tumor associated TCF1$^+$ PD-1$^+$ CD8$^+$ T cells, more therapeutic strategies could be developed to further increase the PD-1/PD-L1 treatment responses in cancer patients. Ultimately, a significantly prolonged survival rate and time could be expected from cancer patients, with more patients could benefit from immunotherapies.

In conclusion, we have shown in murine, and patient derived preclinical models that systemic treatment with an Axl inhibitor, bemcentinib, in clinical trials combined with PD-1 checkpoint blockade leads to anti-tumor responses in *STK11/LKB1* mutant NSCLCs. Combination treatment is associated with TCF1$^+$ CD8 T cell expansion and anti-tumor immune responses. Thus, our data strongly support clinical testing of AXL inhibition in combination with PD-1 checkpoint blockade in *STK11/LKB1* mutant NSCLC patients and potentially in other tumor settings that are refractory to PD-1

blockade and that also exhibit deficits in TCF1$^+$ CD8 T cells. In addition, in these trials it will be important to perform correlative studies that demonstrate, in patients, the effects of AXL inhibition on TCF1$^+$ CD8 T cells as well as investigate alternative mechanisms of increasing type I IFN induction to expand tumor associated TCF1$^+$PD-1$^+$CD8 T cells.

APPENDIX
KEY RESOURCES TABLE

REAGENT or RESOURCE		
Antibodies	**Source**	**Identifier**
InVivoMab anti-mouse PD-1 (RMP1-14)	BioXCell	Cat# BE0146; RRID: AB_10949053
InVivoMab rat IgG2a isotype control (2A3)	BioXCell	Cat# BE0089; RRID: AB_11007769
InVivoMab anti-human PD-1 (J110)	BioXCell	Cat# BE0193; RRID: AB_109850168
InVivoMab mouse IgG1 isotype control (MOPC-21)	BioXCell	Cat# BE0083; RRID: AB_1107784
InVivoMab anti-mouse IFNAR-1 (MAR1-5A3)	BioXCell	Cat# BE0241; RRID: AB_2687723
anti-PD-1 (Pembrolizumab)		N/A
Anti-mCD45 (Flow cytometry, 30-F11)	BioLegend	Cat# 103126; RRID: AB_493535
Anti-mCD3 (Flow cytometry, 145-2C11)	BD Bioscience	Cat# 564379; RRID: AB_2738780
Anti-mCD4 (Flow cytometry, GK1.5)	BioLegend	Cat# 100413; RRID: AB_312698
Anti-mCD8α (Flow cytometry, 53-6.7)	BioLegend	Cat# 100730; RRID: AB_493703
Anti-mCD8b (Flow cytometry, YTS156.7.7)	BioLegend	Cat# 126616; RRID: AB_2562777
Anti-mPD-1 (Flow cytometry, 29F.1A12)	BioLegend	Cat# 135224; RRID: AB_2563523
Anti-mKi-67 (Flow cytometry, 16A8)	BioLegend	Cat# 652404; RRID: AB_2562664
OVA257-264 (SIINFEKL) peptide bound to H-2Kb Monoclonal Antibody (Flow cytometry, 25-D1.16)	eBioscience	Cat# 17-5743-82; RRID: AB_1311286

Anti-h/Mtcf1/7 (Flow cytometry, C63D9)	Cell Signaling Technologies	Cat# 6444; RRID: AB_2797627
Biotin anti-mouse CD45 Antibody (30-F11)	BioLegend	Cat# 101304; RRID: AB_312969
Rabbit (DA1E) mAb IgG XP® Isotype Contorl	Cell Signaling Technologies	Cat# 2975; RRID: AB_10699151
Anti-hCD45 (Flow cytometry, HI30)	BioLegend	Cat# 304021; RRID: AB_493654
Anti-hCD3 (Flow cytometry, HIT3a)	BioLegend	Cat# 300327; RRID: AB_1575010
Fixable Viability Dye eFluor™ 506	Thermo Fisher	Cat# 65-0866-18
iTAg Tetramer/PE – H-2 Kb OVA (SIINFEKL)	MBL	Cat# TB-5001-1
Anti-Fcγiii/ii receptor (clone 2.4G2)	BD Biosciences	CAT# 553141, RRID: AB_394656
TCF1/TCF7 (C63D9) Rabbit mAb	Cell Signaling Technologies	Cat# 2203; RRID: AB_2199302
CD8α (D4W2Z) XP® Rabbit mAb	Cell Signaling Technologies	Cat# 98941; RRID: AB_2756376
LKB1 (D60C5) Rabbit mAb	Cell Signaling Technologies	Cat# 3047; RRID: AB_2198327
AXL (C89E7) Rabbit mAb	Cell Signaling Technologies	Cat# 8661; RRID: AB_11217435
GAPDH (D16H11) Rabbit mAb	Cell Signaling Technologies	Cat# 5174; RRID: AB_10622025
Anti-rabbit IgG, HRP-linked Antibody	Cell Signaling Technologies	Cat# 7074; RRID: AB_2099233
Chemicals, Peptides, and Recombinant Proteins		
TMB Solution (1X)	eBioscience	Cat# 00-4201-56
Sulfadiazine/ Trimethoprim (Aurora Pharmaceutical LLC)	UTSW-Veterinary Drug Services	Cat# 302
GE Healthcare Ficoll-Paque™ Premium	Cytiva	Cat# 17544203
Animal free Collagenase, type A	Sigma	Cat# SCR136
DNAse I	Roche	Cat# 11284932001
Recombinant murine GM-CSF	Peprotech	Cat# 315-03
Recombinant murine IFN-γ	Peprotech	Cat# 210-10
Recombinant human IL-4	Peprotech	Cat# 400-04
Recombinant human GM-CSF	Peprotech	Cat# 300-03
Recombinant human TNFα	Peprotech	Cat# 300-01A

Clophsome®-A-Clodronate Liposomes (Anionic)	FormuMax Scientific	Cat# F70101C-A
$OVA_{257-264}$ (SIINFEKL)	InvivoGen	Cat# vac-sin
Human Ppillomavirus (HPV) E7 protein (49-57)	GenScript	Cat# RP20249
Ovalbumin	Sigma-Aldrich	Cat# A2512
pCpGfree-OVA	InvivoGen	Cat# pcpgf-ova
Bovine serum albumin (BSA)	Jackson Immuno Research	Cat# 001-000-173
Normal Goat Serum Blocking Solution, 2.5%	Vector Laboratories	Cat# S-1012-50
Eosin Phloxine Alcoholic Working Solution	Poly Scientific	Cat# s176
Harris Modified Method Hematoxylin Stains	Fisher Chemical	Cat# SH26500D
Critical Commercial Assays		
CellTiter 96 Aqueous One Solution Cell Proliferation Assay (MTS)	Promega	Cat# G3582
Opal™ 520 Reagent Pack	PerkinElmer	Cat# FP1487001KT
Opal™ 570 Reagent Pack	PerkinElmer	Cat# FP1488001KT
ProLong™ Gold Antifade Mountant with DAPI	Invitrogen	Cat# P36931
Chromium I7 Multiplex Kit, 96 rxns	10x Genomics	Cat# PN-120262
BD Mouse IFN-γ ELISPOT Sets	BD Biosciences	Cat# 551083
VeriKine-HS Mouse IFN Beta ELISA Kit	PBL Assay Science	Cat# 42410
VeriKine Human IFN Beta ELISA Kit	PBL Assay Science	Cat# 414101
True-Nuclear™ Transcription Factor Buffer Set	BioLegend	Cat# 424401
EasySep™ Mouse $CD8^+$ T Cell Isolation Kit	STEMCELL Technologies	Cat# 19853
EasySep™ Human CD34 Positive Selection Kit II	STEMCELL Technologies	Cat# 18780
EasySep™ Mouse Steptavidin RapidSpheres™ Isolation Kit	STEMCELL Technologies	Cat# 19860
Clarity Max Western ECL Substrate	Bio-Rad	Cat# 1705062
ImmPRESS® HRP Horse Anti-Rabbit IgG Polymer Detection Kit	Vector Laboratories	Cat# MP-7401
e-Myco PCR Detection Kits	Bulldog Bio	Cat# 25233
Deposited Data		

Single cell RNA-seq data and TCR sequencing data	This paper	GEO: XXXXXX
Experimental Models: Cell Lines		
KP	Esra Akbay	N/A
KPL	Esra Akbay	N/A
A549 (Male, Adenocarcinoma, NSCLC)	ATCC	N/A
H2122 (Female, Adenocarcinoma, NSCLC)	John Minna and Adi Gazdar	RRID: CVCL_1531
Lenti-X 293T (Female, Kidney)	Takara	Cat# 632180
Experimental Models: Organisms/Strains		
C57BL/6J	UTSW breeding core	Cat# 000664
C57BL/6 (MPF)	Taconic Biosciences	Cat# B6NTac
B6.129S7-Rag1^{tm1Mom}/J mice	Jackson Laboratory	Cat# 002216
NSG-SGM3 mice	Jackson Laboratory	Cat# 013062
B6.129(C)-Batf3^{tm1Kmm}/J mice	Jackson Laboratory	Cat# 013755
C57BL/6-Tg (TcraTcrb)1100Mjb/J mice	Jackson Laboratory	Cat# 003831
Oligonucleotides		
Software and Algorithms		
GraphPad Prism 9.0.0	GraphPad Software, Inc.	https://graphpad.com/scientific-software/prism/
CTL-ImmunoSpot® S6 Analyzer	Cellular Technology Limited	http://www.immunospot.com/ImmunoSpot-analyzers
CytExpert	Beckman Coulter, Inc	https://www.beckman.com/coulter-flow-cytometers/cytoflex/cytexpert
BD FACSAria™ III System	BD Biosciences	https://www.bdbiosciences.com/en-us/instruments/research-instruments/research/cell/sorters/facsaria-iii

FlowJo	Tree Star Inc.	https://www.flowjo.com/solutions/flowjo
CellRanger (v3.1.0)	10x Genomics	https://support.10xgenomics.com/single-cell-gene-expression/software/pipelines/latest/installation
R (v4.0.2)	The R Foundation	https://www.r-project.org
Rstudio 1.3.1093	Rstudio	http://rstudio.com/products/rstudio/
Seurat (v.3.1.0, R package)	(Stuart et al., 2019)	https://github.com/satijalab/seurat
Monocle (v2, R package)	(Qiu et al., 2017; Trapnell et al., 2014)	https://bustools.github.io/BUS_notebooks_R/monocle2.html
SingleR (v.1.3.8, R package)	(Aran et al., 2019)	https://github.com/dviraran/SingleR
ggplot2 (v3.2.1, R package)	(Wickham, 2016)	https://ggplot2.tidyverse.org
Velocyto (v0.17.17, R package)	(La Manno et al., 2018)	http://velocyto.org
Uniform Manifold Approximation and Projection (UMAP)	(McInnes et al., 2018)	https://github.com/lmcinnes/umap
Image Studio Lite	LiCor	http://licor.com/bio/image-studio-lite/
ZEN Digital Imaging	Zeiss	https://www.zeiss.com/microscopy/int/products/microscope-software/zen.html
NDP.View2	Hamamatsu Photonics	https://www.hamamatsu.com/us/en/product/type/U12388-01/index.html

BIBLIOGRAPHY

Abu-Thuraia, A., Goyette, M.-A., Boulais, J., Delliaux, C., Apcher, C., Schott, C., Chidiac, R., Bagci, H., Thibault, M.-P., & Davidson, D. (2020). AXL confers cell migration and invasion by hijacking a PEAK1-regulated focal adhesion protein network. *Nature Communications*, *11*(1), 1–20.

Addeo, A., Banna, G. L., & Weiss, G. J. (2019). Tumor mutation burden—from hopes to doubts. *JAMA Oncology*, *5*(7), 934–935.

Aguilera, T. A., Rafat, M., Castellini, L., Shehade, H., Kariolis, M. S., Hui, A. B.-Y., Stehr, H., Von Eyben, R., Jiang, D., & Ellies, L. G. (2016). Reprogramming the immunological microenvironment through radiation and targeting Axl. *Nature Communications*, *7*(1), 1–14.

Ahmed, T., Vial, M. R., Ost, D., Stewart, J., Hasan, M. A., & Grosu, H. B. (2018). Non-small cell lung cancer transdifferentiation into small cell lung cancer: a case series. *Lung Cancer*, *122*, 220–223.

Albrengues, J., Shields, M. A., Ng, D., Park, C. G., Ambrico, A., Poindexter, M. E., Upadhyay, P., Uyeminami, D. L., Pommier, A., Küttner, V., Bružas, E., Maiorino, L., Bautista, C., Carmona, E. M., Gimotty, P. A., Fearon, D. T., Chang, K., Lyons, S. K., Pinkerton, K. E., … Egeblad, M. (2018). Neutrophil extracellular traps produced during inflammation awaken dormant cancer cells in mice. *Science*, *361*(6409). https://doi.org/10.1126/science.aao4227

Andzinski, L., Kasnitz, N., Stahnke, S., Wu, C., Gereke, M., von Köckritz-Blickwede, M., Schilling, B., Brandau, S., Weiss, S., & Jablonska, J. (2016). Type I IFN s induce anti-tumor polarization of tumor associated neutrophils in mice and human. *International Journal of Cancer*, *138*(8), 1982–1993.

Antonia, S. J., López-Martin, J. A., Bendell, J., Ott, P. A., Taylor, M., Eder, J. P., Jäger, D., Pietanza, M. C., Le, D. T., & de Braud, F. (2016). Nivolumab alone and nivolumab plus ipilimumab in recurrent small-cell lung cancer (CheckMate 032): a multicentre, open-label, phase 1/2 trial. *The Lancet Oncology*, *17*(7), 883–895.

Antony, J., & Huang, R. Y.-J. (2017). AXL-driven EMT state as a targetable conduit in cancer. *Cancer Research*, *77*(14), 3725–3732.

Aran, D., Looney, A. P., Liu, L., Wu, E., Fong, V., Hsu, A., Chak, S., Naikawadi, R. P., Wolters, P. J., & Abate, A. R. (2019). Reference-based analysis of lung single-cell sequencing reveals a transitional profibrotic macrophage. *Nature Immunology*, *20*(2), 163–172.

Araujo, L. H., Souza, B. M., Leite, L. R., Parma, S. A. F., Lopes, N. P., Malta, F. S. V, & Freire, M. C. M. (2021). Molecular profile of KRAS G12C-mutant colorectal and non-small-cell lung cancer. *BMC Cancer*, *21*(1), 1–8.

Arce-Lara, C., Arriola, E., Brunsvig, P., Carcereny, E., Domine, M., Dragnev, K., Felip, E., Campelo, R. G., Krebs, M., & Paz-Ares, L. (2018). P2. 04-27 Ph II Study of Oral Selective AXL Inhibitor Bemcentinib (BGB324) in Combination with Pembrolizumab in Patients with Advanced NSCLC. *Journal of Thoracic Oncology*, *13*(10), S741.

Assoun, S., Theou-Anton, N., Nguenang, M., Cazes, A., Danel, C., Abbar, B., Pluvy, J., Gounant, V., Khalil, A., & Namour, C. (2019). Association of TP53 mutations with response and longer survival under immune checkpoint inhibitors in advanced non-small-cell lung cancer. *Lung Cancer*, *132*, 65–71.

Badawy, A. A., Khedr, G., Omar, A., Bae, S., Arafat, W., & Grant, S. (2018). Site of metastases as prognostic factors in unselected population of stage IV non-small cell lung cancer. *Asian Pacific Journal of Cancer Prevention: APJCP*, *19*(7), 1907.

Bakdash, G., Vogelpoel, L. T. C., Van Capel, T. M., Kapsenberg, M. L., & de Jong, E. C. (2015). Retinoic acid primes human dendritic cells to induce gut-homing, IL-10-producing regulatory T cells. *Mucosal Immunology*, *8*(2), 265–278.

Becht, E., McInnes, L., Healy, J., Dutertre, C.-A., Kwok, I. W. H., Ng, L. G., Ginhoux, F., & Newell, E. W. (2019). Dimensionality reduction for visualizing single-cell data using UMAP. *Nature Biotechnology*, *37*(1), 38–44.

Bindea, G., Mlecnik, B., Tosolini, M., Kirilovsky, A., Waldner, M., Obenauf, A. C., Angell, H., Fredriksen, T., Lafontaine, L., & Berger, A. (2013). Spatiotemporal dynamics of intratumoral immune cells reveal the immune landscape in human cancer. *Immunity*, *39*(4), 782–795.

Biton, J., Mansuet-Lupo, A., Pécuchet, N., Alifano, M., Ouakrim, H., Arrondeau, J., Boudou-Rouquette, P., Goldwasser, F., Leroy, K., & Goc, J. (2018). TP53, STK11, and EGFR mutations predict tumor immune profile and the response to anti–PD-1 in lung adenocarcinoma. *Clinical Cancer Research*, *24*(22), 5710–5723.

Borghaei, H., Paz-Ares, L., Horn, L., Spigel, D. R., Steins, M., Ready, N. E., Chow, L. Q., Vokes, E. E., Felip, E., & Holgado, E. (2015). Nivolumab versus docetaxel in advanced nonsquamous non–small-cell lung cancer. *New England Journal of Medicine*, *373*(17), 1627–1639.

Brahmer, J. R., Horn, L., Antonia, S. J., Spigel, D. R., Gandhi, L., Sequist, L. V, Sankar, V., Ahlers, C. M., Wigginton, J. M., & Kollia, G. (2013). *Survival and long-term follow-up of the phase I trial of nivolumab (Anti-PD-1; BMS-936558; ONO-4538) in patients (pts) with previously treated advanced non-small cell lung cancer (NSCLC).* American Society of Clinical Oncology.

Brahmer, J. R., Tykodi, S. S., Chow, L. Q. M., Hwu, W.-J., Topalian, S. L., Hwu, P., Drake, C. G., Camacho, L. H., Kauh, J., & Odunsi, K. (2012). Safety and

activity of anti–PD-L1 antibody in patients with advanced cancer. *New England Journal of Medicine*, *366*(26), 2455–2465.

Bros, M., Dexheimer, N., Ross, R., Trojandt, S., Höhn, Y., Tampe, J., Sutter, A., Jährling, F., Grabbe, S., & Reske-Kunz, A. B. (2011). Differential gene expression analysis identifies murine Cacnb3 as strongly upregulated in distinct dendritic cell populations upon stimulation. *Gene*, *472*(1–2), 18–27.

Brownson, R. C., Chang, J. C., & Davis, J. R. (1992). Gender and histologic type variations in smoking-related risk of lung cancer. *Epidemiology*, 61–64.

Broz, M. L., Binnewies, M., Boldajipour, B., Nelson, A. E., Pollack, J. L., Erle, D. J., Barczak, A., Rosenblum, M. D., Daud, A., & Barber, D. L. (2014). Dissecting the tumor myeloid compartment reveals rare activating antigen-presenting cells critical for T cell immunity. *Cancer Cell*, *26*(5), 638–652.

Butterfield, L. H., Kaufman, H. L., & Marincola, F. M. (2017). *Cancer immunotherapy principles and practice*. Springer Publishing Company.

Carbone, D. P., Reck, M., Paz-Ares, L., Creelan, B., Horn, L., Steins, M., Felip, E., van den Heuvel, M. M., Ciuleanu, T.-E., & Badin, F. (2017). First-line nivolumab in stage IV or recurrent non–small-cell lung cancer. *New England Journal of Medicine*, *376*(25), 2415–2426.

Carvajal-Hausdorf, D., Altan, M., Velcheti, V., Gettinger, S. N., Herbst, R. S., Rimm, D. L., & Schalper, K. A. (2019). Expression and clinical significance of PD-L1, B7-H3, B7-H4 and TILs in human small cell lung cancer (SCLC). *Journal for Immunotherapy of Cancer*, *7*(1), 1–9.

Cerundolo, V., Silk, J. D., Masri, S. H., & Salio, M. (2009). Harnessing invariant NKT cells in vaccination strategies. *Nature Reviews Immunology*, *9*(1), 28–38.

Chan, M. V., Huo, Y. R., Cao, C., & Ridley, L. (2021). Survival outcomes for surgical resection versus CT-guided percutaneous ablation for stage I non-small cell lung cancer (NSCLC): a systematic review and meta-analysis. *European Radiology*, 1–13.

Chao, M. P., Alizadeh, A. A., Tang, C., Myklebust, J. H., Varghese, B., Gill, S., Jan, M., Cha, A. C., Chan, C. K., & Tan, B. T. (2010). Anti-CD47 antibody synergizes with rituximab to promote phagocytosis and eradicate non-Hodgkin lymphoma. *Cell*, *142*(5), 699–713.

Chen, S., Liu, M., Zhou, Y., Xu, M., Melancon, C. E., & Edwards, J. (2018). *The impact of sample storage time on calculating tumor mutation burden (TMB).* American Society of Clinical Oncology.

Chen, Z., Ji, Z., Ngiow, S. F., Manne, S., Cai, Z., Huang, A. C., Johnson, J., Staupe, R. P., Bengsch, B., Xu, C., Yu, S., Kurachi, M., Herati, R. S., Vella, L. A., Baxter, A. E., Wu, J. E., Khan, O., Beltra, J. C., Giles, J. R., … Wherry,

E. J. (2019). TCF-1-Centered Transcriptional Network Drives an Effector versus Exhausted CD8 T Cell-Fate Decision. *Immunity*, *51*(5), 840-855.e5. https://doi.org/10.1016/j.immuni.2019.09.013

Cho, B. C., Lopes, G., Kowalski, D. M., Kasahara, K., Wu, Y.-L., Castro, G., Turna, H. Z., Cristescu, R., Aurora-Garg, D., & Loboda, A. (2020). Relationship between STK11 and KEAP1 mutational status and efficacy in KEYNOTE-042: pembrolizumab monotherapy versus platinum-based chemotherapy as first-line therapy for PD-L1-positive advanced NSCLC. *Cancer Research*.

Chung, H. C., Lopez-Martin, J. A., Kao, S. C.-H., Miller, W. H., Ros, W., Gao, B., Marabelle, A., Gottfried, M., Zer, A., & Delord, J.-P. (2018). *Phase 2 study of pembrolizumab in advanced small-cell lung cancer (SCLC): KEYNOTE-158.* American Society of Clinical Oncology.

Chung, H. C., Piha-Paul, S. A., Lopez-Martin, J., Schellens, J. H. M., Kao, S., Miller Jr, W. H., Delord, J.-P., Gao, B., Planchard, D., & Gottfried, M. (2020). Pembrolizumab after two or more lines of previous therapy in patients with recurrent or metastatic SCLC: results from the KEYNOTE-028 and KEYNOTE-158 studies. *Journal of Thoracic Oncology*, *15*(4), 618–627.

Dangaj, D., Bruand, M., Grimm, A. J., Ronet, C., Barras, D., Duttagupta, P. A., Lanitis, E., Duraiswamy, J., Tanyi, J. L., Benencia, F., Conejo-Garcia, J., Ramay, H. R., Montone, K. T., Powell, D. J., Gimotty, P. A., Facciabene, A., Jackson, D. G., Weber, J. S., Rodig, S. J., … Coukos, G. (2019). Cooperation between Constitutive and Inducible Chemokines Enables T Cell Engraftment and Immune Attack in Solid Tumors. *Cancer Cell*, 885–900. https://doi.org/10.1016/j.ccell.2019.05.004

de la Chapelle, A. (2003). Microsatellite instability. *New England Journal of Medicine*, *349*(3), 209–210.

DeNardo, D. G., Barreto, J. B., Andreu, P., Vasquez, L., Tawfik, D., Kolhatkar, N., & Coussens, L. M. (2009). CD4+ T cells regulate pulmonary metastasis of mammary carcinomas by enhancing protumor properties of macrophages. *Cancer Cell*, *16*(2), 91–102.

Di Carlo, E., Forni, G., Lollini, P., Colombo, M. P., Modesti, A., & Musiani, P. (2001). The intriguing role of polymorphonuclear neutrophils in antitumor reactions. *Blood, The Journal of the American Society of Hematology*, *97*(2), 339–345.

Diamond, M. S., Kinder, M., Matsushita, H., Mashayekhi, M., Dunn, G. P., Archambault, J. M., Lee, H., Arthur, C. D., White, J. M., & Kalinke, U. (2011). Type I interferon is selectively required by dendritic cells for immune rejection of tumors. *Journal of Experimental Medicine*, *208*(10), 1989–2003.

Dixon, K. O., O'Flynn, J., Klar-Mohamad, N., Daha, M. R., & van Kooten, C.

(2017). Properdin and factor H production by human dendritic cells modulates their T-cell stimulatory capacity and is regulated by IFN-γ. *European Journal of Immunology*, *47*(3), 470–480.

Dorner, B. G., Dorner, M. B., Zhou, X., Opitz, C., Mora, A., Güttler, S., Hutloff, A., Mages, H. W., Ranke, K., & Schaefer, M. (2009). Selective expression of the chemokine receptor XCR1 on cross-presenting dendritic cells determines cooperation with CD8+ T cells. *Immunity*, *31*(5), 823–833.

Drapkin, B. J., & Farago, A. F. (2019). Unexpected synergy reveals new therapeutic strategy in SCLC. *Trends in Pharmacological Sciences*, *40*(5), 295–297.

Dress, R. J., Dutertre, C.-A., Giladi, A., Schlitzer, A., Low, I., Shadan, N. B., Tay, A., Lum, J., Kairi, M. F. B. M., & Hwang, Y. Y. (2019). Plasmacytoid dendritic cells develop from Ly6D+ lymphoid progenitors distinct from the myeloid lineage. *Nature Immunology*, *20*(7), 852–864.

Edelson, B. T., KC, W., Juang, R., Kohyama, M., Benoit, L. A., Klekotka, P. A., Moon, C., Albring, J. C., Ise, W., & Michael, D. G. (2010). Peripheral CD103+ dendritic cells form a unified subset developmentally related to CD8α+ conventional dendritic cells. *Journal of Experimental Medicine*, *207*(4), 823–836.

Edge, S. B., Byrd, D. R., Carducci, M. A., Compton, C. C., Fritz, A. G., & Greene, F. L. (2010). *AJCC cancer staging manual* (Vol. 649). Springer New York.

Ettinger, D. S., Wood, D. E., Aisner, D. L., Akerley, W., Bauman, J. R., Bharat, A., Bruno, D. S., Chang, J. Y., Chirieac, L. R., & D'Amico, T. A. (2021). NCCN Guidelines Insights: Non–Small Cell Lung Cancer, Version 2.2021: Featured Updates to the NCCN Guidelines. *Journal of the National Comprehensive Cancer Network*, *19*(3), 254–266.

Fehrenbacher, L., Spira, A., Ballinger, M., Kowanetz, M., Vansteenkiste, J., Mazieres, J., Park, K., Smith, D., Artal-Cortes, A., & Lewanski, C. (2016). Atezolizumab versus docetaxel for patients with previously treated non-small-cell lung cancer (POPLAR): a multicentre, open-label, phase 2 randomised controlled trial. *The Lancet*, *387*(10030), 1837–1846.

Freedman, N. D., Leitzmann, M. F., Hollenbeck, A. R., Schatzkin, A., & Abnet, C. C. (2008). Cigarette smoking and subsequent risk of lung cancer in men and women: analysis of a prospective cohort study. *The Lancet Oncology*, *9*(7), 649–656.

Fridlender, Z. G., Sun, J., Kim, S., Kapoor, V., Cheng, G., Ling, L., Worthen, G. S., & Albelda, S. M. (2009). Polarization of tumor-associated neutrophil phenotype by TGF-β:"N1" versus "N2" TAN. *Cancer Cell*, *16*(3), 183–194.

Friedman, J., Moore, E. C., Zolkind, P., Robbins, Y., Clavijo, P. E., Sun, L.,

Greene, S., Morisada, M. V, Mydlarz, W. K., & Schmitt, N. (2020). Neoadjuvant PD-1 Immune Checkpoint Blockade Reverses Functional Immunodominance among Tumor Antigen–Specific T Cells. *Clinical Cancer Research*, *26*(3), 679–689.

Frost, N., Kollmeier, J., Vollbrecht, C., Grah, C., Matthes, B., Pultermann, D., von Laffert, M., Lüders, H., Olive, E., & Raspe, M. (2021). KRASG12C/TP53 co-mutations identify long-term responders to first line palliative treatment with pembrolizumab monotherapy in PD-L1 high (≥ 50%) lung adenocarcinoma. *Translational Lung Cancer Research*, *10*(2), 737.

Fujii, S., Shimizu, K., Hemmi, H., Fukui, M., Bonito, A. J., Chen, G., Franck, R. W., Tsuji, M., & Steinman, R. M. (2006). Glycolipid α-C-galactosylceramide is a distinct inducer of dendritic cell function during innate and adaptive immune responses of mice. *Proceedings of the National Academy of Sciences*, *103*(30), 11252–11257.

Fujii, S., Shimizu, K., Smith, C., Bonifaz, L., & Steinman, R. M. (2003). Activation of natural killer T cells by α-galactosylceramide rapidly induces the full maturation of dendritic cells in vivo and thereby acts as an adjuvant for combined CD4 and CD8 T cell immunity to a coadministered protein. *The Journal of Experimental Medicine*, *198*(2), 267–279.

Gadgeel, S., Rodriguez-Abreu, D., Felip, E., Esteban, E., Speranza, G., Reck, M., Hui, R., Boyer, M., Garon, E. B., & Horinouchi, H. (2019). KRAS mutational status and efficacy in KEYNOTE-189: Pembrolizumab (pembro) plus chemotherapy (chemo) vs placebo plus chemo as first-line therapy for metastatic non-squamous NSCLC. *Annals of Oncology*, *30*, xi64–xi65.

Gajewski, T. F., Schreiber, H., & Fu, Y. X. (2013). Innate and adaptive immune cells in the tumor microenvironment. *Nature Immunology*, *14*(10), 1014–1022. https://doi.org/10.1038/ni.2703

Galibert, L., Diemer, G. S., Liu, Z., Johnson, R. S., Smith, J. L., Walzer, T., Comeau, M. R., Rauch, C. T., Wolfson, M. F., & Sorensen, R. A. (2005). Nectin-like protein 2 defines a subset of T-cell zone dendritic cells and is a ligand for class-I-restricted T-cell-associated molecule. *Journal of Biological Chemistry*, *280*(23), 21955–21964.

Galon, J., & Bruni, D. (2019). Approaches to treat immune hot, altered and cold tumours with combination immunotherapies. *Nature Reviews Drug Discovery*, 1. https://doi.org/10.1038/s41573-018-0007-y

Galon, J., Mlecnik, B., Bindea, G., Angell, H. K., Berger, A., Lagorce, C., Lugli, A., Zlobec, I., Hartmann, A., Bifulco, C., Nagtegaal, I. D., Palmqvist, R., Masucci, G. V., Botti, G., Tatangelo, F., Delrio, P., Maio, M., Laghi, L., Grizzi, F., … Pagès, F. (2014). Towards the introduction of the “Immunoscore” in the classification of malignant tumours. *Journal of Pathology*, *232*(2), 199–

209. https://doi.org/10.1002/path.4287

Gandhi, L., Rodríguez-Abreu, D., Gadgeel, S., Esteban, E., Felip, E., De Angelis, F., Domine, M., Clingan, P., Hochmair, M. J., Powell, S. F., Cheng, S. Y. S., Bischoff, H. G., Peled, N., Grossi, F., Jennens, R. R., Reck, M., Hui, R., Garon, E. B., Boyer, M., … Garassino, M. C. (2018). Pembrolizumab plus chemotherapy in metastatic non-small-cell lung cancer. *New England Journal of Medicine*, *378*(22), 2078–2092. https://doi.org/10.1056/NEJMoa1801005

Gandhi, Leena, Rodríguez-Abreu, D., Gadgeel, S., Esteban, E., Felip, E., De Angelis, F., Domine, M., Clingan, P., Hochmair, M. J., & Powell, S. F. (2018). Pembrolizumab plus chemotherapy in metastatic non–small-cell lung cancer. *New England Journal of Medicine*, *378*(22), 2078–2092.

Garon, E. B., Rizvi, N. A., Hui, R., Leighl, N., Balmanoukian, A. S., Eder, J. P., Patnaik, A., Aggarwal, C., Gubens, M., & Horn, L. (2015). Pembrolizumab for the treatment of non–small-cell lung cancer. *New England Journal of Medicine*, *372*(21), 2018–2028.

Gay, C. M., Balaji, K., & Byers, L. A. (2017). Giving AXL the axe: Targeting AXL in human malignancy. *British Journal of Cancer*, *116*(4), 415–423. https://doi.org/10.1038/bjc.2016.428

Gerrard, T. L., Cohen, D. J., & Kaplan, A. M. (1981). Human neutrophil-mediated cytotoxicity to tumor cells. *Journal of the National Cancer Institute*, *66*(3), 483–488.

Goyette, M.-A., Duhamel, S., Aubert, L., Pelletier, A., Savage, P., Thibault, M.-P., Johnson, R. M., Carmeliet, P., Basik, M., & Gaboury, L. (2018). The receptor tyrosine kinase AXL is required at multiple steps of the metastatic cascade during HER2-positive breast cancer progression. *Cell Reports*, *23*(5), 1476–1490.

Guo, X., Zhang, Y., Zheng, L., Zheng, C., Song, J., Zhang, Q., Kang, B., Liu, Z., Jin, L., Xing, R., Gao, R., Zhang, L., Dong, M., Hu, X., Ren, X., Kirchhoff, D., Roider, H. G., Yan, T., & Zhang, Z. (2018a). Global characterization of T cells in non-small-cell lung cancer by single-cell sequencing. *Nature Medicine*, *24*(7), 978–985. https://doi.org/10.1038/s41591-018-0045-3

Guo, X., Zhang, Y., Zheng, L., Zheng, C., Song, J., Zhang, Q., Kang, B., Liu, Z., Jin, L., Xing, R., Gao, R., Zhang, L., Dong, M., Hu, X., Ren, X., Kirchhoff, D., Roider, H. G., Yan, T., & Zhang, Z. (2018b). Global characterization of T cells in non-small-cell lung cancer by single-cell sequencing. *Nature Medicine*, *24*(7), 978–985. https://doi.org/10.1038/s41591-018-0045-3

Haczku, A. (2008). Protective role of the lung collectins surfactant protein A and surfactant protein D in airway inflammation. *Journal of Allergy and Clinical Immunology*, *122*(5), 861–879.

Han, C., Liu, Z., Zhang, Y., Shen, A., Dong, C., Zhang, A., Moore, C., Ren, Z., Lu, C., Cao, X., Zhang, C. L., Qiao, J., & Fu, Y. X. (2020). Tumor cells suppress radiation-induced immunity by hijacking caspase 9 signaling. *Nature Immunology*, *21*(5), 546–554. https://doi.org/10.1038/s41590-020-0641-5

Hanahan, D, & Weinberg, R. (2015). *Chapter 2 : Hallmarks of Cancer : An Organizing Principle for Cancer Medicine*.

Hanahan, Douglas, & Weinberg, R. A. (2011). Hallmarks of cancer: the next generation. *Cell*, *144*(5), 646–674.

Hao, N.-B., Lü, M.-H., Fan, Y.-H., Cao, Y.-L., Zhang, Z.-R., & Yang, S.-M. (2012). Macrophages in tumor microenvironments and the progression of tumors. *Clinical and Developmental Immunology*, *2012*.

Hartmann, E., Wollenberg, B., Rothenfusser, S., Wagner, M., Wellisch, D., Mack, B., Giese, T., Gires, O., Endres, S., & Hartmann, G. (2003). Identification and functional analysis of tumor-infiltrating plasmacytoid dendritic cells in head and neck cancer. *Cancer Research*, *63*(19), 6478–6487.

Hellmann, M. D., Ciuleanu, T.-E., Pluzanski, A., Lee, J. S., Otterson, G. A., Audigier-Valette, C., Minenza, E., Linardou, H., Burgers, S., & Salman, P. (2018). Nivolumab plus ipilimumab in lung cancer with a high tumor mutational burden. *New England Journal of Medicine*, *378*(22), 2093–2104.

Hellmann, M. D., Paz-Ares, L., Bernabe Caro, R., Zurawski, B., Kim, S.-W., Carcereny Costa, E., Park, K., Alexandru, A., Lupinacci, L., & de la Mora Jimenez, E. (2019). Nivolumab plus ipilimumab in advanced non–small-cell lung cancer. *New England Journal of Medicine*, *381*(21), 2020–2031.

Herbst, R. S., Baas, P., Kim, D.-W., Felip, E., Pérez-Gracia, J. L., Han, J.-Y., Molina, J., Kim, J.-H., Arvis, C. D., & Ahn, M.-J. (2016). Pembrolizumab versus docetaxel for previously treated, PD-L1-positive, advanced non-small-cell lung cancer (KEYNOTE-010): a randomised controlled trial. *The Lancet*, *387*(10027), 1540–1550.

Herbst, R. S., Morgensztern, D., & Boshoff, C. (2018). The biology and management of non-small cell lung cancer. *Nature*, *553*(7689), 446–454. https://doi.org/10.1038/nature25183

Hermans, I. F., Silk, J. D., Gileadi, U., Salio, M., Mathew, B., Ritter, G., Schmidt, R., Harris, A. L., Old, L., & Cerundolo, V. (2003). NKT cells enhance CD4+ and CD8+ T cell responses to soluble antigen in vivo through direct interaction with dendritic cells. *The Journal of Immunology*, *171*(10), 5140–5147.

Hiraoka, K., Miyamoto, M., Cho, Y., Suzuoki, M., Oshikiri, T., Nakakubo, Y., Itoh, T., Ohbuchi, T., & Kondo, S. (2006). *Concurrent infiltration by CD8 þ T cells and CD4 þ T cells is a favourable prognostic factor in non-small-cell lung*

carcinoma. *January*, 275–280. https://doi.org/10.1038/sj.bjc.6602934

Hodi, F. S., O'Day, S. J., McDermott, D. F., Weber, R. W., Sosman, J. A., Haanen, J. B., Gonzalez, R., Robert, C., Schadendorf, D., & Hassel, J. C. (2010). Improved survival with ipilimumab in patients with metastatic melanoma. *New England Journal of Medicine*, *363*(8), 711–723.

Hollstein, P. E., Eichner, L. J., Brun, S. N., Kamireddy, A., Svensson, R. U., Vera, L. I., Ross, D. S., Rymoff, T. J., Hutchins, A., Galvez, H. M., Williams, A. E., Shokhirev, M. N., Screaton, R. A., Berdeaux, R., & Shaw, R. J. (2019). The AMPK-related kinases SIK1 and SIK3 mediate key tumor-suppressive effects of LKB1 in NSCLC. *Cancer Discovery*, *9*(11), 1606–1627. https://doi.org/10.1158/2159-8290.CD-18-1261

Holmgaard, R. B., Zamarin, D., Li, Y., Gasmi, B., Munn, D. H., Allison, J. P., Merghoub, T., & Wolchok, J. D. (2015). Tumor-expressed IDO recruits and activates MDSCs in a Treg-dependent manner. *Cell Reports*, *13*(2), 412–424.

Im, S. J., Hashimoto, M., Gerner, M. Y., Lee, J., Kissick, H. T., Burger, M. C., Shan, Q., Hale, J. S., Lee, J., Nasti, T. H., Sharpe, A. H., Freeman, G. J., Germain, R. N., Nakaya, H. I., Xue, H. H., & Ahmed, R. (2016). Defining CD8+ T cells that provide the proliferative burst after PD-1 therapy. *Nature*, *537*(7620), 417–421. https://doi.org/10.1038/nature19330

Ireland, A. S., Micinski, A. M., Kastner, D. W., Guo, B., Wait, S. J., Spainhower, K. B., Conley, C. C., Chen, O. S., Guthrie, M. R., & Soltero, D. (2020). MYC drives temporal evolution of small cell lung cancer subtypes by reprogramming neuroendocrine fate. *Cancer Cell*, *38*(1), 60–78.

Jablonska, J., Leschner, S., Westphal, K., Lienenklaus, S., & Weiss, S. (2010). Neutrophils responsive to endogenous IFN-β regulate tumor angiogenesis and growth in a mouse tumor model. *The Journal of Clinical Investigation*, *120*(4), 1151–1164.

Jamal-Hanjani, M., Wilson, G. A., McGranahan, N., Birkbak, N. J., Watkins, T. B. K., Veeriah, S., Shafi, S., Johnson, D. H., Mitter, R., & Rosenthal, R. (2017). Tracking the evolution of non–small-cell lung cancer. *New England Journal of Medicine*, *376*(22), 2109–2121.

Jeanson, A., Tomasini, P., Souquet-Bressand, M., Brandone, N., Boucekine, M., Grangeon, M., Chaleat, S., Khobta, N., Milia, J., & Mhanna, L. (2019). Efficacy of immune checkpoint inhibitors in KRAS-mutant non-small cell lung cancer (NSCLC). *Journal of Thoracic Oncology*, *14*(6), 1095–1101.

Ji, H., Ramsey, M. R., Hayes, D. N., Fan, C., McNamara, K., Kozlowski, P., Torrice, C., Wu, M. C., Shimamura, T., Perera, S. A., Liang, M. C., Cai, D., Naumov, G. N., Bao, L., Contreras, C. M., Li, D., Chen, L., Krishnamurthy, J., Koivunen, J., … Wong, K. K. (2007). LKB1 modulates lung cancer

differentiation and metastasis. *Nature*, *448*(7155), 807–810. https://doi.org/10.1038/nature06030

Junt, T., Moseman, E. A., Iannacone, M., Massberg, S., Lang, P. A., Boes, M., Fink, K., Henrickson, S. E., Shayakhmetov, D. M., & Di Paolo, N. C. (2007). Subcapsular sinus macrophages in lymph nodes clear lymph-borne viruses and present them to antiviral B cells. *Nature*, *450*(7166), 110–114.

Kadara, H., Choi, M., Zhang, J., Parra, E. R., Rodriguez-Canales, J., Gaffney, S. G., Zhao, Z., Behrens, C., Fujimoto, J., & Chow, C. (2017). Whole-exome sequencing and immune profiling of early-stage lung adenocarcinoma with fully annotated clinical follow-up. *Annals of Oncology*, *28*(1), 75–82.

Kettunen, E., Hernandez-Vargas, H., Cros, M., Durand, G., Le Calvez-Kelm, F., Stuopelyte, K., Jarmalaite, S., Salmenkivi, K., Anttila, S., & Wolff, H. (2017). Asbestos-associated genome-wide DNA methylation changes in lung cancer. *International Journal of Cancer*, *141*(10), 2014–2029.

Kim, D., Bach, D.-H., Fan, Y.-H., Hong, J.-Y., Park, H. J., & Lee, S. K. (2019). AXL degradation in combination with EGFR-TKI can delay and overcome acquired resistance in human non-small cell lung cancer cells. *Cell Death & Disease*, *10*(5), 1–12.

Kim, J., Hu, Z., Cai, L., Li, K., Choi, E., Faubert, B., Bezwada, D., Rodriguez-Canales, J., Villalobos, P., Lin, Y. F., Ni, M., Huffman, K. E., Girard, L., Byers, L. A., Unsal-Kacmaz, K., Peña, C. G., Heymach, J. V., Wauters, E., Vansteenkiste, J., … Deberardinis, R. J. (2017). CPS1 maintains pyrimidine pools and DNA synthesis in KRAS/LKB1-mutant lung cancer cells. *Nature*, *546*(7656), 168–172. https://doi.org/10.1038/nature22359

Kim, S.-H., Cho, E., Kim, Y. I., Han, C., Choi, B. K., & Kwon, B. S. (2021). Adoptive immunotherapy with transient anti-CD4 treatment enhances anti-tumor response by increasing IL-18Rαhi CD8+ T cells. *Nature Communications*, *12*(1), 1–15.

Koivunen, J. P., Kim, J., Lee, J., Rogers, A. M., Park, J. O., Zhao, X., Naoki, K., Okamoto, I., Nakagawa, K., & Yeap, B. Y. (2008). Mutations in the LKB1 tumour suppressor are frequently detected in tumours from Caucasian but not Asian lung cancer patients. *British Journal of Cancer*, *99*(2), 245–252.

Kortlever, R. M., Sodir, N. M., Wilson, C. H., Burkhart, D. L., Pellegrinet, L., Brown Swigart, L., Littlewood, T. D., & Evan, G. I. (2017). Myc Cooperates with Ras by Programming Inflammation and Immune Suppression. *Cell*, *171*(6), 1301-1315.e14. https://doi.org/10.1016/j.cell.2017.11.013

Koyama, S., Akbay, E. A., Li, Y. Y., Aref, A. R., Skoulidis, F., Herter-Sprie, G. S., Buczkowski, K. A., Liu, Y., Awad, M. M., Denning, W. L., Diao, L., Wang, J., Parra-Cuentas, E. R., Wistuba, I. I., Soucheray, M., Thai, T., Asahina, H., Kitajima, S., Altabef, A., … Wong, K. K. (2016a). STK11/LKB1 deficiency

promotes neutrophil recruitment and proinflammatory cytokine production to suppress T-cell activity in the lung tumor microenvironment. *Cancer Research*, *76*(5), 999–1008. https://doi.org/10.1158/0008-5472.CAN-15-1439

Koyama, S., Akbay, E. A., Li, Y. Y., Aref, A. R., Skoulidis, F., Herter-Sprie, G. S., Buczkowski, K. A., Liu, Y., Awad, M. M., Denning, W. L., Diao, L., Wang, J., Parra-Cuentas, E. R., Wistuba, I. I., Soucheray, M., Thai, T., Asahina, H., Kitajima, S., Altabef, A., … Wong, K. K. (2016b). STK11/LKB1 deficiency promotes neutrophil recruitment and proinflammatory cytokine production to suppress T-cell activity in the lung tumor microenvironment. *Cancer Research*, *76*(5), 999–1008. https://doi.org/10.1158/0008-5472.CAN-15-1439

Kumar, V., Patel, S., Tcyganov, E., & Gabrilovich, D. I. (2016). The nature of myeloid-derived suppressor cells in the tumor microenvironment. *Trends in Immunology*, *37*(3), 208–220.

Kurtulus, S., Madi, A., Kuchroo, V. K., Regev, A., & Correspondence, A. C. A. (2018). Checkpoint Blockade Immunotherapy Induces Dynamic Changes in PD-1-CD8 + Tumor-Infiltrating T Cells. *Immunity*, *50*(1), 181-194.e6. https://doi.org/10.1016/j.immuni.2018.11.014

La Manno, G., Soldatov, R., Zeisel, A., Braun, E., Hochgerner, H., Petukhov, V., Lidschreiber, K., Kastriti, M. E., Lönnerberg, P., Furlan, A., Fan, J., Borm, L. E., Liu, Z., van Bruggen, D., Guo, J., He, X., Barker, R., Sundström, E., Castelo-Branco, G., … Kharchenko, P. V. (2018). RNA velocity of single cells. *Nature*, *560*(7719), 494–498. https://doi.org/10.1038/s41586-018-0414-6

Larsen, J. E., & Minna, J. D. (2011). Molecular biology of lung cancer: clinical implications. *Clinics in Chest Medicine*, *32*(4), 703–740.

Leach, D. R., Krummel, M. F., & Allison, J. P. (1996). Enhancement of antitumor immunity by CTLA-4 blockade. *Science*, *271*(5256), 1734–1736.

Lee, C. K., Man, J., Lord, S., Links, M., Gebski, V., Mok, T., & Yang, J. C.-H. (2017). Checkpoint inhibitors in metastatic EGFR-mutated non–small cell lung cancer—a meta-analysis. *Journal of Thoracic Oncology*, *12*(2), 403–407.

Li, B., Liu, J. S., & Liu, X. S. (2017). Revisit linear regression-based deconvolution methods for tumor gene expression data. *Genome Biology*, *18*(1), 127. https://doi.org/10.1186/s13059-017-1256-5

Li, W., Lu, L., Lu, J., Wang, X., Yang, C., Jin, J., Wu, L., Hong, X., Li, F., Cao, D., Yang, Y., Wu, M., Su, B., Cheng, J., Yang, X., Di, W., & Deng, L. (2020). cGAS-STING-mediated DNA sensing maintains CD8+ T cell stemness and promotes antitumor T cell therapy. *Science Translational Medicine*, *12*(549),

1–15. https://doi.org/10.1126/scitranslmed.aay9013

Linehan, J. L., Dileepan, T., Kashem, S. W., Kaplan, D. H., Cleary, P., & Jenkins, M. K. (2015). Generation of Th17 cells in response to intranasal infection requires TGF-β1 from dendritic cells and IL-6 from CD301b+ dendritic cells. *Proceedings of the National Academy of Sciences*, *112*(41), 12782–12787.

Lisberg, A., Cummings, A., Goldman, J. W., Bornazyan, K., Reese, N., Wang, T., Coluzzi, P., Ledezma, B., Mendenhall, M., & Hunt, J. (2018). A phase II study of pembrolizumab in EGFR-mutant, PD-L1+, tyrosine kinase inhibitor naïve patients with advanced NSCLC. *Journal of Thoracic Oncology*, *13*(8), 1138–1145.

Liu, X., Pu, Y., Cron, K., Deng, L., Kline, J., Frazier, W. A., Xu, H., Peng, H., Fu, Y. X., & Xu, M. M. (2015). CD47 blockade triggers T cell-mediated destruction of immunogenic tumors. *Nature Medicine*, *21*(10), 1209–1215. https://doi.org/10.1038/nm.3931

Liu, Z., Han, C., Dong, C., Shen, A., Hsu, E., Ren, Z., Lu, C., Liu, L., Zhang, A., & Timmerman, C. (2019). Hypofractionated EGFR tyrosine kinase inhibitor limits tumor relapse through triggering innate and adaptive immunity. *Science Immunology*, *4*(38).

Lorenzo-González, M., Ruano-Ravina, A., Torres-Durán, M., Kelsey, K. T., Provencio, M., Parente-Lamelas, I., Leiro-Fernández, V., Vidal-García, I., Castro-Añón, O., & Martínez, C. (2019). Lung cancer and residential radon in never-smokers: A pooling study in the Northwest of Spain. *Environmental Research*, *172*, 713–718.

Lotsberg, M. L., Wnuk-Lipinska, K., Terry, S., Tan, T. Z., Lu, N., Trachsel-Moncho, L., Røsland, G. V, Siraji, M. I., Hellesøy, M., & Rayford, A. (2020). AXL targeting abrogates autophagic flux and induces immunogenic cell death in drug-resistant cancer cells. *Journal of Thoracic Oncology*, *15*(6), 973–999.

Ludwig, K. F., Du, W., Sorrelle, N. B., Wnuk-lipinska, K., Topalovski, M., Toombs, J. E., Cruz, V. H., Yabuuchi, S., Rajeshkumar, N. V, Maitra, A., Lorens, J. B., & Brekken, R. A. (2018). *Small-Molecule Inhibition of Axl Targets Tumor Immune Suppression and Enhances Chemotherapy in Pancreatic Cancer*. *78*(10), 246–256. https://doi.org/10.1158/0008-5472.CAN-17-1973

Luoma, A. M., Suo, S., Williams, H. L., Sharova, T., Sullivan, K., Manos, M., Bowling, P., Hodi, F. S., Rahma, O., Sullivan, R. J., Boland, G. M., Nowak, J. A., Dougan, S. K., Dougan, M., Yuan, G. C., & Wucherpfennig, K. W. (2020). Molecular Pathways of Colon Inflammation Induced by Cancer Immunotherapy. *Cell*, *182*(3), 655-671.e22. https://doi.org/10.1016/j.cell.2020.06.001

Maier, B., Leader, A. M., Chen, S. T., Tung, N., Chang, C., LeBerichel, J.,

Chudnovskiy, A., Maskey, S., Walker, L., & Finnigan, J. P. (2020). A conserved dendritic-cell regulatory program limits antitumour immunity. *Nature*, *580*(7802), 257–262.

Mantovani, A., Allavena, P., Sica, A., & Balkwill, F. (2008). Cancer-related inflammation. *Nature*, *454*(7203), 436–444.

Marabelle, A., Le, D. T., Ascierto, P. A., Di Giacomo, A. M., De Jesus-Acosta, A., Delord, J.-P., Geva, R., Gottfried, M., Penel, N., & Hansen, A. R. (2020). Efficacy of pembrolizumab in patients with noncolorectal high microsatellite instability/mismatch repair–deficient cancer: Results from the phase II KEYNOTE-158 study. *Journal of Clinical Oncology*, *38*(1), 1.

Matteson, R. (2010). *DepMap: Dependency Mapping of Applications Using Operating System Events*.

McInnes, L., Healy, J., & Melville, J. (2018). Umap: Uniform manifold approximation and projection for dimension reduction. *ArXiv Preprint ArXiv:1802.03426*.

Mender, I., Zhang, A., Ren, Z., Han, C., Deng, Y., Siteni, S., Li, H., Zhu, J., Vemula, A., Shay, J. W., & Fu, Y. X. (2020). Telomere Stress Potentiates STING-Dependent Anti-tumor Immunity. *Cancer Cell*, 1–12. https://doi.org/10.1016/j.ccell.2020.05.020

Miller, B. C., Sen, D. R., Al Abosy, R., Bi, K., Virkud, Y. V., LaFleur, M. W., Yates, K. B., Lako, A., Felt, K., Naik, G. S., Manos, M., Gjini, E., Kuchroo, J. R., Ishizuka, J. J., Collier, J. L., Griffin, G. K., Maleri, S., Comstock, D. E., Weiss, S. A., … Haining, W. N. (2019). Subsets of exhausted CD8 + T cells differentially mediate tumor control and respond to checkpoint blockade. *Nature Immunology*, *20*(3), 326–336. https://doi.org/10.1038/s41590-019-0312-6

Mishalian, I., Bayuh, R., Levy, L., Zolotarov, L., Michaeli, J., & Fridlender, Z. G. (2013). Tumor-associated neutrophils (TAN) develop pro-tumorigenic properties during tumor progression. *Cancer Immunology, Immunotherapy*, *62*(11), 1745–1756.

Miyano, K., Matsushita, S., Tsuchida, T., & Nakamura, K. (2016). Inhibitory effect of a histamine 4 receptor antagonist on CCL17 and CCL22 production by monocyte-derived Langerhans cells in patients with atopic dermatitis. *The Journal of Dermatology*, *43*(9), 1024–1029.

Mok, T. S. K., Wu, Y.-L., Kudaba, I., Kowalski, D. M., Cho, B. C., Turna, H. Z., Castro Jr, G., Srimuninnimit, V., Laktionov, K. K., & Bondarenko, I. (2019). Pembrolizumab versus chemotherapy for previously untreated, PD-L1-expressing, locally advanced or metastatic non-small-cell lung cancer (KEYNOTE-042): a randomised, open-label, controlled, phase 3 trial. *The Lancet*, *393*(10183), 1819–1830.

Mori, L., Lepore, M., & De Libero, G. (2016). The Immunology of CD1- and MR1-Restricted T Cells. *Annual Review of Immunology*, *34*(1), 479–510. https://doi.org/10.1146/annurev-immunol-032414-112008

Nosho, K., Baba, Y., Tanaka, N., Shima, K., Hayashi, M., Meyerhardt, J. A., Giovannucci, E., Dranoff, G., Fuchs, C. S., & Ogino, S. (2010). Tumour-infiltrating T-cell subsets, molecular changes in colorectal cancer, and prognosis: Cohort study and literature review. *Journal of Pathology*, *222*(4), 350–366. https://doi.org/10.1002/path.2774

Oliveira, L. D. M., Teixeira, F. M. E., & Sato, M. N. (2018). Impact of Retinoic Acid on Immune Cells and Inflammatory Diseases. *Mediators of Inflammation*, *2018*. https://doi.org/10.1155/2018/3067126

Olsson, A. C., Vermeulen, R., Schüz, J., Kromhout, H., Pesch, B., Peters, S., Behrens, T., Portengen, L., Mirabelli, D., & Gustavsson, P. (2017). Exposure–response analyses of asbestos and lung cancer subtypes in a pooled analysis of case–control studies. *Epidemiology (Cambridge, Mass.)*, *28*(2), 288.

Ott, P. A., Bang, Y. J., Piha-Paul, S. A., Razak, A. R. A., Bennouna, J., Soria, J. C., Rugo, H. S., Cohen, R. B., O'Neil, B. H., & Mehnert, J. M. (2019). T-cell–inflamed gene-expression profile, programmed death ligand 1 expression, and tumor mutational burden predict efficacy in patients treated with pembrolizumab across 20 cancers: KEYNOTE-028. *Journal of Clinical Oncology*, *37*(4), 318–327.

Papillon-Cavanagh, S., Doshi, P., Dobrin, R., Szustakowski, J., & Walsh, A. M. (2020). STK11 and KEAP1 mutations as prognostic biomarkers in an observational real-world lung adenocarcinoma cohort. *ESMO Open*, *5*(2), e000706.

Park, C. Y., Majeti, R., & Weissman, I. L. (2008). In vivo evaluation of human hematopoiesis through xenotransplantation of purified hematopoietic stem cells from umbilical cord blood. *Nature Protocols*, *3*(12), 1932.

Pass, H. I., Carbone, D. P., Johnson, D. H., Minna, J. D., Scagliotti, G. V, & Turrisi, A. T. (2012). *Principles and Practice of Lung Cancer: the official reference text of the International Association for the Study of Lung Cancer (IASLC)*. Lippincott Williams & Wilkins.

Pavan, A., Attili, I., Pasello, G., Guarneri, V., Conte, P. F., & Bonanno, L. (2019). Immunotherapy in small-cell lung cancer: from molecular promises to clinical challenges. *Journal for Immunotherapy of Cancer*, *7*(1), 1–13.

Pavlova, N. N., & Thompson, C. B. (2016). The emerging hallmarks of cancer metabolism. *Cell Metabolism*, *23*(1), 27–47.

Pedroza-Gonzalez, A., Xu, K., Wu, T.-C., Aspord, C., Tindle, S., Marches, F., Gallegos, M., Burton, E. C., Savino, D., & Hori, T. (2011). Thymic stromal

lymphopoietin fosters human breast tumor growth by promoting type 2 inflammation. *Journal of Experimental Medicine*, *208*(3), 479–490.

Perez-Moreno, P., Brambilla, E., Thomas, R., & Soria, J.-C. (2012). Squamous cell carcinoma of the lung: molecular subtypes and therapeutic opportunities. *Clinical Cancer Research*, *18*(9), 2443–2451.

Pope Iii, C. A., Burnett, R. T., Thun, M. J., Calle, E. E., Krewski, D., Ito, K., & Thurston, G. D. (2002). Lung cancer, cardiopulmonary mortality, and long-term exposure to fine particulate air pollution. *Jama*, *287*(9), 1132–1141.

Qiu, X., Mao, Q., Tang, Y., Wang, L., Chawla, R., Pliner, H. A., & Trapnell, C. (2017). Reversed graph embedding resolves complex single-cell trajectories. *Nature Methods*, *14*(10), 979.

Ready, N., Hellmann, M. D., Awad, M. M., Otterson, G. A., Gutierrez, M., Gainor, J. F., Borghaei, H., Jolivet, J., Horn, L., & Mates, M. (2019). First-line nivolumab plus ipilimumab in advanced non–small-cell lung cancer (CheckMate 568): outcomes by programmed death ligand 1 and tumor mutational burden as biomarkers. *Journal of Clinical Oncology*, *37*(12), 992.

Reck, M., Rodriguez-Abreu, D., Robinson, A., Hui, R., Csoszi, T., Fulop, A., Gottfried, M., Peled, N., Tafreshi, A., & Cuffe, S. (2019). *Updated analysis of KEYNOTE-024: pembrolizumab versus platinum-based chemotherapy for advanced non-small-cell lung cancer with PD-L1 tumor proportion score of 50% or greater*.

Ren, Z., Guo, J., Liao, J., Luan, Y., Liu, Z., Sun, Z., Liu, X., Liang, Y., Peng, H., & Fu, Y. X. (2017). CTLA-4 limits anti-CD20-mediated tumor regression. *Clinical Cancer Research*, *23*(1), 193–203. https://doi.org/10.1158/1078-0432.CCR-16-0040

Rizvi, N. A., Hellmann, M. D., Snyder, A., Kvistborg, P., Makarov, V., Havel, J. J., Lee, W., Yuan, J., Wong, P., & Ho, T. S. (2015). Mutational landscape determines sensitivity to PD-1 blockade in non–small cell lung cancer. *Science*, *348*(6230), 124–128.

Roberts, E. W., Broz, M. L., Binnewies, M., Headley, M. B., Nelson, A. E., Wolf, D. M., Kaisho, T., Bogunovic, D., Bhardwaj, N., & Krummel, M. F. (2016). Critical role for CD103+/CD141+ dendritic cells bearing CCR7 for tumor antigen trafficking and priming of T cell immunity in melanoma. *Cancer Cell*, *30*(2), 324–336.

Rothlin, C. V., Ghosh, S., Zuniga, E. I., Oldstone, M. B. A., & Lemke, G. (2007). TAM Receptors Are Pleiotropic Inhibitors of the Innate Immune Response. *Cell*, *131*(6), 1124–1136. https://doi.org/10.1016/j.cell.2007.10.034

Rudin, C. M., Awad, M. M., Navarro, A., Gottfried, M., Peters, S., Csőszi, T., Cheema, P. K., Rodriguez-Abreu, D., Wollner, M., & Czyzewicz, G. (2020). *KEYNOTE-604: Pembrolizumab (pembro) or placebo plus etoposide and*

platinum (EP) as first-line therapy for extensive-stage (ES) small-cell lung cancer (SCLC). American Society of Clinical Oncology.

Rudin, C. M., Poirier, J. T., Byers, L. A., Dive, C., Dowlati, A., George, J., Heymach, J. V, Johnson, J. E., Lehman, J. M., & MacPherson, D. (2019). Molecular subtypes of small cell lung cancer: a synthesis of human and mouse model data. *Nature Reviews Cancer*, *19*(5), 289–297.

Salio, M., Silk, J. D., Yvonne Jones, E., & Cerundolo, V. (2014). Biology of CD1- and MR1-restricted T cells. *Annual Review of Immunology*, *32*, 323–366. https://doi.org/10.1146/annurev-immunol-032713-120243

Saltos, A., Shafique, M., & Chiappori, A. (2020). Update on the biology, management, and treatment of small cell lung cancer (SCLC). *Frontiers in Oncology*, *10*.

Samet, J. M. (1991). Health benefits of smoking cessation. *Clinics in Chest Medicine*, *12*(4), 669–679.

Sancho, D., Joffre, O. P., Keller, A. M., Rogers, N. C., Martinez, D., Hernanz-Falcón, P., Rosewell, I., & e Sousa, C. R. (2009). Identification of a dendritic cell receptor that couples sensing of necrosis to immunity. *Nature*, *458*(7240), 899–903.

Sangaletti, S., Tripodo, C., Chiodoni, C., Guarnotta, C., Cappetti, B., Casalini, P., Piconese, S., Parenza, M., Guiducci, C., & Vitali, C. (2012). Neutrophil extracellular traps mediate transfer of cytoplasmic neutrophil antigens to myeloid dendritic cells toward ANCA induction and associated autoimmunity. *Blood, The Journal of the American Society of Hematology*, *120*(15), 3007–3018.

Sanjana, N. E., Shalem, O., & Zhang, F. (2014). Improved vectors and genome-wide libraries for CRISPR screening. *Nature Methods*, *11*(8), 783.

Schlitzer, A., Sivakamasundari, V., Chen, J., Sumatoh, H. R. Bin, Schreuder, J., Lum, J., Malleret, B., Zhang, S., Larbi, A., & Zolezzi, F. (2015). Identification of cDC1-and cDC2-committed DC progenitors reveals early lineage priming at the common DC progenitor stage in the bone marrow. *Nature Immunology*, *16*(7), 718–728.

Schmid, E. T., Pang, I. K., Carrera Silva, E. A., Bosurgi, L., Miner, J. J., Diamond, M. S., Iwasaki, A., & Rothlin, C. V. (2016). AXL receptor tyrosine kinase is required for T cell priming and antiviral immunity. *ELife*, *5*, 1–18. https://doi.org/10.7554/elife.12414

Seitz, H. M., Camenisch, T. D., Lemke, G., Earp, H. S., & Matsushima, G. K. (2007). Macrophages and Dendritic Cells Use Different Axl/Mertk/Tyro3 Receptors in Clearance of Apoptotic Cells. *The Journal of Immunology*, *178*(9), 5635–5642. https://doi.org/10.4049/jimmunol.178.9.5635

Shackelford, D. B., & Shaw, R. J. (2009). The LKB1–AMPK pathway: metabolism and growth control in tumour suppression. *Nature Reviews Cancer*, *9*(8), 563–575.

Shankar, A., Dubey, A., Saini, D., Singh, M., Prasad, C. P., Roy, S., Bharati, S. J., Rinki, M., Singh, N., & Seth, T. (2019). Environmental and occupational determinants of lung cancer. *Translational Lung Cancer Research*, *8*(Suppl 1), S31.

Shaverdian, N., Lisberg, A. E., Bornazyan, K., Veruttipong, D., Goldman, J. W., Formenti, S. C., Garon, E. B., & Lee, P. (2017). Previous radiotherapy and the clinical activity and toxicity of pembrolizumab in the treatment of non-small-cell lung cancer: a secondary analysis of the KEYNOTE-001 phase 1 trial. *The Lancet Oncology*, *18*(7), 895–903.

Shiao, S. L., Ruffell, B., DeNardo, D. G., Faddegon, B. A., Park, C. C., & Coussens, L. M. (2015). TH2-polarized CD4+ T cells and macrophages limit efficacy of radiotherapy. *Cancer Immunology Research*, *3*(5), 518–525.

Shire, N. J., Klein, A. B., Golozar, A., Collins, J. M., Fraeman, K. H., Nordstrom, B. L., McEwen, R., Hembrough, T., & Rizvi, N. A. (2020). STK11 (LKB1) mutations in metastatic NSCLC: Prognostic value in the real world. *Plos One*, *15*(9), e0238358.

Siddik, Z. H. (2002). Mechanisms of action of cancer chemotherapeutic agents: DNA-interactive alkylating agents and antitumour platinum-based drugs. *The Cancer Handbook*, *1*.

Siddiqui, I., Schaeuble, K., Chennupati, V., Fuertes Marraco, S. A., Calderon-Copete, S., Pais Ferreira, D., Carmona, S. J., Scarpellino, L., Gfeller, D., Pradervand, S., Luther, S. A., Speiser, D. E., & Held, W. (2019). Intratumoral Tcf1 + PD-1 + CD8 + T Cells with Stem-like Properties Promote Tumor Control in Response to Vaccination and Checkpoint Blockade Immunotherapy. *Immunity*, *50*(1), 195-211.e10. https://doi.org/10.1016/j.immuni.2018.12.021

Siddiqui, I., Schaeuble, K., Chennupati, V., Marraco, S. A. F., Calderon-Copete, S., Ferreira, D. P., Carmona, S. J., Scarpellino, L., Gfeller, D., & Pradervand, S. (2019). Intratumoral Tcf1+ PD-1+ CD8+ T cells with stem-like properties promote tumor control in response to vaccination and checkpoint blockade immunotherapy. *Immunity*, *50*(1), 195–211.

Siegel, R. L., Miller, K. D., Fuchs, H. E., & Jemal, A. (2021). Cancer Statistics, 2021. *CA: A Cancer Journal for Clinicians*, *71*(1), 7–33.

Silk, J. D., Hermans, I. F., Gileadi, U., Chong, T. W., Shepherd, D., Salio, M., Mathew, B., Schmidt, R. R., Lunt, S. J., & Williams, K. J. (2004). Utilizing the adjuvant properties of CD1d-dependent NK T cells in T cell–mediated immunotherapy. *The Journal of Clinical Investigation*, *114*(12), 1800–1811.

Singal, G., Miller, P. G., Agarwala, V., He, J., Gossai, A., Frank, S., Bourque, D., Bowser, B., Caron, T., & Baydur, E. (2017). Development and validation of a real-world clinicogenomic database. *Am. Soc. Clin. Oncol*, *35*, 2514.

Skoulidis, F., Arbour, K. C., Hellmann, M. D., Patil, P. D., Marmarelis, M. E., Awad, M. M., Murray, J. C., Hellyer, J., Gainor, J. F., & Dimou, A. (2019). *Association of STK11/LKB1 genomic alterations with lack of benefit from the addition of pembrolizumab to platinum doublet chemotherapy in non-squamous non-small cell lung cancer.* American Society of Clinical Oncology.

Skoulidis, F., Byers, L. A., Diao, L., Papadimitrakopoulou, V. A., Tong, P., Izzo, J., Behrens, C., Kadara, H., Parra, E. R., & Canales, J. R. (2015). Co-occurring genomic alterations define major subsets of KRAS-mutant lung adenocarcinoma with distinct biology, immune profiles, and therapeutic vulnerabilities. *Cancer Discovery*, *5*(8), 860–877.

Skoulidis, F., Goldberg, M. E., Greenawalt, D. M., Hellmann, M. D., Awad, M. M., Gainor, J. F., Schrock, A. B., Hartmaier, R. J., Trabucco, S. E., Gay, L., Ali, S. M., Elvin, J. A., Singal, G., Ross, J. S., Fabrizio, D., Szabo, P. M., Chang, H., Sasson, A., Srinivasan, S., … Heymach, J. V. (2018a). STK11/LKB1 mutations and PD-1 inhibitor resistance in KRAS-mutant lung adenocarcinoma. *Cancer Discovery*, *8*(7), 822–835. https://doi.org/10.1158/2159-8290.CD-18-0099

Skoulidis, F., Goldberg, M. E., Greenawalt, D. M., Hellmann, M. D., Awad, M. M., Gainor, J. F., Schrock, A. B., Hartmaier, R. J., Trabucco, S. E., Gay, L., Ali, S. M., Elvin, J. A., Singal, G., Ross, J. S., Fabrizio, D., Szabo, P. M., Chang, H., Sasson, A., Srinivasan, S., … Heymach, J. V. (2018b). STK11/LKB1 mutations and PD-1 inhibitor resistance in KRAS-mutant lung adenocarcinoma. *Cancer Discovery*, *8*(7), 822–835. https://doi.org/10.1158/2159-8290.CD-18-0099

Solis, L. M., Behrens, C., Raso, M. G., Lin, H. Y., Kadara, H., Yuan, P., Galindo, H., Tang, X., Lee, J. J., & Kalhor, N. (2012). Histologic patterns and molecular characteristics of lung adenocarcinoma associated with clinical outcome. *Cancer*, *118*(11), 2889–2899.

Soltys, C.-L. M., Kovacic, S., & Dyck, J. R. B. (2006). Activation of cardiac AMP-activated protein kinase by LKB1 expression or chemical hypoxia is blunted by increased Akt activity. *American Journal of Physiology-Heart and Circulatory Physiology*, *290*(6), H2472–H2479.

Song, A., Song, J., Tang, X., & Croft, M. (2007). Cooperation between CD4 and CD8 T cells for anti-tumor activity is enhanced by OX40 signals. *European Journal of Immunology*, *37*(5), 1224–1232.

Stuart, T., Butler, A., Hoffman, P., Hafemeister, C., Papalexi, E., Mauck, W. M.,

Hao, Y., Stoeckius, M., Smibert, P., & Satija, R. (2019). Comprehensive Integration of Single-Cell Data. *Cell*, *177*(7), 1888-1902.e21. https://doi.org/10.1016/j.cell.2019.05.031

Tachihara, M., Negoro, S., Inoue, T., Tamiya, M., Akazawa, Y., Uenami, T., Urata, Y., Hattori, Y., Hata, A., & Katakami, N. (2018). Efficacy of anti-PD-1/PD-L1 antibodies after discontinuation due to adverse events in non-small cell lung cancer patients (HANSHIN 0316). *BMC Cancer*, *18*(1), 1–6.

Tang, H., Wang, Y., Chlewicki, L. K., Zhang, Y., Guo, J., Liang, W., Wang, J., Wang, X., & Fu, Y. X. (2016). Facilitating T Cell Infiltration in Tumor Microenvironment Overcomes Resistance to PD-L1 Blockade. *Cancer Cell*, *29*(3), 285–296. https://doi.org/10.1016/j.ccell.2016.02.004

Taniguchi, H., Yamada, T., Wang, R., Tanimura, K., Adachi, Y., Nishiyama, A., Tanimoto, A., Takeuchi, S., Araujo, L. H., & Boroni, M. (2019). AXL confers intrinsic resistance to osimertinib and advances the emergence of tolerant cells. *Nature Communications*, *10*(1), 1–14.

Tazawa, H., Okada, F., Kobayashi, T., Tada, M., Mori, Y., Une, Y., Sendo, F., Kobayashi, M., & Hosokawa, M. (2003). Infiltration of neutrophils is required for acquisition of metastatic phenotype of benign murine fibrosarcoma cells: implication of inflammation-associated carcinogenesis and tumor progression. *The American Journal of Pathology*, *163*(6), 2221–2232.

Teijeira, Á., Garasa, S., Gato, M., Alfaro, C., Migueliz, I., Cirella, A., de Andrea, C., Ochoa, M. C., Otano, I., & Etxeberria, I. (2020). CXCR1 and CXCR2 chemokine receptor agonists produced by tumors induce neutrophil extracellular traps that interfere with immune cytotoxicity. *Immunity*, *52*(5), 856–871.

Theelen, W. S. M. E., Peulen, H. M. U., Lalezari, F., van der Noort, V., De Vries, J. F., Aerts, J. G. J. V, Dumoulin, D. W., Bahce, I., Niemeijer, A.-L. N., & De Langen, A. J. (2019). Effect of pembrolizumab after stereotactic body radiotherapy vs pembrolizumab alone on tumor response in patients with advanced non–small cell lung cancer: results of the PEMBRO-RT phase 2 randomized clinical trial. *JAMA Oncology*, *5*(9), 1276–1282.

Trapnell, C., Cacchiarelli, D., Grimsby, J., Pokharel, P., Li, S., Morse, M., Lennon, N. J., Livak, K. J., Mikkelsen, T. S., & Rinn, J. L. (2014). The dynamics and regulators of cell fate decisions are revealed by pseudotemporal ordering of single cells. *Nature Biotechnology*, *32*(4), 381.

Tseng, D., Volkmer, J.-P., Willingham, S. B., Contreras-Trujillo, H., Fathman, J. W., Fernhoff, N. B., Seita, J., Inlay, M. A., Weiskopf, K., & Miyanishi, M. (2013). Anti-CD47 antibody–mediated phagocytosis of cancer by macrophages primes an effective antitumor T-cell response. *Proceedings of the National Academy of Sciences*, *110*(27), 11103–11108.

Tsukita, Y., Fujino, N., Miyauchi, E., Saito, R., Fujishima, F., Itakura, K., Kyogoku, Y., Okutomo, K., Yamada, M., & Okazaki, T. (2019). Axl kinase drives immune checkpoint and chemokine signalling pathways in lung adenocarcinomas. *Molecular Cancer*, *18*(1), 1–6.

Utzschneider, D. T., Charmoy, M., Chennupati, V., Pousse, L., Ferreira, D. P., Calderon-Copete, S., Danilo, M., Alfei, F., Hofmann, M., Wieland, D., Pradervand, S., Thimme, R., Zehn, D., & Held, W. (2016). T Cell Factor 1-Expressing Memory-like CD8+ T Cells Sustain the Immune Response to Chronic Viral Infections. *Immunity*, *45*(2), 415–427. https://doi.org/10.1016/j.immuni.2016.07.021

Varnum, B. C., Young, C., Elliott, G., Garcia, A., Bartley, T. D., Fridell, Y.-W., Hunt, R. W., Trail, G., Clogston, C., & Toso, R. J. (1995). Axl receptor tyrosine kinase stimulated by the vitamin K-dependent protein encoded by growth-arrest-specific gene 6. *Nature*, *373*(6515), 623–626.

Vono, M., Lin, A., Norrby-Teglund, A., Koup, R. A., Liang, F., & Loré, K. (2017). Neutrophils acquire the capacity for antigen presentation to memory CD4+ T cells in vitro and ex vivo. *Blood, The Journal of the American Society of Hematology*, *129*(14), 1991–2001.

Warth, A., Koerner, S., Penzel, R., Muley, T., Dienemann, H., Schirmacher, P., von Knebel-Doeberitz, M., Weichert, W., & Kloor, M. (2016). Microsatellite instability in pulmonary adenocarcinomas: a comprehensive study of 480 cases. *Virchows Archiv*, *468*(3), 313–319.

Wei, S., Kryczek, I., Zou, L., Daniel, B., Cheng, P., Mottram, P., Curiel, T., Lange, A., & Zou, W. (2005). Plasmacytoid dendritic cells induce CD8+ regulatory T cells in human ovarian carcinoma. *Cancer Research*, *65*(12), 5020–5026.

Weinberg, R. A. (2013). *The biology of cancer*. Garland science.

Wickham, H. (2016). *ggplot2: elegant graphics for data analysis*. springer.

Willingham, S. B., Volkmer, J.-P., Gentles, A. J., Sahoo, D., Dalerba, P., Mitra, S. S., Wang, J., Contreras-Trujillo, H., Martin, R., & Cohen, J. D. (2012). The CD47-signal regulatory protein alpha (SIRPa) interaction is a therapeutic target for human solid tumors. *Proceedings of the National Academy of Sciences*, *109*(17), 6662–6667.

Wistuba, I. I., & Gazdar, A. F. (2006). Lung cancer preneoplasia. *Annu. Rev. Pathol. Mech. Dis.*, *1*, 331–348.

Woo, S. R., Fuertes, M. B., Corrales, L., Spranger, S., Furdyna, M. J., Leung, M. Y. K., Duggan, R., Wang, Y., Barber, G. N., Fitzgerald, K. A., Alegre, M. L., & Gajewski, T. F. (2014). STING-dependent cytosolic DNA sensing mediates innate immune recognition of immunogenic tumors. *Immunity*, *41*(5), 830–842. https://doi.org/10.1016/j.immuni.2014.10.017

Wunderlich, M., Chou, F. S., Link, K., Mizukawa, B., Perry, R. L., Carroll, M., & Mulloy, J. C. (2010). AML xenograft efficiency is significantly improved in NOD/SCID-IL2RG mice constitutively expressing human SCF, GM-CSF and IL-3. *Leukemia*, *24*(10), 1785–1788.

Yang, X., Zhang, X., Fu, M. L., Weichselbaum, R. R., Gajewski, T. F., Guo, Y., & Fu, Y.-X. (2014). Targeting the tumor microenvironment with interferon-β bridges innate and adaptive immune responses. *Cancer Cell*, *25*(1), 37–48.

Yost, K. E., Satpathy, A. T., Wells, D. K., Qi, Y., Wang, C., Kageyama, R., McNamara, K. L., Granja, J. M., Sarin, K. Y., Brown, R. A., Gupta, R. K., Curtis, C., Bucktrout, S. L., Davis, M. M., Chang, A. L. S., & Chang, H. Y. (2019). Clonal replacement of tumor-specific T cells following PD-1 blockade. *Nature Medicine*, *25*(8), 1251–1259. https://doi.org/10.1038/s41591-019-0522-3

Zagórska, A., Través, P. G., Lew, E. D., Dransfield, I., & Lemke, G. (2014). Diversification of TAM receptor tyrosine kinase function. *Nature Immunology*, *15*(10), 920–928.

Zhang, A., Ren, Z., Tseng, K. F., Liu, X., Li, H., Lu, C., Cai, Y., Minna, J. D., & Fu, Y. X. (2021). Dual targeting of CTLA-4 and CD47 on Treg cells promotes immunity against solid tumors. *Science Translational Medicine*, *13*(605), 1–16. https://doi.org/10.1126/scitranslmed.abg8693

Zhong, D., Liu, X., Khuri, F. R., Sun, S.-Y., Vertino, P. M., & Zhou, W. (2008). LKB1 is necessary for Akt-mediated phosphorylation of proapoptotic proteins. *Cancer Research*, *68*(18), 7270–7277.

Zhou, T., Damsky, W., Weizman, O. El, McGeary, M. K., Hartmann, K. P., Rosen, C. E., Fischer, S., Jackson, R., Flavell, R. A., Wang, J., Sanmamed, M. F., Bosenberg, M. W., & Ring, A. M. (2020). IL-18BP is a secreted immune checkpoint and barrier to IL-18 immunotherapy. *Nature*, *583*(7817), 609–614. https://doi.org/10.1038/s41586-020-2422-6